Stability and superconductivity of light-atom systems under extreme pressure

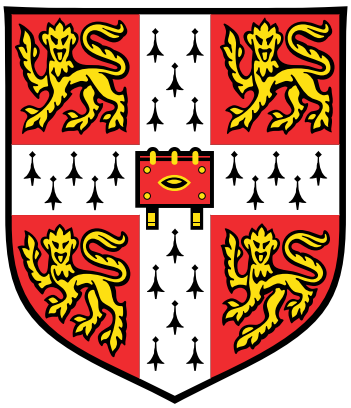

Alice Maude Shipley

Supervisor: Prof. Richard Needs

Department of Physics
University of Cambridge

This dissertation is submitted for the degree of
Doctor of Philosophy

Hughes Hall

March 2021

To Pop

Declaration

This thesis is the result of my own work and includes nothing which is the outcome of work done in collaboration except as declared in the Preface and specified in the text. It is not substantially the same as any that I have submitted, or, is being concurrently submitted for a degree or diploma or other qualification at the University of Cambridge or any other University or similar institution except as declared in the Preface and specified in the text. I further state that no substantial part of my thesis has already been submitted, or, is being concurrently submitted for any such degree, diploma or other qualification at the University of Cambridge or any other University or similar institution except as declared in the Preface and specified in the text. It does not exceed the prescribed word limit for the relevant Degree Committee.

Alice Maude Shipley
March 2021

Abstract

The use of high pressure in physics provides access to unusual chemistry, rich phase behaviour, and various interesting phenomena. One of the most sought after phenomena of recent years is high-temperature superconductivity, which has been predicted in solid hydrogen and experimentally verified in numerous metal hydrides.

This thesis adds to the knowledge of these high-pressure light-atom systems and introduces new tools for predicting their superconducting properties. It showcases the calculation of an anharmonic phase diagram of solid hydrogen, demonstrates that current theoretical techniques can produce structures and superconducting critical temperatures (T_c) in agreement with experiment for the record-holding binary hydride LaH_{10}, and reveals a metastable hexagonal phase of this material that provides an explanation for recent experimental observations. It also addresses the real need to reduce the operational pressure of superconducting hydrides and offers a solution through the use of machine learning methods, leading to the discovery of several superconductors inhabiting favourable regions of P-T_c space.

It is common for papers in this field to focus on the stability and superconductivity of a limited number of metal hydrides, largely because the electron-phonon calculations involved are computationally expensive and because it is not clear which hydrides are potential high-T_c candidates *before* performing these calculations. This drastically slows down the rate of discovery. The work presented in this thesis provides a solution to this problem; by identifying physically motivated descriptors from scattering theory and density of states calculations, we are able to construct a model for T_c and therefore obtain a method for cheaply identifying the most promising candidate structures. Incorporating this screening step into a high-throughput workflow allows us to study superconductivity in binary hydrides from across the whole periodic table, resulting in one of the most comprehensive studies of superconductivity in binary hydrides ever produced and leading to the identification of several above- and near-room-temperature candidates.

The methods developed in this thesis could be expanded to other classes of materials, including ternary hydrides and other light binaries, and used as a guide to designing high-throughput workflows for other material properties. The findings may bring us closer to the ultimate goal of first-principles material design.

Acknowledgements

I am thankful to my supervisor, Prof. Richard Needs, for sharing with me his knowledge of high-pressure physics and enthusiasm for discovery. He has granted me a large amount of freedom in my research, for which I am grateful. I collaborated with Prof. Chris Pickard throughout the final two years of my PhD and to attempt to put into words how much I learnt from him during this time would be doing him a disservice. I have also been fortunate enough to work with several other experts in my field, including Dr Bartomeu Monserrat and Dr Joseph Nelson, whose advice in the early stages of my research was invaluable. Dr John Trail was a supportive and knowledgeable collaborator on the solid hydrogen work, and I am grateful for the many emails exchanged with Dr Po-Hao Chang when I first became acquainted with Gaspari-Gyorffy theory. Special thanks are also due to Prof. Mike Payne and Dr Michael Rutter for their advice and support, and Prof. Andrew Green, without whom I would not have considered condensed matter physics in the first place.

I've been lucky to work alongside so many great students and post docs in TCM. In particular, I'd like to thank my office mates, Max and Ollie, as well as Michael, Mark, and Elis, who (along with many others) helped make my time here so enjoyable. Much of my work on superconducting hydrides was completed in collaboration with Michael and working with him was both the most productive and the most fun part of my PhD.

Finally, thank you to my parents, grandparents, Ben, and Rodion for their love, support, and encouragement.

Table of contents

List of figures **xv**

List of tables **xix**

1 Introduction **1**

2 Background theory **5**

2.1 Preliminaries 5

2.1.1 Spin, antisymmetry, and fermionic wavefunctions 5

2.1.2 The Born-Oppenheimer approximation 6

2.2 Electronic structure methods 8

2.2.1 Hartree and Hartree-Fock methods 8

2.2.2 Density functional theory 13

2.2.3 *Ab initio* random structure searching 25

2.2.4 Convex hulls and stability at the static-lattice level 28

2.3 Vibrations in solids: the harmonic approximation 29

2.3.1 Finite displacements and implementation in CAESAR 31

2.3.2 Density functional perturbation theory 33

2.3.3 Dynamic and thermodynamic stability 37

2.4 Beyond the harmonic approximation 39

2.4.1 Independent mode framework 40

2.4.2 Vibrational self-consistent field 40

2.4.3 Thermodynamic integration 43

2.5 Electron-phonon interactions and superconductivity 44

2.5.1 The coupled electron-phonon system 45

2.5.2 Migdal-Eliashberg theory 47

2.5.3 Coulomb pseudopotential and approximate equations for T_c 51

2.6 Gaspari-Gyorffy electron-phonon coupling estimates 53

3 The phase diagram of solid hydrogen 57
3.1 Motivation . . . 57
3.2 Phases of solid hydrogen . . . 58
3.3 Previous theoretical studies . . . 61
3.4 Methodology and computational details . . . 62
3.4.1 Purpose-built exchange-correlation functionals . . . 62
3.4.2 Crystal structure prediction . . . 63
3.4.3 Static-lattice calculations . . . 64
3.4.4 Harmonic phonon calculations . . . 65
3.4.5 Accounting for anharmonicity . . . 65
3.5 Predicted phase behaviour . . . 67
3.6 Conclusions . . . 77

4 Stability and superconductivity of lanthanum and yttrium decahydrides 79
4.1 Motivation . . . 79
4.2 Methodology and computational details . . . 80
4.2.1 Phonons and superconductivity . . . 80
4.2.2 Pseudopotential testing . . . 82
4.2.3 Identifying candidate structures . . . 83
4.3 Phase behaviour and superconducting properties . . . 84
4.3.1 Lanthanum decahydride, LaH_{10} . . . 84
4.3.2 Yttrium decahydride, YH_{10} . . . 89
4.4 Common approximations in superconductivity calculations . . . 91
4.4.1 The electronic density of states . . . 91
4.4.2 Neglecting anharmonicity . . . 96
4.4.3 Impact on findings for high-pressure hydrides . . . 97
4.5 Conclusions . . . 97

5 Prediction of low-pressure hydride superconductors using machine learning 99
5.1 Motivation . . . 99
5.2 Trends in superconducting hydrides . . . 100
5.2.1 Neural network construction . . . 102
5.2.2 Assessing model behaviour and predictions . . . 103
5.3 Selection of candidate structures . . . 106
5.3.1 Structure searching for promising compositions . . . 106
5.3.2 Enthalpy and metallicity . . . 108
5.4 Superconducting properties . . . 109

5.5 Potential critical temperature ranking techniques . . . 112
5.6 Conclusions . . . 114

6 High-throughput discovery of high-temperature superconductors 115
6.1 Motivation . . . 115
6.2 Methodology . . . 116
6.2.1 Physically motivated descriptors . . . 116
6.2.2 Calculation details: searching, regression, and superconductivity . . . 120
6.2.3 T_c model and the iterative training phase . . . 122
6.2.4 Promising systems and focused searches . . . 125
6.3 Results and discussion . . . 126
6.3.1 Aside: dealing with dynamic instabilities . . . 127
6.3.2 Dynamically stable superconductors . . . 129
6.3.3 Comments on the Allen-Dynes equation . . . 135
6.4 Geometry-based screening for high-T_c hydrides . . . 136
6.4.1 Introducing geometry-based measures . . . 136
6.4.2 Use in high-throughput search scenarios . . . 140
6.5 Conclusions . . . 141

7 Conclusions 143

References 147

Appendix A The exchange-correlation hole and the sum rule 169

Appendix B Gaspari-Gyorffy theory proofs 171
B.1 Expressing matrix elements in terms of phase shifts . . . 171
B.2 Calculating the free-scatterer density of states . . . 171

Appendix C Cs-H and Rb-H enthalpy plots and metallicity 173

List of figures

1.1 Cross-section of a diamond anvil cell experiment. 2

2.1 Schematic diagram of the Kohn-Sham scheme 17
2.2 A 12-atom hydrogen cluster in a supercell 20
2.3 Demonstrating the action of a pseudopotential 23
2.4 The steepest descent and conjugate gradient methods 25
2.5 Imposing minimum atomic separations 26
2.6 Neighbouring basins and hypervolumes in AIRSS 27
2.7 A schematic convex hull for a binary system 28

3.1 Primitive cell of $P2_1/c$-24 59
3.2 Primitive cell of $C2/c$-24 59
3.3 Primitive cell of $P6_122$-36 60
3.4 Supercell of *Cmca*-4 60
3.5 Supercell of *Cmca*-12 60
3.6 Primitive cell of *Pc*-48 61
3.7 Supercell of *Ibam*-8 61
3.8 Primitive cell of $Pca2_1$-48 61
3.9 Primitive cell of $Pna2_1$-48 62
3.10 Mode mapping for *Cmca*-12 at 350 GPa 67
3.11 Static-lattice enthalpy of various hydrogen structures 68
3.12 Harmonic zero-point energies for hydrogen 70
3.13 Gibbs free energy for hydrogen, indicating predicted phase stability at 0 K at the harmonic level 72
3.14 Zero-point anharmonic corrections for hydrogen 73
3.15 Gibbs free energies for hydrogen (O_3) with anharmonic corrections 74
3.16 Gibbs free energies for hydrogen (O_4) with anharmonic corrections 75
3.17 A DFT-PBE harmonic phase diagram of solid hydrogen 76

3.18 Anharmonic phase diagram of solid hydrogen calculated using the O_3 functional 77
3.19 Anharmonic phase diagram of solid hydrogen calculated using the O_4 functional 77

4.1 Dependence of T_c on the double-delta smearing width for $Fm\bar{3}m$-YH_{10} at 350 GPa . . . 81
4.2 Dependence of T_c on the double-delta smearing width for $Im\bar{3}m$-YH_6 at 160 GPa . . . 82
4.3 Static-lattice convex hull for the Y-H system at 400 GPa . . . 83
4.4 Competitive structures of LaH_{10} . . . 84
4.5 Enthalpies of LaH_{10} candidate structures . . . 85
4.6 Gibbs free energy of LaH_{10} structures, indicating phase stability . . . 86
4.7 $T_c(P)$ for LaH_{10} structures, obtained from the Eliashberg equations . . . 86
4.8 An accurate convex hull for the La-H system at 150 GPa . . . 87
4.9 A convex hull for the La-H system at 150 GPa, calculated without the 4f component in the La pseudopotential . . . 88
4.10 Competitive structures of YH_{10} . . . 89
4.11 Gibbs free energy of YH_{10} structures, indicating phase stability . . . 90
4.12 $T_c(P)$ for YH_{10} structures, obtained from the Eliashberg equations . . . 90
4.13 The DOS for $Im\bar{3}m$-H_3S at 200 GPa . . . 92
4.14 The DOS for $Fm\bar{3}m$-LaH_{10} at 250 GPa . . . 93
4.15 The DOS for $Fm\bar{3}m$-LaH_{10} at 250 GPa, including AHC corrections at 0 K and 300 K . . . 96

5.1 A P-T_c plot for our binary hydride literature dataset . . . 101
5.2 Neural network topology . . . 103
5.3 Behaviour of binary hydride machine learning model . . . 104
5.4 Distribution of hydrogen content and atomic number in top 10% of hydrides 105
5.5 The periodic table of optimal binary hydrides according to the predictions of our machine learning model . . . 106
5.6 Convex hull for Cs-H system at 50 GPa . . . 107
5.7 Convex hull for Rb-H system at 50 GPa . . . 108
5.8 Eliashberg function for *Immm*-RbH_{12} and *Pmma*-RbH_3 . . . 111

6.1 η_H against T_c for the literature set . . . 117
6.2 η_X against T_c for the literature set . . . 118
6.3 $N_H(E_F)/N(E_F)$ against T_c for the literature set . . . 118
6.4 $N_H(E_F)/N(E_F)$ against η_H for the literature set . . . 119
6.5 A flowchart summarising our high-throughput methodology . . . 124

6.6 Logarithmic chart showing the number of structures studied at each stage of the training process 124
6.7 Final Allen-Dynes T_c values for the structures found in this work 126
6.8 As Fig. 6.7, but with Eliashberg T_c values 127
6.9 $Pm\bar{3}m$-NaH_6 structure found at 100 GPa 129
6.10 $Im\bar{3}m$-CaH_6 structure found at 100 GPa 130
6.11 Eliashberg function for $Im\bar{3}m$-CaH_6 at 100 GPa, illustrating the origin of the large difference between Allen-Dynes and Eliashberg T_c values 131
6.12 $P6_3mc$-AcH_{12} structure found at 200 GPa 132
6.13 $Fm\bar{3}m$-MgH_{13} structure found at 200 GPa 132
6.14 $F\bar{4}3m$-YH_9 and $Immm$-ScH_8 structures found at 300 GPa 133
6.15 $P6/mmm$-LiH_2 structure found at 300 GPa 134
6.16 $Pm\bar{3}$-MgH_{12} structure found at 500 GPa 134
6.17 Comparing critical temperatures obtained from the Eliashberg and Allen-Dynes equations 135
6.18 Plotting shortest hydrogen-hydrogen distance against T_c 137
6.19 Plotting maximum cage measure against T_c 138
6.20 Structures with high maximum cage measure 139
6.21 Plotting the combined geometric measure against T_c 140

C.1 Enthalpy vs pressure for CsH_7 structures 173
C.2 Enthalpy vs pressure for RbH_3 structures 174
C.3 Enthalpy vs pressure for RbH_{12} structures 175
C.4 N(E_F) at 50 and 150 GPa for Cs-H and Rb-H structures 176

List of tables

3.1 Corrected pressures derived from polynomial, Birch–Murnaghan, and Vinet equations of state 71

5.1 Critical temperatures for promising hydride compositions 110
5.2 Testing the ability of two quantities, η_H and $N_H(E_F)/N(E_F)$, to rank binary hydride structures 113

6.1 Superconducting properties of dynamically stable superconductors 128

Preface

The work presented in Chapter 3 is unpublished. Dr John Trail constructed the exchange-correlation functionals as part of an earlier publication and provided advice. Prof. Chris Pickard found the new *Cc*-32 structure. All other work presented in Chapter 3 is my own.

Large parts of Chapter 4 have been published as *"Stability and superconductivity of lanthanum and yttrium decahydrides"*, A. M. Shipley, M. J. Hutcheon, M. S. Johnson, R. J. Needs, and C. J. Pickard. Phys. Rev. B **101**, 224511 (2020). CJP performed structure searching for the La-H system. I performed pseudopotential testing, confirmed the La-H search results, performed structure searching for the Y-H system, constructed enthalpy plots, analysed results, and discovered the link to experiment. MJH performed phonon and electron-phonon calculations, giving the Gibbs free energy and T_c of each phase. MSJ performed convergence testing and validation. I investigated the impact some common approximations made in superconductivity calculations may have on our results.

Chapter 5 has been published as *"Predicting novel superconducting hydrides using machine learning approaches"*, M. J. Hutcheon, A. M. Shipley, and R. J. Needs. Phys. Rev. B **101**, 144505 (2020). MJH and I designed the project, chose model inputs and built the literature dataset together. MJH trained and validated the machine learning model and extracted predictions. I performed the structure searching and constructed enthalpy plots. I suggested (and tested) the two T_c ranking methods and implemented Gaspari-Gyorffy theory in an existing code (Dr Po-Hao Chang provided some advice by email). MJH performed electron-phonon calculations to obtain T_c.

Part of the work presented in Chapter 6 has been submitted as *"High-throughput discovery of high-temperature conventional superconductors"*, A. M. Shipley, M. J. Hutcheon, R. J. Needs, and C. J. Pickard (with equal contributions from the first two authors). CJP performed structure searching in both the training and results phases. I ran partial density of states and Gaspari-Gyorffy theory calculations for literature structures, then constructed, trained and validated a T_c model. I screened the search structures based on both stability and the model predictions. MJH optimised an existing electron-phonon code and calculated T_c for the best predicted structures. I updated the model iteratively using these results. The study on geometry-based screening of superconductors is my own and is not published elsewhere.

Some work on ternary hydrides was also completed during the course of my PhD, but is not detailed in this thesis; the manuscript *"Design principles for hydrogen-based superconductors at moderate pressure"* (Z. Zhang, T. Cui, M. J. Hutcheon, A. M. Shipley, H. Song, M. Du, V. Z. Kresin, D. Duan, C. J. Pickard, and Y. Yao) has been submitted in connection with this work.

Chapter 1

Introduction

Quantum mechanics is the theory that dominates on the atomic scale. However, direct solution of the equations of quantum mechanics for anything beyond the simplest systems rapidly becomes intractable. This poses a challenge for condensed matter physics, which typically involves the study of many interacting particles. With this difficulty, however, comes a richness of behaviour and phenomena which intrigues physicists, materials scientists, engineers, and chemists alike.

Across these disciplines, a huge amount of effort has gone into formulating theories and approximations that make the application of quantum mechanics to non-trivial systems feasible. This thesis, focused largely on density functional theory (DFT) approaches, concerns the continued development of such methods and their application to materials under extreme pressure. Pressure is an important tool in physics and materials science - under pressure, unusual stoichiometries are stabilised and phase behaviour can become extremely rich (even in the simplest materials such as pure hydrogen). This seems to run contrary to long-held beliefs regarding the behaviour of solids under pressure, i.e., that they should become simpler, more homogeneous, and more symmetric [1].

In particular, this thesis investigates the behaviour of high-pressure *light-atom* systems, including solid hydrogen and metal hydrides. Light-atom systems present particular challenges as they have large vibrational energies, which can have a substantial impact on phase stability and can also display a large degree of anharmonicity. Interesting phenomena, that would not be predicted at ambient conditions, can also emerge in such systems. The richness and complexity of the phase diagrams of these materials is therefore not the only driving force behind their study; high-temperature conventional superconductivity is predicted in solid hydrogen and has been experimentally verified in a large number of metal hydrides under pressure. Prediction and optimisation of this phenomenon is the main focus of the latter parts of this thesis.

High pressure physics is a rapidly evolving field of research from both an experimental and theoretical perspective. High pressure can be achieved in experiment using static pressure in diamond anvil cells (DACs) or dynamic pressure (via shock compression). Recent experimental advances allow DACs to routinely achieve pressures of hundreds of gigapascals (GPa), allowing experimental study of solid hydrogen and high-pressure hydrides. A schematic cross-section of such an experiment is shown in Fig. 1.1.

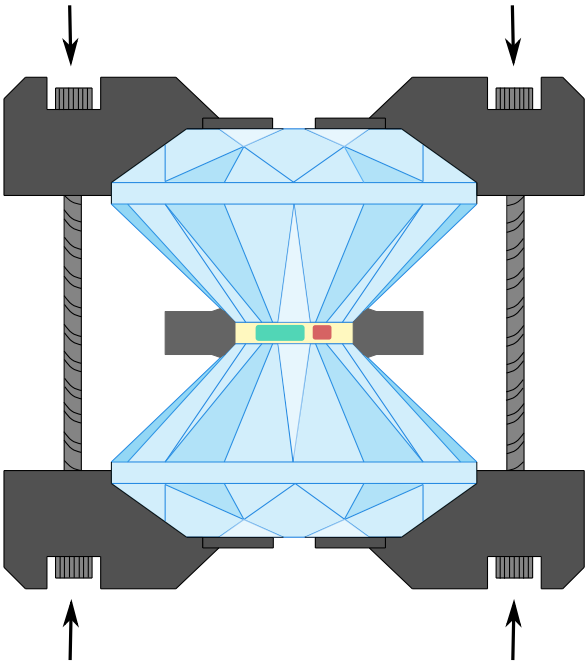

Fig. 1.1 The cross-section of a DAC experiment, consisting of a sample (shown in green) compressed between the faces of two opposing diamonds. Force is applied mechanically and the uniaxial pressure generated is transformed into uniform hydrostatic pressure by surrounding the sample with a pressure-transmitting medium. Argon, xenon, and helium have been shown to be good pressure transmitters [2], but other inert substances can also be used. A material whose behaviour under pressure is known and well-characterised can be used to measure the applied pressure. Common pressure standards include ruby [3], whose fluorescence line shifts have been calibrated up to high pressures, and various simple metals. X-rays and visible light can be passed through the diamonds, and so x-ray diffraction, fluorescence, optical absorption, and Raman scattering measurements can be made directly under pressure. Magnetic fields can be applied externally and electrodes can be attached to the sample to allow nuclear magnetic resonance and electrical measurements to be made, respectively. The sample can be heated either using these electrode contacts or by laser heating.

Adding to this, in recent years theorists have demonstrated that their first-principles technniques have predictive, as well as explanatory, capabilities. With the advent of crystal

structure prediction methods, efficient DFT and phonon codes, and approaches for modelling phenomena such as conventional superconductivity, it is now possible to accurately simulate unknown materials and make predictions about their properties. The next logical step is towards material design - the ability to choose certain elements and arrangements of atoms in order to produce a desirable material property. This thesis suggests some steps in this direction in terms of conventional superconductivity in binary hydrides.

Chapter 2 presents the background theory required to understand and evaluate the work presented in this thesis. We describe some of the commonly used electronic structure methods (focusing in detail on DFT), introduce crystal structure prediction methods, explain the concepts of dynamic and thermodynamic stability, and describe the various approaches used to calculate both vibrational and superconducting properties.

In Chapter 3, we begin applying these techniques and calculate the anharmonic phase diagram of solid hydrogen over a large pressure range within the framework of DFT. We do so in order to assess the accuracy of two exchange-correlation functionals purpose-built for this system in a previous work. The flexibility afforded in the construction of these functionals means that their performance may give an indication of the best overall performance of semi-local DFT in this system, which has previously been postulated to be lacking.

In Chapter 4, we turn to an interesting related problem. Solid hydrogen is predicted to be a room-temperature superconductor at high enough pressures. However, the pressure required even to metallise hydrogen has proved difficult to obtain. Some hydrides metallise and become superconducting at pressures which are much more accessible and, in recent years, the study of metal hydrides has led to a dramatic increase in the highest experimentally measured superconducting critical temperature (T_c). The record-breaking experimental T_c at the time this work was performed was for LaH_{10}. We study this system from first principles, predicting a metastable hexagonal phase at experimentally relevant pressures. The existence of this phase provides an explanation for the observation of hcp impurities in experiment. We also predict the phase behaviour and superconducting properties of YH_{10}, which has an even larger predicted T_c and is likely to be the subject of future experiments, and perform a systematic investigation of a frequently-overlooked computational parameter. We go on to look at some common approximations made in calculations of T_c. We discuss the origin of these approximations, quantify the error in T_c they may produce for metal hydrides, and discuss whether this will impact the findings of this Chapter and the remainder of this thesis.

In Chapter 5, in recognition of the large amount of binary hydride T_c data available in the literature, we build a machine learning model to predict the operational pressure and T_c of a given binary hydride from simple material descriptors. We recognise that the challenge of achieving superconductivity near ambient conditions is as much about reducing operational

pressure as it is about increasing T_c. We therefore treat pressure and temperature on an equal footing in our model and use it to make suggestions for compositions to study for superconductivity closer to ambient conditions. Critical temperatures are calculated for the energetically competitive candidates emerging from our searches. The addition of these data points significantly extends the frontier in P-T_c space towards ambient conditions compared to our literature dataset.

In Chapter 6, we embark on an ambitious periodic-table-wide search for superconductivity in binary hydrides across a large pressure range. We do this with the goal of identifying as many high-T_c candidates as possible and obtaining an overview of the trends in superconductivity. To achieve this, we recognise that two filters can be applied to the large set of structures obtained in structure searching. Firstly, only structures on or just above the convex hull are considered. Secondly, some screening based on potential superconducting ability needs to be applied. To perform this second step, we identify cheap, *physically motivated* descriptors, based on density of states and scattering theory calculations, and build an iteratively-updated model for T_c. We ultimately find a large number of high-T_c materials, including several near- and above-room-temperature candidates, and demonstrate that our method is extremely effective. We are able to draw some conclusions about the importance of considering metastable structures and discuss how our techniques could be applied to other systems. We then introduce two geometry-based measures which can be used to categorise binary hydrides. Since these measures are practically free to calculate for a given input structure, we investigate their ability to identify potential high-T_c candidates in a truly high-throughput scenario, i.e., one in which they are used directly at the structure searching level.

Finally, in Chapter 7, we summarise the progress made by this thesis. We also make some suggestions about fruitful directions for future research, paying particular attention to ongoing work in ternary hydride and light binary systems. We discuss the construction of high-throughput workflows for other material properties and the future prospects for first-principles material design.

Chapter 2

Background theory

2.1 Preliminaries

2.1.1 Spin, antisymmetry, and fermionic wavefunctions

The spin-statistics theorem [4, 5] states that the global wavefunctions of identical particles with integer spins (called *bosons*) must remain unchanged when any pair of particles is swapped, while those of identical particles with half-integer spins (called *fermions*) must change sign under any such swap. Electrons are fermions with spin $1/2$ and therefore must have antisymmetric wavefunctions.

Now, consider the independent-electron case, where the total wavefunction is given by $\phi(r_1)\phi(r_2)$ for two electrons each described by the same single-particle wavefunction. Forming the simplest antisymmetric combination, we have

$$\Psi^A(r_1, r_2) = \frac{1}{\sqrt{2}}[\phi(r_1)\phi(r_2) - \phi(r_2)\phi(r_1)], \tag{2.1}$$

which is zero at every point in space and is therefore unphysical. In order to have a physically meaningful antisymmetric wavefunction for two independent particles, the two single-particle wavefunctions have to be different. This situation generalises to any number of particles and is known as the Pauli exclusion principle. Electrons can be spin-up and spin-down, so although every electron must have a different *global* wavefunction, two electrons can have the same spatial wavefunction provided they have opposite spins.

The antisymmetrisation of a wavefunction describing more than two electrons is more complicated because the result must change sign under the exchange of *any* pair of particles. The antisymmetrisation of a wavefunction describing N electrons can be achieved using a

Slater determinant [6] of single-particle states

$$\Psi^A(r_1, r_2, ...r_N) = \frac{1}{\sqrt{N!}} \begin{vmatrix} \phi_1(r_1) & \phi_2(r_1) & ... & \phi_N(r_1) \\ \phi_1(r_2) & \phi_2(r_2) & ... & \phi_N(r_2) \\ ... & ... & ... & ... \\ \phi_1(r_N) & \phi_2(r_N) & ... & \phi_N(r_N) \end{vmatrix} . \quad (2.2)$$

This expression is often abbreviated to just its leading diagonal. Only a small subset of all possible fermionic wavefunctions can be written as a single Slater determinant.

2.1.2 The Born-Oppenheimer approximation

The non-relativistic Hamiltonian for a system of M nuclei and N electrons, in atomic units, is

$$\hat{H} = -\frac{1}{2}\sum_i^N \nabla_i^2 - \sum_\alpha^M \frac{1}{2m_\alpha}\nabla_\alpha^2 - \sum_i^N \sum_\alpha^M \frac{Z_\alpha}{|\mathbf{r}_i - \mathbf{R}_\alpha|} + \frac{1}{2}\sum_i^N \sum_{j\neq i} \frac{1}{|\mathbf{r}_i - \mathbf{r}_j|} + \frac{1}{2}\sum_\alpha^M \sum_{\beta\neq\alpha} \frac{Z_\alpha Z_\beta}{|\mathbf{R}_\alpha - \mathbf{R}_\beta|}, \quad (2.3)$$

where i, j label electrons and α, β label nuclei. It is reasonable to assume that the total momenta of the electrons and nuclei are comparable, since the forces exerted on these particles due to their charge are of the same order of magnitude. However, the nuclei are much heavier than the electrons, so we can imagine that the electrons relax rapidly to their given configuration on the timescale of nuclear motion. With this in mind, we may expect to be able to decouple the dynamics of the nuclei from that of the electrons; this forms the basis of the Born-Oppenheimer [7] or adiabatic approximation.

Considering the behaviour of the electrons in a static array of nuclei - the so-called electronic problem - we write

$$\left(-\frac{1}{2}\sum_i \nabla_i^2 - \sum_i \sum_\alpha \frac{Z_\alpha}{|\mathbf{r}_i - \mathbf{R}_\alpha|} + \frac{1}{2}\sum_i \sum_{j\neq i} \frac{1}{|\mathbf{r}_i - \mathbf{r}_j|} + \frac{1}{2}\sum_\alpha \sum_{\beta\neq\alpha} \frac{Z_\alpha Z_\beta}{|\mathbf{R}_\alpha - \mathbf{R}_\beta|} \right) \psi_n(\{\mathbf{r}_i\};\{\mathbf{R}_\alpha\}) = \varepsilon_n(\{\mathbf{R}_\alpha\})\psi_n(\{\mathbf{r}_i\};\{\mathbf{R}_\alpha\}), \quad (2.4)$$

where the electronic eigenfunctions, $\{\psi_n\}$, depend on the nuclear configuration, $\{\mathbf{R}_\alpha\}$, parametrically and the collection of terms in brackets on the left-hand side forms the electronic Hamiltonian, $\hat{H}_{el}$. Since $\hat{H}_{el}$ is Hermitian, the electronic eigenfunctions form a complete,

orthogonal basis and we can expand the total wavefunction of the system as

$$\Psi(\{\mathbf{r}_i\},\{\mathbf{R}_\alpha\}) = \sum_n \psi_n(\{\mathbf{r}_i\};\{\mathbf{R}_\alpha\})\phi_n(\{\mathbf{R}_\alpha\}), \tag{2.5}$$

where the expansion coefficients, ϕ_n, depend on the nuclear configuration. Acting on this total wavefunction with the full Hamiltonian of Eq. (2.3) and using the result of Eq. (2.4),

$$\begin{aligned}\hat{H}\Psi(\{\mathbf{r}_i\},\{\mathbf{R}_\alpha\}) = \sum_n \left(-\sum_\alpha \frac{1}{2m_\alpha}\nabla_\alpha^2 + \varepsilon_n(\{\mathbf{R}_\alpha\}) \right) \psi_n(\{\mathbf{r}_i\};\{\mathbf{R}_\alpha\})\phi_n(\{\mathbf{R}_\alpha\}) \\ = E\sum_n \psi_n(\{\mathbf{r}_i\};\{\mathbf{R}_\alpha\})\phi_n(\{\mathbf{R}_\alpha\}),\end{aligned} \tag{2.6}$$

where E is the total energy of the system. Since the operator ∇_α^2 also acts on $\psi_n(\{\mathbf{r}_i\};\{\mathbf{R}_\alpha\})$,

$$\begin{aligned}\hat{H}\Psi(\{\mathbf{r}_i\},\{\mathbf{R}_\alpha\}) = \sum_n \psi_n(\{\mathbf{r}_i\};\{\mathbf{R}_\alpha\}) \left(-\sum_\alpha \frac{1}{2m_\alpha}\nabla_\alpha^2 + \varepsilon_n(\{\mathbf{R}_\alpha\}) \right) \phi_n(\{\mathbf{R}_\alpha\}) \\ -\sum_n \left[\sum_\alpha \frac{1}{2m_\alpha} \left(2\nabla_\alpha\phi_n(\{\mathbf{R}_\alpha\})\cdot\nabla_\alpha\psi_n(\{\mathbf{r}_i\};\{\mathbf{R}_\alpha\}) + \phi_n(\{\mathbf{R}_\alpha\})\nabla_\alpha^2\psi_n(\{\mathbf{r}_i\};\{\mathbf{R}_\alpha\}) \right) \right].\end{aligned} \tag{2.7}$$

Multiplying Eq. (2.7) by $\psi_m^*(\{\mathbf{r}_i\};\{\mathbf{R}_\alpha\})$ (where $m \neq n$) and integrating the result using the orthogonality of the electronic eigenfunctions, we obtain

$$\begin{aligned}0 = \left(-\sum_\alpha \frac{1}{2m_\alpha}\nabla_\alpha^2 + \varepsilon_m - E \right)\phi_m \\ -\sum_n \left[\sum_\alpha \frac{1}{2m_\alpha} \left(2\nabla_\alpha\phi_n \langle\psi_m|\nabla_\alpha|\psi_n\rangle + \phi_n \langle\psi_m|\nabla_\alpha^2|\psi_n\rangle \right) \right].\end{aligned} \tag{2.8}$$

Remembering that $m \neq n$, the coupling terms on the second line of Eq. (2.8) are known as the non-adiabatic terms; using perturbation theory, it can be formally shown that they contribute very little to the total energy. The explicit derivation amounts to treating the nuclear kinetic energy as a perturbation to the electronic Hamiltonian and showing that the non-adiabatic terms can be safely neglected [7]. With the neglect of these terms, the dynamics of the nuclei and electrons are decoupled. One can therefore fix the nuclear positions and solve the electronic Schrödinger equation with the external potential generated by the nuclei, leading to a different electronic problem for each set of nuclear coordinates. For the nuclear dynamics, we then have a Hamiltonian where the solution of the electronic Schrödinger equation plays

the role of a potential

$$\hat{H}_{vib}\phi_m(\{\mathbf{R}_\alpha\}) = \Big(-\sum_\alpha \frac{1}{2m_\alpha}\nabla_\alpha^2 + \varepsilon_m(\{\mathbf{R}_\alpha\})\Big)\phi_m(\{\mathbf{R}_\alpha\}) = E_m\phi_m(\{\mathbf{R}_\alpha\}). \tag{2.9}$$

We often call this potential the Born-Oppenheimer (BO) energy surface; it describes the potential energy as a function of nuclear positions. Since it relies on a perturbative expansion, the assumptions behind the Born-Oppenheimer approximation are well-justified when the gap between the ground and excited state energies is larger than the typical energy scale of nuclear motion [8]. This amounts to saying that nuclear motion cannot excite electronic transitions. In metals, however, phenomena beyond the Born-Oppenheimer approximation (such as phonon-mediated superconductivity and phonon-induced renormalisation of electronic properties, as we will meet later) can occur. Non-adiabatic effects may dominate in some situations, such as in the surface chemistry of certain metals [9]. Despite this, the Born-Oppenheimer approximation is still routinely used for metallic systems; it has proved effective in a large range of cases [8] and there is no widely used, computationally feasible alternative at present.

2.2 Electronic structure methods

When we perform first-principles simulations of quantum systems, we attempt to find a representation of the many-body wavefunction, $\Psi(r_1, r_2, ..r_N)$. The dimension of this wavefunction is $3(N+M)$, meaning that recording just one state of the system is a considerable challenge and the many-body problem is generally intractable without further approximations [10]. A great deal of work within both the quantum chemistry and solid-state physics communities has gone into establishing accurate, and efficient, approximations. In this section, we introduce some of the methods used to solve the electronic problem arising in the Born-Oppenheimer approximation.

2.2.1 Hartree and Hartree-Fock methods

The non-interacting electron picture

The approximation in which all electron-electron interactions are neglected in their entirety represents a drastic simplification of the electronic Hamiltonian [11]. It amounts to decoupling the electrons from one another and describing the system using a series of one-electron Hamiltonians,

$$\hat{h}_i = -\frac{1}{2}\nabla_i^2 - \sum_\alpha^M \frac{Z_\alpha}{|\mathbf{r}_i - \mathbf{R}_\alpha|}. \tag{2.10}$$

The full Hamiltonian is then given by $\hat{H} = \sum_i \hat{h}_i$ and is solved by a set of spin orbitals which satisfy eigenvalue equations of the form $\hat{h}_i \psi_i = \varepsilon_i \psi_i$. The resulting electronic wavefunction is given by a Hartree product,

$$\Psi^H = \psi_1 \psi_2 ... \psi_N, \tag{2.11}$$

with the energy of this state being $E = \langle \Psi^H | \hat{H} | \Psi^H \rangle = \varepsilon_1 + \varepsilon_2 + ... \varepsilon_N$, provided it is normalised.

The Hartree self-consistent field method

The non-interacting electron approach is very limited, but it can be improved by accounting for the electron-electron interactions in some way. As a first step towards reintroducing these interactions, we can assume that the electrons in our system move in an averaged potential created by the fixed nuclei and all the other electrons [12]. This idea is the basis of the Hartree self-consistent field (SCF) method; a mean-field approximation in which each electron interacts with the average distribution of the other electrons in the system.

Each single-particle Hamiltonian will now take the form

$$\hat{h}_i = -\frac{1}{2}\nabla_i^2 + V_{ext}(\mathbf{r}) + V_i^H(\mathbf{r}), \tag{2.12}$$

where $V_{ext}(\mathbf{r})$ is introduced as shorthand for the external potential generated by the nuclei. We see that the electrons remain decoupled from one another, meaning our total wavefunction can still take the form of a Hartree product. $V_i^H(\mathbf{r})$ is the Hartree potential, given by

$$V_i^H(\mathbf{r}) = \sum_{j \neq i} \int \frac{|\psi_j(r_j)|^2}{|\mathbf{r}_i - \mathbf{r}_j|} dx_j, \tag{2.13}$$

where $(x_j) \equiv (\mathbf{r}_j, \sigma_j)$ represents both the spatial and spin degrees of freedom. When the number of electrons under consideration is large, the self-interaction term ($i = j$), which corresponds to the unphysical interaction of an electron with its own charge density, can be included without greatly altering the result. When the first quantitative calculations on atoms were carried out by Hartree [12], he excluded these terms, but their inclusion is now considered beneficial as it makes the Hartree term identical for all electrons. As well as the direct computational advantage, this avoids the non-orthogonality that would arise between electronic states derived from different Hamiltonians.

To solve the Hartree SCF equations, we must make an initial guess at the orbitals in order to calculate the Hartree term. We can then solve the eigenvalue equations with Hamiltonians defined by Eq. (2.12) and obtain a new set of single-particle orbitals. It then becomes

necessary to cycle through the equations iteratively until the input and output orbitals match to within a chosen tolerance. In this method, although we can choose to fill our electronic orbitals in a way that is consistent with the concept of indistinguishable particles, we still do not have a total wavefunction that is antisymmetric by construction.

The Hartree-Fock method

We can apply the variational principle for the electronic ground state to a Hartree product trial wavefunction, giving

$$E_{GS} \leq \langle \prod_i \psi_i(x_i) | \hat{H}_{el} | \prod_i \psi_i(x_i) \rangle \,, \tag{2.14}$$

where $\hat{H}_{el}$ is the full electronic Hamiltonian we met earlier. The minimisation of this expression (subject to normalisation of the single-particle states) leads to the Hartree SCF equations, meaning application of the variational principle to an assumed Hartree product wavefunction reduces the Hamiltonian to a sum of single-particle Hamiltonians as defined by Eq. (2.12). To make this method fully consistent with the principle of indistinguishable particles, Fock proposed performing the above minimisation with a normalised Slater determinant trial wavefunction instead [13]. Working with this new assumption, one arrives at the Hartree-Fock (HF) equations, given by

$$\hat{F}\psi_i(x_i) = \varepsilon_i \psi_i(x_i), \tag{2.15}$$

where $\hat{F}$ is the Fock operator, defined as

$$\hat{F} = -\frac{1}{2}\nabla_i^2 - \sum_\alpha \frac{Z_\alpha}{|\mathbf{r}_i - \mathbf{R}_\alpha|} + \sum_{j \neq i} \left(\hat{J}_j(x) - \hat{K}_j(x) \right). \tag{2.16}$$

The Coulomb operator, $\hat{J}$, leads to energy terms which correspond to the interaction of ψ_i with the mean-field due to the other electrons,

$$\hat{J}_j(x)\psi_i(x_i) = \int \frac{|\psi_j(x_j)|^2}{|\mathbf{r}_i - \mathbf{r}_j|} dx_j \psi_i(x_i). \tag{2.17}$$

The exchange operator, $\hat{K}$, arises purely because the wavefunction is now expressed as a determinant, rather than a simple Hartree product,

$$\hat{K}_j(x)\psi_i(x_i) = \delta_{\sigma_i,\sigma_j} \int \frac{\psi_j^*(x_j)\psi_i(x_j)}{|\mathbf{r}_i - \mathbf{r}_j|} dx_j \psi_j(x_i). \tag{2.18}$$

The existence of $\hat{K}$ is therefore a consequence of the Pauli exclusion principle, meaning it has no classical interpretation. As expected from our knowledge of this principle, non-zero exchange integrals are only found for pairs of electrons with the same spin. Since calculation of the exchange term involves an integral of ψ_i over all of space, $\hat{K}$ is termed a "non-local" operator and computation of exchange integrals is usually the most expensive component of these calculations. In contrast to the Hartree SCF method, HF is a self-interaction-free theory by definition since the Coulomb and exchange terms cancel each other exactly for the case of an electron interacting with its own charge density [13]. This means we can drop the $j \neq i$ condition in Eq. 2.16.

Since the Fock operator depends on the state on which it acts, the HF equations must also be solved iteratively. The total energy of the system can then be obtained by adding the electronic energy to the total internuclear repulsion energy. It is important to remember that by only including the electron-electron interaction as an average effect, we ignore electron *correlation*, i.e., the fact that, beyond the effect of the Pauli exclusion principle on same-spin electrons, the motion of one particular electron in our system is affected by the positions of all the other electrons.

Slater [14] showed that HF can be regarded as a set of Schrödinger equations with each electron moving in a potential determined by all charges in the system corrected by removal of an exchange charge equivalent to 1 electron. This correction, known as an exchange hole, surrounds the electron under investigation. Splitting the density into densities of up and down spins, we have a different exchange hole for each one of these (if they are different) and for each wavefunction; this is what leads to the complicated form of HF [14].

Post-HF methods

The larger the basis set used to represent the states in HF, the lower the calculated total energy will be. However, the HF energy eventually tends to a limit. This limit is not the true energy of the system, but is identified as the lowest energy achievable using a single Slater determinant to represent the electronic wavefunction. We already know that the HF limit cannot be the true energy of the system because the theory neglects both relativistic effects and electron correlation. If we choose to ignore relativistic effects (a reasonable assumption for lighter atoms), the HF correlation energy is defined as

$$E_c = E_{GS} - E_{HF}, \tag{2.19}$$

where E_{GS} is the true ground-state energy of the system. We can see that the correlation energy must be negative; HF can be derived from application of the variational principle,

meaning $E_{HF} \geq E_{GS}$ and therefore $E_c \leq 0$. Intuitively, we can imagine that including correlation allows the electrons to better avoid one another - opposite spin electrons can now create a "correlation hole", which is not possible in a mean-field picture. The neglect of correlation can be accounted for (to some degree) by post-HF methods, some of which are introduced below.

In configuration interaction (CI) the wavefunction is taken to be a linear combination of Slater determinants, each one corresponding to a different electronic configuration. Full CI includes all possible excited configurations[1] of the same symmetry as the ground state:

$$\Psi_{FCI} = \left(\mathbf{1} + \sum_{p=1}^{N} \hat{C}_p\right)\psi_0. \tag{2.20}$$

Here ψ_0 is the mean-field reference state and the operator $\hat{C}_p$ produces an order p excitation. Typically, due to the large cost of CI calculations, a restricted number of excited configurations are included. Perturbative approaches are also possible. Many-body perturbation theory in which the HF wavefunction appears as the zero-order solution (and excited states are expressed in terms of changes in orbital filling) is called Møller-Plesset perturbation theory [15]. Another alternative is the coupled-cluster method, which is capable of providing highly accurate energies for moderate-sized molecules (up to $\sim$100 electrons) [16]. Here, the fully-correlated state is expressed as

$$\Psi_{CC} = e^{\hat{T}}\psi_0, \tag{2.21}$$

where the cluster operator, $\hat{T}$, can be decomposed into operators that produce excitations of increasing order. This operator sum tends to be truncated; a coupled-cluster singles and doubles (CCSD) calculation, for example, corresponds to $\Psi_{CCSD} = e^{(\hat{T}_1+\hat{T}_2)}\psi_0$. The coupled-cluster method offers numerical advantages because terms such as $\hat{T}_2^2/2$, arising from operator exponentiation, produce quadruple excitations, but their coefficients can be expressed in terms of products of double excitation coefficients [16]. The method also has certain systematic advantages stemming from its size extensivity. One of the most celebrated high-level methods of quantum chemistry is CCSD(T), whereby a CCSD calculation is extended to include the effect of triple excitations using perturbation theory.

[1] The excitations we refer to in these methods are not real excited states of the system, but simply represent changes to the filling of electronic states.

2.2.2 Density functional theory

While the methods we have met so far begin with an approximation of the *form* of the electronic wavefunction, density functional theory (DFT) is a framework in which the total energy and other properties of the system are calculated from the electron density instead. DFT is currently the most widely used electronic structure method as it offers a good trade-off between accuracy and cost for a wide variety of systems.

Hohenberg-Kohn theorems

In the 1960s, Hohenberg and Kohn [17] developed a formal variational principle for the ground-state energy in which the electron density, $\rho(\mathbf{r})$, is the variable function. Firstly, they showed that the external potential of a given system is a *unique* functional of the electron density. Secondly, it follows that the ground-state energy is also a functional of the density and that only the exact ground-state density gives the exact ground-state energy, $E_{GS} = E[\rho_{GS}(\mathbf{r})]$. This allows the formulation of a variational principle,

$$E[\rho(\mathbf{r})] \geq E[\rho_{GS}(\mathbf{r})]. \tag{2.22}$$

To prove the first of these statements, consider N electrons in an external potential, $V_{ext}(\mathbf{r})$. In the following we will assume that the ground-state, ψ_0, corresponding to this potential is non-degenerate, although the proof can be extended to degenerate ground states too. The proof proceeds, following the original paper Ref. [17], by assuming that another potential, $V'_{ext}(\mathbf{r})$, with the ground state ψ'_0 gives rise to the same electron density, $\rho(\mathbf{r})$. We assume that the two potentials differ by more than a constant, meaning that ψ'_0 cannot equal ψ_0 because they satisfy Schrödinger equations with different Hamiltonians. We denote the Hamiltonians associated with ground states ψ_0 and ψ'_0 as $\hat{H}$ and $\hat{H}'$, respectively, and the associated ground-state energies as E and E'.

For any normalised ψ'_0, the variational principle tells us

$$E' = \langle \psi'_0 | \hat{H}' | \psi'_0 \rangle < \langle \psi_0 | \hat{H}' | \psi_0 \rangle = \langle \psi_0 | \hat{H} + \hat{H}' - \hat{H} | \psi_0 \rangle ,$$

$$E' < \langle \psi_0 | \hat{H} | \psi_0 \rangle + \langle \psi_0 | V'_{ext} - V_{ext} | \psi_0 \rangle = E + \int (V'_{ext}(\mathbf{r}) - V_{ext}(\mathbf{r}))\rho(\mathbf{r}) d\mathbf{r}. \tag{2.23}$$

However, we also know that

$$E = \langle \psi_0 | \hat{H} | \psi_0 \rangle < \langle \psi'_0 | \hat{H} | \psi'_0 \rangle = \langle \psi'_0 | \hat{H}' + \hat{H} - \hat{H}' | \psi'_0 \rangle ,$$

$$E < E' + \int (V_{ext}(\mathbf{r}) - V'_{ext}(\mathbf{r}))\rho(\mathbf{r}) d\mathbf{r}. \tag{2.24}$$

Adding Eq. (2.23) and Eq. (2.24), we find $E' + E < E + E'$; an obvious inconsistency. Thus, $V_{ext}(\mathbf{r})$ is, to within a trivial additive constant, a unique functional of $\rho(\mathbf{r})$.

Now, since $V_{ext}(\mathbf{r})$ (a unique functional of $\rho(\mathbf{r})$) determines the Hamiltonian $\hat{H}$, the electronic ground state, the kinetic energy and the interaction energy are all also functionals of $\rho(\mathbf{r})$. We can therefore write the total energy in the form

$$E[\rho(\mathbf{r})] = F[\rho(\mathbf{r})] + \int V_{ext}(\mathbf{r})\rho(\mathbf{r})d\mathbf{r}, \tag{2.25}$$

where $F[\rho(\mathbf{r})] = \langle\psi|\hat{T} + \hat{V}_{ee}|\psi\rangle$ is called the universal functional as it is valid for any number of particles in any external potential. Here, $\langle\psi|\hat{T}|\psi\rangle$ is the kinetic energy and $\hat{V}_{ee}$ represents *all* electron-electron interactions.

The second Hohenberg-Kohn (HK) theorem is a variational theorem. We let $\rho(\mathbf{r})$ be the ground-state density corresponding to external potential $V_{ext}(\mathbf{r})$. We again consider another external potential, $V'_{ext}(\mathbf{r})$, differing from $V_{ext}(\mathbf{r})$ by more than a constant. Using the first HK theorem, if ψ_0 is the ground state corresponding to $\rho(\mathbf{r})$, it cannot be the ground state of the Hamiltonian determined by $V'_{ext}(\mathbf{r})$. Therefore, by the variational principle,

$$E_{V'}[\psi_0] = F[\rho(\mathbf{r})] + \int d\mathbf{r}V'_{ext}(\mathbf{r})\rho(\mathbf{r}) \geq E_{V',0}, \tag{2.26}$$

where $E_{V',0}$ is the ground-state energy of the Hamiltonian defined by $V'_{ext}(\mathbf{r})$. The minimum of $E[\rho(\mathbf{r})]$ is therefore the ground-state energy of the system and the minimiser corresponds to the ground-state density.

Constrained search formalism

Levy's 1979 constrained search formalism [18, 19] formalised the ideas of Hohenberg and Kohn. We can rewrite the HK variational principle for the total energy in two steps

$$E[\rho(\mathbf{r})] = min_{\rho}\left[Q[\rho(\mathbf{r})] + \int d\mathbf{r}V_{ext}(\mathbf{r})\rho(\mathbf{r})\right] \tag{2.27}$$

where the minimisation is over all N-particle densities and

$$Q[\rho(\mathbf{r})] = min_{\psi\to\rho}\,\langle\psi|\hat{T} + \hat{V}_{ee}|\psi\rangle \tag{2.28}$$

where minimisation is over all antisymmetric wavefunctions which yield density $\rho(\mathbf{r})$ [18]. The object $Q[\rho(\mathbf{r})]$ appearing here is sometimes called the Levy-Lieb functional.

The Levy-Lieb construction is defined for *any* density derivable from a wavefunction for N electrons. Such a density is described as N-representable and the existence of such

a wavefunction for any density (satisfying basic physical conditions) is known. The HK (universal) functional, on the other hand, is defined *only* for densities that can be generated by some external potential - this is termed v-representability and the conditions for such densities are not known in general. The two functionals, however, must match one another at the minimum in total energy, therefore the constrained search formalism can be seen as a formal extension or generalisation of the HK theorems.

Kohn-Sham equations

Kohn and Sham [20] furthered the development of the HK theorems and devised a scheme for their implementation. As we have seen, the total energy can be written in the form of Eq. (2.25). Kohn and Sham suggested that the universal functional could be reformulated as

$$F[\rho(\mathbf{r})] = E_{KE}[\rho(\mathbf{r})] + E_H[\rho(\mathbf{r})] + E_{XC}[\rho(\mathbf{r})]. \tag{2.29}$$

Here,

- $E_{KE}[\rho(\mathbf{r})]$ is the kinetic energy for a system with no electron-electron interactions,
- $E_H[\rho(\mathbf{r})]$ is the energy arising from the Hartree potential, describing the classical interactions between two charge densities, $\frac{1}{2}\int d\mathbf{r}d\mathbf{r}' \frac{\rho(\mathbf{r})\rho(\mathbf{r}')}{|\mathbf{r}-\mathbf{r}'|}$,
- $E_{XC}[\rho(\mathbf{r})]$ is the exchange-correlation functional, which contains all remaining contributions to the electron-electron interaction.

A key difference between HF and DFT is that exact DFT contains *all* the effects of exchange and correlation, whereas in HF only exchange is accounted for. Thus, if we can find the precise form of the exchange-correlation functional, we can compute the total energy of the system exactly via

$$E[\rho(\mathbf{r})] = E_{KE}[\rho(\mathbf{r})] + E_H[\rho(\mathbf{r})] + E_{XC}[\rho(\mathbf{r})] + \int V_{ext}(\mathbf{r})\rho(\mathbf{r})d\mathbf{r}. \tag{2.30}$$

Faced with difficulties in expressing the kinetic energy component purely in terms of the density, Kohn and Sham next proposed the re-introduction of a wavefunction-like object [20]. The single-particle wavefunctions are related to our primary object of interest, the electron density, via

$$\rho(r) = \sum_{i=1}^{N} |\psi_i(\mathbf{r})|^2. \tag{2.31}$$

Since $\rho(\mathbf{r})$ is a function of $\{\psi_i\}$, minimisation of $E[\rho(\mathbf{r})]$ with respect to ψ is a non-linear optimisation problem. We consider variation of $E[\rho(\mathbf{r})]$ with respect to ψ_i^*,

$$\frac{\delta E[\rho(\mathbf{r})]}{\delta \psi_i^*(\mathbf{r})} = \frac{\delta E_{KE}}{\delta \psi_i^*(\mathbf{r})} + \left[\frac{\delta E_H[\rho(\mathbf{r})]}{\delta \rho(\mathbf{r})} + \frac{\delta E_{XC}[\rho(\mathbf{r})]}{\delta \rho(\mathbf{r})} + V_{ext}[\rho(\mathbf{r})] \right] \frac{\delta \rho(\mathbf{r})}{\delta \psi_i^*} = 0, \tag{2.32}$$

subject to the orthonormality condition $\langle \psi_i | \psi_j \rangle = \delta_{ij}$. We use

$$\frac{\delta E_{KE}}{\delta \psi_i^*(\mathbf{r})} = -\frac{1}{2}\nabla^2 \psi_i(\mathbf{r})$$

$$\frac{\delta \rho(\mathbf{r})}{\delta \psi_i^*} = \psi_i(\mathbf{r})$$

and apply the usual Lagrange method for handling constraints. This gives the Kohn-Sham (KS) equations

$$\hat{H}_{KS}\Big(\psi_i(\mathbf{r})\Big) = \left\{ \frac{-\nabla_i^2}{2} + V_{KS}(\mathbf{r}) \right\} \psi_i(\mathbf{r}) = \varepsilon_i \psi_i(\mathbf{r}), \tag{2.33}$$

where $V_{KS}(\mathbf{r}) = V_{ext}(\mathbf{r}) + V_H(\mathbf{r}) + V_{XC}(\mathbf{r})$ is the KS potential, and $V_H(\mathbf{r})$ and $V_{XC}(\mathbf{r})$ are the functional derivates of $E_H[\rho(\mathbf{r})]$ and $E_{XC}[\rho(\mathbf{r})]$ with respect to $\rho(\mathbf{r})$. To minimise $E[\rho(\mathbf{r})]$, only the lowest N eigenvalues and associated eigenvectors of the KS Hamiltonian need to be computed. These are called the KS eigenvalues and the occupied KS orbitals, respectively.

The KS equations are solved by first making an initial guess at the electron density. We then fix the electron density $\rho = \rho_{in}$ and compute the N lowest eigenvalues and associated eigenvectors. The output density, ρ_{out}, can then be obtained using Eq. (2.31), but ρ_{out} does not necessarily match ρ_{in} due to the fixing of the Hamiltonian during this process. Therefore, a new input density is generated based on some combination of ρ_{in} and ρ_{out} (although modern schemes would also include some number of previous $\{\rho_{in}\}$ in construction of a new density to improve convergence). The process is repeated until the input and output electron densities match to within a chosen tolerance, as shown in Fig. 2.1. The electronic ground-state energy is calculated from the KS eigenvalues as

$$E = \sum_i^N \varepsilon_i - E_H[\rho(\mathbf{r})] - \int V_{XC}(\mathbf{r})\rho(\mathbf{r})d\mathbf{r} + E_{XC}[\rho(\mathbf{r})]. \tag{2.34}$$

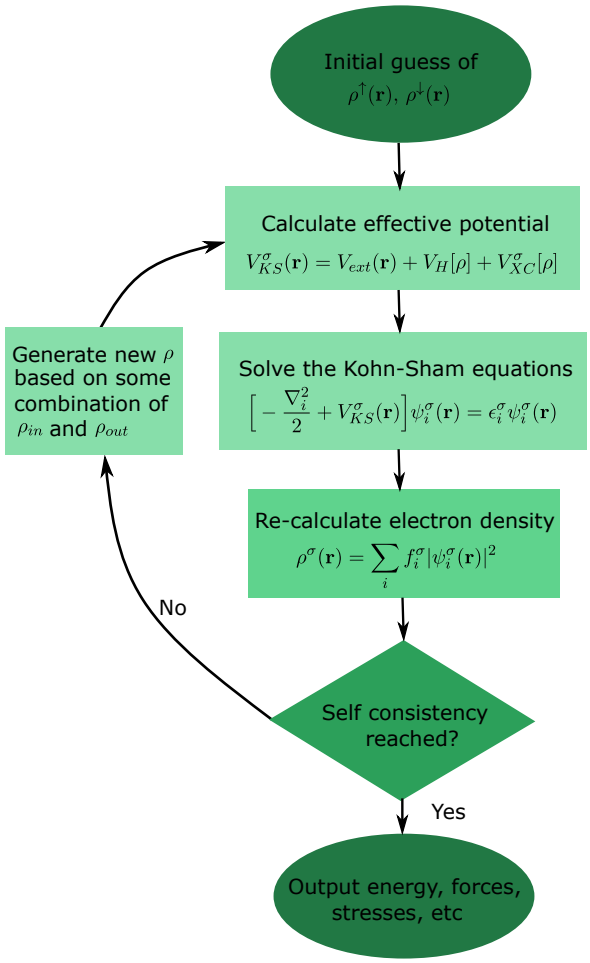

Fig. 2.1 A schematic diagram of the KS scheme.

From Eq. (2.33), it is clear that the KS scheme amounts to solving the problem of independent electrons in an effective potential, $V_{KS}(\mathbf{r})$. KS-DFT hence provides a way to map an interacting problem onto a non-interacting one. $V_{XC}(\mathbf{r})$ is defined to force the particles to behave like ground-state interacting electrons, i.e., it compensates for all the physics lost by invoking the single-particle picture. The cost associated with this is a lack of physical meaning for the KS orbitals and associated energies; the eigenvalues may have meaning within the framework itself (for example, Janak's theorem [21] states that the eigenvalue is the derivative of the total energy with respect to the occupation of a state), but only the highest-occupied orbital energy is said to have real *physical* meaning (being equal to the negative of the ionisation energy [22, 23] in exact KS). Another remaining, and very important, issue is that although we have discussed "exact DFT" up until now, we do not actually know the exact form of the exchange-correlation energy. We will meet some commonly-used approximations for the exchange-correlation functional shortly.

Aside: scope and validity of DFT

Several important works have discussed the possible extensions of DFT, and the set of densities, potentials and Hamiltonians for which there are guaranteed and unique solutions. These include Refs. [18, 19] as discussed previously. These topics are, however, beyond the scope of this thesis; an interested reader is referred to Refs. [22, 24, 25, 26, 27, 28, 29].

Exchange-correlation functionals

As we have seen, DFT provides an exact framework for studying electronic systems. However, a general form for the exchange-correlation functional is not known and it therefore must be approximated. As demonstrated in Appendix A, the exchange-correlation energy can be written as

$$E_{XC}[\rho(\mathbf{r},\sigma)] = \frac{1}{2}\sum_{\sigma,\sigma'}\int d\mathbf{r}d\mathbf{r}'\frac{\rho(\mathbf{r},\sigma)\rho_{XC}(\mathbf{r},\sigma;\mathbf{r}',\sigma')}{|\mathbf{r}-\mathbf{r}'|} \tag{2.35}$$

where $\rho_{XC}(\mathbf{r},\sigma;\mathbf{r}',\sigma')$ is the spin-dependent exchange-correlation hole density, which captures the fact that each electron creates a depletion of density around itself [11]. The exact exchange-correlation hole obeys a condition known as the sum rule (also derived in Appendix A):

$$\sum_{\sigma'}\int d\mathbf{r}'\rho_{XC}(\mathbf{r},\sigma;\mathbf{r}',\sigma') = -1. \tag{2.36}$$

It is common to rewrite Eq. 2.35 as

$$E_{XC}[\rho(\mathbf{r},\sigma)] = \int d\mathbf{r}\rho(\mathbf{r})\varepsilon_{XC}(\mathbf{r},\rho(\mathbf{r})). \tag{2.37}$$

As well as the sum rule, the exact exchange-correlation energy obeys the Lieb-Oxford bound [30] and has certain scaling properties. These limits can be used in the construction of approximate exchange-correlation functionals.

A large amount of effort has gone into obtaining suitable forms for the exchange-correlation energy. Theorists often refer to the Jacob's ladder of functionals; the local density approximation (LDA) occupies the first rung. In the LDA, the exchange-correlation energy at a given point is taken to be the same as that of a homogeneous electron gas[2] of the same density [31]. It therefore amounts to choosing an ε_{XC} that only depends on the electron density at the point of interest. For a homogeneous electron gas, the exchange contribution can be derived exactly and most modern implementations of LDA use a correlation part based on parameterisation [32] of Ceperley and Alder's 1980 quantum Monte Carlo calculation

[2]The homogeneous (or uniform) electron gas is a system of electrons under the influence of a Hamiltonian containing no external potential.

[33]. The LDA obeys the sum rule and has been known to give surprisingly good results for such a simple approximation.

Functionals on the second rung, the generalised gradient approximations (GGAs), include the gradient of the density, $\nabla\rho(\mathbf{r})$, as an independent variable [31]. The work that led to the development of the GGA was motivated by observations that exchange energy errors often dominate in the LDA. GGAs are based on a truncated gradient expansion approximation which preserves known properties of the exact exchange-correlation hole (namely its negativity and the sum rule) [34]. The GGA is not unique and many different forms exist. The parameters in the Perdew–Burke-Ernzerhof (PBE) [35] and PW91 [36] functionals were determined through application of theoretical limits and properties, while some parameters in BLYP (consisting of Becke-88 exchange [37] and Lee-Yang-Parr (LYP) correlation [38]) were determined by fitting to atomic HF data for noble gases. Although LYP correlation depends on the Laplacian (local kinetic energy) of the density, it is usually classified as a GGA rather than being placed on the next rung of the ladder as a meta-GGA. GGAs soften and expand bonds; this sometimes corrects and sometimes over-corrects the results obtained using LDA [35].

A somewhat separate category of functionals are the hybrid functionals, which include a fraction of exact (HF) exchange [31]; examples include the well-known B3LYP. Another group of functionals are the van der Waals (vdW) functionals, built with the aim of accounting for long-ranged interactions, such as vdW forces, which are especially important in soft matter systems [39, 40].

Periodicity and unit cells

In this thesis, we exclusively study periodic systems, meaning whole crystals that can be split up into repeating units called unit cells. No further partitioning of a unit cell can itself be used to construct the crystal. A *primitive cell* is a unit cell containing a single lattice point; its shape is described by the primitive lattice vectors, $\{\mathbf{a}_1, \mathbf{a}_2, \mathbf{a}_3\}$. These vectors are linearly independent and any linear combination of them,

$$\mathbf{R} = A_1\mathbf{a}_1 + A_2\mathbf{a}_2 + A_3\mathbf{a}_3 \tag{2.38}$$

(where $\{A_i\}$ are integers), is called a lattice vector. Translation by a lattice vector leaves the crystal unchanged.

Crystals are also periodic in reciprocal space. Reciprocal space can therefore be described by reciprocal primitive lattice vectors, $\{\mathbf{b}_1, \mathbf{b}_2, \mathbf{b}_3\}$, which define the wavevectors for plane waves with the same periodicity as the primitive lattice. These vectors satisfy $\mathbf{b}_i \cdot \mathbf{a}_j = 2\pi\delta_{ij}$

and we can form a general reciprocal lattice vector **G** by taking a linear combination,

$$\mathbf{G} = B_1\mathbf{b}_1 + B_2\mathbf{b}_2 + B_3\mathbf{b}_3, \tag{2.39}$$

where $\{B_i\}$ are integers.

In some cases, the full symmetry of a crystal is not obvious from the primitive cell and a conventional cell may be used instead. A *conventional cell* is the smallest unit cell whose axes follow the symmetry axes of the crystal structure. The volume of the conventional cell is always an integer multiple of the primitive cell volume. The Wigner-Seitz cell of a lattice point is defined as the volume that encloses all points in space that are closer to this particular lattice point than to any other; it has the highest point symmetry of any unit cell. The equivalent of the Wigner-Seitz cell for the reciprocal lattice is called the Brillouin zone.

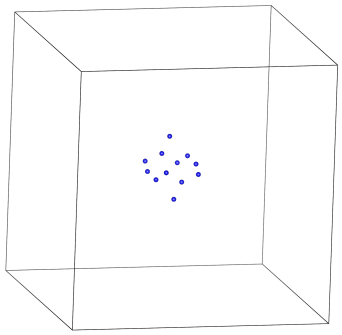

Fig. 2.2 The energy of this 12-atom hydrogen cluster can be found using the same techniques applied to perfect crystals by converging the result with respect to the size of the supercell.

Non-periodic entities can also be studied using periodic boundary conditions provided a cell can be chosen to mimic the aperiodic behaviour (for example, a large cell representing a perfect crystal with a single defect or one molecule in an otherwise empty simulation cell). This is the so-called supercell approach, as illustrated in Fig. 2.2. The properties of interest must be converged with respect to supercell size; this amounts to ensuring that the simulation cell is large enough for the defect, isolated molecule, cluster, or surface not to interact significantly with its own periodic images.

Bloch's theorem

If we have a periodic external potential of the form

$$V_{ext}(\mathbf{r}+\mathbf{R}) = V_{ext}(\mathbf{r}),$$

where $\mathbf{R}$ is a lattice vector, Bloch's theorem states that the density must have the same periodicity and therefore the possible wavefunctions are "quasi-periodic". This means $\psi(\mathbf{r}+\mathbf{R}) = \zeta(\mathbf{R})\psi(\mathbf{r})$, where $|\zeta(\mathbf{R})|^2 = 1$. From this, we see that $\zeta(\mathbf{R}) = e^{i\chi(\mathbf{R})}$ is the most general solution. We know

$$\psi(\mathbf{r}+\mathbf{R}+\mathbf{R}') = \psi((\mathbf{r}+\mathbf{R})+\mathbf{R}') = \zeta(\mathbf{R})\zeta(\mathbf{R}')\psi(\mathbf{r}),$$

but also

$$\psi(\mathbf{r}+\mathbf{R}+\mathbf{R}') = \psi(\mathbf{r}+(\mathbf{R}+\mathbf{R}')) = \zeta(\mathbf{R}+\mathbf{R}')\psi(\mathbf{r}).$$

Therefore,

$$\zeta(\mathbf{R}+\mathbf{R}') = \zeta(\mathbf{R})\zeta(\mathbf{R}') \Rightarrow \chi(\mathbf{R}+\mathbf{R}') = \chi(\mathbf{R})+\chi(\mathbf{R}'),$$

meaning $\chi(\mathbf{R})$ is linear in $\mathbf{R}$, i.e., $\chi(\mathbf{R}) = \mathbf{k}\cdot\mathbf{R}$, where $\mathbf{k}$ must be an arbitrary vector in *reciprocal* space (termed a "$\mathbf{k}$-point").

We will write a KS orbital as

$$\psi_{nk}(\mathbf{r}) = e^{i\mathbf{k}\cdot\mathbf{r}}u_{nk}(\mathbf{r}), \tag{2.40}$$

where n labels the particular electronic solution and u_{nk} has the same periodicity as the overall crystal. Combining Eq. (2.40) and the periodicity of the Bloch function u_{nk},

$$\psi_{nk}(\mathbf{r}+\mathbf{R}) = e^{i\mathbf{k}\cdot(\mathbf{r}+\mathbf{R})}u_{nk}(\mathbf{r}+\mathbf{R}) = e^{i\mathbf{k}\cdot\mathbf{R}}e^{i\mathbf{k}\cdot\mathbf{r}}u_{nk}(\mathbf{r}) = e^{i\mathbf{k}\cdot\mathbf{R}}\psi_{nk}(\mathbf{r}),$$

proving that this representation of the KS orbital fulfills Bloch's theorem as required.

Plane-wave representation

Any periodic function can be expanded exactly in terms of plane waves; they form an unbiased, non-localised basis set as the functions extend over all of space. The main electronic structure codes used in this thesis, CASTEP [41] and QUANTUM ESPRESSO [42, 43], are both plane-wave DFT codes. We can express the periodic Bloch function part of our KS orbitals, $u_{nk}(\mathbf{r})$, as a plane wave expansion

$$u_{nk}(\mathbf{r}) = \sum_G A_{Gnk}e^{i\mathbf{G}\cdot\mathbf{r}}, \tag{2.41}$$

where $\mathbf{G}$ are reciprocal lattice vectors, which we know satisfy $\mathbf{G}\cdot\mathbf{R} = 2m\pi$ (for integer m and any lattice vector $\mathbf{R}$) by definition, and A_{Gnk} are expansion coefficients. Putting together

Eq. 2.40 and Eq. 2.41, we therefore express our KS orbital as

$$\psi_{nk}(\mathbf{r}) = \sum_G A_{Gnk} e^{i(\mathbf{G}+\mathbf{k})\cdot\mathbf{r}}. \tag{2.42}$$

Inserting this expression into the KS eigenvalue equation, Eq. (2.33), and multiplying by $e^{-i(\mathbf{G}'+\mathbf{k})\cdot\mathbf{r}}$, we obtain

$$\sum_G \left[\left(\frac{1}{2}|\mathbf{k}+\mathbf{G}|^2 + V_{KS}(\mathbf{r}) \right) A_{Gnk} e^{i(\mathbf{G}-\mathbf{G}')\cdot\mathbf{r}} \right] = \varepsilon_{nk} \sum_G A_{Gnk} e^{i(\mathbf{G}-\mathbf{G}')\cdot\mathbf{r}}.$$

This can be integrated over the unit cell of our system (thus eliminating the $e^{i(\mathbf{G}-\mathbf{G}')\cdot\mathbf{r}}$ factor from constant terms) to give a matrix equation

$$\sum_G H_{GG'}(\mathbf{k}) A_{G'nk} = \varepsilon_{nk} A_{Gnk}. \tag{2.43}$$

Here, $H_{GG'}(\mathbf{k}) = \frac{1}{2}|\mathbf{k}+\mathbf{G}|^2 \delta_{GG'} + V_{KS}(\mathbf{G}-\mathbf{G}')$, where $V_{KS}(\mathbf{G}-\mathbf{G}')$ is the Fourier transform of the effective KS potential. The eigenvalues and eigenvectors solving Eq. (2.43) have the same periodicity as the reciprocal lattice, so we can choose to restrict ourselves to wavevectors, $\mathbf{k}$, in just the first Brillouin zone.

However, to make the calculation tractable we need to truncate the plane wave basis set. From the above, we see that only plane waves with kinetic energy

$$\frac{1}{2}|\mathbf{k}+\mathbf{G}|^2 \leq E_{cut} \tag{2.44}$$

are included in the calculation. The size of the plane-wave basis set used in a DFT calculation is hence controlled by a single parameter, the cut-off energy, E_{cut}. This provides us with a finite basis set which is *systematically improvable*; a feature that gives plane-wave basis sets a significant advantage over other alternatives. Other advantages associated with use of a plane-wave basis set are:

- the set of vectors $\{\mathbf{G}\}$ lies on the reciprocal lattice, which allows efficient utilisation of fast Fourier transforms to move between real- and reciprocal-space quantities,
- forces are often simpler to compute with plane waves than with localised basis sets,
- physical quantities tend to converge quite smoothly with E_{cut}.

However, a large number of plane waves are typically required to represent orbitals accurately, meaning $\hat{H}_{KS}$ has a large dimension and its exact diagonalisation becomes difficult. Utilisa-

tion of pseudopotentials and algorithms to compute only the lowest required eigenvalues and eigenvectors is therefore key.

Pseudopotentials

The orbitals of valence electrons acquire their complicated oscillatory behaviour because they must be orthogonal to the core electron orbitals. In the pseudopotential approximation, the core energy levels are removed and the Pauli exclusion principle is enforced by replacing these levels and the bare Coulomb potential close to the nucleus with a modified, weaker "pseudopotential". The pseudopotential is described as weak because cancellation between the Coulomb potential and repulsive Pauli term can be almost complete in the core region [44]. In a plane-wave representation, the regions of space where the wavefunction varies rapidly are described by large **G** components, so use of a pseudopotential to remove the oscillatory behaviour of the valence orbitals is particularly important. Pseudopotentials allow valence atomic orbitals to be described using significantly lower cut-off energies. They also reduce the number of KS orbitals required at all by effectively removing the core electrons from the calculation. The combination of these two effects means that pseudopotentials confer huge computational advantages.

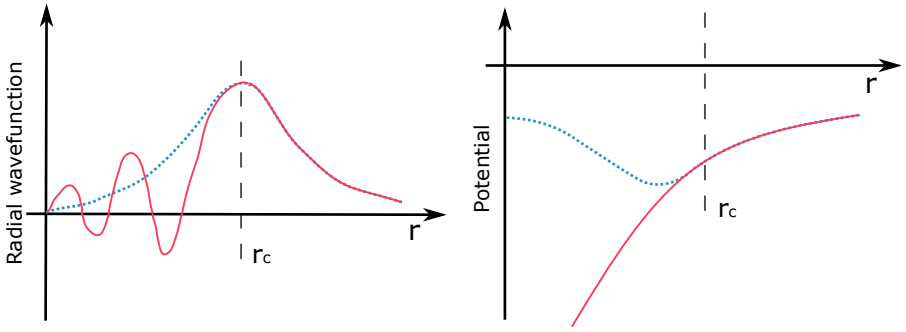

Fig. 2.3 An illustration demonstrating the action of a pseudopotential. The true wavefunction and potential are shown as solid red lines, while the pseudowavefunction and pseudopotential are shown as dotted blue lines. Oscillatory behaviour is suppressed within the core region when the true potential is replaced with a pseudopotential.

To construct a pseudopotential for a particular element, the otherwise identical all-electron problem is solved, then a smooth pseudo-orbital $\psi_{ps}(\mathbf{r})$ (that also fits the problem) is constructed and the Schrödinger equation is inverted to obtain the required pseudopotential. In order for the constructed $\psi_{ps}(\mathbf{r})$ to fit the problem and predict the same properties as the corresponding all-electron orbital, $\psi_{a-e}(\mathbf{r})$, it must satisfy a number of simple criteria. First of all, it is clear that the eigenvalue associated with each $\psi_{ps}(\mathbf{r})$ must be the same as the

one for the corresponding $\psi_{a-e}(\mathbf{r})$. Each $\psi_{ps}(\mathbf{r})$ must also match this $\psi_{a-e}(\mathbf{r})$ outside a chosen cut-off radius (r_c), and the first and second derivatives of the pseudo-orbitals and all-electron orbitals must match at r_c too. This leaves a fair amount of freedom in pseudo-orbital construction, but they usually designed to be as smooth as possible. A schematic diagram showing a hypothetical potential and corresponding radial wavefunction, alongside a weaker pseudopotential and its corresponding smoother pseudowavefunction is shown in Fig. 2.3.

We also stipulate that the total electronic charge of the valence electrons contained *within* r_c must be equal for ψ_{ps} and the all-electron orbital - this condition comes about because each orbital in standard KS-DFT is normalised. Pseudopotentials that obey this condition are called norm-conserving [45]. There also exists a class of pseudopotentials - called ultrasoft pseudopotentials [46] - in which this condition is relaxed during construction and imposed in an auxilliary step of the DFT calculation instead. Ultrasoft pseudopotentials can be further optimised and are often more accurate than norm-conserving alternatives.

k-point sampling

In principle, implementation of plane-wave DFT requires eigenvectors at all **k**-points within the first Brillouin zone to be calculated. However, if contributions to the quantity of interest vary slowly over reciprocal space, a smaller number of points can be sampled. The computational cost can, in most cases, be reduced using a scheme such as the one of Monkhorst and Pack [47], which assigns a weight to each special point **k** on a grid [44]. Using special points allows accurate expansion of the function of interest and interpolation between the points, making integration of periodic functions of the wavevector extremely efficient [47]. Crystal symmetries can also be utilised; they relate equivalent **k**-points, so that the only ones that need to be treated explicitly are those within the irreducible wedge of the Brillouin zone.

Forces and geometry optimisation

We will often be interested in the force acting on an individual atom; this is given by the derivative of the total energy with respect to the atomic position. These derivatives can be calculated using the finite differences method, where the energy is evaluated at several displacements and a numerical derivative calculated, or using the Hellmann-Feynman theorem [48, 49] described here. If λ represents a perturbation (an atomic displacement in

this case),

$$\frac{\partial E}{\partial \lambda} = \langle \frac{\partial \Psi}{\partial \lambda} | H | \Psi \rangle + \langle \Psi | \frac{\partial H}{\partial \lambda} | \Psi \rangle + \langle \Psi | H | \frac{\partial \Psi}{\partial \lambda} \rangle = \\ \langle \Psi | \frac{\partial H}{\partial \lambda} | \Psi \rangle + E \frac{\partial}{\partial \lambda} \langle \Psi | \Psi \rangle = \langle \Psi | \frac{\partial H}{\partial \lambda} | \Psi \rangle \quad (2.45)$$

since E is real and ψ is normalised. These forces are cheap to evaluate once we have ψ and the change in energy with respect to lattice vectors can be obtained in a similar way. Access to these quantities then allows the utilisation of optimisation techniques to find local minima of the BO energy surface (where all forces are zero). These minima correspond to stable crystal structures and the process of locating them is known as geometry optimisation.

Many different geometry optimisation methods exist. Steepest descents is the simplest approach; at each iteration, we take a downhill step from our current position along the steepest gradient and use line minimisation to find the optimal step length. Conjugate gradients is an improvement on steepest descents, which can be very slow to converge. The direction of downhill motion in this method is constructed to be conjugate to all previous search directions, thus producing more rapid convergence. In the Broyden-Fletcher-Goldfard-Shanno (BFGS) algorithm, a guess at the Hessian is constructed, allowing one to move straight to nearby minima. The convergence of this algorithm is generally good and it obtains extra physical information in the form of the Hessian. BFGS is usually the method of choice in modern calculations and will be used throughout this thesis. A schematic diagram of the steepest descent and conjugate gradient algorithms is shown in Fig. 2.4.

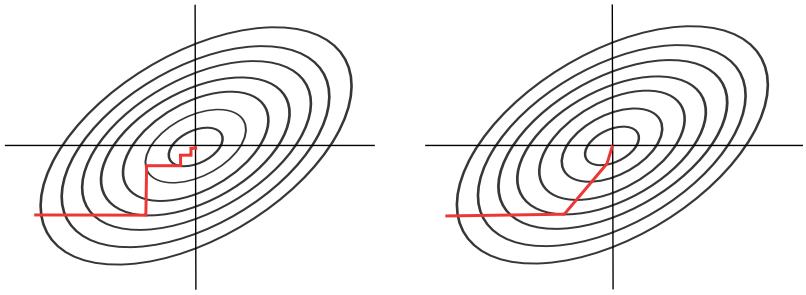

Fig. 2.4 An illustration of the steepest descent and conjugate gradient methods, respectively.

2.2.3 *Ab initio* random structure searching

As we have just seen, stable structures reside in minima of the potential energy surface (PES), so it should be possible to use DFT to map these surfaces and find the lowest energy structure of any material under any given conditions. The problem is that the number of PES minima increases exponentially with the number of atoms in the system [50] and each one

must be considered in order to definitively establish which one is the global minimum. The simplest possible strategy for a given composition would be to generate initial structures (i.e., unit cell shapes and sizes, and nuclear configurations) completely at random and then relax them to nearby minima of the PES using standard geometry optimisation techniques. However, in practice, it is necessary to bias searches towards "sensible" structures. In *ab initio* random structure searching (AIRSS) [50, 51] this is achieved by applying constraints (on, for example, density, structure symmetry, atomic separation or stoichiometry) in the initial structure generation process. If we are interested in molecular systems, randomly placing entire molecules in the simulation cell rather than their constituent atoms might also improve searching efficiency. The process of structure generation and relaxation is run in a high-throughput manner and repeated a huge number of times; once the same low-enthalpy structures have been found numerous times, the search is halted and the lowest enthalpy candidates can be extracted and studied further.

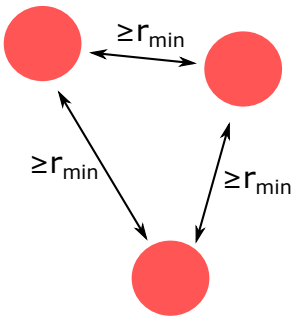

Fig. 2.5 Imposing a (species-dependent) minimum separation in the initial random configuration helps to avoid undesirable regions of configuration space (in which atoms are very close together and there are almost no minima [50]).

AIRSS has proved successful in a huge variety of different systems [52]. A number of intrinsic features of the PES, largely stemming from its relative smoothness at low energies, means that the method is much more efficient than would otherwise be expected:

- on moving from one basin (defined as the set of points for which relaxation leads to the same minimum) to a neighbouring one, if the energy barrier between the two basins is small, it is more likely that the neighbour will have a lower energy [50] (see Fig. 2.6 and the closely related Bell-Evans-Polanyi principle [53]),
- low-energy basins are expected to occur near other low-energy basins [50] (meaning "shaking" procedures can be effective),

- basins with lower energy minima tend to have larger hyper-volumes in structure space [50], acting directly in favour of the searcher as these basins are more likely to be sampled (see Fig. 2.6).

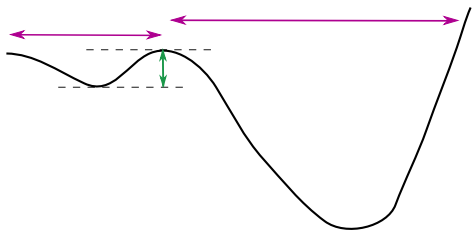

Fig. 2.6 If the energy barrier between two basins is small, the neighbour is more likely to have a lower energy. The lower energy the minimum, the larger its associated hyper-volume tends to be.

In saddle-point AIRSS (sp-AIRSS) [54], the ideas of AIRSS are applied while enforcing strict symmetry constraints. This allows the discovery of structures residing on saddle-points of the PES which may be stabilised by vibrational effects.

There are many other crystal structure prediction methods available. Simulated annealing [55, 56, 57] is a Monte Carlo technique in which the current approximate state is replaced by a randomly chosen nearby state. The probability of accepting the new state is 1 if it is lower in energy than the current one and $e^{-\Delta E/T}$, where ΔE is the energy difference between the two states, otherwise. This means that at $T = 0$ only lower energy states are accessible and it is possible to become trapped in local minima. T is therefore typically given a large initial value which is gradually reduced. There are many types of evolutionary algorithms [58], which can be applied to optimisation and search problems, with genetic algorithms being the most popular type. In this class of methods, an ensemble of structures is generated and each member is assigned a "fitness" (in this case, an energy or enthalpy). A fraction of these structures is selected, with a bias based on their fitness, for reproduction and a mutation step may also be performed. It is common to relax the structures to their nearest minima at each step using traditional geometry optimisation techniques and the whole process is repeated many times. A related class of algorithms are particle swarm optimisation methods [59]. Ref. [60] gives a more detailed description of these methods and others, including basin hopping and minima hopping. Although different methods will have different benefits, these alternative algorithms are at a computational disadvantage to AIRSS because they are not inherently parallelisable. One downside of AIRSS, however, is that it does not actively explore around minima or provide access to low-barrier transition pathways. In this thesis, since we are only interested in locating favourable local minima or saddle-points, all structure searching is performed using either AIRSS or sp-AIRSS.

2.2.4 Convex hulls and stability at the static-lattice level

While a structure may be the lowest in enthalpy for a given stoichiometry, this does not necessarily mean that the structure is thermodynamically stable in relation to other structures formed from the same elements. To work out if a certain stoichiometry is stable to decomposition, we can construct a convex hull from formation energies and elemental chemical potentials. The formation energy of a binary structure A_xB_y is calculated as

$$E_{form}(A_xB_y) = E(A_xB_y) - xE(A) - yE(B), \tag{2.46}$$

where the energies on the right-hand side are converged DFT ground-state energies. The convex hull is then constructed by plotting the formation energy for each structure as a function of composition (as illustrated in the Fig. 2.7).

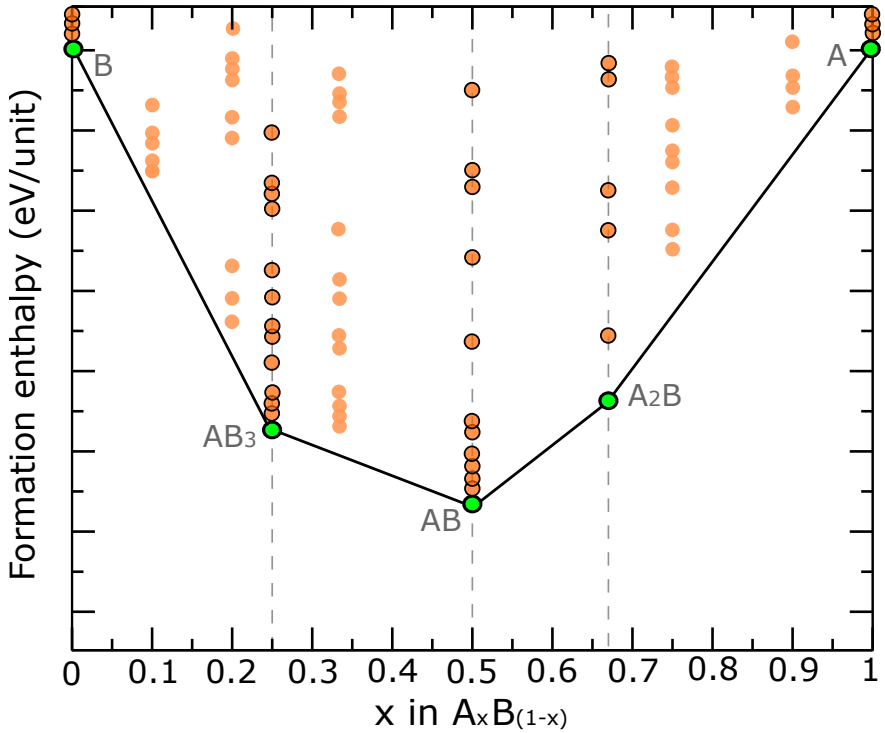

Fig. 2.7 A schematic diagram of a convex hull for a binary system. The green points represent the lowest energy structures of stable stoichiometries. The outlined orange points are higher energy structures of these stable stoichiometries. The other orange points correspond to structures of stoichiometries which are not stable to decomposition (at this level of theory).

For a binary system, any stoichiometry for which a structure sits on the bottom tie-line of the hull is considered to be stable at the level of theory used. A large number of structures is typically required to construct these diagrams and crystal structure prediction methods

are often used for generating these. Due to the large number of structures involved, convex hulls tend to be calculated at the static-lattice level (where nuclear motion is neglected), but vibrational zero-point energies and temperature effects can sometimes have an impact on the results. Eq. 2.46 is easily extended to ternary structures and beyond, and more complicated hulls can be constructed for these systems.

2.3 Vibrations in solids: the harmonic approximation

As we saw in Section 2.1.2, after invoking the Born-Oppenheimer approximation, the nuclear or vibrational Hamiltonian is given by

$$\hat{H}_{vib} = -\frac{1}{2}\sum_{\alpha}\frac{1}{m_\alpha}\nabla_\alpha^2 + \varepsilon_{BO}(\{\mathbf{R}_\alpha\}) \tag{2.47}$$

where the BO energy surface, $\varepsilon_{BO}(\{\mathbf{R}_\alpha\})$, describes the potential energy as a function of nuclear positions and is therefore a function of $3M$ variables. M is typically large, so solution of the equations describing vibrational motion presents a significant computational challenge.

The harmonic approximation simplifies the description of nuclear vibrations. It is valid when the vibrational amplitudes are small, meaning the atoms do not deviate far from their equilibrium positions. We consider an infinite periodic solid with M atoms in the primitive cell, and denote the origin of the λth primitive cell as $\mathbf{R}_p(\lambda)$. The equilibrium position of atom k in this unit cell is given by

$$\mathbf{r}_0(\lambda,k) = \mathbf{R}_p(\lambda) + \mathbf{r}(k). \tag{2.48}$$

However, due to quantum and thermal fluctations, the *instantaneous* position of the kth atom in the λth unit cell is actually given by

$$\mathbf{r}(\lambda,k) = \mathbf{r}_0(\lambda,k) + \mathbf{u}(\lambda,k), \tag{2.49}$$

where $\mathbf{u}(\lambda,k)$ is an atomic displacement. We can express ε_{BO} as a function of these displacements by performing a Taylor expansion around the equilibrium atomic positions. In the harmonic approximation we only keep the terms in this expansion up to second order,

$$\varepsilon_{harm} = \varepsilon_0 + \frac{1}{2}\sum_{\lambda,k,j,\lambda',k',j'} C_{jj'}(\lambda k,\lambda' k')u_j(\lambda,k)u_{j'}(\lambda',k'), \tag{2.50}$$

where ε_0 is the potential energy at equilibrium, j and j' denote Cartesian directions, and C is the matrix of interatomic force constants with elements given by

$$C_{jj'}(\lambda k, \lambda' k') = \left. \frac{\partial^2 \varepsilon_{BO}}{\partial u_j(\lambda, k) \partial u_{j'}(\lambda', k')} \right|_0 . \tag{2.51}$$

The subscript indicates that the derivative is evaluated at the equilibrium atomic positions. No first order term appears in Eq. (2.50) because the first derivatives of the potential energy evaluated at the equilibrium positions are zero by definition. The constant ε_0 term is neglected in the following since it does not affect the motion of the atoms.

The equations of motion for the atoms in our system are

$$m_k \frac{d^2 u_j(\lambda, k)}{dt^2} = - \sum_{\lambda' k' j'} C_{jj'}(\lambda k, \lambda' k') u_{j'}(\lambda', k'), \tag{2.52}$$

where m_k is the mass of atom k. To simplify this, we can write the displacement in a mass-weighted plane wave representation $u_j(\lambda, k) = (\xi_{jk}/\sqrt{m_k}) e^{-i(\mathbf{k} \cdot \mathbf{R}_p(\lambda) - \omega t)}$, which is consistent with equations of motion being invariant under translation by $\mathbf{R}_p(\mu)$. Here ξ_{jk} is independent of both λ and t. The equations of motion then become

$$\omega^2 \xi_{jk} e^{-i(\mathbf{k} \cdot \mathbf{R}_p(\lambda))} = \sum_{\lambda' k' j'} \frac{1}{\sqrt{m_k m_{k'}}} C_{jj'}(\lambda k, \lambda' k') \xi_{j'k'} e^{-i(\mathbf{k}' \cdot \mathbf{R}_p(\lambda'))}. \tag{2.53}$$

Eq. (2.53) can be rewritten as

$$\sum_{k' j'} D_{jk, j'k'}(\mathbf{k}) \xi_{j'k'} = \omega^2 \xi_{jk}, \tag{2.54}$$

where

$$D_{jk, j'k'}(\mathbf{k}) = \frac{1}{\sqrt{m_k m_{k'}}} \sum_{\lambda'} C_{jj'}(\lambda k, \lambda' k') e^{i\mathbf{k} \cdot (\mathbf{R}_p(\lambda) - \mathbf{R}_p(\lambda'))} \tag{2.55}$$

is the dynamical matrix. Non-trivial solutions to Eq. (2.54) are found when

$$|D_{jk, j'k'}(\mathbf{k}) - \omega^2_{n\mathbf{k}} \delta_{kk'} \delta_{jj'}| = 0, \tag{2.56}$$

where n is the branch index and takes values from 1 to $3M$ and $\mathbf{k}$ is the wavevector. $\omega^2_{n\mathbf{k}}$ are the eigenvalues of the dynamical matrix and $\xi(n, \mathbf{k})$ are the associated eigenvectors. In full

form, we write the displacement as

$$u_j(\lambda,k) = \frac{\xi_{jk}(n,\mathbf{k})}{\sqrt{m_k}} e^{-i(\mathbf{k}\cdot\mathbf{R}_p(\lambda)-\omega_{n\mathbf{k}}t)} \tag{2.57}$$

for the normal mode labelled by $(n,\mathbf{k})$. The general motion of the atoms is then a linear combination of these normal modes.

Furthermore, it is possible to simultaneously diagonalise the kinetic energy and potential energy terms in the harmonic vibrational Hamiltonian by rewriting them in terms of normal coordinates defined by

$$q'_{n\mathbf{k}} = \frac{1}{\sqrt{N_p}} \sum_{\lambda k j} \sqrt{m_k} u_j(\lambda,k) e^{-i\mathbf{k}\cdot\mathbf{R}_p(\lambda)} \xi^*_{jk}(n,\mathbf{k}), \tag{2.58}$$

where N_p is the number of primitive cells in the calculation. We can construct real normal coordinates by taking linear combinations of these:

$$q_{n\mathbf{k}} = \frac{1}{\sqrt{2}}[q'_{n\mathbf{k}} + q'_{n-\mathbf{k}}] \text{ and } q_{n-\mathbf{k}} = \frac{i}{\sqrt{2}}[q'_{n\mathbf{k}} - q'_{n-\mathbf{k}}].$$

The vibrational Hamiltonian then becomes

$$\hat{H}_{vib} = -\frac{1}{2}\sum_{n\mathbf{k}} \frac{\partial^2}{\partial q^2_{n\mathbf{k}}} + \frac{1}{2}\sum_{n\mathbf{k}} \omega^2_{n\mathbf{k}} q^2_{n\mathbf{k}}, \tag{2.59}$$

which we recognise as being equivalent to a system of non-interacting simple harmonic oscillators with frequencies $\omega_{n\mathbf{k}}$. The quasiparticles corresponding to these oscillators are known as phonons and the dependence of these frequencies on the wave vector is called the phonon dispersion. Since this Hamiltonian is separable, the total vibrational wavefunction can be written as a product of single-mode eigenstates, each of which can be found analytically along with its energy.

2.3.1 Finite displacements and implementation in CAESAR

As we have seen, in order to obtain harmonic frequencies and, ultimately, vibrational contributions to the energy within the harmonic approximation, we need to construct the dynamical matrix from the matrix of force constants. Force constants can be extracted from second derivatives of the total energy with respect to atomic displacements. These derivatives can be calculated using direct methods, which will be discussed here, or perturbative methods, which will be discussed in more detail in Section 2.3.2. Direct methods involve calculating

derivatives using finite differences; this is the approach taken in CAESAR, a code capable of performing both harmonic and anharmonic phonon calculations, which is used in Chapter 3. Although originally developed by Dr Bartomeu Monserrat, the version of CAESAR used in this thesis was developed by Mark Johnson and is described in Ref. [61].

In a finite differences framework, we consider small displacements of all the atoms in the system in turn. The displacement of atom k in the cell at $\mathbf{R}_p(\lambda)$ in Cartesian direction j leads to a small force on atom k' in the unit cell at $\mathbf{R}_p(\lambda')$ in direction j'. These forces are routinely calculated in DFT codes. The matrix of force constants is related to this by

$$C_{jj'}(\lambda k,\lambda' k') = \left.\frac{\partial^2 \varepsilon_{BO}}{\partial u_j(\lambda,k)\partial u_{j'}(\lambda',k')}\right|_0 \approx \frac{\delta F^{\lambda',k';j'}_{\lambda,k;j}}{\delta u_j(\lambda,k)}. \tag{2.60}$$

A finite differences approach can be used with any underlying electronic structure method and, since the atomic displacements are made explicitly and the resulting energies are computed exactly, we capture contributions to all orders in the displacement and the method is therefore suitable even for large perturbations. However, only phonons commensurate with the simulation cell can be captured exactly in this framework [62]. Traditionally, very large simulation cells were required and these calculations often became intractable. However, this problem was addressed by the introduction of non-diagonal supercells [62], which allows supercells containing far fewer primitive cells to be used.

In order to explain the concept of non-diagonal supercells, which is utilised in CAESAR, we must introduce some notation. A supercell is expressed as

$$\begin{pmatrix}\mathbf{a}_{s_1}\\ \mathbf{a}_{s_2}\\ \mathbf{a}_{s_3}\end{pmatrix} = \begin{pmatrix}S_{11} & S_{12} & S_{13}\\ S_{21} & S_{22} & S_{23}\\ S_{31} & S_{32} & S_{33}\end{pmatrix}\begin{pmatrix}\mathbf{a}_1\\ \mathbf{a}_2\\ \mathbf{a}_3\end{pmatrix} \tag{2.61}$$

where $\{\mathbf{a}_i\}$ are the primitive lattice vectors as before, $\{\mathbf{a}_{s_i}\}$ are the supercell lattice vectors, and the supercell matrix, S, consists of integer elements, S_{ij}. A diagonal supercell is simply one that is generated by a diagonal supercell matrix and the number of primitive cells in a supercell is given by the determinant of this matrix, $|S|$ [62].

We know that the reciprocal primitive lattice vectors can be written in terms of the primitive lattice vectors as

$$\begin{pmatrix}\mathbf{b}_1\\ \mathbf{b}_2\\ \mathbf{b}_3\end{pmatrix} = 2\pi\begin{pmatrix}\mathbf{a}_1\\ \mathbf{a}_2\\ \mathbf{a}_3\end{pmatrix}^{-T} \tag{2.62}$$

Combining Eq. (2.61) and Eq. (2.62), the reciprocal supercell lattice vectors are expressed as

$$\begin{pmatrix} \mathbf{b}_{s_1} \\ \mathbf{b}_{s_2} \\ \mathbf{b}_{s_3} \end{pmatrix} = \begin{pmatrix} \bar{S}_{11} & \bar{S}_{12} & \bar{S}_{13} \\ \bar{S}_{21} & \bar{S}_{22} & \bar{S}_{23} \\ \bar{S}_{31} & \bar{S}_{32} & \bar{S}_{33} \end{pmatrix} \begin{pmatrix} \mathbf{b}_1 \\ \mathbf{b}_2 \\ \mathbf{b}_3 \end{pmatrix} \tag{2.63}$$

where $\bar{S}_{ij} = (S^{-1})_{ji}$. An arbitary **k**-point can then be expressed in fractional coordinates, using a basis of either reciprocal primitive lattice vectors or reciprocal supercell lattice vectors. The fractional coordinates of an arbitary **k**-point with respect to these two bases are related by

$$\begin{pmatrix} k_{s_1} \\ k_{s_2} \\ k_{s_3} \end{pmatrix} = \begin{pmatrix} S_{11} & S_{12} & S_{13} \\ S_{21} & S_{22} & S_{23} \\ S_{31} & S_{32} & S_{33} \end{pmatrix} \begin{pmatrix} k_{p_1} \\ k_{p_2} \\ k_{p_3} \end{pmatrix} \tag{2.64}$$

If the fractional coordinates with respect to the reciprocal supercell lattice vectors are integers, we say that perturbations characterised by wavevector **k** are *commensurate* with the supercell generated by S and we are hence able to capture the effect of the perturbation exactly [62].

With this in mind, it is clear that if we have a perturbation characterised by a wavevector of reduced fractional coordinates

$$\begin{pmatrix} m_1/n_1 \\ m_2/n_2 \\ m_3/n_3 \end{pmatrix} \tag{2.65}$$

with respect to the reciprocal primitive lattice vectors and we are restricted to a diagonal supercell matrix, the supercell must contain (at least) $n_1 n_2 n_3$ primitive cells in order for the perturbation to be commensurate with it. Ref. [62] showed that by allowing non-zero off-diagonal elements to appear in the supercell matrix, this number can be reduced to the least common multiple of n_1, n_2 and n_3. This means that problems requiring an $N \times N \times N$ vibrational grid, which previously required N^3 primitive cells in the simulation cell, now only require N primitive cells, representing a dramatic reduction in computational cost.

2.3.2 Density functional perturbation theory

Many physical properties - including vibrational ones - can be calculated by considering a system's response to some form of perturbation. Density functional perturbation theory (DFPT) is a technique that allows calculation of these properties within the density functional

framework that we have already introduced. While finite differences is used in CAESAR [61] (used in Chapter 3) to extract vibrational properties, QUANTUM ESPRESSO [42, 43] (used in Chapters 4, 5, and 6) employs DFPT. There are two main DFPT formalisms: Baroni's [63] and Gonze's [64]. While the two approaches may seem rather disconnected at first, they can actually be shown to be equivalent. Here we will introduce DFPT in the context of a general perturbation (and hence in relation to a general property of interest).

Formalism I

We look first at Baroni's formalism. The basic idea underpinning DFPT is that the wavefunction, electron density and potential may all be written as a perturbation series,

$$X(\lambda) = X^{(0)} + \lambda X^{(1)} + \lambda^2 X^{(2)} + ..., \tag{2.66}$$

where X is the given physical quantity, λ is the perturbing parameter (always assumed to be small), and $X^{(n)} = \frac{1}{n!}\frac{d^n X}{d\lambda^n}|_{\lambda=0}$. If we are within the framework of DFT, the variation in KS orbitals is determined by solution of the Sternheimer equation [65, 66, 67],

$$(H_{KS}^{(0)} - \varepsilon_n^{(0)})\,|\psi_n^{(1)}\rangle = -(H_{KS}^{(1)} - \varepsilon_n^{(1)})\,|\psi_n^{(0)}\rangle\,, \tag{2.67}$$

which is obtained by expanding the KS equations to first order. Here, the first order KS potential is given by

$$H_{KS}^{(1)} = T^{(1)} + V_{ext}^{(1)}(\mathbf{r}) + \int \frac{\rho^{(1)}(\mathbf{r}')}{|\mathbf{r}-\mathbf{r}'|}d\mathbf{r}' + \int \frac{\partial V_{xc}}{\partial \rho(\mathbf{r}')}\rho^{(1)}(\mathbf{r}')d\mathbf{r}'. \tag{2.68}$$

Multiplying Eq. 2.67 by $\langle\psi_n^{(0)}|$ and $\langle\psi_m^{(0)}|$ in turn, and using $\langle\psi_n^{(0)}|\psi_m^{(1)}\rangle = 0$, we get

$$\varepsilon_n^{(1)} = \langle\psi_n^{(0)}|H_{KS}^{(1)}|\psi_n^{(0)}\rangle\,, \tag{2.69}$$

$$|\psi_n^{(1)}\rangle = \sum_{m\neq n} \frac{\langle\psi_m^{(0)}|H_{KS}^{(1)}|\psi_n^{(0)}\rangle}{\varepsilon_n^{(0)} - \varepsilon_m^{(0)}}\,|\psi_m^{(0)}\rangle\,, \tag{2.70}$$

which we recognise as the usual first order perturbation theory result. These form a set of self-consistent equations that must be solved in order to determine the behaviour of the perturbed system. In a way, these equations are analogous to the KS equations in the unperturbed case, but with the KS eigenvalue equation replaced by solution of a linear system, Eq. 2.67 [68]. The first order electron density can be determined by considering how the unperturbed

density relates to the orbitals and then using Eq. 2.70:

$$\rho^{(1)}(\mathbf{r}) = \sum_{n=1}^{N} \psi_n^{(0)*}(\mathbf{r})\psi_n^{(1)}(\mathbf{r}) + \psi_n^{(1)*}(\mathbf{r})\psi_n^{(0)}(\mathbf{r}) = 2\sum_{n=1}^{N}\sum_{m\neq n} \psi_n^{(0)*}(\mathbf{r})\psi_m^{(0)}(\mathbf{r})\frac{\langle\psi_m^{(0)}|H_{KS}^{(1)}|\psi_n^{(0)}\rangle}{\varepsilon_n^{(0)} - \varepsilon_m^{(0)}}. \quad (2.71)$$

Contributions in Eq. 2.71 due to products of occupied states cancel out. Therefore, if we identify the label n with valence (v) states, the label m refers only to the conduction (c) band. It then becomes apparent that the electron density only responds to perturbations that couple the valence and conduction manifolds [68].

While explicit evaluation of $|\psi_n^{(1)}\rangle$ via the usual Eq. 2.70 requires knowledge of the full spectrum of the KS Hamiltonian and extensive sums over empty (conduction) bands, only knowledge of the occupied states is needed to construct the right-hand side of Eq. 2.67 [68]. Then, since we now know that the system's response depends only on the component of the perturbation that couples the valence manifold to the conduction one, we can actually replace the right-hand side of Eq. 2.67 with $-P_c H_{KS}^{(1)}|\psi_n^{(0)}\rangle$ [68] where P_c is the projector onto the conduction band manifold, given by

$$P_c = \mathbf{1} - P_v = \mathbf{1} - \sum_v |\psi_v^{(0)}\rangle\langle\psi_v^{(0)}| = \sum_c |\psi_c^{(0)}\rangle\langle\psi_c^{(0)}|. \quad (2.72)$$

Adding some multiple of the projector P_v to the linear operator on the left-hand side of Eq. 2.67 to make it non-singular [68] leads to

$$(H_{KS}^{(0)} + \alpha P_v - \varepsilon_n^{(0)})|\psi_n^{(1)}\rangle = -P_c H_{KS}^{(1)}|\psi_n^{(0)}\rangle. \quad (2.73)$$

Solution of the Sternheimer equation therefore amounts to solving this modified linear problem, which can be achieved rather efficiently. We see that solution of this equation (and hence determination the first order correction to the KS orbitals) only requires knowledge of the occupied KS states and it therefore has a numerical complexity similar to self-consistent solution of the unperturbed system. Higher order terms in the perturbation series for the orbitals, energy or density can then be obtained as needed. The method is not restricted to local perturbations (in contrast to methods which rely on the inversion of the dielectric matrix) or short wavelengths (in contrast to direct methods with limited supercell size) [63]. Metals may experience a change in occupation of the electronic states on application of the perturbation, so separate, but similar, formulae exist for metallic systems.

Formalism II

The central ingredient of the second formalism of DFPT is the $(2n+1)$ theorem [69] of perturbation theory. The theorem states that only changes in the eigenfunctions up to order n are required in order to compute the $(2n+1)$th derivative of the energy. We have already seen that this is the case for atomic displacements when $n = 0$ ($2n+1 = 1$) as this corresponds to the Hellmann-Feynman theorem for calculating forces. Ref. [69] also showed that the second order change in the energy obeys a minimisation principle with respect to variations in the corresponding first order wavefunction. Ref. [70] applied these ideas directly to the KS energy functional and showed that the formalism contains, as a special case, the treatment of linear-response coefficients suggested by Baroni. The existence of a $(2n+1)$ theorem in DFT therefore leads to a *variational* formalism of DFPT; Gonze [64] formalised this idea by explicitly proving the existence of even-order variational principles for constrained functionals. Writing the second order energy using the $(2n+1)$ theorem, we can show that the Euler-Lagrange equation associated with its minimisation is the Sternheimer equation, demonstrating the equivalence of the two formalisms discussed here.

Application to vibrational properties

Now that we have introduced DFPT in general terms, we can consider using this theoretical framework to obtain vibrational properties within the harmonic approximation. In order to do so, we must consider perturbations in ionic positions; the dynamical matrix encountered in Section 2.3 can then easily be connected to the second order derivatives of the energy calculated at a specified phonon wavevector, $\mathbf{q}$. From Gonze's formalism [64], we know that the DFPT problem can be solved by minimising the second order energy. This variational technique for solving DFPT is considered to be more robust than Baroni's original method and has the added conceptional benefit of more closely resembling the ordinary DFT problem. The expression for the second order energy in DFT can be obtained simply from the KS equation and written as a functional of the first order density (although there are ionic as well as electronic contributions to consider). The resulting expression can be minimised with respect to the first order wavefunctions using a standard minimisation scheme. The dynamical matrix at a given $\mathbf{q}$ is then evaluated from the converged first order wavefunctions and density.

DFPT has the benefit of being able to treat incommensurate perturbations in a single unit cell, i.e., without the need to construct supercells. This property of the theory becomes apparent when it is noticed that the Sternheimer equation can be rewritten entirely in terms of lattice-periodic functions. Once the equations are solved to obtain the first order wavefunction

and density, response to any **q**-vector can be obtained simply by incorporating the relevant phase factor. This gives the method a significant advantage over the finite differences alternative we met earlier.

2.3.3 Dynamic and thermodynamic stability

Within the static-lattice approximation, in which nuclear motion is neglected entirely, we are effectively modelling the atoms as classical particles at 0 K. This is the cheapest and lowest order approximation available to us; after geometry optimisation, the free energy of the system can be calculated without any further work on our part because it is simply given by the value of the PES at the nuclear configuration of interest.

Since the relevant energy scales in the electronic system are typically much larger than those associated with nuclear motion, this rather severe approximation is actually more useful than may initially be thought. Even in light-atom systems, which can have large vibrational energies, the static-lattice approximation often captures enough of the energetics to allow us to identify and eliminate structures whose free energy is too high to warrant further investigation. This idea is, of course, utilised in AIRSS whenever we select structures from an enthalpy ranking or use static-lattice convex hulls to identify relevant stoichiometries.

We've seen that the next level of approximation available to us is the harmonic approximation. By assuming that the harmonic approximation holds separately at each volume, we obtain the quasi-harmonic approximation (QHA). Within the QHA, the Helmholtz free energy at a given volume and temperature is

$$F(V,T) = E_{DFT}(V,T) + F_{vib}(V,T), \tag{2.74}$$

where the first term is the electronic energy and the second term is the harmonic free energy contribution. At a given pressure and temperature, the structure with the lowest *Gibbs* free energy is the most thermodynamically stable, but in order to calculate the Gibbs free energy we first need to calculate the "phonon-corrected" pressure. This is the pressure obtained once the phonon contributions to the energy are included via Eq. 2.74.

Phonon-corrected pressures can be determined by considering how the free energy, F, relates to pressure. We know that $F = U - TS$ where U is the internal energy of the system (which has both electronic and phonon components) and TS is the entropic contribution. From thermodynamics, we also know that $dU = \delta Q + \delta W$ and (for reversible processes) the energy added as heat is $\delta Q = TdS$ and the work done on the system is $\delta W = -PdV$. This gives $dU = TdS - PdV = d(TS) - SdT - PdV$ and therefore $dF = d(U - TS) = -SdT - PdV$,

leading to

$$P(V) = -\left(\frac{\delta F}{\delta V}\right)\Big|_T. \tag{2.75}$$

Corrected pressures can therefore be obtained by computing derivatives of F (with respect to V) numerically; this will not be a preferable option in this thesis due to the large pressure ranges involved in most of our calculations and the computational limit on how densely we can afford to calculate data points. To circumvent this problem, F can be fitted as a polynomial of V using the available data points and a derivative can be taken in this way instead.

An alternative way of calculating phonon-corrected pressures is using a known equation of state. The Birch-Murnaghan equation of state [71], where

$$E(V) = E_0 + \frac{9V_0B_0}{16}\left[\left(\left(\frac{V_0}{V}\right)^{2/3} - 1\right)^3 B_0' + \left(\left(\frac{V_0}{V}\right)^{2/3} - 1\right)^2 \left(6 - 4\left(\frac{V_0}{V}\right)^{2/3}\right)\right] \tag{2.76}$$

and

$$P(V) = \frac{3B_0}{2}\left(\left(\frac{V_0}{V}\right)^{7/3} - \left(\frac{V_0}{V}\right)^{5/3}\right)\left[1 + \frac{3}{4}(B_0' - 4)\left(\left(\frac{V_0}{V}\right)^{2/3} - 1\right)\right] \tag{2.77}$$

is a popular choice. We can fit the equation for $E(V)$ to our F as a function of inverse volume, extract the fitting coefficients, V_0 and B_0, and use these to calculate the corrected pressure at a given volume using Eq. 2.77. Upper and lower bounds can be imposed during fitting process based on physical knowledge (e.g., V_0 and B_0 should both be positive) and the quality of the fit needs to be monitored carefully.

An alternative equation of state is the Vinet exponential equation:

$$E(V) = E_0 + \frac{2B_0V_0}{(B_0' - 1)^2}\left[2 - \left(5 + 3\left(\frac{V}{V_0}\right)^{1/3}(B_0' - 1) - 3B_0'\right) exp\left(-\frac{3}{2}(B_0' - 1)\left(\left(\frac{V}{V_0}\right)^{1/3} - 1\right)\right)\right] \tag{2.78}$$

and

$$P(V) = 3B_0\left(\frac{V}{V_0}\right)^{-2/3}\left[1 - \left(\frac{V}{V_0}\right)^{1/3}\right] exp\left(-\frac{3}{2}(B_0' - 1)\left[\left(\frac{V}{V_0}\right)^{1/3} - 1\right]\right). \tag{2.79}$$

Once the corrected pressures, $P(V)$, have been obtained using one of these methods, the dependence can be numerically inverted to give $V(P)$, the Gibbs free energy can be calculated as $G(P,T) = F(V(P),T) + PV(P)$, and the predicted phase behaviour can be determined.

Dynamic stability requires that no infinitesimal perturbation to the crystal structure will result in a reduction of the energy - it therefore means that the structure is in a local minimum. In cases where this is not true, the harmonic frequencies associated with one or more normal modes will be imaginary, meaning that the free energy cannot be properly defined and the structure is unstable under the harmonic approximation. Such structures can be dealt with either by further relaxation - following the imaginary mode(s) until we reach a minimum, giving the predicted phase behaviour strictly within the harmonic approximation - or can be treated with more costly methods which account for anharmonicity as we will explore in Section 2.4.

2.4 Beyond the harmonic approximation

The QHA is very commonly used, but it is not always an appropriate way to describe a system's vibrational properties as the harmonic approximation fails when atoms deviate too far from their equilibrium positions. This may be the case for systems containing light atoms or at high temperatures. The harmonic approximation is also inappropriate for modelling structures which correspond to a saddle-point of the PES rather than a minimum. Corrections arising from the anharmonic nature of the interatomic potential are therefore crucial in a sizeable class of physical systems. Anharmonicity has previously been found to play a large role in determining the phase diagram of water ice [72, 73] and of solid hydrogen [74], and leads to an inverse isotope effect in superconducting palladium hydride [75].

Imaginary time path integral simulations can be used to obtain vibrational properties that are essentially exact for a given potential [76]. However, these simulations are extremely computationally expensive and other frameworks for calculating approximations to the anharmonic free energy have been developed over the years. In this section, we describe some commonly used methods: the independent mode approximation; the vibrational self-consistent field method; and path integral approaches. Methods based on Monte Carlo sampling, in which a set of PES samples is generated stochastically and used to calculate free energies and other expectation values directly, also exist. There is an accuracy-applicability trade-off with vibrational methods, just as there is with electronic ones [77]. The vibrational equivalents of the Møller-Plesset, configuration interaction and coupled cluster theories (VMP, VCI and VCC) are accurate, but limited to rather small molecules in the gas phase

[77]. In Ref. [76] the cost and accuracy of various vibrational methods for three-dimensional periodic systems is evaluated.

2.4.1 Independent mode framework

In order to approximate the anharmonic nature of the true PES, we can consider expanding the potential in terms of harmonic normal mode coordinates. This is called the principal axes approximation (PAA) [78], which will be introduced more formally below. In the full expansion, the potential would be expressed as the potential generated at the equilibrium configuration added to anharmonic independent mode terms, followed by terms which represent pair-wise and higher order coupling between the normal modes. Truncation after the anharmonic independent mode terms represents one of the simplest anharmonic approximations - the independent mode framework (IMF). The modes remain independent in this representation, so the system can be solved in a similar way to the harmonic system introduced before.

2.4.2 Vibrational self-consistent field

Full application of the vibrational self-consistent field (VSCF) method to 3-dimensional, periodic systems was introduced in Ref. [78], the content of which we briefly recap here. First, we must employ the PAA and map the BO energy surface out to large amplitudes along normal mode coordinates. Large amplitudes are used (in contrast to standard harmonic calculations) in order to access the regions of configuration space where anharmonicity becomes important. Mathematically, the PAA amounts to writing the BO energy surface as

$$E_{el}(\mathbf{Q}) = E_{el}(\mathbf{0}) + \sum_{n\mathbf{k}} V_{n\mathbf{k}}(q_{n\mathbf{k}}) + \frac{1}{2} \sum_{n\mathbf{k}n'\mathbf{k}'} V_{n\mathbf{k}n'\mathbf{k}'}(q_{n\mathbf{k}}, q_{n'\mathbf{k}'}) + ..., \tag{2.80}$$

where $\{q_{n\mathbf{k}}\}$ are the harmonic phonon normal coordinates, $\mathbf{Q}$ is the collective phonon coordinate and $(n\mathbf{k}) = (n'\mathbf{k}')$ is excluded from the second sum. The terms in the first sum are referred to as independent phonon terms [78] and are given by

$$V_{n\mathbf{k}}(q_{n\mathbf{k}}) = E_{el}(0, ..., q_{n\mathbf{k}}, ...0) - E_{el}(\mathbf{0}). \tag{2.81}$$

These are the terms retained in the IMF. The terms in the next sum are two-body terms, given by

$$V_{n\mathbf{k}n'\mathbf{k}'}(q_{n\mathbf{k}}, q_{n'\mathbf{k}'}) = E_{el}(0, ..., q_{n\mathbf{k}}, ..., q_{n'\mathbf{k}'}, ...0) - V_{n\mathbf{k}}(q_{n\mathbf{k}}) - V_{n'\mathbf{k}'}(q_{n'\mathbf{k}'}) - E_{el}(\mathbf{0}), \tag{2.82}$$

which induce pair-wise coupling between the phonon modes. We can continue the series in Eq. (2.80), but higher order terms are expected to be small [78].

Within the PAA, the nuclear Hamiltonian is then given by

$$\hat{H}_{vib} = \sum_{n\mathbf{k}} -\frac{1}{2}\frac{\partial^2}{\partial q_{n\mathbf{k}}^2} + E_{el}(\mathbf{Q}) \tag{2.83}$$

and we have $\hat{H}_{vib}\,|\phi(\mathbf{Q})\rangle = E_{vib}\,|\phi(\mathbf{Q})\rangle$, where $|\phi(\mathbf{Q})\rangle$ is the anharmonic wavefunction and E_{vib} is the anharmonic energy. Retaining terms beyond the independent phonon ones leads to coupling of the previously independent normal modes and this complicates the solution of the Schrödinger equation [76]. To solve this problem, the energy is minimised with respect to a set of single-mode states that form a Hartree product for the trial wavefunction, $|\phi(\mathbf{Q})\rangle = \prod_{n\mathbf{k}} |\phi_{n\mathbf{k}}(q_{n\mathbf{k}})\rangle$. This amounts to a mean-field treatment; the VSCF method is, therefore, the vibrational equivalent of Hartree-Fock theory. The minimisation leads to the VSCF equations [78]:

$$\left(-\frac{1}{2}\frac{\partial^2}{\partial q_{n\mathbf{k}}^2} + \bar{V}_{n\mathbf{k}}(q_{n\mathbf{k}}) \right) |\phi_{n\mathbf{k}}(q_{n\mathbf{k}})\rangle = \lambda_{n\mathbf{k}}\,|\phi_{n\mathbf{k}}(q_{n\mathbf{k}})\rangle \tag{2.84}$$

where $\bar{V}_{n\mathbf{k}}(q_{n\mathbf{k}}) = \langle \prod_{n'\mathbf{k}'} \phi_{n'\mathbf{k}'}(q_{n'\mathbf{k}'}) | E_{el}(\mathbf{Q}) | \prod_{n'\mathbf{k}'} \phi_{n'\mathbf{k}'}(q_{n'\mathbf{k}'}) \rangle$ (with the $(n\mathbf{k}) = (n'\mathbf{k}')$ case excluded), and $\lambda_{n\mathbf{k}}$ is a vibrational energy eigenvalue. It is then straight-forward to show that the final vibrational energy is given by

$$E_{vib} = \sum_{n\mathbf{k}} \lambda_{n\mathbf{k}} + \langle \prod_{n\mathbf{k}} \phi_{n\mathbf{k}}(q_{n\mathbf{k}}) | E_{el}(\mathbf{Q}) - \sum_{n\mathbf{k}} \bar{V}_{n\mathbf{k}}(q_{n\mathbf{k}}) | \prod_{n\mathbf{k}} \phi_{n\mathbf{k}}(q_{n\mathbf{k}}) \rangle\,. \tag{2.85}$$

At fixed cell size IMF and VSCF provide the temperature dependence of the free energy without any additional electronic structure evaluations. This is because solution of the VSCF equations leads to a set of excited eigenstates; these in turn can be used to construct excited anharmonic wavefunctions as

$$|\phi^{\mathbf{S}}(\mathbf{Q})\rangle = \prod_{n\mathbf{k}} |\phi_{n\mathbf{k}}^{s_{n\mathbf{k}}}(q_{n\mathbf{k}})\rangle \tag{2.86}$$

where $s_{n\mathbf{k}}$ are elements of vector $\mathbf{S}$ and define the individual state of the excited states. The approximate anharmonic wavefunction $|\phi^{\mathbf{S}}(\mathbf{Q})\rangle$ has an energy $E_{\mathbf{S}}$ and the anharmonic free energy can be calculated as a function of temperature using

$$F = -\frac{1}{\beta}\ln Z \tag{2.87}$$

where $Z = \sum_{\mathbf{S}} e^{-\beta E_{\mathbf{S}}}$ and β is the inverse temperature. This means that the anharmonic free energy can be approximated at any temperature without the need to perform any additional electronic structure calculations. That said, it is also possible to populate the approximate energy surface itself at some finite temperature by distributing the electrons appropriately [78].

The final VSCF Hamiltonian is equivalent to the PAA, but with coefficients calculated self-consistently rather than drawn directly from the PES [61]. The anharmonic terms can generally be truncated at a shorter range than the harmonic terms (since they have coefficients that fall off faster with distance [61]), meaning that in real calculations the anharmonic terms can be computed using a smaller **q**-point grid than the harmonic ones.

Aside: VSCF in CAESAR

Anharmonic calculations in CAESAR are performed using the VSCF method with a number of modifications. We know that the symmetries of a crystal map the equilibrium position of every atom onto the equilibrium position of an atom of the same species. This, of course, does not always map an atom to near itself, but atoms of the same species can be relabelled so that they remain near their equilibrium positions after transformation. Combining symmetries with relabelling means that, rather than acting on atoms, the combined symmetries can be thought of as acting on atomic displacements [61] and this confers computational advantages. The PES in CAESAR is fitted to a set of carefully chosen samples, each of which is an individual electronic structure calculation at a particular nuclear configuration. There are a number of possible PES representations; CAESAR uses a basis set representation which has the advantage that symmetry operations can be applied one basis function at a time and the representations are often amenable to analytic (rather than numerical) integration [61].

To illustrate some more points about implementation, the simplest VSCF potential is $V = \sum_j V_j(q_j)$ and the states are given by $|\phi(Q)\rangle = \prod_j |\phi_j(q_j)\rangle$ (where we now use $j \equiv n\mathbf{k}$ to simplify the expressions). We have seen that each single-mode potential is the average across all modes except the one of interest. The eigenvalue equations obeyed by the single-mode states, Eq. 2.84, and the equations defining the single-mode potentials must be solved self-consistently since the former (which gives all states $\{|\phi_j\rangle\}$) has a Hamiltonian that includes $\bar{V}_j$, which itself depends on all $|\phi_{j'}\rangle$. Expanding each single-mode potential in the same manner as the full potential [61] gives

$$V_j = \sum_{n_j} V_{n_j} q_j^{n_j}, \tag{2.88}$$

where V_{n_j} is a constant coefficient - these coefficients can be combined into a single vector $\mathbf{V}$ which completely describes the set of single-mode potentials. Each iteration of the self-consistency scheme starts with the vector $\mathbf{V}$. This is fed into the single-mode eigenvalue equations to give the single-mode states $\{|\phi_j\rangle\}$, then the states are used to generate a new set of single-mode potentials, giving a new coefficient vector $\mathbf{V}'$. A vector $\mathbf{V}$ for the next iteration can be generated by feeding the current $\mathbf{V}$ and $\mathbf{V}'$ into an adapted Pulay scheme [61], aiming to reach the self-consistency condition $\mathbf{V} = \mathbf{V}'$ to within a defined tolerance.

However, symmetries are difficult (or impossible) to apply at arbitrary $\mathbf{q}$-points in a single-mode representation. This stems from the fact that the PAA is not symmetry-invariant. Since the normal modes of the crystal can be separated into subspaces of degenerate modes, the PAA can be made symmetry-invariant by changing its definition [61]. Instead of limiting the terms in the PES expansion to those containing up to a given number of normal modes, the terms can be limited to those with normal modes from a given number of subspaces [61]. CAESAR therefore runs VSCF in the language of single-subspace (rather than single-mode) objects [61], where each subspace contains all modes that have the same harmonic frequencies at $\mathbf{q}$ and $-\mathbf{q}$. The process can be expensive when large subspaces are present.

Another issue is size consistency; a method is said to be size-consistent when it predicts thermodynamic observables with the correct volume dependence [77]. Crystal models should, of course, be size-consistent. Extensive quantities (such as energy and entropy) are asymptotically proportional to the volume of the system or number of atoms, whereas intensive quantities (excitation energies, pressure, and temperature) are asymptotically constant. The harmonic approximation is naturally size-consistent. The PAA and VSCF, however, are fundamentally size inconsistent. This issue is considered in detail in Ref. [61].

2.4.3 Thermodynamic integration

The concept of thermodynamic integration was introduced by Kirkwood [79]. It is based on the idea that (to within statistical accuracy) the exact free energy difference between two states can be calculated as the work done to reversibly transform one state into the other [76]. This method can be used to calculate the quantum anharmonic correction to the (known) classical harmonic free energy in two steps.

Firstly, the classical anharmonic correction can be calculated as the work done while turning on the anharmonic part of the interaction. The Hamiltonian describing this change is defined as $H^{\lambda} = (1-\lambda)H^{har} + \lambda H$, where the parameter λ takes the potential from harmonic to fully anharmonic as it varies from 0 to 1 [76]. The classical anharmonic free energy correction, ΔA_{cl}, at a given temperature is then obtained by computing the integral of

the thermodynamic "force" along λ's path:

$$\Delta A_{cl} = \int_0^1 d\lambda \left(\frac{\partial A}{\partial \lambda}\right) = \int_0^1 d\lambda \, \langle V - V^{har} \rangle_{H^\lambda} \,, \tag{2.89}$$

where $\langle ... \rangle_{H^\lambda}$ is the sampled average according to the intermediate Hamiltonian (determined by the current λ value) [76]. Molecular dynamics (MD) simulations are used to sample various points along the path and the classical canonical ensemble is used in this first step.

Next, an additional thermodynamic integration must be performed in order to transform the particles from classical to quantum in nature [76] and obtain the corresponding free energy correction. The Hamiltonian defined to describe this change includes a parameter that scales the mass of the particles. The quantum free energy correction can then be computed by sampling along this mass path using path integral MD in the quantum canonical ensemble. The combined value of these two integrals gives the total quantum anharmonic correction to the free energy.

2.5 Electron-phonon interactions and superconductivity

Superconductivity is a macroscopic quantum-mechanical phenomenon. Conventional superconductivity, which we will study in this thesis, is mediated by phonons and can be described by the Bardeen-Cooper-Schrieffer (BCS) theory of superconductivity [80] and its extensions. BCS theory describes an attractive interaction between electrons that can overcome the Coulomb interaction; the electrons become correlated and form "Cooper pairs". At low enough temperatures (defined by the system-specific superconducting critical temperature, T_c), electrons remain paired regardless of other effects, leading to the characteristics of the superconducting state, such as an abrupt fall to zero resistivity and the Meissner effect. According to BCS, T_c is related to a typical phonon frequency $\langle \omega \rangle$ by

$$T_c = 1.14 \, \langle \omega \rangle \, e^{(-1/N(\varepsilon_F)V)}, \tag{2.90}$$

where $N(\varepsilon_F)$ is the electronic density of states (DOS) at the Fermi level and V is the pairing potential arising from the electron-phonon interaction.

Described in more formal terms, in conventional superconductors exchange of virtual phonons produces an attractive interaction between electrons close to the Fermi level. Electrons in Cooper pairs are boson-like, meaning they can occupy the same level (or "condense") and a gap, Δ, opens up in the energy spectrum. This gap relates to the energy required to break a Cooper pair and therefore depends on the pairing potential. At $T = 0$, Δ has a

maximum, while for $T > T_c$, $\Delta = 0$ and the material is a normal metal. BCS fails for strong electron-phonon coupling; the reason is that the interaction it describes is instantaneous in nature [81] and does not incorporate enough of the physics of the electron-phonon system. It is therefore not an appropriate theory for use in our work on high-pressure hydrides.

A more realistic description comes from Migdal-Eliashberg theory. This theory was formulated when Eliashberg [82] generalised the time-dependence of the electron-phonon interaction - building on Migdal's earlier work with normal metals. Migdal [83] showed that a perturbation series for the vertex function of the electron-phonon interaction converges rapidly, regardless of whether the interaction is weak or strong. Therefore, by Migdal's theorem, only leading terms in the Feynman diagram of the self-energy need to be included. The neglected terms are of the order of $(m/M)^{1/2} \propto \omega_D/\varepsilon_F$, where m is electron mass, M is nuclear mass, ω_D is the Debye frequency or characteristic phonon frequency, and ε_F is the Fermi energy. Migdal-Eliashberg theory accounts for retardation effects and variations of it can also work for multiband and anisotropic superconductors.

Aside from direct solution of the complicated Eliashberg equations, key quantities derived directly from the Hamiltonian of the coupled electron-phonon system can be used in the approximate McMillan [84] or Allen-Dynes [85] equations, which are simpler methods for calculating T_c.

2.5.1 The coupled electron-phonon system

The Hamiltonian of a coupled electron-phonon system is

$$\hat{H} = \sum_{n\mathbf{k}} \varepsilon_{n\mathbf{k}} \hat{c}^{\dagger}_{n\mathbf{k}} \hat{c}_{n\mathbf{k}} + \sum_{\mathbf{q}\nu} \omega_{\mathbf{q}\nu} (\hat{a}^{\dagger}_{\mathbf{q}\nu} \hat{a}_{\mathbf{q}\nu} + \frac{1}{2}) + N_p^{-1/2} \sum_{\mathbf{q},\mathbf{k},m,n,\nu} g_{mn\nu}(\mathbf{k},\mathbf{q}) \hat{c}^{\dagger}_{m,\mathbf{k}+\mathbf{q}} \hat{c}_{n\mathbf{k}} (\hat{a}_{\mathbf{q}\nu} + \hat{a}^{\dagger}_{-\mathbf{q}\nu}). \quad (2.91)$$

The first two terms describe the electron and phonon subsystems, respectively, in standard 2nd quantised form. The electronic part assumes that the system can be described in terms of well-defined quasiparticle excitations [86]; in this work we calculate $\varepsilon_{n\mathbf{k}}$ as single-particle KS eigenvalues. The phonon term is only meaningful within the Born-Oppenheimer and harmonic approximations, with the phonon frequencies, $\omega_{\mathbf{q}\nu}$, calculated as described earlier. The third term describes electron-phonon coupling to first order in atomic displacements (it represents an electron in an occupied state $|n,\mathbf{k}\rangle$ coupled to an unoccupied state $|m,\mathbf{k}+\mathbf{q}\rangle$ by a phonon with momentum $\mathbf{q}$). The coupling strength of this interaction is determined by $g_{mn\nu}(\mathbf{k},\mathbf{q})$, which can be calculated from first principles using DFPT. N_p is the number

of unit cells in the supercell, as before. An additional fourth term describing electron-phonon coupling to the second order in atomic displacements plays an important role in the temperature-dependence of band structures and has a coupling strength $g^{DW}_{mn\nu\nu'}(\mathbf{k},\mathbf{q},\mathbf{q}')$ [86]. Calculation of this term is much more complicated, however, and it is usually ignored entirely. We will revisit this in Chapter 4. Linking back to the Born-Oppenheimer approximation, which we have assumed up until now, electron-phonon interactions allow the motion of nuclei to induce transitions between different electronic states. Taking these interactions into consideration therefore constitutes a relaxation of the Born-Oppenheimer approximation.

If a phonon with momentum $\mathbf{q}$ and frequency $\omega_{\mathbf{q}\nu}$ provides coupling between the initial state $|n,\mathbf{k}\rangle$ and final state $|m,\mathbf{k}+\mathbf{q}\rangle$, while displacing the set of atoms at positions $\{r_\kappa\}$ with masses $\{m_\kappa\}$ along the eigenvectors $\{\xi_\kappa(\nu,\mathbf{q})\}$, the resulting coupling strength is given by the matrix element

$$g_{mn\nu}(\mathbf{k},\mathbf{q}) = \langle m,\mathbf{k}+\mathbf{q}|\frac{1}{\sqrt{2\omega_{\mathbf{q}\nu}}}\sum_\kappa \frac{\xi_\kappa(\nu,\mathbf{q})}{\sqrt{m_\kappa}}\cdot\frac{\partial V_{KS}}{\partial r_\kappa}|n,\mathbf{k}\rangle\,, \tag{2.92}$$

where we sum over the atoms concerned, $\frac{\partial V_{KS}}{\partial r_\kappa}$ is the resulting change in the KS potential associated with a given atomic displacement, and the integration is performed over a single unit cell. The resulting (lowest order) electron-electron interaction is due to a virtual phonon exchange, where we have an effective electron-electron interaction given by

$$V_{el-ph-el}(\mathbf{k}_1,\mathbf{k}_2,\mathbf{q})_{nn'mm'} = g_{nn'\nu}(\mathbf{k}_1,\mathbf{q})g_{mm'\nu}(\mathbf{k}_2,\mathbf{q})\frac{\omega_{\mathbf{q}\nu}}{(\varepsilon_{\mathbf{k}_1 n}-\varepsilon_{\mathbf{k}_1 n'})^2-\omega^2_{\mathbf{q}\nu}}. \tag{2.93}$$

Since the initial state needs to be occupied and the final one unoccupied, only states close to one another either side of the Fermi surface (within $\pm k_B T$) will contribute significantly to the interaction.

As a result of the coupling, the phonons obtain a linewidth given by

$$\gamma_{\mathbf{q}\nu} = 2\pi\omega_{\mathbf{q}\nu}\sum_{mnk}|g_{mn\nu}(\mathbf{k},\mathbf{q})|^2\delta(\varepsilon_{m,\mathbf{k}+\mathbf{q}}-\varepsilon_F)\delta(\varepsilon_{n,\mathbf{k}}-\varepsilon_F). \tag{2.94}$$

These linewidths are typically interpolated onto a finer $\mathbf{q}$-point grid than the one they were originally calculated on in order to construct the electron-boson spectral function,

$$\alpha^2F(\omega) = \frac{1}{2\pi N(\varepsilon_F)}\sum_{\mathbf{q}\nu}\frac{\gamma_{\mathbf{q}\nu}}{\omega_{\mathbf{q}\nu}}\delta(\omega-\omega_{\mathbf{q}\nu}). \tag{2.95}$$

The electron-phonon coupling constant, an important parameter for characterising conventional superconductors, is then given by

$$\lambda = 2\int d\omega \frac{\alpha^2 F(\omega)}{\omega}. \tag{2.96}$$

From these quantities, we can obtain the superconducting critical temperature, either by direct solution of the Eliashberg equations or using approximate formulae, which we will introduce later.

The spectral function and double-delta smearing

We see that the electron-phonon coupling matrix elements relate to the linewidths, and hence the spectral function, via a double-delta integration on the Fermi surface (see Eq. 2.94). Accurate calculation of this integral requires dense sampling in both the electronic (**k**) and the phononic (**q**) grids. However, for the finite **k**-point grids that must be used in DFT, the energies $\varepsilon_{n,\mathbf{k}}$ will never lie exactly on the Fermi level. In this thesis, we overcome this by following the method suggested in Ref. [87] - smearing the delta-functions in Eq. 2.94 into finite-width Gaussians with a characteristic smearing width σ. Ideally, the smallest possible value of σ should be used (for infinitely dense **k**- and **q**-point grids, convergence is achieved when σ approaches zero). For finite grids, however (even when they are well-converged), using too small a value of σ results in a poor reproduction of Fermi surface characteristics. To ensure we are not in this numerically poor regime, one therefore has to find a range of σ values yielding similar results (either for the integrals or for T_c directly) for converged **k**-point grids of different sizes [87]. The smallest value of σ for which the two grids agree should then be used to read off the result. This computational subtlety and its impact on predicted T_c will be a focus of Chapter 4.

2.5.2 Migdal-Eliashberg theory

Migdal theory

The natural way to discuss many-body electron-phonon systems is in terms of Green functions and propagators [81], which can be defined in terms of the relevant self-energies. The Migdal equation gives a simplified expression for the electron self-energy in the normal state; Migdal argued that higher order vertex corrections can be ignored, by showing that they are all of the order $(m/M)^{1/2}$ compared to the bare vertex [81, 83]. To begin describing our electron-

phonon system in this language, the one-electron Green function is

$$G(\mathbf{k}, i\omega_m) = [G_0(\mathbf{k}, i\omega_m)^{-1} - \Sigma(\mathbf{k}, i\omega_m)]^{-1} \tag{2.97}$$

and the phonon propagator is

$$D(\mathbf{q}, i\nu_n) = [D_0(\mathbf{q}, i\nu_n)^{-1} - \Pi(\mathbf{q}, i\nu_n)]^{-1}, \tag{2.98}$$

where $\Sigma(\mathbf{k}, i\omega_m)$ is the usual electron self-energy and $\Pi(\mathbf{q}, i\nu_n)$ is the phonon self-energy. The subscript 0 indicates a non-interacting propagator, here these are given by

$$G_0(\mathbf{k}, i\omega_m) = [i\omega_m - (\varepsilon_\mathbf{k} - \mu)]^{-1} \tag{2.99}$$

$$D_0(\mathbf{q}, i\nu_n) = [-M(\omega^2(\mathbf{q}) + \nu_n^2)]^{-1} \tag{2.100}$$

where $\varepsilon_\mathbf{k}$ and $\omega(\mathbf{q})$ take their usual definitions as the single-electron dispersion and the phonon dispersion, respectively, and μ is the chemical potential. Here we are using the finite temperature Matsubara formalism with fermion $i\omega_m = i\pi T(2m-1)$ and boson $i\nu_n = i2\pi Tn$ Matsubara frequencies (where T is temperature, and m and n are integers) [81].

We write the electron and phonon self-energies as

$$\Sigma(\mathbf{k}, i\omega_m) = -\frac{1}{N\beta} \sum_{\mathbf{k}', m'} g_{\mathbf{k}\mathbf{k}'} D(\mathbf{k} - \mathbf{k}', i\omega_m - i\omega_{m'}) \\ G(\mathbf{k}', i\omega_{m'}) \Gamma(\mathbf{k}', i\omega_{m'}; \mathbf{k}, i\omega_m; \mathbf{k} - \mathbf{k}', i\omega_m - i\omega_{m'}) \tag{2.101}$$

and

$$\Pi(\mathbf{q}, i\nu_n) = \frac{2}{N\beta} \sum_{\mathbf{k}, m} g_{\mathbf{k}, \mathbf{k}+\mathbf{q}} G(\mathbf{k}+\mathbf{q}, i\omega_m + i\nu_n) G(\mathbf{k}, i\omega_m) \Gamma(\mathbf{k}+\mathbf{q}, i\omega_m + i\nu_n; \mathbf{k}, i\omega_m; \mathbf{q}, i\nu_n), \tag{2.102}$$

where the sums extend over all integers and momenta in the first Brillouin zone [81]. The vertex function, Γ, appearing here is fully represented by an infinite set of diagrams, however, Migdal's approximation amounts to setting Γ equal to just the bare vertex, g [83]. Then,

$$\Sigma(\mathbf{k}, i\omega_m) = -\frac{1}{N\beta} \sum_{\mathbf{k}', m'} |g_{\mathbf{k}\mathbf{k}'}|^2 D(\mathbf{k} - \mathbf{k}', i\omega_m - i\omega_{m'}) G(\mathbf{k}', i\omega_{m'}). \tag{2.103}$$

We are then able to define the electron-phonon spectral function

$$\alpha^2 F(\mathbf{k}, \mathbf{k}', \nu) = N(\mu) |g_{\mathbf{k}, \mathbf{k}'}|^2 B(\mathbf{k} - \mathbf{k}', \nu) \tag{2.104}$$

where we have used the fact that the phonon propagator can be written in terms of its spectral representation [81] as

$$D(\mathbf{q}, i\nu_n) = \int_0^\infty d\nu B(\mathbf{q}, \nu) \frac{2\nu}{(i\nu_n)^2 - \nu^2}. \tag{2.105}$$

The spectral function $\alpha^2F(\mathbf{k}, \mathbf{k}', \nu)$ has the Fermi-surface average

$$\alpha^2F(\nu) = \frac{1}{N(\mu)^2} \sum_{\mathbf{k},\mathbf{k}'} \alpha^2F(\mathbf{k}, \mathbf{k}', \nu)\delta(\varepsilon_\mathbf{k} - \mu)\delta(\varepsilon_{\mathbf{k}'} - \mu), \tag{2.106}$$

from which an electron-phonon coupling constant (or "mass enhancement parameter" [81]) can be defined as before.

Eliashberg theory

Eliashberg theory [82] is valid to within the validity of Migdal theory (i.e., when only single phonon scattering terms contribute significantly to the electron self-energy). The coupling it describes is local in space, but retarded in time (reflecting the delay in the development of lattice overscreening) [81]. The results, known collectively as the Eliashberg equations, can be summarised as

$$\Sigma(\mathbf{k}, i\omega_m) \equiv \frac{1}{N\beta} \sum_{\mathbf{k}',m'} \frac{\lambda_{\mathbf{k}\mathbf{k}'}(i\omega_m - i\omega_{m'})}{N(\mu)} G(\mathbf{k}', i\omega_{m'}), \tag{2.107}$$

$$G(\mathbf{k}, i\omega_m) = \frac{G_n^{-1}(\mathbf{k}, i\omega_m)}{G_n^{-1}(\mathbf{k}, i\omega_m)G_n^{-1}(-\mathbf{k}, -i\omega_m) + \phi(\mathbf{k}, i\omega_m)\bar{\phi}(\mathbf{k}, i\omega_m)}, \tag{2.108}$$

$$\phi(\mathbf{k}, i\omega_m) \equiv \frac{1}{N\beta} \sum_{\mathbf{k}',m'} \left[\frac{\lambda_{\mathbf{k}\mathbf{k}'}(i\omega_m - i\omega_{m'})}{N(\mu)} - V_{\mathbf{k}\mathbf{k}'} \right] F(\mathbf{k}', i\omega_{m'}), \tag{2.109}$$

$$F(\mathbf{k}, i\omega_m) = \frac{\phi(\mathbf{k}, i\omega_m)}{G_n^{-1}(\mathbf{k}, i\omega_m)G_n^{-1}(-\mathbf{k}, -i\omega_m) + \phi(-\mathbf{k}, -i\omega_m)\bar{\phi}(-\mathbf{k}, -i\omega_m)}, \tag{2.110}$$

where a number of quantities are recognisable from the previous section, $G_n^{-1}(\mathbf{k}, i\omega_m) = G_0^{-1}(\mathbf{k}, i\omega_m) - \Sigma(\mathbf{k}, i\omega_m)$, $N(\mu)$ is the DOS at the chemical potential, and $V_{\mathbf{k}\mathbf{k}'}$ is the pairing interaction (which also includes a direct Coulomb repulsion component for the interaction between electrons [88]). In order to understand the origin of F and the additional self-energy, $\phi(\mathbf{k}, i\omega)$, we note that the one-electron Green function we met earlier can be defined as a function of imaginary time via $G(\mathbf{k}, \tau - \tau') \equiv -\langle T_\tau c_{\mathbf{k}\sigma}(\tau) c^\dagger_{\mathbf{k}\sigma}(\tau') \rangle$, where the angular brakets denote a thermodynamic average. This object can be Fourier expanded in imaginary

frequency, leading to the expression $G(\mathbf{k}, i\omega_m) = \int_0^\beta d\tau G(\mathbf{k}, \tau) e^{i\omega_m \tau}$. However, we must also take anomalous amplitudes into account in order to describe the superconducting state [81]; these take the form $F(\mathbf{k}, \tau) \equiv -\langle T_\tau c_{\mathbf{k}\uparrow}(\tau) c^\dagger_{-\mathbf{k}\downarrow}(0)\rangle$, from which $F(\mathbf{k}, i\omega)$ is defined in the same manner as $G(\mathbf{k}, i\omega_m)$ via a Fourier transform. Given these two quantities, we can then define two different self-energies. The first, $\Sigma(\mathbf{k}, i\omega_m)$ is the usual electron self-energy, as we met before, generalised for the superconducting state [81]. The second is the anomalous self-energy, $\phi(\mathbf{k}, i\omega_m)$ as given above, which determines the anomalous pairing amplitude and is considered to be an order parameter in this system [88].

The form of the Eliashberg equations given here takes a kernel given by [81]

$$\lambda_{\mathbf{k}\mathbf{k}'}(z) \equiv \int_0^\infty \frac{2\nu\alpha^2 F(\mathbf{k}, \mathbf{k}', \nu)}{\nu^2 - z^2} d\nu, \tag{2.111}$$

where $\alpha^2 F(\mathbf{k}, \mathbf{k}', \nu)$ is defined by Eq. 2.104. This highly non-linear set of equations must then be solved self-consistently. It is standard practice to separate the self-energy $\Sigma(\mathbf{k}, i\omega_m)$ into its even and odd components, thus splitting Eq. 2.107 into two equations and defining two new functions, Z and χ,

$$i\omega_m \Big[1 - Z(\mathbf{k}, i\omega_m)\Big] \equiv \frac{1}{2}\Big[\Sigma(\mathbf{k}, i\omega_m) - \Sigma(\mathbf{k}, -i\omega_m)\Big] \tag{2.112}$$

$$\chi(\mathbf{k}, i\omega_m) \equiv \frac{1}{2}\Big[\Sigma(\mathbf{k}, i\omega_m) + \Sigma(\mathbf{k}, -i\omega_m)\Big] \tag{2.113}$$

Equations for $Z(\mathbf{k}, i\omega_m)$, $\chi(\mathbf{k}, i\omega_m)$ and $\phi(\mathbf{k}, i\omega_m)$ in terms of one another can be determined from the definition of $\Sigma(\mathbf{k}, i\omega_m)$. If we then drop the wavevector dependence of the coupling function, Z, χ and ϕ also become wavevector-independent [88]. Integration over the first Brillouin zone can then be performed, replacing the sum over wavevectors with an energy integral over the DOS. It is standard here to assume a constant DOS around the Fermi level, allowing us to take this quantity outside the integral and simplify the expressions; the validity of this assumption for high-pressure hydrides is assessed in Chapter 4. These integrals are extended and the $V_{\mathbf{k}\mathbf{k}'}$ term must be treated carefully. The inclusion of Coulomb interactions in Eliashberg theory is difficult and a renormalised electron-electron interaction parameter (termed a Coulomb pseudopotential) is introduced to deal with this - we will meet this quantity properly in Section 2.5.3. Simplified equations for Z and ϕ, which now contain T_c, emerge from the integration. A different order parameter is usually preferred at this point; it is defined as $\Delta(\omega_m) \equiv \phi(\omega_m)/Z(\omega_m)$ and is called the gap function [88]. The resulting equations, now for Z and $Z\Delta$ rather than Z and ϕ, are termed the gap equations.

So far, we have written the Eliashberg equations (and the resulting gap equations) as functions of imaginary frequency and these can be solved to give T_c. The equations can also be extended above the real axis to give access to dynamic quantities, but these are not the focus of this thesis. To compute T_c, we need to specify $\alpha^2F(\nu)$ and the Coulomb pseudopotential, obtain the gap function and Z, and linearise the gap equations [88]. In this thesis, the spectral function is calculated within the framework of DFPT using QUANTUM ESPRESSO [42, 43] and the Eliashberg system is solved using ELK [89].

2.5.3 Coulomb pseudopotential and approximate equations for T_c

Coulomb pseudopotential

As we have touched upon, including the Coulomb interaction alongside the pairing interaction in the Eliashberg equations presents some difficulties; the Coulomb interaction has a short (essentially instantaneous) interaction time and there is therefore no natural cut-off to ensure a convergent sum over Matsubara frequencies [90]. This is typically dealt with by using an energy window, ω_c, to define a renormalised electron-electron interaction

$$\mu^* = \frac{\mu_c}{1+\mu_c ln(\varepsilon_F/\omega_c)}, \tag{2.114}$$

where μ^* is a Morel-Anderson pseudopotential [91] and μ_c is the average electron-electron matrix element (or typical screened Coulomb interaction) multiplied by the DOS at the Fermi level. Eq. 2.114 often leads to estimates of $\mu^* \sim 0.1$-0.15, which is compatible with values obtained by fitting to tunnelling spectroscopy data for various conventional superconductors.

The McMillan and Allen-Dynes formulae

Solving the Eliashberg system is a substantial task and, although numerical solutions are now readily available [81], a simpler approach introduced by McMillan [84] is still commonly used. The McMillan formula was derived from the results of numerical calculations performed for several values of T_c and μ^* using a spectral function derived from the phonon density of states of Nb. It relates λ from Eq. 2.96 directly to T_c via

$$T_c = \frac{\omega_D}{1.45} exp\left(-\frac{1.04(1+\lambda)}{\lambda-\mu^*(1+0.62\lambda)}\right). \tag{2.115}$$

Due to the fixed range of numerical solutions used in its construction, the McMillan formula gives an upper limit on T_c even as $\lambda \to \infty$. Conversely, taking the limit of the

Eliashberg equations puts no upper limit on T_c. The McMillan formula is often refined by substitution of $\omega_D/1.45$ for $\omega_{log}/1.2$ [92], where

$$\omega_{log} = exp\Big(\frac{2}{\lambda}\int d\omega log(\omega)\frac{\alpha^2F(\omega)}{\omega}\Big) \tag{2.116}$$

This weighted average of the phonon frequencies is seen as more representative of the spectrum. In order to better describe strong coupling, Allen and Dynes [85] later introduced simple multiplicative factors, f_1 and f_2, to this modified expression for T_c. f_1 is termed the "strong-coupled correction" and f_2 the "shape correction", and they depend only on ω_{log}, $\bar{\omega}_2 = \langle\omega^2\rangle^{1/2}$, μ^* and λ.

The isotope effect

The discovery of an isotope effect on T_c historically played a large role in the development of theories for conventional superconductivity [81] and observation of this effect remains an important tool in confirming the superconducting mechanism in new materials. In the BCS equation, Eq. 2.90, the isotope effect is clear from the prefactor; in the harmonic approximation phonon frequencies are inversely proportional to the square root of the atomic mass. The isotope coefficient for an elemental superconductor is therefore

$$\beta = -\frac{d\ln T_c}{d\ln M} = \frac{1}{2} \tag{2.117}$$

since the interaction itself is mass-independent. In Eliashberg theory, λ remains independent of M and with $\mu^* = 0$ we also obtain $\beta = 1/2$ [81]. Potential sources of deviation [75] from this value are then:

- non-elemental superconductors (an isotopic substitution will result in varying changes in T_c, depending on how the species being substituted contributes to the important phonon modes),
- non-zero μ^*,
- anharmonicity,
- contribution from a non-conventional mechanism of superconductivity.

2.6 Gaspari-Gyorffy electron-phonon coupling estimates

We have seen how conventional superconductivity can be treated within the framework of DFT. However, full electron-phonon calculations are expensive and other methods for estimating the strength of the electron-phonon coupling have been developed. Some of the main ideas developed in this thesis rely on the repurposing of estimates derived from a scattering-based theory; this theory is introduced here for later use in Chapters 5 and 6.

McMillan [84] showed that for strong-coupled superconductors the electron-phonon coupling constant, λ, can be expressed as

$$\lambda = 2\int \frac{\alpha^2 F(\omega)}{\omega} d\omega = \frac{N(E_F)\langle I^2\rangle}{M\langle\omega^2\rangle} \tag{2.118}$$

where E_F is now used to represent the Fermi energy, $\langle I^2\rangle$ is the Fermi-surface-averaged interaction matrix element and the average squared phonon frequency is given by

$$\langle\omega^2\rangle = \frac{\int \omega\alpha^2 F(\omega) d\omega}{\int \frac{\alpha^2 F(\omega)}{\omega} d\omega}.$$

λ can also be rewritten as

$$\lambda = \frac{\eta}{M\langle\omega^2\rangle}, \tag{2.119}$$

where η is the so-called Hopfield parameter. Hopfield was one of the first to highlight the importance of the local environment in determining the degree of electron-phonon coupling [93], showing that electron-phonon interactions mainly consist of scatterings which change the angular momentum of the electron.

In situations where mass, and hence frequency, differences allow vibrational modes to be separated into groups with different atomic character (such as we may see in binary hydrides) we can define element-specific coupling constants and Hopfield parameters:

$$\lambda = \sum_j \lambda_j = \sum_j \frac{\eta_j}{M_j\langle\omega_j^2\rangle}, \tag{2.120}$$

where j is the atom type.

The quantity $\langle I^2\rangle$ appearing in Eq. 2.118 is expressed in a real-space representation as

$$\langle I^2\rangle = \frac{V^2}{(2\pi)^6 N^2(E_F)} \int d^3k \int d^3k' \int d^3r \int d^3r' \nabla V(\mathbf{r})\cdot\nabla V(\mathbf{r}')\psi_{\mathbf{k}}^*(\mathbf{r})\psi_{\mathbf{k}'}(\mathbf{r})$$
$$\psi_{\mathbf{k}'}^*(\mathbf{r}')\psi_{\mathbf{k}}(\mathbf{r}')\delta(E-E_k)\delta(E-E_{k'}), \tag{2.121}$$

where $V(\mathbf{r})$ is the potential due to a single ion, $\psi_{\mathbf{k}}(\mathbf{r})$ is a one-electron Bloch wavefunction, and E_k is the corresponding eigenvalue. Gaspari-Gyorffy (GG) theory [94] builds on Hopfield's observations and allows us to reduce the expression for $\langle I^2 \rangle$, and therefore also the Hopfield parameter, to a combination of single-site characteristics - namely electronic scattering phase shifts and partial densities of state (PDOS) [95]. Although GG theory was originally derived for elemental transition metals, recent work has emerged using this theory for alkali metals [96] and metal hydrides under high pressure [95, 97]. Development of such a simple expression is possible because GG theory is based in the rigid muffin-tin approximation (RMTA)[3] framework, meaning the $V(\mathbf{r})$ in $\langle I^2 \rangle$ is taken to be a muffin-tin potential and three main approximations can be applied [95]:

- the potential is spherical and negligible beyond the species-dependent atomic sphere, defined by R_{MT},
- the change in potential due to a displaced atom can be approximated by a rigid shift of the atomic potential,
- the direction-dependence of the wavefunction coefficients is averaged out.

To start using these approximations, for a spherically symmetric potential, we have

$$\psi_{\mathbf{k}}(\mathbf{r}) = \sum_{l} \sum_{m=-l}^{l} a_{lm}(\mathbf{k}) R_l(r, E_k) Y_l^m(\hat{r}), \tag{2.122}$$

where l is the angular momentum, $Y_l^m(\hat{r})$ are spherical harmonics, and $R_l(r, E_k)$ is the scattering solution of the Schrödinger equation such that, for $r > R_{MT}$,

$$R_l(r, E_k) = cos(\delta_l(E_k)) j_l(kr) - sin(\delta_l(E_k)) n_l(kr). \tag{2.123}$$

Here δ_l are the scattering phase shifts, j_l are spherical Bessel functions, n_l are Neumann functions (Bessel functions of the second kind) and $k = \sqrt{E_k}$. $\psi_{\mathbf{k}}(\mathbf{r})$ reduces to a plane wave

[3]The muffin-tin approximation involves spherically averaging the potential inside spheres surrounding each nucleus (defined by a separate muffin-tin radius R_{MT} for each species) and volume-averaging the potential in the rest of the crystal, leaving behind a constant interstitial potential. When calculating electron-phonon interactions in this picture, it is usual to assume that the muffin-tin potential moves "rigidly" when an atom is displaced. Essentially this assumption means that when one atomic nucleus is displaced while the others are held fixed, the total potential change seen by an electron is proportional to the gradient of the muffin-tin potential [98]. The augmented plane wave method, which we use here, relies on the muffin-tin approximation. Within this method, wavefunctions are constructed by matching solutions of the Schrödinger equation within each sphere with plane wave solutions in the interstitial region. Within the muffin tins, wavefunctions can be expanded in terms of spherical harmonics and the eigenfunctions of the radial wave equation.

in the limit of small phase shifts [99]. We make the assumption of spherical bands, which amounts to

$$a_{lm}(\mathbf{k}) = a_l(E_k)Y_l^m(\hat{k}). \tag{2.124}$$

Inserting Eqs. 2.122 and 2.124 into Eq. 2.121 and performing all the angular integrations, we have [94]

$$\langle I^2 \rangle = \Big(\frac{E_F}{\pi^2}\Big)\frac{1}{N^2(E_F)}\sum_l 2(l+1)\left|\int_0^{R_{MT}} drr^2 R_l \frac{dV}{dr} R_{l+1}\right|^2 \frac{N_l(E_F)N_{l+1}(E_F)}{N_l^{(1)}N_{l+1}^{(1)}} \tag{2.125}$$

in atomic units. The PDOS $N_l(E_F)$ is defined via

$$N(E_F) = \sum_l N_l(E_F) = \frac{V}{(2\pi)^3}\sum_l \sum_{m=-l}^{l} \int_0^{R_{MT}} drr^2 R_l^2 \int d^3k \delta(E_F - E_k) a_{lm}^*(\mathbf{k}) a_{lm}(\mathbf{k}),$$

where the radial function is again identical to the expression for a single scatterer. As shown in Appendix B.1, the integral appearing in Eq. 2.125 can in fact be evaluated directly as

$$\int_0^{R_{MT}} drr^2 R_l \frac{dV}{dr} R_{l+1} = sin(\delta_{l+1} - \delta_l).$$

This leads to the final form of the rigid-ion GG formula

$$\langle I^2 \rangle = \frac{E_F}{\pi^2 N^2(E_F)} \sum_l \frac{2(l+1)sin^2(\delta_{l+1} - \delta_l)N_l(E_F)N_{l+1}(E_F)}{N_l^{(1)}N_{l+1}^{(1)}},$$

where $N_l^{(1)}$ is called the free-scatterer DOS, which is the DOS at the Fermi level of a single muffin-tin potential in a zero-potential background.

E_F, $N(E_F)$ and $N_l(E_F)$ are all easily accessible from a standard PDOS calculation, but we need to calculate the scattering phases shifts and the free-scatterer DOS. Focusing on the former first, the radial wave equation is

$$\frac{d^2(rR_l)}{dr^2} = \Big[V(r) + \frac{l(l+1)}{r^2} - E\Big](rR_l). \tag{2.126}$$

By continuity, we must be able to match the radial wavefunction's logarithmic derivative, $L_l = R_l'/R_l$, inside and outside the muffin-tin at $r = R_{MT}$. Inside the muffin-tin, we can obtain the logarithmic derivative by integrating Eq. 2.126. Outside the muffin-tin, the logarithmic derivative is expressible in terms of phase shifts which characterise the long-

distance behaviour of the wavefunction via

$$tan\Big(\delta_l(R_{MT},E_F)\Big) = \frac{j_l'(kR_{MT}) - j_l(kR_{MT})L_l(R_{MT},E_F)}{n_l'(kR_{MT}) - n_l(kR_{MT})L_l(R_{MT},E_F)}, \tag{2.127}$$

where $k = \sqrt{E_F}$. We can therefore calculate the logarithmic derivative inside, match this to the logarithmic derivative outside at $r = R_{MT}$ and then use this to calculate δ_l from Eq. 2.127 [100].

Turning to the free-scatterer DOS, this quantity can be expressed as

$$N_l^{(1)} = \frac{\sqrt{E_F}}{\pi}(2l+1)\int_0^{R_{MT}} R_l^2(r,E_F)r^2 dr. \tag{2.128}$$

As shown in Appendix B.2, the integral appearing here can be written as

$$\int_0^{R_{MT}} R_l^2(r,E)r^2 dr = -R_l^2(R_{MT},E)R_{MT}^2 \frac{\partial}{\partial E}\left(\frac{R_l'(R_{MT},E)}{R_l(R_{MT},E)}\right),$$

where the energy derivative of the logarithmic derivative appearing on the right-hand side can be calculated by evaluating the logarithmic derivative at slightly different energies close to E_F. Since we need to match the radial wavefunction at the muffin-tin radius, we can simply use Eq. 2.123 to calculate the $R_l^2(R_{MT},E)$ factor. We now have all the components needed to calculate $\langle I^2 \rangle$ for each atom type, which can be multiplied by $N(E_F)$ to give η_j. All that is required to obtain these η_j estimates is therefore a self-consistent DOS calculation, partitioned by both atom and l.

I implemented GG theory in the ELK (L)APW code [89] (originally as part of the work presented in Chapter 5 and Ref. [101]) for use in this thesis. Although η was introduced in the context of atom types, j, we actually calculate this quantity individually for each atom in the unit cell and then add these together to give total species-specific values. This is because the calculated value is not identical for atoms of the same type unless they sit on equivalent positions in the crystal. In contrast to previous work in the literature, this thesis does not attempt to obtain quantitative estimates of T_c from the $\{\eta_j\}$, but instead repurposes them for screening and modelling applications (see Chapter 5 and 6).

Chapter 3

The phase diagram of solid hydrogen

3.1 Motivation

Hydrogen is the simplest of all atoms and the most abundant element in the universe. Despite this, the behaviour of hydrogen under high pressure is far from simple. Solid hydrogen possesses a rich phase diagram [102] and has been a substance of theoretical and experimental interest for decades. The centres of large planets contain hydrogen under very high pressure, meaning that the state of dense hydrogen has important astrophysical consequences. Additionally, in 1968 Ashcroft predicted that at high enough pressures solid hydrogen should become a room-temperature superconductor [103], with the light mass of the hydrogen atom allowing high critical temperatures to be reached via a phonon-mediated mechanism.

High-pressure hydrogen can be studied in DAC experiments (see Fig. 1.1), but there are various technical difficulties associated with reaching a highly compressed state and making measurements on the resulting samples. Experimental data, while useful for locating phase transitions [104], is usually not sufficient to fully characterise the structural properties of the various phases. Information obtained from x-ray diffraction is limited because x-rays are almost insensitive to the positions of individual hydrogen atoms in molecular phases [105, 106]. Raman and infrared spectra measured at high pressures can be hard to interpret and neutron scattering signals are weak because DAC experiments are limited to small sample sizes. These effects only become more pronounced at higher pressures as samples become more compressed and we approach the regime where hydrogen is expected to become metallic [107]. Deuterium systems, as well as more complicated mixed-isotope combinations [108], are studied in an effort to obtain information about quantum and thermal nuclear motion. Research in this area is ongoing, with nuclear magnetic resonance spectroscopy

recently highlighted as a potentially promising structural probe in high-pressure systems, including solid hydrogen [109].

In Chapter 2, we covered the principles of DFT, crystal structure prediction using AIRSS, vibrational calculations (at both the harmonic and anharmonic levels) and their implementation in CAESAR, and how the resulting information can be used to construct pressure-temperature phase diagrams. We can now put these techniques to use in studying pure hydrogen under extreme pressure; a substance that we have seen is of fundamental interest to many in the high-pressure physics community and beyond. We produce pressure-temperature phase diagrams from first principles by employing two purpose-built exchange-correlation functionals. Comparing these phase diagrams to the available experimental data and results from previous Monte Carlo calculations, we can make some comments about the suitability of semi-local DFT for this system. Solid hydrogen, with its predicted exotic properties, also serves as a stepping stone to the metal hydrides which are the focus of the latter parts of this thesis.

The work presented in this Chapter is unpublished. As detailed in the Preface, the *Cc*-32 structure studied here was found by C. J. Pickard. The exchange-correlation functionals tested were constructed by J. R. Trail in Ref. [110] and he provided helpful advice on the work presented in this Chapter.

3.2 Phases of solid hydrogen

The low-pressure phase I of solid hydrogen, identified in experiment, consists of freely rotating molecules on a hexagonal close-packed (hcp) lattice [111]. Phase I is not usually included in theoretical studies because its description requires full quantum mechanical treatment of the protons. A transition to phase II occurs at about 110 GPa, where changes in the low-frequency regions of the Raman and infrared spectra are consistent with a pressure-induced orientational ordering [112]. Within phase II, this orientational ordering means the molecules are no longer freely rotating [105]; it is therefore often referred to as a "broken-symmetry" phase.

At higher pressures, a transition to phase III is observed, accompanied by a large discontinuity in the Raman spectrum and an increase in infrared activity. X-ray diffraction data indicates that hydrogen molecules in phases II and III are still in the vicinity of the sites of an hcp lattice up to 183 GPa [113]. This observation was recently confirmed for phase III with measurements extending up to 212 GPa at room temperature [106]. The phase II-III transition is located roughly at 160 GPa at 100 K, with the small regions of phase-coexistence observed in experiment attributed to pressure gradients in the samples [113].

Phase IV, characterised by two vibrons in its Raman spectrum, was discovered at 300 K and pressures above 220-230 GPa [114, 115, 116]. Phase V was later reported at higher pressures (above 325 GPa at 300 K) by experimentalists [117]. Based on optical observations, the authors speculated that this phase might be a precursor to a metallic state. In another recent study, experimentalists reported identifying phase VI at 360 GPa and temperatures less than 200 K [118] and claimed that the phase was likely to be metallic. An experimental phase diagram of high-pressure hydrogen, constructed from data collected by a number of different research groups, is shown in Fig. 1 of Ref. [119].

Although some uncertainty remains, candidate structures have been identified for most observed phases of solid hydrogen. These structures have largely been found using AIRSS [50]. Several candidate molecular structures for phase II, all very close in energy, have been noted - a structure of $P2_1/c$ symmetry with 24 atoms in its unit cell [111] (Fig. 3.1) is usually considered in theoretical studies. It consists of molecules arranged on a distorted hcp lattice.

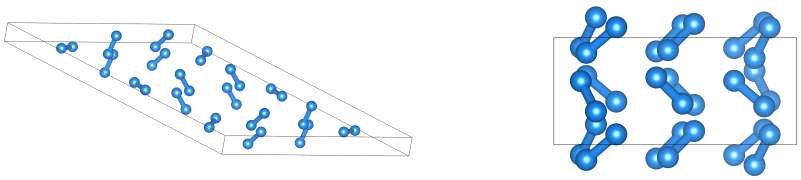

Fig. 3.1 The primitive cell of $P2_1/c$-24 at 175 GPa.

Pickard and Needs [111] reported finding a molecular, monoclinic structure of $C2/c$ symmetry, with 24 atoms in its unit cell (Fig. 3.2), which was a good candidate for phase III. Later, an additional candidate for this phase was identified [120]. The hexagonal $P6_122$ structure, with 36 atoms in its unit cell (Fig. 3.3), provides better agreement with the available x-ray diffraction data [113, 121]. Theorists suggested that phase III may be polymorphic, with $P6_122$-36 being stable below 200-210 GPa and $C2/c$-24 above [120, 122]. Vibrational effects were found to play a central role in the stabilisation of the new structure [120].

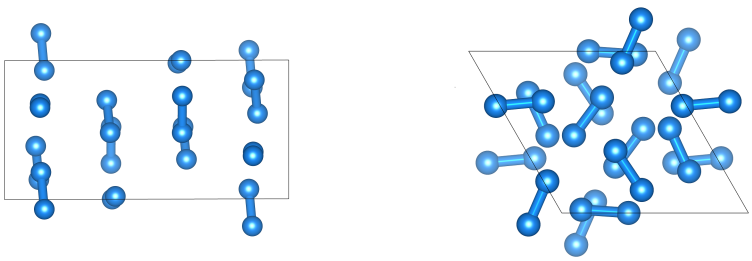

Fig. 3.2 The primitive cell of $C2/c$-24 at 300 GPa.

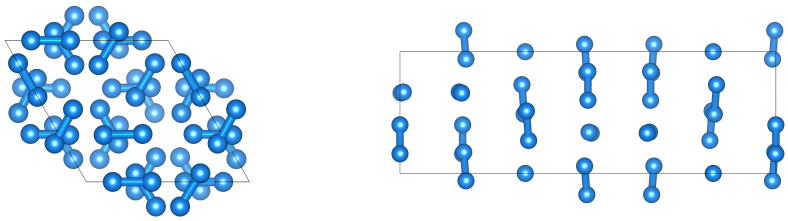

Fig. 3.3 The primitive cell of $P6_122$-36 at 200 GPa.

Cmca-4 and *Cmca*-12, shown in Figs. 3.4 and 3.5 respectively, are other low energy structures which are frequently identified in searches. $C2/c$-24, *Cmca*-4 and *Cmca*-12 consist of layers of molecules whose bonds lie in the same plane, forming distorted hexagonal patterns. *Cmca*-4 is a metallic molecular structure and has weaker molecular bonds than $C2/c$-24 and *Cmca*-12 [123].

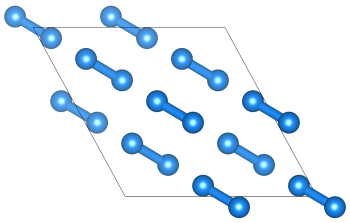

Fig. 3.4 A 2x2x1 supercell of *Cmca*-4 at 300 GPa.

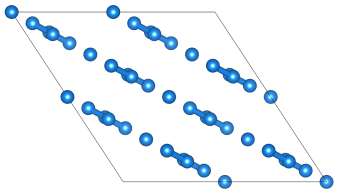

Fig. 3.5 A 2x2x2 supercell of *Cmca*-12 at 300 GPa.

Mixed structures, consisting of alternating layers of strongly bonded molecules and weakly bonded graphene-like sheets were originally found to be compatible with phase IV [115, 124]. The lower-frequency vibrational modes originating from the weaker bonds were predicted to stabilise these structures near room-temperature. The best candidate for phase IV from AIRSS is a structure of *Pc* symmetry with 48 atoms in its unit cell [124] (Fig. 3.6). Molecular dynamics simulations, however, suggest instead that a hexagonal structure of rotating molecules and trimer motifs, exhibiting three distinct layer types, is stable at high temperatures [125, 126]. The modelled finite temperature Raman spectrum associated with this structure agrees with experimental data, whereas that of the *Pc* structure does not

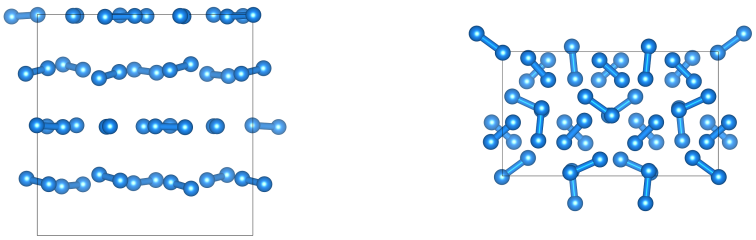

Fig. 3.6 The primitive cell of *Pc*-48 at 275 GPa.

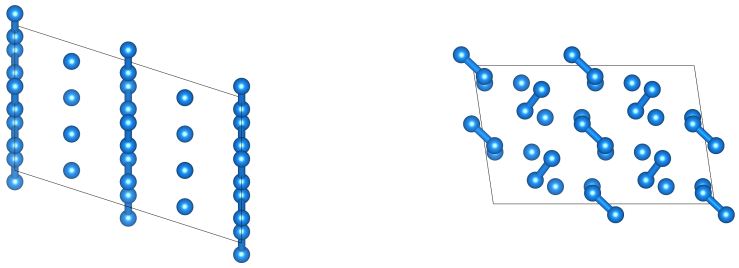

Fig. 3.7 A 2x2x2 supercell of *Ibam*-8 at 400 GPa.

[125, 127]. The idea that the *Pc* structure is not necessarily a good match to the phase IV experimental data has since been reiterated [128].

Several candidate structures for phase V have recently been found using sp-AIRSS, including *Ibam*-8 (Fig. 3.7), $Pca2_1$-48 (Fig. 3.8) and $Pna2_1$-48 (Fig. 3.9) [54]. *Pc*-48, $Pca2_1$-48 and $Pna2_1$-48 consist of two distinct types of layers, as does *Ibam*-8 which is an extreme member of the family of mixed structures [54]. $I4_1/amd$-2 is a model for solid hydrogen's first atomic phase [129].

3.3 Previous theoretical studies

While high-pressure experiments are difficult, computational studies of solid hydrogen are also not straightforward. Some properties of the phase diagram, for example the melt line, can be well-modelled by molecular dynamics simulations neglecting quantum nuclear

Fig. 3.8 The primitive cell of $Pca2_1$-48 at 350 GPa.

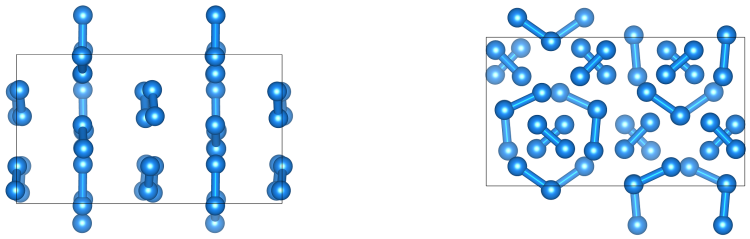

Fig. 3.9 The primitive cell of $Pna2_1$-48 at 350 GPa.

effects [130]. However, due to the light mass of the proton, there are typically large zero-point vibrational energies to consider, meaning static-lattice descriptions are not necessarily indicative of phase stability. Additionally, enthalpy differences between competing structures tend to be on the order of meV/atom, meaning that accurate calculation of the relative energies is required [111].

Although DFT is the method of choice for many other systems, solid hydrogen phase diagrams predicted using different standard exchange-correlation functionals do not qualitatively agree with one another [131]. The difference in energies obtained using different functionals is considerably larger than the energy differences between structures for any fixed functional [132]. Comparison against diffusion Monte Carlo (DMC) results has highlighted these issues [131]. A study comparing the use of LDA [32], PBE [35] and BLYP [37, 38] for solid hydrogen found that at the static-lattice level, the three functionals gave very different transition pressures, with BLYP being in slightly better agreement with experiment [133]. It was also found that the range in zero-point energies calculated with different functionals was greater than 10 meV/atom [133]. Other studies have considered the performance of vdW functionals [123] and meta-GGAs [122]. As a specific illustration, *Pc*-48 is energetically competitive within DMC and is stabilised further by the inclusion of vibrations [74]. Within DFT-PBE, however, the metallic *Cmca*-4 dominates at mid-to-high pressures over a large temperature range instead [74, 134].

3.4 Methodology and computational details

3.4.1 Purpose-built exchange-correlation functionals

There is a large amount of evidence to suggest that DFT (with standard exchange-correlation functionals) is not entirely appropriate for the description of solid hydrogen. However, due to the high cost of DMC, DFT is arguably still the best method for investigating the behaviour of this system. It is therefore crucial to consider robust improvements that can be made. Trail *et al.* [110] constructed exchange-correlation functionals specifically designed to provide

an accurate description of hydrogen at high pressures. Our aim is now to establish the performance of these functionals and determine whether a reasonable phase diagram of solid hydrogen can, in fact, be calculated within semi-local DFT.

In order to generate the purpose-built functionals, clusters containing 1-12 pairs of hydrogen atoms were cut directly from the bulk structures of $P2_1/c$-24, $C2/c$-24, Pc-48, $Cmca$-12, and $Cmca$-4 at a range of pressures [110]. Highly accurate CCSD(T) calculations were then performed to obtain a reference energy for each cluster. The optimised functionals were constructed by taking the individual components of the well-known B3LYP functional, and determining their coefficients by minimising the difference between the CCSD(T) and DFT energies of the clusters using an iterative approach [110]. This amounts to writing

$$\begin{aligned} E_{KS}[\rho_i] = T[\rho_i] + V[\rho_i] + \alpha_0^{(i)} E_X^{HF}[\rho_i] \\ + \alpha_1^{(i)} E_X^{B88}[\rho_i] + \alpha_2^{(i)} E_X^{LDA}[\rho_i] \\ + \alpha_3^{(i)} E_C^{LYP}[\rho_i] + \alpha_4^{(i)} E_C^{LDA}[\rho_i] + E_{D3} \end{aligned} \quad (3.1)$$

where ρ_i is the electron density, $\{\alpha_j^{(i)}\}$ are linear parameters, E_X^{HF} is the exact HF exchange energy [13], E_X^{B88} and E_C^{LYP} are the BLYP-parameterised exchange and correlation functionals [37, 38], E_X^{LDA} and E_C^{LDA} are the exchange and correlation components of the LDA functional, and E_{D3} is an optional dispersion correction. A penalty function was minimised with respect to $\{\alpha_j\}$ at fixed electron density, providing a new set of coefficients with which the process was repeated until convergence was reached.

Several different functionals were produced in Ref. [110]. Hybrid functionals ($\alpha_0 \neq 0$) were not included in our study as the cost would become prohibitive even when considering only a small number of structures. We study the performance of a GGA that obeys the homogeneous electron gas limit ($\alpha_0 + \alpha_1 + \alpha_2 = 1$ and $\alpha_3 + \alpha_4 = 1$) and a GGA that does not; these are referred to as O_3 and O_4, respectively, in line with Ref. [110].

3.4.2 Crystal structure prediction

A large number of the structures considered in this Chapter come from previous AIRSS studies, as detailed above. Historically, most of these searches were carried out using PBE. Therefore, in order to confirm that we were still considering the relevant structures, we performed our own AIRSS searches using O_3 and O_4 at 100, 200, 300 and 400 GPa. The plane-wave DFT code CASTEP [41], a **k**-point spacing of $2\pi \times 0.05$ Å^{-1}, a cut-off energy of 500 eV and the H_00.recpot pseudopotential included with CASTEP were used. Initial structures were generated containing 8, 10, 12, 14, 16, 18, 20, 24 or 48 atoms, a minimum

hydrogen-hydrogen separation of 0.6Å was imposed, and around 20,000 structures were generated using each functional. The *Cmca*-4, *Cmca*-12, $P2_1/c$-24, $C2/c$-24 and *Pc*-48 structures were all recovered using both O_3 and O_4. It should be noted that any structures that are dynamically unstable at the searching pressure will not be located using AIRSS (unless a modification such as sp-AIRSS is used) as they do not reside in local minima of the PES.

We found that the energy landscape at 100 GPa was complicated, with a large number of structures found to be close in energy to one another. A structure of *Cc* symmetry with 32 atoms in its unit cell, actually found during PBE searches performed in tandem with this work, was particularly interesting to us as it appeared to be marginally more stable than $P2_1/c$-24 at the static-lattice level. A $Pca2_1$-8 structure was also identified a large number of times using O_3. In this Chapter, as well as these two structures, we consider all the existing AIRSS candidates introduced in Section 3.2

3.4.3 Static-lattice calculations

Geometry optimisations using O_3 and O_4 were performed with CASTEP at pressures ranging from 50 to 550 GPa. Since we are using custom exchange-correlation functionals, the pseudopotential H_00.recpot, included in the CASTEP package, was used after careful testing. Final enthalpies were converged to within 0.01 meV/atom with respect to **k**-point sampling and cut-off energy, and forces were converged to within less than 0.01 eV/Å for all structures.

To validate our pseudopotential choice, we compared the structural and vibrational properties predicted using it to results obtained using the bare Coulomb potential. After separate convergence testing, we performed geometry optimisations using both pseudopotentials for *Cmca*-4, *Cmca*-12 and $C2/c$-24 at 250 GPa and for *Ibam*-8 and $I4_1/amd$-2 at 400 GPa. The O_3 functional was used for these tests. The relative energies matched to within <0.9 meV/atom. On moving from the bare Coulomb potential to H_00.recpot, we observed a small ($<0.2\%$) increase in lattice parameters for each structure and a $\sim 0.2\%$ decrease in strong molecular bond lengths. For *Cmca*-4, *Cmca*-12 and $C2/c$-24 at 250 GPa, we then performed well-converged harmonic phonon calculations using the two different pseudopotentials. The final results showed a maximum difference of 0.35 meV/atom for harmonic vibrational energies between the two pseudopotentials. This maximum difference is observed for the largest temperature value under consideration (600 K), so the actual effect on our results (which are valid up to a slightly lower maximum temperature due to an inability to describe melting) is less than this. In all cases, the phonon dispersion and density of states were not qualitatively changed by the choice of pseudopotential. Separate convergence tests were also performed in order to determine an appropriate value of electronic smearing (used to accelerate convergence with **k**-point sampling for metals).

3.4.4 Harmonic phonon calculations

All vibrational calculations in this Chapter were performed using CAESAR [61]. In order to obtain harmonic phonon frequencies (and the modes along which to map the BO energy surface in VSCF), it is necessary to compute the matrix of force constants. CAESAR uses non-diagonal supercells [62], which makes the use of a finite differences approach computationally feasible here. Atomic displacements with a magnitude of 0.02 Bohr were used to perform the harmonic calculations.

It is essential to investigate the convergence of the harmonic phonon frequencies and free energy contributions with respect to the vibrational grid size. Here, all absolute harmonic vibrational free energies were converged with respect to **q**-point sampling to within less than 0.2 meV/atom. The harmonic free energies were also converged to within less than 0.1 meV/atom with respect to the **k**-point spacing and cut-off energy used in the underlying CASTEP single-point energy calculations. Harmonic calculations were performed at a minimum of 5 pressure points for each structure, with the pressure ranges chosen based on a combination of findings from previous studies and our static-lattice results.

3.4.5 Accounting for anharmonicity

Previous studies have found that while the QHA is capable of producing free energies with an accuracy of about 10 meV/atom, this is not enough to reliably predict the hydrogen phase diagram [132]. We therefore also calculated anharmonic corrections to the vibrational energies using VSCF; this theory and its implementation in CAESAR is described in Chapter 2. Anharmonic corrections were calculated at 3 pressure points for each structure (spread out over the same structure-specific pressure ranges used at the harmonic level). 5 pressure points were considered for the $C2/c$-24 structure as it is competitive over a large pressure range.

Current limitations of the code (which is still being actively developed) mean that full convergence tests for anharmonic vibrational grid size were not possible for all structures. However, the tests that could be completed suggested that total anharmonic vibrational free energies were converged to within 1 meV/atom. The grids used for structures for which direct convergence tests could not be performed were then chosen to be roughly in agreement with converged grid sizes for structures with the same number of atoms or similar unit cell size. With the code in its current form, anharmonic calculations could not be performed at a reasonable cost for the $I4_1/amd$-2 structure, so it is not considered at the anharmonic level.

When performing anharmonic calculations, atomic displacements are controlled by a maximum displacement parameter - the largest distance of any sampling point from the

equilibrium position. This was typically set to 0.6-0.7 Bohr in the lower pressure regions (a much larger amplitude than was used in the harmonic calculations), but was decreased with pressure (and if any atoms approached each other too closely). Since mass-reduced coordinates are used in CAESAR, if we were considering a system with more than one atom type, modes with higher contributions from heavier atoms would have their maximum displacement scaled downwards.

There are several convergence parameters to consider in CAESAR. A polynomial representation of the potential is used. User inputs then decide the order up to which the potential is expanded and the maximum number of degenerate subspaces which may be coupled together. With the current version of the code, only one direct test of the former was possible - it was found for $P2_1/c$-24 at 160 GPa that expanding the potential up to order 4 converged the anharmonic free energy to within $<$1 meV/atom. For other structures, although direct convergence tests were not possible, we were able to assess the appropriateness of this parameter through mode mapping. First, by mapping out all modes and examining both the harmonic and anharmonic potentials associated with them, we were able to identify those with the most anharmonic character. Then, for these specific modes, we were able to perform fresh electronic structure calculations at various points along the mode to calculate the true potential for comparison to our harmonic results and the anharmonic approximation calculated using VSCF. An example of these tests for *Cmca*-12 at 350 GPa (using O_3) is illustrated in Fig. 3.10. For all structures tested in this way, it appeared that a potential expansion of up to order 4 was able to well represent the true PES up to reasonable displacements. This value was therefore used for all calculations.

Within the bounds of the code, using a coupling order greater than 1 is currently not feasible for this system - it is thought that this will only have a significant impact in extreme cases [135], but it is something that would be important to check in future work. Another parameter controls the number of states along each mode in the basis used for the VSCF calculation; this could be tested extensively and it was found that 10 states was more than sufficient (with anharmonic free energies converged to within 0.01 meV/atom) for all structures. This is unsurprising as it has been found that only around 30 states are required for structures which are maximally anharmonic and totally unstable at the harmonic level [135].

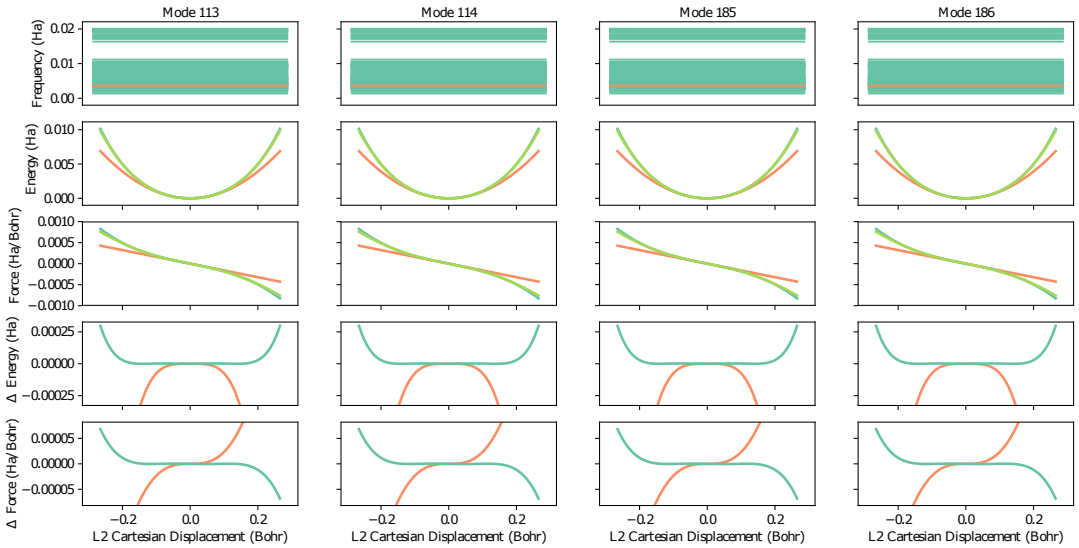

Fig. 3.10 A study of the most anharmonic modes in *Cmca*-12 at 350 GPa. The top panels show the harmonic phonon spectrum with the frequency of the specific subspace highlighted in orange. The next two sets of panels show the energy and force along the mode, respectively. Values from the harmonic PES are shown in orange, values from the anharmonic PES (with the potential expanded up to order 4) are shown in blue-green, and values from the true PES are shown in light green. The final two sets of panels show the harmonic and anharmonic energies and forces, respectively, relative to those obtained from the true PES. It is clear that the anharmonic PES provides a much better fit to the true potential than its harmonic counterpart, and that the anharmonic PES provides a good representation out to amplitudes that would be explored in a typical crystal.

3.5 Predicted phase behaviour

Figs. 3.11a and 3.11b show the static-lattice enthalpies calculated using O_3 and O_4, respectively, plotted relative to the enthalpy of $C2/c$-24. The reader is directed to Fig. 2 of Ref. [74] for PBE and BLYP static-lattice enthalpy plots, as well as one calculated using DMC. Ref. [74] studies a subset of the structures considered here.

At the static-lattice level, improvement over PBE is evident for both O_3 and O_4 (in that the new functionals produce results closer to the DMC results), most notably in terms of destabilising *Cmca*-4. O_3 performs very similarly to BLYP for the structures considered in Ref. [74]. O_4 performs somewhat better than BLYP, bringing the results closer to those calculated using DMC; it increases the static-lattice $P2_1/c$-24 to $C2/c$-24 transition pressure and significantly destabilises *Cmca*-4. For both new functionals, very small energy differences

are observed between the phase II candidates, between $C2/c$-24 and $P6_122$-36, and between the various phase V candidates, hinting at the important role vibrational effects will play in determining predicted phase stability.

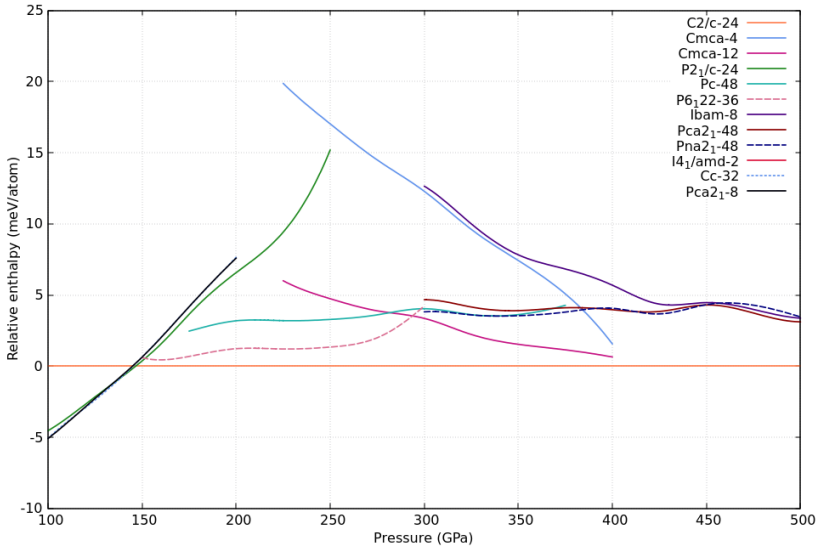

(a) Static-lattice enthalpies for O_3.

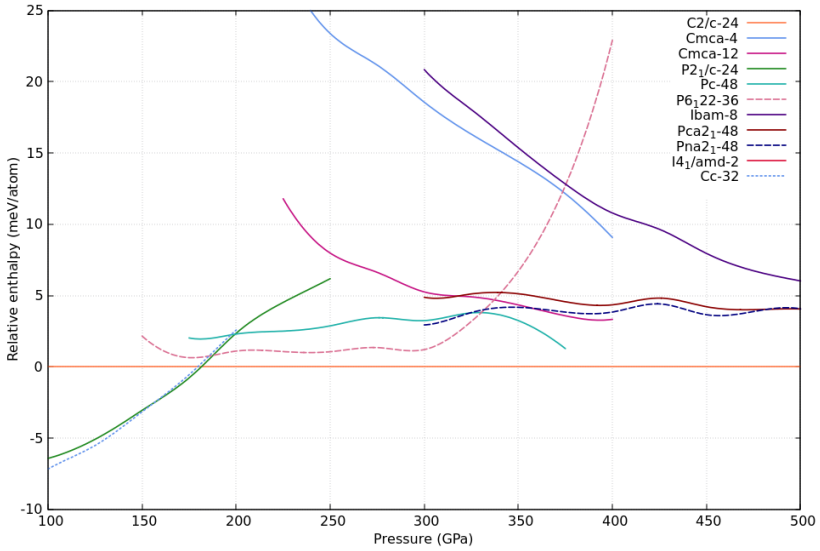

(b) Static-lattice enthalpies for O_4.

Fig. 3.11 Static-lattice enthalpies as a function of pressure, relative to $C2/c$-24.

It is important to also pay some attention to the geometries predicted by these new functionals. Benchmarking against DMC results has established that PBE considerably overestimates bond lengths over the 100-300 GPa range [131], while others have found that PBE produces bond lengths which agree well with experiment in the higher pressure

region [54]. Studying the bond lengths predicted by O_3 and O_4, we find that the strong molecular bonds predicted by O_3 are typically 2-5% shorter than those given by PBE and 0.5-1% longer than those given by BLYP. O_4 predicts the shortest bonds of all, with the strong molecular bonds typically being 1.5-3.5% shorter than the bond lengths predicted by BLYP. The pressure-dependence of the bond lengths predicted using both O_3 and O_4 is, on average, more BLYP-like than PBE-like. Producing static-lattice enthalpy plots for fixed O_3-predicted geometries but with O_4 used to calculate the enthalpies and vice versa, we also found that the energetics have a much larger impact than the underlying geometry on the final relative enthalpies.

The zero-point energy contributions calculated within the harmonic approximation using O_3 and O_4 are shown in Figs. 3.12a and 3.12b, respectively. We note that, for the relevant subset of structures, the *relative* harmonic zero-point energies for both O_3 and O_4 agree qualitatively with those calculated using PBE (see Fig. 3(a) of Ref. [74]). Previous investigations found little difference between the relative harmonic vibrational energies calculated using PBE and BLYP [74], so this observation is perhaps of little surprise. The absolute O_3 vibrational energies, however, are $\sim$5 meV/atom larger than those calculated using PBE for all structures at a given pressure. The absolute vibrational energies obtained for molecular and mixed-character structures using O_4 are then another 5-9 meV/atom greater than the corresponding values for O_3. This behaviour can be attributed to the shorter molecular bonds predicted by O_4. It is important to note that the harmonic results presented here should be taken with caution - many of these structures are dynamically unstable, meaning they have imaginary phonon frequencies and the vibrational energies therefore appear reduced. These structures include *Ibam*-8, *Pca*2_1-48, *Pna*2_1-48, and *Pc*-48. Dynamic instability of these structures at the harmonic level has been noted in previous studies [54, 124, 129]. Anharmonic calculations are needed in these cases in order to meaningfully interpret the results. As well as these zero-point energy contributions, harmonic vibrational free energies up to temperatures of 550 K were obtained in the same calculation.

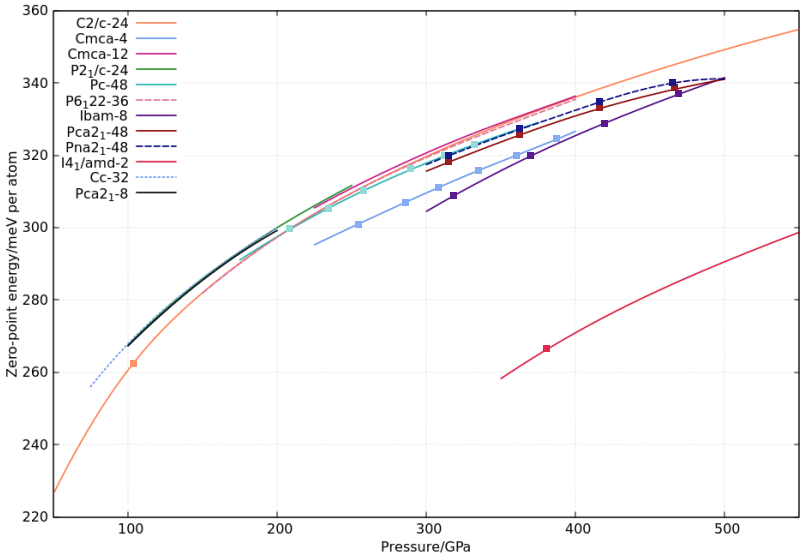

(a) Calculated using O_3 within the harmonic approximation.

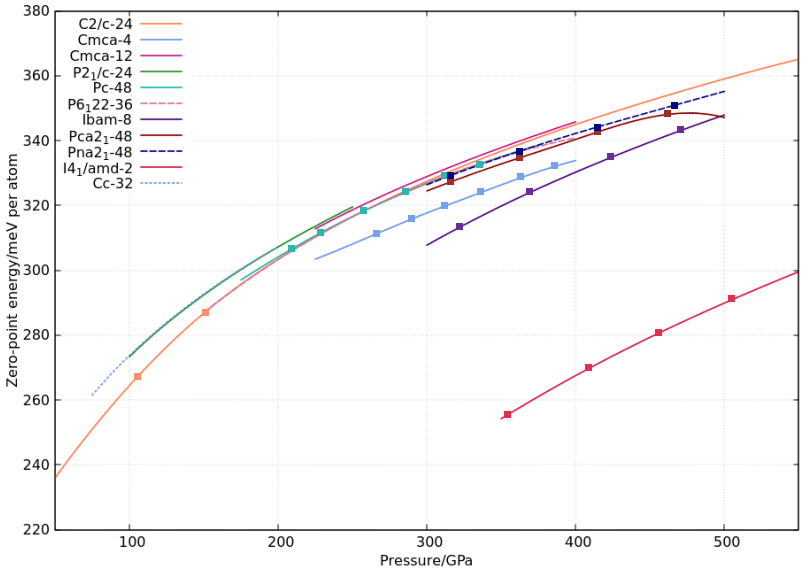

(b) Calculated using O_4 within the harmonic approximation.

Fig. 3.12 Harmonic zero-point energy contribution per atom. Points marked with squares indicate that the structure was found to be dynamically unstable at that pressure.

We now turn to calculating harmonic Gibbs free energies. As addressed in Chapter 2, in order to obtain phonon-corrected pressures, we need points dense enough in the pressure direction for fitting to a known equation of state to be possible. We therefore interpolate the harmonic vibrational energies (at each temperature) onto the dense set of pressure values used in the initial geometry optimisation and static-lattice calculations. A minimum curvature

scheme was used for the interpolation, although it was found that using cubic splines gave the same results to within 0.05 meV per atom.

For the cases of $C2/c$-24 (O_3, T = 0 K), *Cmca*-4 (O_3, T = 200 K) and $Pca2_1$-48 (O_4, T = 400 K), we fitted polynomials to F and differentiated the result to get an expression for $P(V)$, according to Eq. 2.75. P could then be converged with respect to the order of the polynomial, with the fit monitored carefully to prevent over-fitting and the appearance of spurious oscillations. For the same test cases, we also obtained corrected pressures using both the Birch-Murnaghan and exponential equations of state. We found that each of these three methods gave fairly similar numerical answers for all structures - an example of this is shown in Table 3.1.

Volume/Å^3 per atom	P_{DFT}/GPa	P_{poly}	P_{BM}	P_{Vinet}
1.4525	325.0004	340.6587	339.7047	338.4931
1.4071	349.9927	366.2867	365.5995	364.8323
1.3659	375.0068	392.0405	391.4151	391.1412
1.3284	399.9903	417.7658	417.0628	417.2109
1.2625	450.0078	468.9993	468.0043	468.9124
1.2061	500.0544	519.5113	518.4480	520.0177

Table 3.1 Comparing the phonon-corrected pressures obtained using the polynomial, Birch–Murnaghan and Vinet equations of state for $Pca2_1$-48 (O_4) at 400 K.

At each pressure and temperature, the structure with the lowest Gibbs free energy is the most stable. The true test for comparing these pressure correction methods is therefore a comparison of the relative Gibbs free energies. Comparing relative Gibbs free energies calculated (using O_3 and O_4) at a number of different temperatures using both the Birch-Murnaghan and Vinet exponential equations of state, we found that the choice of equation of state made no difference to the predicted phase behaviour and had negligble (< 3 GPa) impact on predicted transition pressures. We use the Birch-Murnaghan equation of state for the remainder of this Chapter.

The harmonic Gibbs free energies computed using O_3 and O_4 at 0 K are shown in Figs. 3.13a and 3.13b, respectively, although - since results for all temperatures are obtained in the same harmonic calculation at no extra cost - these plots were produced at a number of different temperatures.

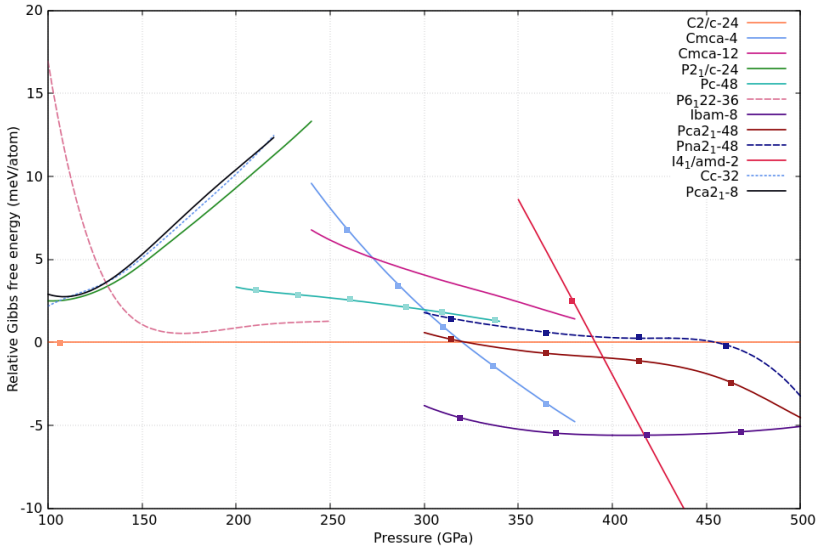

(a) Relative Gibbs free energy calculated using O_3 at T = 0 K.

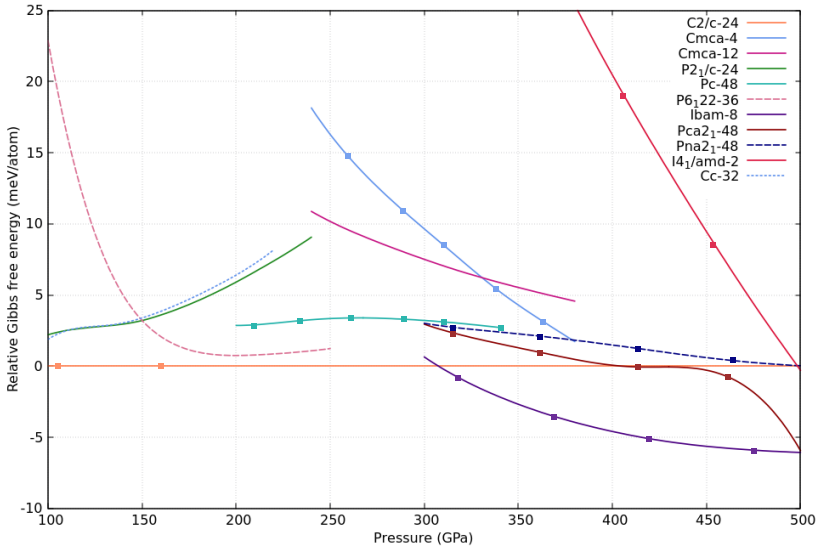

(b) Relative Gibbs free energy calculated using O_4 at T = 0 K.

Fig. 3.13 Gibbs free energy relative to $C2/c$-24, indicating predicted phase stability at 0 K at the harmonic level. Points marked with squares indicate that the structure was found to be dynamically unstable at that pressure.

Although we now have the harmonic Gibbs free energies as a function of pressure and temperature, we are unable to construct a pressure-temperature phase diagram at the harmonic level since a number of the structures are dynamically unstable. We must therefore proceed with constructing anharmonic phase diagrams instead. The anharmonic corrections to the energy at 0 K are plotted for O_3 in Fig. 3.14a and for O_4 in Fig. 3.14b, although they were

obtained at a range of temperatures without the need for any additional electronic structure calculations (as detailed in Chapter 2).

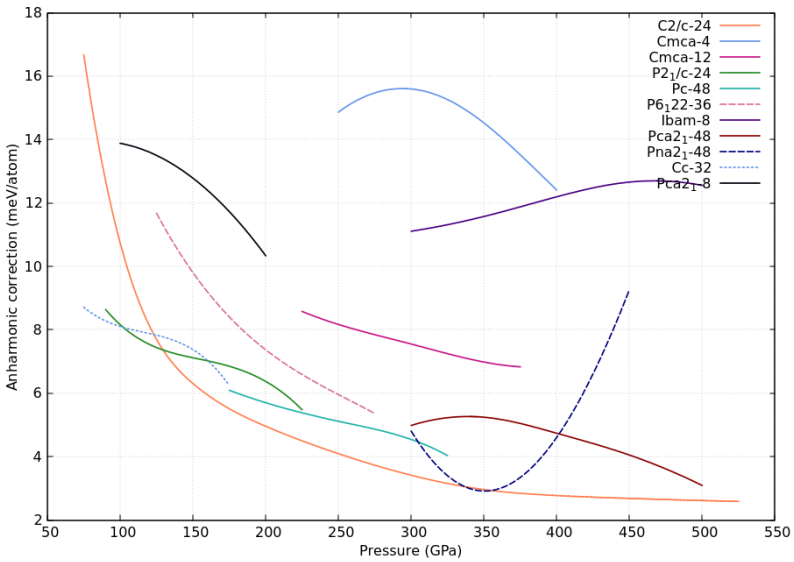

(a) Zero-point anharmonic corrections calculated using O_3.

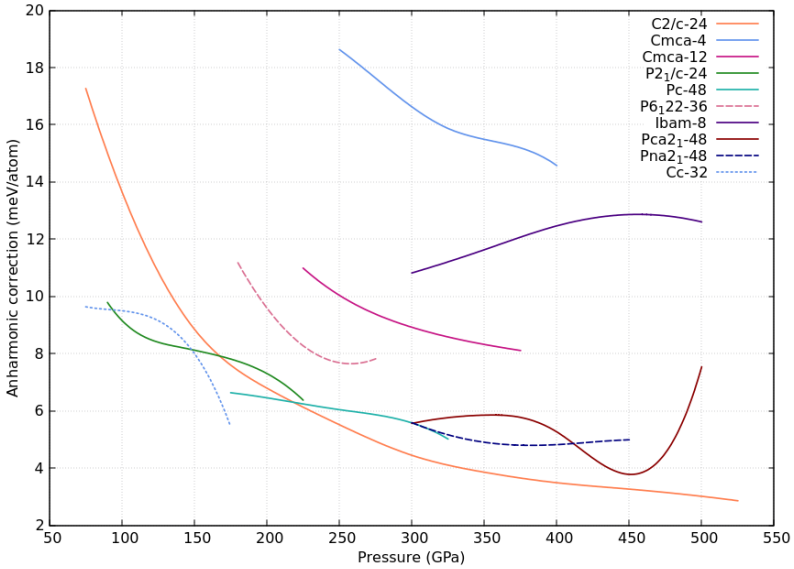

(b) Zero-point anharmonic corrections calculated using O_4.

Fig. 3.14 Zero-point anharmonic corrections calculated using custom-built functionals.

Cc-32 and $P2_1/c$-24 are both stabilised by anharmonicity in the low pressure region. *Cmca*-4 is destabilised by anharmonicity, as is *Cmca*-12 but to a slightly lesser extent. *Ibam*-8, which was dynamically unstable at the harmonic level also has a fairly large anharmonic correction. We see qualitative agreement with the anharmonic calculations of Ref. [74] for the subset of structures they study.

The Gibbs free energies, including anharmonic corrections, for O_3 and O_4 are plotted in Figs. 3.15a/3.15b and Figs. 3.16a/3.16b, respectively. As in the harmonic case, we employed a minimum curvature interpolation scheme and the Birch-Murnaghan equation of state to obtain these Gibbs free energies.

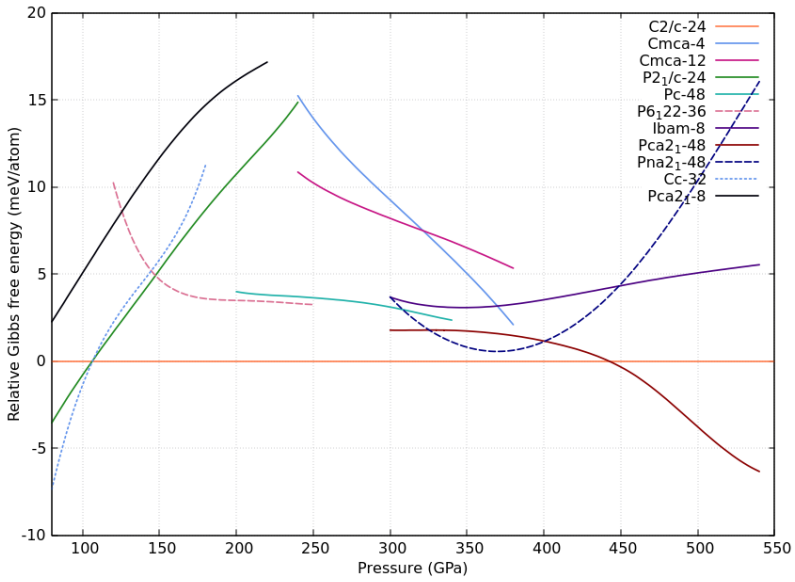

(a) Gibbs free energy per atom including anharmonic corrections (plotted relative to $C2/c$-24) calculated using O_3 at 0 K.

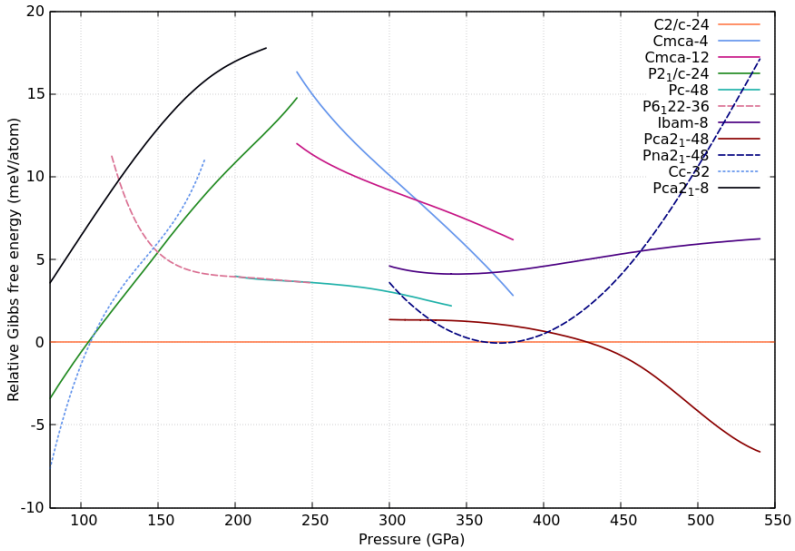

(b) Gibbs free energy per atom including anharmonic corrections (plotted relative to $C2/c$-24) calculated using O_3 at 400 K.

Fig. 3.15 Relative Gibbs free energies for hydrogen (O_3) with anharmonic corrections.

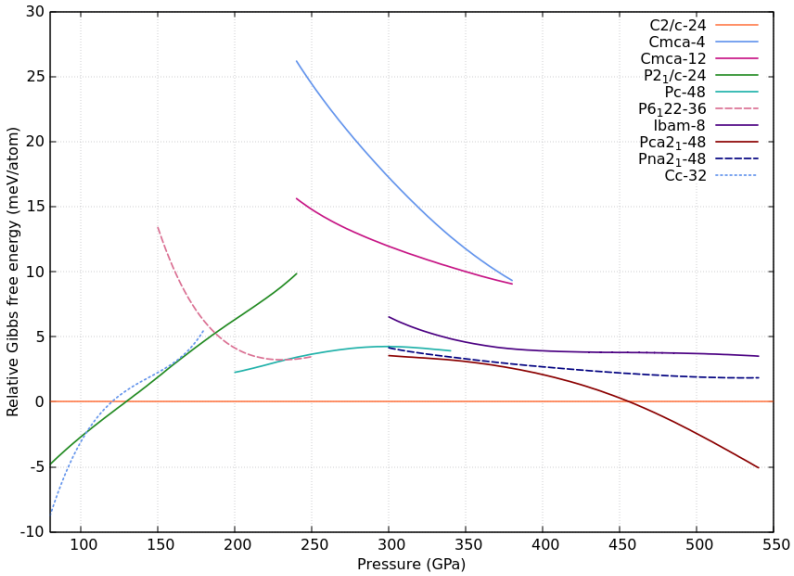

(a) Gibbs free energy per atom including anharmonic corrections (plotted relative to $C2/c$-24) calculated using O_4 at 0 K.

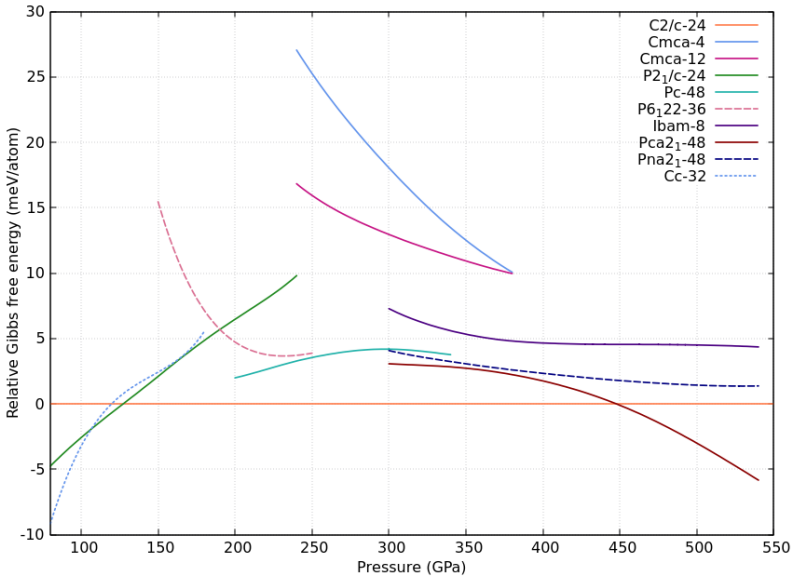

(b) Gibbs free energy per atom including anharmonic corrections (plotted relative to $C2/c$-24) calculated using O_4 at 400 K.

Fig. 3.16 Relative Gibbs free energies for hydrogen (O_4) with anharmonic corrections.

For O_3, it is clear that both Cc-32 and $P2_1/c$-24 are competitive in the low pressure region. Although *Cmca*-4 is greatly destabilised compared to the harmonic case, its relative Gibbs free energy has a fairly steep downwards gradient and it looks like the structure could potentially possess a region of stability at high pressure (outside the pressure range in which it is studied here). This still represents a large improvement over harmonic studies, which

incorrectly predict *Cmca*-4 to be stable across a large mid-pressure range. $P6_122$-36 does not become the most stable structure for any pressure or temperature when the O_3 functional is used, although it remains within 5 meV/atom of $C2/c$-24 over a 100 GPa pressure range. *Pc*-48 also never becomes the most stable structure, but it is within 3 meV/atom of $C2/c$-24 at 400 K and 300 GPa. $Pca2_1$-48 becomes the most stable structure at higher pressures. $Pna2_1$-48 also has a brief window of stability above 400 K, but calculations at slightly more dense pressure points would be needed to determine if this is a true prediction.

For O_4, fairly similar behaviour to O_3 is seen overall, although *Cmca*-4 is destabilised even further - extrapolating its predicted Gibbs free energy to outside the pressure range studied here shows that this structure should not become the most stable candidate at any point. *Ibam*-8 is rendered fairly uncompetitive with both functionals. At 500 K, *Pc*-48 is within 3.4 meV/atom of $C2/c$-24 at 250 GPa and within 1.8 meV/atom at 200 GPa.

From the relative Gibbs free energy plots of Figs. 3.15a, 3.15b, 3.16a and 3.16b (and those produced at other temperatures), anharmonic phase diagrams can be plotted for each functional to show the most stable structure in each region of pressure-temperature space. A harmonic PBE phase diagram constructed using data from Ref. [74], a study which included $P2_1/c$-24, $C2/c$-24, *Cmca*-4, *Cmca*-12 and *Pc*-48, is displayed in Fig.3.17 in order to provide comparison to the anharmonic phase diagrams produced by O_3 and O_4 here (Figs. 3.18 and 3.19). We also refer the reader to Fig. 5 of Ref. [74] (a DMC phase diagram with anharmonic corrections) for the same purpose.

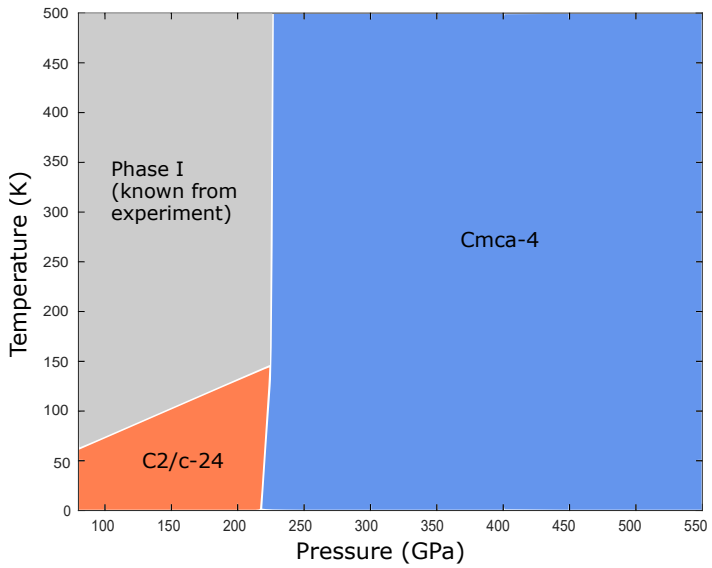

Fig. 3.17 A DFT-PBE harmonic phase diagram of solid hydrogen produced using data from Ref. [74].

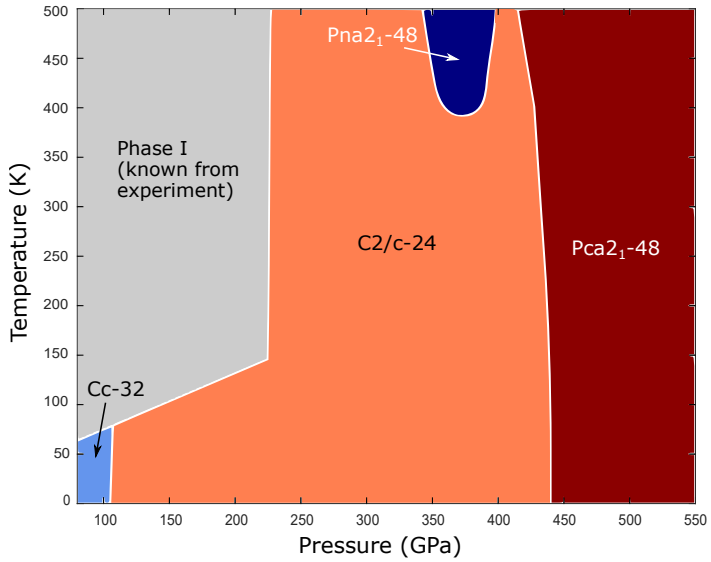

Fig. 3.18 Anharmonic phase diagram of solid hydrogen calculated using the O_3 functional (phase I region as in Fig. 3.17 - constructed using data from Ref. [74]).

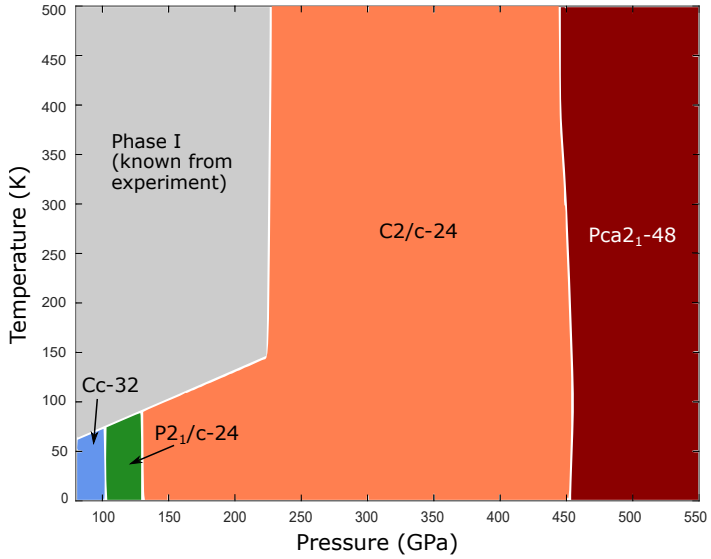

Fig. 3.19 Anharmonic phase diagram of solid hydrogen calculated using the O_4 functional (phase I region as in Fig. 3.17 - constructed using data from Ref. [74]).

3.6 Conclusions

Although we may not wish to draw definitive conclusions about the performance of these new functionals until we are able to check anharmonic vibrational grid convergence for all structures and assess the effect of coupling between degenerate subspaces, we are still able

to make some comments. The most obvious combined effect of the new functionals and the anharmonic corrections, compared to results calculated with PBE at the harmonic level, is the destabilisation of *Cmca*-4, bringing the results closer to both experimental findings and the DMC results of Ref. [74]. Both O_3 and O_4 predict a large region of stability for $C2/c$-24 (in line with the DMC-anharmonic findings) and in stark contrast to the PBE-DFT harmonic findings. O_3 predicts a transition from a phase II candidate (*Cc*-32) to phase III candidate ($C2/c$-24) at $\sim$110 GPa, with fairly little temperature dependence. For O_4, the transition from a phase II candidate to a phase III candidate is predicted at a higher pressure ($\sim$130 GPa), which is slightly closer to the experimentally observed transition. Another important observation is that the new *Cc*-32 structure is extremely energetically competitive with $P2_1/c$-24, meaning it should be included in future studies of solid hydrogen and considered seriously in relation to experiment. Both functionals predict that the phase V candidate $Pca2_1$-48 is the most stable structure at high pressure, although the present results place the transition at a higher pressure than previously observed. Unfortunately, no region of stability is predicted for *Pc*-48, meaning these functionals do not produce results fully in agreement with accurate DMC calculations, at least to within the levels of convergence achievable within this study. They do, however, appear to offer notable improvement over PBE and may be useful for future structure searching studies.

Chapter 4

Stability and superconductivity of lanthanum and yttrium decahydrides

4.1 Motivation

Using the techniques applied in Chapter 3, we are now able to move from pure hydrogen to a closely related class of materials where interesting properties may be more readily experimentally accessible. Hydrogen was predicted to be a room-temperature superconductor at high pressure in 1968 [103], but the pressures required to metallise hydrogen are difficult to obtain experimentally [114, 136, 137, 138, 139, 140]. It has been suggested that hydrides will have lower metallisation pressures than pure hydrogen due to the *chemical pre-compression* caused by the presence of other elements [141]; these materials can therefore potentially become superconducting at more readily accessible pressures too. This idea has motivated a surge of research examining potential superconductivity in high-pressure hydrides, with several reviews summarising recent developments in the field [52, 60, 142, 143, 144, 145, 146].

Theoretical studies of ScH_3, LaH_3 [147], YH_3, YH_4 and YH_6 [148, 149, 150] were among the first to identify hydrides of rare-earth elements in particular as potential high-temperature superconductors. Others have focused on heavier rare-earth hydrides, exploring the synthesis and superconducting properties of cerium [151, 152], praseodymium [153] and neodymium [154] hydrides. Recent first-principles studies of rare-earth hydrides reported finding structures with high hydrogen content, with cage-like arrangements of hydrogen atoms surrounding the non-hydrogen element [155, 156]. Of particular note, a T_c of 264-286 K was calculated for an $Fm\bar{3}m$ structure of LaH_{10} at 210 GPa [155], while the analogous YH_{10} structure was calculated to have an even larger T_c of 305-326 K (well over room

temperature) at 250 GPa. Slight distortions of the cubic LaH_{10} phase were found to lead to $C2/m$ and $R\bar{3}m$ structures at lower pressures [157, 158], although Ref. [159] showed that inclusion of quantum effects makes the PES much simpler and renders $Fm\bar{3}m$ as the true ground state. In 2018/19, these predictions were followed by experimental measurement of critical temperatures reaching 260 K in LaH_{10} at 170-200 GPa [160, 161]. LaH_{10} therefore took the record for highest experimentally measured T_c, surpassing the previous record-holder, high-pressure hydride $Im\bar{3}m$-H_3S (T_c = 203 K) [162], by more than 50 K. The observed high-T_c phase was determined to be a structure with an fcc arrangement of lanthanum atoms, lending support to theoretical predictions.

In this Chapter, within the framework of DFT, we study both LaH_{10} and YH_{10} using crystal structure prediction methods and compute the phase behaviour and superconducting properties of these materials from first principles. A large portion of the work presented in this Chapter is published as Ref. [163]. As detailed in the Preface, C. J. Pickard performed the structure searching for the La-H system. I performed pseudopotential testing, confirmed La-H search results, performed structure searching for the Y-H system, constructed enthalpy plots, analysed results, and discovered the link to experiment. M. J. Hutcheon performed the phonon and electron-phonon calculations, allowing us to obtain the Gibbs free energy and T_c for each phase. I investigated the impact that various approximations made in superconductivity calculations may have on the findings of this Chapter and the remainder of this thesis.

4.2 Methodology and computational details

4.2.1 Phonons and superconductivity

In this Chapter, we calculate the Kohn-Sham eigenvalues, harmonic phonon frequencies, and electron-phonon coupling strengths, $g_{mn\nu}(\mathbf{k},\mathbf{q})$, appearing in the Hamiltonian of the coupled electron-phonon system (see Eq. 2.91) using the QUANTUM ESPRESSO code [42, 43]. As we saw in Chapter 2, this allows us to construct the electron-boson spectral function, $\alpha^2F(\omega)$, and calculate the electron-phonon coupling constant, λ. We extract the superconducting critical temperature by solution of the Eliashberg equations using the ELK code [89]. In the process of these calculations, we also obtain the electronic and vibrational densities of states, with the latter being obtained at various temperatures at no extra cost within the harmonic approximation. Therefore, by performing these calculations at a number of different DFT input pressures we are also able to derive the Gibbs free energy of each candidate structure as a function of both pressure and temperature, allowing us to construct a full pressure-temperature phase diagram for each of the systems studied.

Well-converged **k**-point grids with a spacing of at most $2\pi\times0.015$ Å^{-1} and an 820 eV plane wave cut-off were used for all electron-phonon calculations. The **q**-point grids used were typically 8 times smaller than the **k**-point grids and were Fourier interpolated to 10 times their original size. For the cubic systems studied here, this corresponds to $\geq 24\times24\times24$ **k**-point grids and a $3\times3\times3$ **q**-point grid Fourier-interpolated to $30\times30\times30$.

As discussed in Chapter 2, in order to evaluate the double-delta sum in the calculation of interaction linewidths (Eq. 2.94) for finite **k**- and **q**-point grids, we follow the method detailed in Appendix A of Ref. [87]. This involves smearing the delta functions with Gaussians characterised by a smearing width σ. We identify the optimal smearing parameter by plotting the final T_c result as a function of σ for different (but sufficiently converged) **k**-point grids [87] and identifying the point at which discrepancies start to emerge. This process is shown in Figs. 4.1 and 4.2. It is clear from these figures that the smearing value used can have a large impact on the predicted T_c and we found that choosing a sensible smearing value in a systematic way was therefore crucial to ensure the accuracy of results.

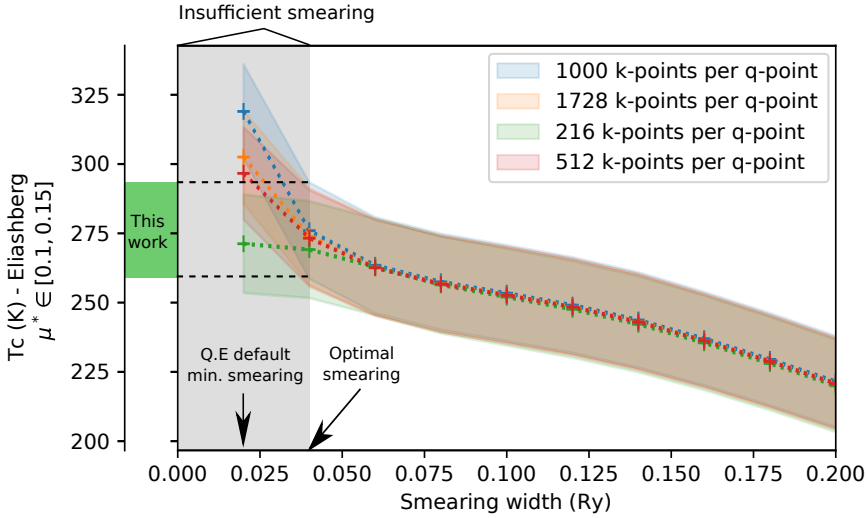

Fig. 4.1 The dependence of T_c on the double-delta smearing width, σ, for $Fm\bar{3}m$-YH_{10} at 350 GPa. The region of insufficient smearing is shaded. Our choice of σ for this structure and pressure is marked, along with the T_c range it corresponds to. The smallest smearing value used in an electron-phonon calculation with default QUANTUM ESPRESSO settings is also shown. It is clear that using a value of smearing that is too low, rather than using results from multiple **k**-point grids to pick an appropriate value, will lead to an overstimation of T_c for this system.

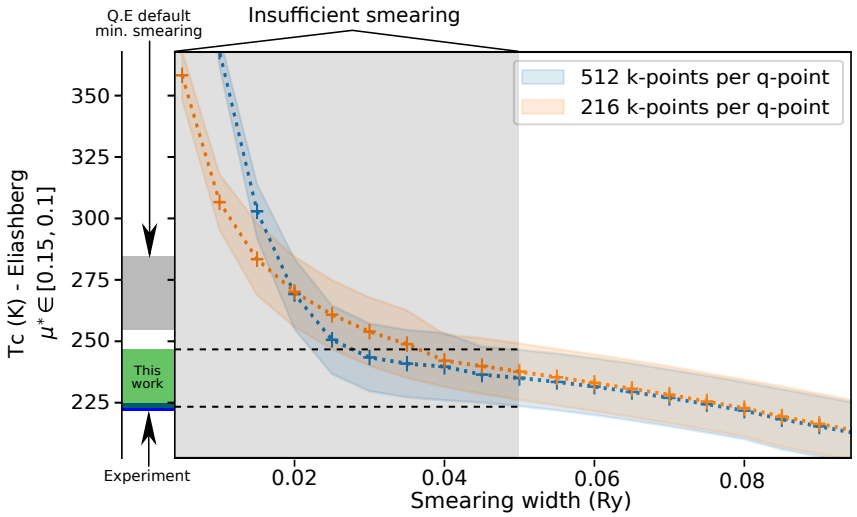

Fig. 4.2 The dependence of T_c on the double-delta smearing width, σ, for $Im\bar{3}m$-YH_6 at 160 GPa. A recent experimental measurement [164] for this material at 166 GPa is labelled; it falls just within the T_c range calculated with an appropriately chosen σ. Refs. [164, 165] highlighted that previously calculated T_c values for this system were considerably higher than their experimental observations and we note that similar behaviour is seen when insufficient smearing is used. The results of Ref. [150], which used accurate Wannier interpolation techniques to study the same structure, are in agreement with ours.

4.2.2 Pseudopotential testing

While the geometry optimisation, phonon, and electron-phonon calculations in this Chapter were carried out using QUANTUM ESPRESSO [42, 43], the structure searching calculations used CASTEP [41] as the underlying electronic structure code. In order to validate the pseudopotentials used in each case[1], we compared the QUANTUM ESPRESSO and CASTEP pressure-volume curves produced for $Fm\bar{3}m$-LaH_{10} and $Im\bar{3}m$-YH_6 to data obtained using the all-electron code WIEN2K [166]. The WIEN2K data used for comparison here was calculated for Refs. [156, 158][2]. We found both QUANTUM ESPRESSO and CASTEP were able to reproduce the all-electron results, but noted that use of a slightly modified pseudopotential for lanthanum in CASTEP (with the addition of a fractional 4f component to the electronic configuration used) was crucial in order to achieve this for LaH_{10}. This point is illustrated by comparing the otherwise identical convex hulls of Fig. 4.8 and Fig. 4.9, which were calculated with and without the additional 4f component, respectively.

[1]Scalar-relativistic, ultrasoft pseudopotentials downloaded from the QUANTUM ESPRESSO website, and CASTEP on-the-fly pseudopotentials generated using default strings for hydrogen and yttrium and a modified string (2|2.3|5|6|7|50U:60:51:52:43{4f0.1}(qc=4.5)[4f0.1]) for lanthanum

[2]The data was provided to us by Hanyu Liu and Feng Peng.

4.2.3 Identifying candidate structures

All structures studied in this work were identified from first principles using AIRSS [50]. The PBE functional, CASTEP QC5 pseudopotentials, a 400 eV plane wave cut-off and a **k**-point spacing of $2\pi\times0.05$ Å^{-1} were used in all searches unless otherwise stated. Around 22,000 initial structures were generated for both LaH_{10} and YH_{10}, each with between 1 and 4 formula units (f.u.) in the simulation cell. The C2X software [167] was used for converting between CASTEP and QUANTUM ESPRESSO file formats, allowing us to easily pass candidate structures from the searching to the calculation stage, and also for reporting the space groups of structures at various tolerances.

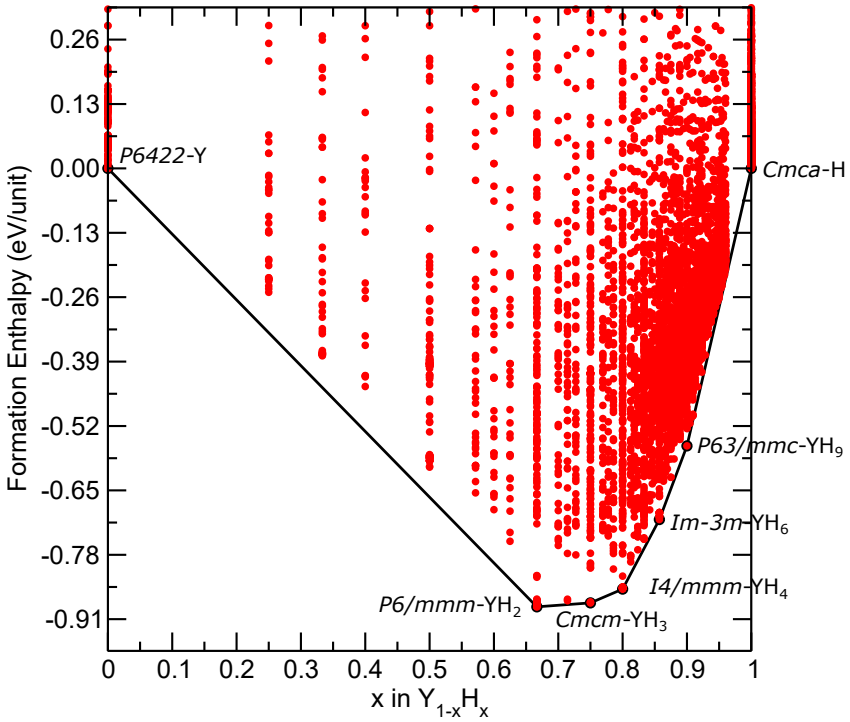

Fig. 4.3 An example convex hull for the Y-H system (with on-hull structures labelled), showing that YH_{10} is metastable at the static-lattice level at 400 GPa. We note that our Y-H hull identifies the YH_4, YH_6 and YH_9 structures recently reported in experiment [164, 165] (of $I4/mmm$, $Im\bar{3}m$ and $P6_3/mmc$ symmetry, respectively), highlighting the success of crystal structure prediction methods.

Before beginning detailed searches specifically for the LaH_{10} and YH_{10} stoichiometries, we constructed well-converged static-lattice convex hulls for the La-H and Y-H systems using AIRSS and qhull [168]; an example of which is illustrated in Fig. 4.3. Our convex hulls showed that the LaH_{10} and YH_{10} stoichiometries are on (or close to) the static-lattice

convex hulls over the pressure ranges we study here (∼150-500 GPa for LaH_{10} and ≥300 GPa for YH_{10}), confirming the findings of previous work [156].

4.3 Phase behaviour and superconducting properties

In this section, we report the main candidates arising from structure searching in each system, as well as the predicted phase behaviour, the calculated superconducting properties of each phase, and how these results link to observations in past and future experiments. All the final results we report here are given in terms of phonon-corrected pressures (as introduced in Chapter 2), meaning the effective pressures calculated once the energy associated with the phonons is included. These corrected pressures are obtained by fitting the Birch-Murnaghan [71] equation of state to our data. Where static ("input") DFT pressures are reported instead, they are labelled as P_{DFT}. This second set of pressures is used purely to facilitate comparison with previous work in the literature since these results are not always reported in terms of phonon-corrected pressures. These static DFT pressures are simply an input parameter to the DFT geometry optimisation.

4.3.1 Lanthanum decahydride, LaH_{10}

Low enthalpy candidates found using AIRSS for LaH_{10} included the record-breaking $Fm\bar{3}m$ structure, as well as the $R\bar{3}m$ and $C2/m$ distortions which had also been reported previously. The searches also revealed a new hexagonal structure of $P6_3/mmc$ symmetry. These structures are shown in Fig. 4.4. Another $C2/m$ structure (with 3 f.u. per unit cell, rather than 2) was also found to be energetically competitive, but was not considered further as initial calculations suggested it behaves similarly to the 2 f.u. structure over the pressure range of interest.

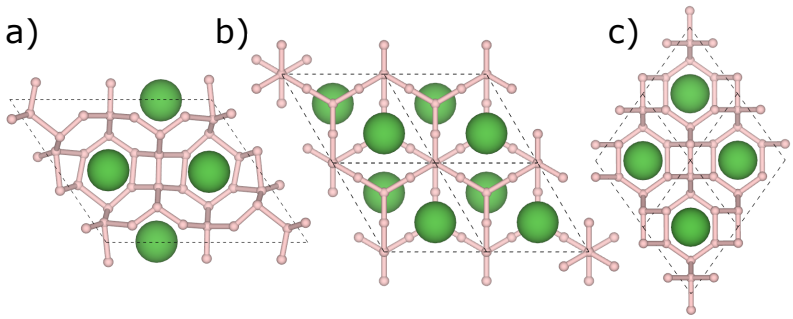

Fig. 4.4 Structures of LaH_{10}. (a) 2 f.u./cell $C2/m$, (b) 2 f.u./cell $P6_3/mmc$, (c) 1 f.u./cell $Fm\bar{3}m$. The $R\bar{3}m$ structure is not shown as it is visually indistinguishable from the $Fm\bar{3}m$ structure at the pressures of interest.

During the searches, we also found several other previously unreported structures at low pressures with space groups $Pnnm$, $C2$ and $P2_12_12_1$ and unit cells containing 2, 3 and 4 f.u., respectively. The latter two are among the lowest enthalpy structures in the low-pressure region (see Fig. 4.5). However, we note that these structures are distortions of the high-symmetry $Fm\bar{3}m$ structure and, similarly to the case of $R\bar{3}m$ noted in Ref. [159], it is possible that anharmonic effects may remove them from the PES altogether. In addition to this, the low symmetry and large unit cells of these structures make converged phonon and electron-phonon calculations prohibitively expensive; they were therefore not considered further.

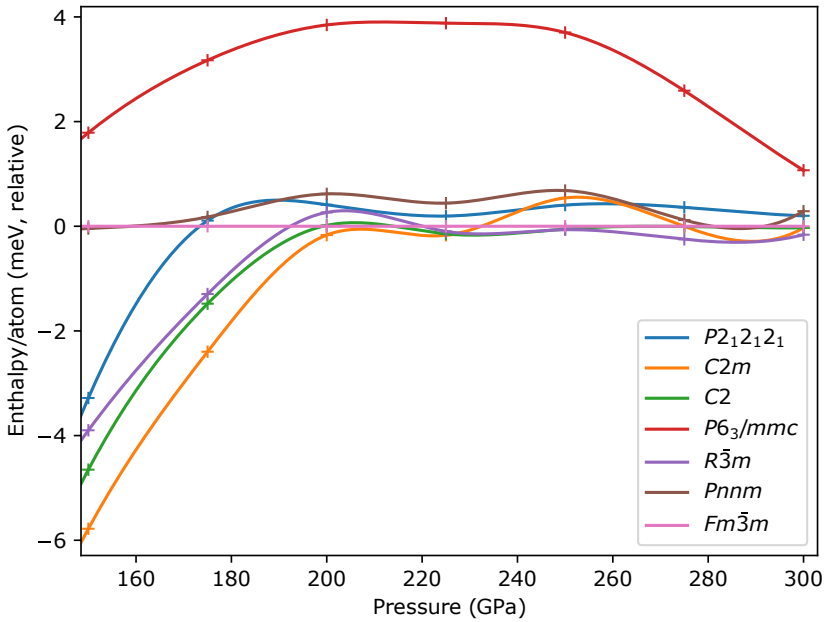

Fig. 4.5 DFT enthalpies of LaH_{10} candidate structures. We see that the large-unit-cell $C2$ and $P2_12_12_1$ structures are energetically competitive at low pressures.

The phase behaviour we predict for LaH_{10} is shown in Fig. 4.6 and the corresponding critical temperatures calculated for the four phases are shown in Fig. 4.7. Our calculations for the $Fm\bar{3}m$ phase include unstable phonon modes for $P_{DFT} \leq 210$ GPa. In the harmonic picture, explicitly taking into account this dynamical instability leads to a window of stability for the $C2/m$ phase, which is the stable structure reached if we follow the unstable mode. This is in agreement with previous calculations [157, 158]. However, we note that under the assumption that the unstable modes can be neglected in the calculation of the Gibbs free energy, we obtain the same behaviour as the anharmonic calculations of Ref. [159], which found $Fm\bar{3}m$ to be the only phase with a predicted region of stability at lower pressures. With increasing pressure, as also noted in previous theoretical work [159], the $R\bar{3}m$ structure closely approaches $Fm\bar{3}m$ symmetry. We see this reflected in the fact that the Gibbs free

energy and predicted T_c of these two structures are virtually identical above about 225 GPa. We therefore expect that these phases may not be distinguishable in experiment at higher pressures.

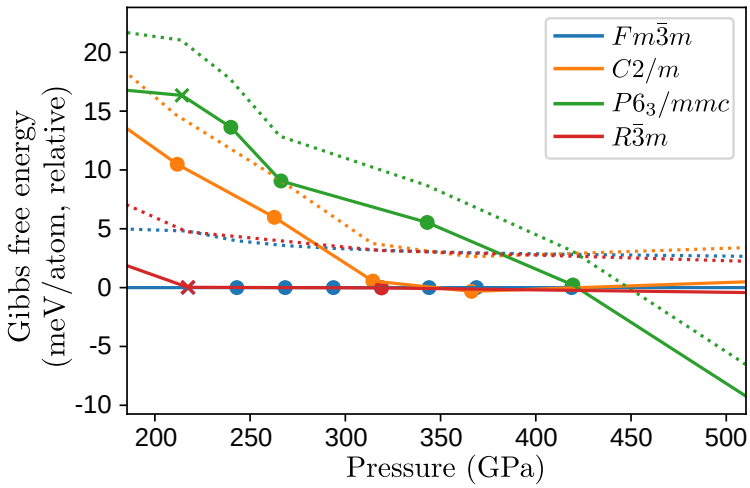

Fig. 4.6 The Gibbs free energy as a function of pressure for candidate structures of LaH_{10}, plotted relative to a third-order Birch-Murnaghan fit of the $Fm\bar{3}m$ data. The crosses represent calculations with unstable phonon modes - these points are not included in the fit. The solid lines show the predicted Gibbs free energy at 300 K, while the dashed lines are at 0 K.

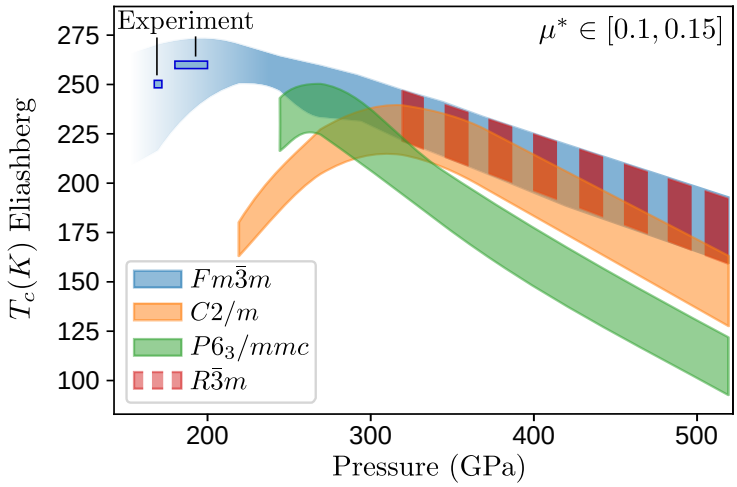

Fig. 4.7 Critical temperature as a function of pressure, $T_c(P)$, for the candidate LaH_{10} structures, obtained from direct solution of the Eliashberg equations. The width of the lines arises from our treatment of μ^* [91] as an empirical parameter with a range 0.1-0.15. The $Fm\bar{3}m$ result has been extended into the region where it is dynamically unstable (shaded according to unstable fraction of the phonon density of states) in order to facilitate comparison with the experimental results of Refs. [160, 161]. This extension was achieved by removing the contribution of unstable phonon modes (in their entirety) to the Eliashberg function while maintaining its normalisation.

Although the cubic phase enjoys a large region of stability, we do predict a phase transition at higher pressures; at 300 K, the $P6_3/mmc$ structure becomes the most thermodynamically favourable candidate at pressures above ∼420 GPa. More importantly, this hexagonal phase is also predicted to be metastable (although eventually dynamically unstable) at low pressures, lying within 20 meV/atom of the cubic phase down to the 150-200 GPa region that was probed in experiment [160, 161]. This new structure therefore provides a plausible explanation for the experimental observation of hcp impurities in fcc-LaH_{10} samples at 170 GPa in Ref. [161].

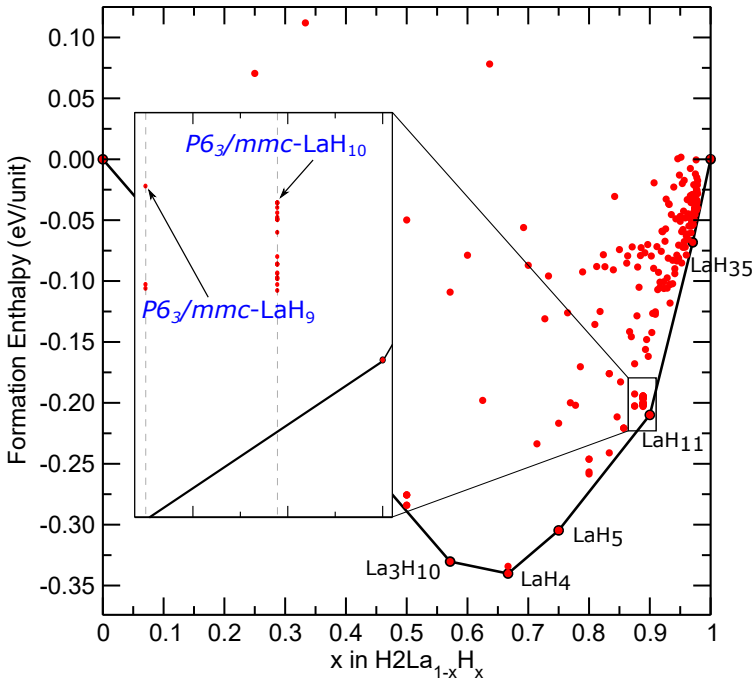

Fig. 4.8 A convex hull for the La-H system at 150 GPa, accurately calculated using a **k**-point spacing of $2\pi\times0.03$ Å^{-1} and a 700 eV plane-wave cut-off. On-hull structures are labelled. The on-the-fly pseudopotential string used for lanthanum included an additional 4f component. As discussed before, a pseudopotential without this fractional addition was unable to reproduce the all-electron $Fm\bar{3}m$-LaH_{10} pressure-volume curve during testing and also leads to a qualitatively different convex hull as shown in Fig. 4.9. In agreement with Ref. [169], we find that LaH_9 is not on the hull at this pressure. However, we also find that LaH_{16} does not lie on the hull at 150 GPa, despite finding the $P6/mmm$-LaH_{16} structure studied in-depth in that previous work.

We note that a low-energy hexagonal LaH_9 structure predicted previously in the experimentally relevant pressure region [169] could offer an alternative explanation for the observation of hcp impurities. However, the authors of Ref. [161] determined that the two kinds of hcp impurities in their samples likely possessed LaH_{10} stoichiometry. To further

explore this, we calculated a high-quality La-H static-lattice convex hull at 150 GPa (see Fig. 4.8). It shows that the $P6_3/mmc$-LaH_{10} structure predicted in this work lies closer to the hull than the $P6_3/mmc$-LaH_9 structure of Ref. [169]. Combining these two pieces of evidence, we believe it is likely that the hcp impurities originate from our $P6_3/mmc$-LaH_{10} phase.

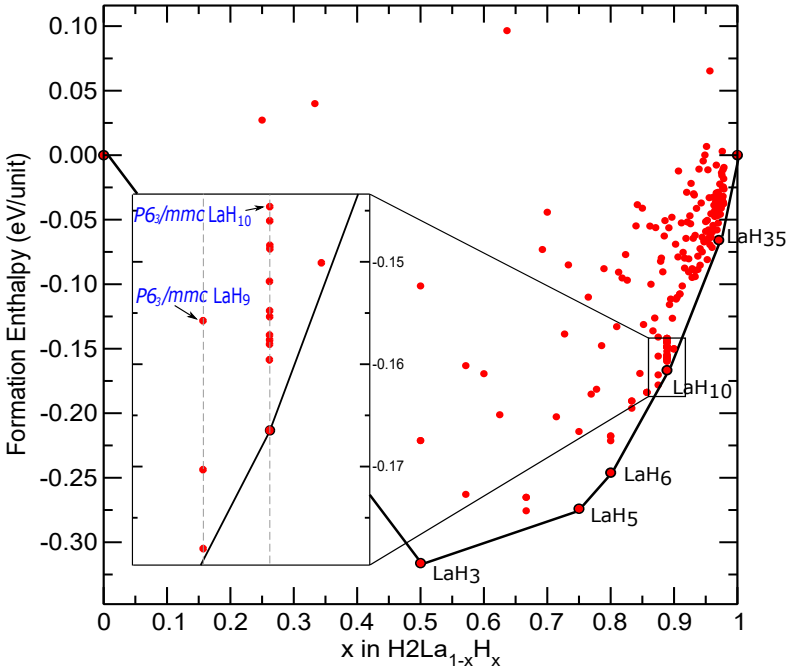

Fig. 4.9 As Fig. 4.8, but calculated without the 4f electron component in the lanthanum pseudopotential. We see that LaH_3, LaH_5, LaH_6, LaH_{10} and LaH_{35} are found on the hull, compared to La_3H_{10}, LaH_4, LaH_5, LaH_{11} and LaH_{35} with the modified pseudopotential, highlighting the importance of the 4f electron contribution.

Turning now to the predicted superconducting properties, we calculate a T_c of 232-259 K for $Fm\bar{3}m$-LaH_{10} at 269 GPa (P_{DFT} = 250 GPa), which is lower than the previous theoretical result of T_c = 257-274 K at the same input pressure [155]. However, we observe an increase in T_c on reduction of the double-delta smearing parameter to below our calculated optimal value, potentially explaining this discrepancy. Careful choice of smearing has previously been noted as important in other hydride systems, with the authors of Ref. [170] even showing that incorrect values can lead to predictions of superconductivity in systems where the phenomenon is not even present, and we wish to highlight its importance here. While $Fm\bar{3}m$ may be the "stand out" phase - with its high predicted T_c value coupled with direct observation in experiment - all four candidates considered here are in fact high-T_c superconductors, with peaks in T_c below 350 GPa. The high calculated T_c for the hexagonal phase suggests that, if this phase is indeed responsible for the hcp impurities observed in experiment, it would not have a great impact on the observed T_c of the majority cubic sample.

We note a previous calculation of T_c for the cubic LaH_{10} structure at 200 GPa [156], however, in agreement with other calculations [157, 158] we find $Fm\bar{3}m$ to be dynamically unstable at this pressure. This dynamical instability means that, working within the standard harmonic picture, we cannot compute a T_c value for this phase to compare directly with experiment, which found T_c = 250 K at around 170 GPa [161] and T_c = 260 K at 180-200 GPa [160]. However, by ignoring the contribution of the unstable phonon modes to the Eliashberg function at pressures $\leq$ 210 GPa we are able to obtain a rough estimate of T_c in this region. These results are depicted as the faded-out section in Fig. 4.7, where the process is described briefly in the caption, and it is clear that the results we obtain are in good agreement with both sets of experimental results. For the $C2/m$ phase, using an optimal value of smearing we calculate T_c = 205-225 K at 262 GPa (P_{DFT} = 250 GPa), compared to T_c = 229-245 K at the same input pressure in Ref. [158]. Again, we note that this discrepancy may be explained by choice of the double-delta smearing parameter.

4.3.2 Yttrium decahydride, YH_{10}

In the YH_{10} system, studied at higher pressures in order to facilitate both the stabilisation and metallisation of this lighter composition, we find structures with similar atomic arrangements to those seen in LaH_{10}. The lowest enthalpy candidates for YH_{10} found using AIRSS include $Fm\bar{3}m$, which had been identified and studied previously, a slight distortion of this structure, $R\bar{3}m$, and structures of $P6_3/mmc$ and $Cmcm$ symmetry. These structures are shown in Fig. 4.10.

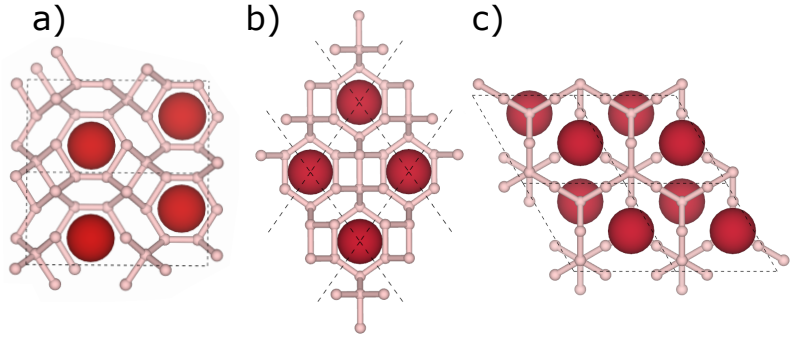

Fig. 4.10 Structures of YH_{10}. (a) 2 f.u./cell $Cmcm$, (b) 1 f.u./cell $Fm\bar{3}m$, (c) 2 f.u./cell $P6_3/mmc$. The $R\bar{3}m$ structure is, again, not shown because it is visually indistinguishable from the cubic structure.

The phase behaviour we predict for YH_{10} is shown in Fig. 4.11 and the corresponding critical temperatures we calculate for these four phases are shown in Fig. 4.12.

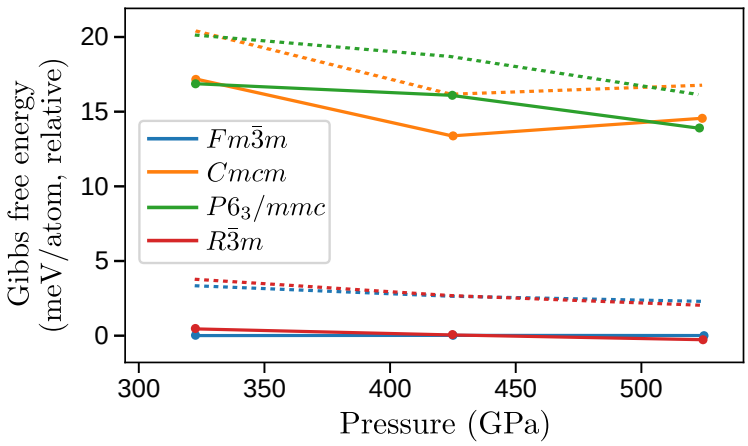

Fig. 4.11 The Gibbs free energy as a function of pressure for candidate structures of YH_{10}, plotted relative to a third-order Birch-Murnaghan fit of the $Fm\bar{3}m$ data. The solid lines show the predicted Gibbs free energy at 300 K, while the dashed lines are at 0 K.

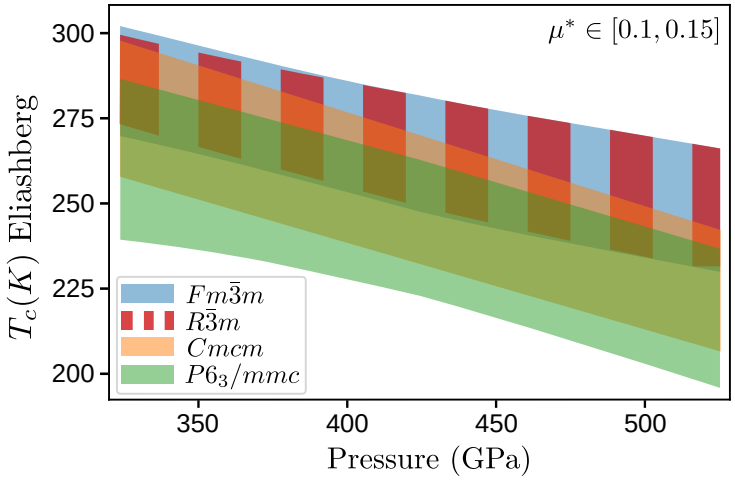

Fig. 4.12 Critical temperature as a function of pressure, $T_c(P)$, for the YH_{10} candidate structures, obtained from direct solution of the Eliashberg equations. μ^* is taken to have a value between 0.1 and 0.15, leading to a T_c range rather than a single value.

In contrast to the case of LaH_{10}, we do not predict any phase transitions within the predicted range of stability of the YH_{10} stoichiometry [156]; our calculations predict that the cubic structure remains the most stable at all pressures. However, the difference in Gibbs free energy and T_c between the $Fm\bar{3}m$ and $R\bar{3}m$ phases is exceedingly small (see Fig. 4.11); this is because $R\bar{3}m$ is a small distortion of the cubic phase and the results therefore reflect their structural similarity at high pressures.

We see that all four YH_{10} structures considered possess high critical temperatures across the whole pressure range, with T_c decreasing with increasing pressure. Previous calculations

for $Fm\bar{3}m$ found T_c = 305-326 K at 250 GPa [155] and T_c = 303 K at 400 GPa [156]. Here, we calculate T_c = 270-302 K at 324 GPa (P_{DFT} = 300 GPa) and T_c = 250-280 K at 425 GPa (P_{DFT} = 400 GPa). Our more conservative T_c results may again be explained by considering the smearing parameter used to approximate the double-delta integral. We were able to reproduce the results of previous calculations by using the minimum default smearing employed in QUANTUM ESPRESSO, which, in this specific case, overestimates T_c by $\sim$30 K (see Fig. 4.1) compared to optimal smearing. We also note that our $Fm\bar{3}m$ results agree with those obtained using accurate Wannier interpolation techniques [150]. Using the same method to calculate an optimal smearing also produces results in agreement with recent experimental measurements for $Im\bar{3}m$-YH_6 [164], as shown in Fig. 4.2.

4.4 Common approximations in superconductivity calculations

In order to calculate T_c within a DFT framework, as is done in this Chapter and throughout the remainder of this thesis, a number of approximations are usually made. In Eliashberg theory, when we rewrite the momentum sum as an energy integral we simplify the equations by assuming that the DOS takes a constant value over the range of integration. This is done because the pairing interaction only couples states very close to the Fermi level, however, the DOS around the Fermi level is system-dependent and it does not necessarily take a constant value. The energy dependence of the DOS near the Fermi level, as well as the zero-point and temperature-dependent renormalisation of the DOS as a whole, is neglected in standard calculations of T_c. Although there are methods for incorporating its effects, anharmonicity is usually also neglected since it is prohibitively expensive to consider for anything beyond a few structures or pressure values. Here we explore these ideas in more detail and assess their importance in the context of superconducting hydrides such as LaH_{10} and YH_{10}.

4.4.1 The electronic density of states

Energy dependence around the Fermi level

In original studies of H_2S and H_3S, the energy dependence of the DOS was neglected (as is standard) in order to simplify the Eliashberg equations; the authors of Ref. [171] then went beyond the constant DOS approximation by explicitly considering the electronic structure around the Fermi level. This is a process that is straightforward in theory, but numerically expensive [171]. They found a strong energy dependence of the DOS as a consequence of the

van Hove singularity around the Fermi level for $Im\bar{3}m$-H_3S; this energy dependence is clearly visible in Fig. 4.13, which was calculated for this Chapter. The constant DOS approximation is therefore not appropriate in this situation. In fact, the predicted T_c of H_3S falls by 34% when the energy dependence of the DOS is taken into account, while for H_2S T_c increases by 15% [171].

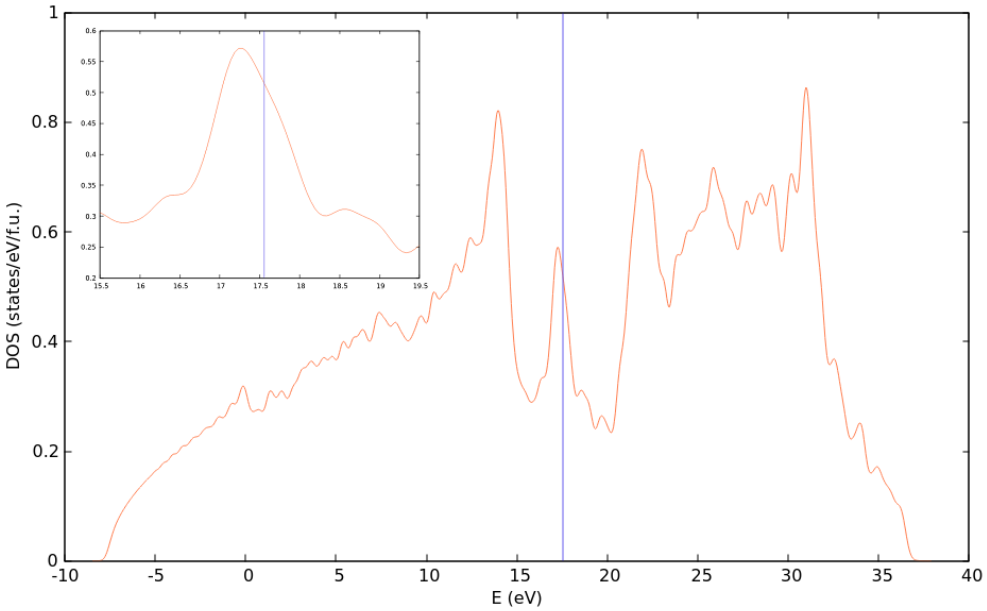

Fig. 4.13 The electronic DOS for $Im\bar{3}m$-H_3S at 200 GPa calculated using QUANTUM ESPRESSO. The Fermi energy is marked with a vertical line.

The DOS of the cubic LaH_{10} structure studied in this Chapter is shown in Fig. 4.14. Considering the energy scale of the phonons - the logarithmic average phonon frequency, $\omega_{\ln}$, for this structure is 871 $cm^{-1} \sim 0.1$ eV at 250 GPa [169] - and the less dramatic features near the Fermi energy, we predict that taking the energy dependence of the DOS into account will not have as large an impact on the calculated T_c as it did for H_3S. We do, however, expect it to still make some quantitative difference.

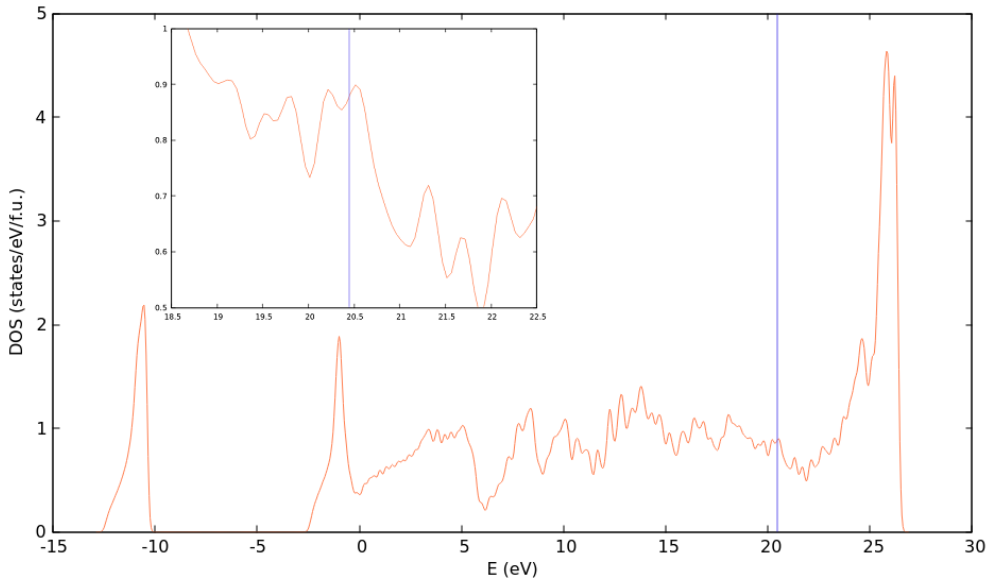

Fig. 4.14 The electronic DOS for $Fm\bar{3}m$-LaH_{10} at 250 GPa calculated using QUANTUM ESPRESSO. The Fermi energy is marked with a vertical line. On the phonon energy scale, the constant DOS approximation does not fail as badly for this system as it does for H_3S.

Zero-point and temperature-dependent renormalisation

Allen-Heine-Cardona (AHC) theory [172, 173, 174] provides a perturbative approach to calculating shifts in the electronic eigenvalues due to zero-point motion and temperature effects. The theory therefore enables us to approximate both the zero-point renormalisation (ZPR) and temperature dependence of the DOS. Here, we will cover the basic ideas of this theory before applying it to the cubic LaH_{10} structure studied in this Chapter.

AHC theory relies on the Born-Oppenheimer (adiabatic) approximation and applies perturbation theory to second order in atomic displacements [172]. Following the original Ref. [172], we consider identical atoms with thermal displacements, $\mathbf{u}_l$ (where l labels the average position), and assume the total potential can be written as a sum of potentials from individual atoms. The electron-atom interaction, $V(\mathbf{r}-\mathbf{l}-\mathbf{u}_l)$, can then be written as a Taylor expansion about the equilibrium positions, $\mathbf{u}_l = 0$. If $\hat{H}_0$ is the unperturbed Hamiltonian (where these displacements are neglected) with associated eigenstates $|n,\mathbf{k}\rangle$ and energies $\varepsilon_{n\mathbf{k}}$, the two leading-order corrections to the Hamiltonian are given by

$$\hat{H}_1 = \sum_l \mathbf{u}_l \cdot \nabla_l V(\mathbf{r}-\mathbf{l}), \tag{4.1}$$

$$\hat{H}_2 = \frac{1}{2}\sum_l \mathbf{u}_l\mathbf{u}_l \cdot \nabla_l\nabla_l V(\mathbf{r}-\mathbf{l}). \tag{4.2}$$

Here $\mathbf{u}_l$ are time-dependent operators, but within the adiabatic approximation (as introduced in Chapter 2) we neglect this dependence [172]. Then, by perturbation theory, in the presence of a configuration of displacements $\{\mathbf{u}_l\}$ we have

$$E_{n\mathbf{k}}(\{\mathbf{u}_l\}) = \varepsilon_{n\mathbf{k}} + \langle n\mathbf{k}|(\hat{H}_1 + \hat{H}_2)|n\mathbf{k}\rangle + \sum_{n'\mathbf{k}'}{}' \frac{|\langle n'\mathbf{k}'|\hat{H}_1|n\mathbf{k}\rangle|^2}{\varepsilon_{n\mathbf{k}} - \varepsilon_{n'\mathbf{k}'}}, \tag{4.3}$$

where the prime on the sum means that the $(n'\mathbf{k}') = (n\mathbf{k})$ case is neglected and $\hat{H}_2$ is not included in this sum since we are only considering terms up to second order in the displacements. Now, we can define the temperature-dependent energy, $E_{n\mathbf{k}}(T)$, as $E_{n\mathbf{k}}(\{\mathbf{u}_l\})$ thermally averaged over the ensemble of displacements,

$$E_{n\mathbf{k}}(T) = \varepsilon_{n\mathbf{k}} + \frac{1}{2}\sum_l \langle n\mathbf{k}|\nabla_l\nabla_l V|n\mathbf{k}\rangle \cdot \overline{\mathbf{u}_l\mathbf{u}_l} + \sum_{ll'}\sum_{n'\mathbf{k}'} \frac{\langle n\mathbf{k}|\nabla_l V|n'\mathbf{k}'\rangle \langle n'\mathbf{k}'|\nabla'_l V|n\mathbf{k}\rangle \cdot \overline{\mathbf{u}_l\mathbf{u}_{l'}}}{\varepsilon_{n\mathbf{k}} - \varepsilon_{n'\mathbf{k}'}}. \tag{4.4}$$

The first (unperturbed) term is unchanged since it corresponds to $\mathbf{u}_l = 0$. The second term now includes the $\hat{H}_2$ contribution only since $\overline{\mathbf{u}_l}$ (the thermal average of $\mathbf{u}_l$) vanishes in the harmonic approximation. This term describes thermal expansion in an anharmonic theory [172].

The two correction terms in Eq. 4.4 correspond to the Debye-Waller (DW) and Fan self-energy [175, 176] theories, in order of appearance. These two lines of thought were initially developed independently, meaning that usually only one of them was included in calculations [177] until AHC theory unified them. As can be seen from their form, the DW term represents the effect of the second order electron-phonon interaction taken to first order in perturbation theory, while the Fan term is the first order electron-phonon interaction taken to second order in perturbation theory.

To simplify this expression for $E_{n\mathbf{k}}(T)$, we can also take into account translational invariance. The energy takes its unperturbed value, $E_{n\mathbf{k}} = \varepsilon_{n\mathbf{k}}$, both when $\mathbf{u}_l = 0$ and when $\mathbf{u}_l$ is a constant independent of l (corresponding to a shift of the whole lattice). Requiring translational invariance to hold for corrections up to second order leads to

$$0 = \left[\frac{1}{2}\sum_l \langle n\mathbf{k}|\nabla_l\nabla_l V|n\mathbf{k}\rangle + \sum_{ll'}\sum_{n'\mathbf{k}'} \frac{\langle n\mathbf{k}|\nabla_l V|n'\mathbf{k}'\rangle \langle n'\mathbf{k}'|\nabla'_l V|n\mathbf{k}\rangle}{\varepsilon_{n\mathbf{k}} - \varepsilon_{n'\mathbf{k}'}}\right] \cdot \overline{\mathbf{u}_l\mathbf{u}_l}, \tag{4.5}$$

We can now rewrite the DW term in the same form as the self-energy correction [172] to give

$$E_{n\mathbf{k}}(T) = \varepsilon_{n\mathbf{k}} + \sum_{ll'}\sum_{n'\mathbf{k}'} \frac{\langle n\mathbf{k}|\nabla_l V|n'\mathbf{k}'\rangle \langle n'\mathbf{k}'|\nabla'_l V|n\mathbf{k}\rangle}{\varepsilon_{n\mathbf{k}} - \varepsilon_{n'\mathbf{k}'}} \cdot \left[\overline{\mathbf{u}_l\mathbf{u}_{l'}} - \overline{\mathbf{u}_l\mathbf{u}_l}\right]. \tag{4.6}$$

The self-energy term can have $n' = n$ and $n \neq n'$ (interband and intraband) transitions, while the DW term is cast in the form of interband transitions [172]. To avoid summation over a large number of empty bands, the Fan term can be reformulated using the Sternheimer equation and the resulting linear system can then be solved iteratively using the same techniques as in DFPT [177].

AHC theory relies on the so-called rigid-ion approximation (since the Hamiltonian used in its derivation depends on potentials generated individually by each atom). It should be noted that in the KS system, the Hartree and exchange-correlation potentials both depend on the electron density, the response of which to the displacement of one atom is affected by the other atoms in the system [171]. The potential term in the DFT Hamiltonian therefore cannot be expressed as a sum of individual atomic potentials. However, the rigid-ion approximation is still expected to work reasonably well in the KS system as a consequence of electronic screening [171].

AHC theory returns renormalised energy eigenvalues evaluated on a grid of **k**-points. To get the DOS with zero-point renormalisation or temperature-dependent corrections, we simply need to ensure that we have sampled a dense enough grid of these points and then use the renormalised eigenvalues in the standard DOS formula.

Ref. [171] studied the effect of ZPR on the electronic and superconducting properties of sulfur hydrides. They observed an enhancement of the DOS around the Fermi level for H_3S (and suppression for H_2S). To calculate a corrected T_c, they treated the renormalised electron energy dispersion as an input for the superconductivity calculations. The calculated shift in T_c was of the order of 10 K - an increase for H_3S and a decrease for H_2S [171]. We performed similar calculations to obtain both the ZPR and temperature dependence of the DOS for $Fm\bar{3}m$-LaH_{10} at 250 GPa. The Fan self-energy and the DW contributions were calculated with a random grid of transferred momenta using the YAMBO code [178, 179]. After performing convergence tests, we used a 30×30×30 **k**-point grid, 32 **q**-points and a 150 Ha cut-off to produce the final result shown in Fig. 4.15. Examining the DOS near the Fermi level, it is clear that taking the ZPR and temperature dependence of the DOS into account in this way could lead to a substantial change in the predicted superconducting properties for this system.

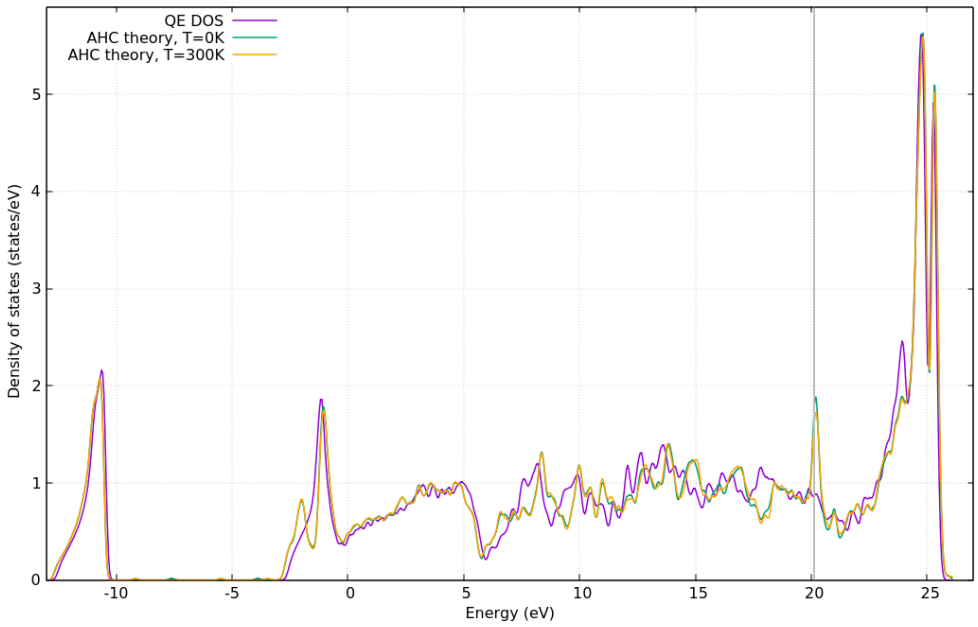

Fig. 4.15 The electronic DOS for $Fm\bar{3}m$-LaH_{10} at 250 GPa. The standard DOS was calculated with QUANTUM ESPRESSO, while the AHC-corrected DOS at 0 K and 300 K also used the YAMBO code. The Fermi energy is marked with a grey vertical line.

There is, however, a question of whether AHC theory is appropriate in light-atom systems at all; it breaks down for hydrogen [180] and Ref. [181] found that AHC theory was insufficient for studying electron-phonon coupling in the molecular crystals CH_4, NH_3, H_2O and HF. Quantitatively different results were also obtained for perturbative and non-perturbative methods when studying corrections to the thermal band gap in helium at terapascal pressures [182]. These previous findings suggest that AHC theory may not be suitable for hydrides and that an alternative approach, based on Monte Carlo sampling of the harmonic or anharmonic wavefunctions, may be needed.

4.4.2 Neglecting anharmonicity

Anharmonicity is an important effect to include in studies of light-atom systems if there are a number of phases very close together in energy or if some structures exhibit dynamic instabilities at the harmonic level. Both of these cases were seen in the solid hydrogen study of Chapter 3. However, the inclusion of anharmonicity when predicting T_c (although essential in cases such as palladium hydrides [75], which exhibit an inverse isotope effect due to anharmonicity, and aluminium hydrides [183], in which superconductivity may be entirely suppressed by anharmonicity) will not always be crucial. Depending on the purpose of the specific study, the determination of anharmonic corrections to T_c will often not be

worth the expense of the calculations given the number of other factors, as we have touched on here, that can lead to T_c corrections of a similar order of magnitude.

4.4.3 Impact on findings for high-pressure hydrides

We have seen that a number of different approximations used in standard superconductivity calculations, such as the ones performed in this Chapter, lead to errors in T_c of around 20-40 K for the sulfur hydride system. For some of these approximations, we have demonstrated that corrections of a similar magnitude may be seen for LaH_{10}. However, since these approximations are all expensive to include (even individually) and all result in similar errors in T_c, it is neither sensible nor feasible to attempt to adjust for them in a typical calculation. In fact, the superconductivity calculations presented earlier in this Chapter and in Chapters 5 and 6 would not have been feasible if it weren't for all of the approximations discussed here. Additionally, standard theoretical studies of hydride superconductors have been seen to give reasonable results in comparison to experiment. We have already seen that this is the case for cubic LaH_{10}.

Our focus in this Chapter and in the remainder of this thesis is on high-T_c materials for which T_c errors of $\sim$30 K would not particularly alarm us or affect our overall conclusions. These approximations therefore do not impact the findings of this thesis, but they are important to be aware of. There may be certain cases in which it is necessary to go beyond the standard treatment of superconductivity in order to capture the behaviour of a specific system.

4.5 Conclusions

We have identified a new hexagonal phase of LaH_{10} with $P6_3/mmc$ symmetry. Our calculations show a pressure-induced phase transition into this new phase from the cubic phase believed to be observed in experiment [160, 161]. The overall phase behaviour predicted within the harmonic picture is $C2/m \rightarrow Fm\bar{3}m \rightarrow P6_3/mmc$ with all three of these phases predicted to be high-T_c superconductors. However, making the assumption that the unstable modes can be neglected here gives the same picture as the anharmonic calculations of Ref. [159] where $Fm\bar{3}m$ is the true ground state at lower pressures. Neglect of these unstable $Fm\bar{3}m$ modes below 210 GPa in the calculation of T_c also produces results in good agreement with the two available experimental results. The new hexagonal phase predicted is metastable at lower pressures and therefore offers a direct explanation for the experimental observation of hcp impurities in Ref. [161]. We also examined and discussed the impact that a number of

approximations made in standard superconductivity calculations could have on the predicted superconducting properties of LaH_{10}.

We found that YH_{10} adopts very similar structures to LaH_{10}, with a structure of $P6_3/mmc$ symmetry again amongst the most energetically competitive candidates. Over the pressure range considered the $Fm\bar{3}m$/$R\bar{3}m$ phase remains the most stable. The difference in Gibbs free energy between these two structures is extremely small, meaning synthesis of a pure sample of either could be difficult. All four YH_{10} candidate structures studied here have $T_c >$ 200 K across the whole 300-550 GPa pressure range, with the highest critical temperature seen at the lowest pressures, making this composition an extremely desirable candidate for experimental synthesis. Other high-T_c Y-H stoichiometries have been synthesised in recent experiments [165].

We found the double-delta smearing parameter employed in superconductivity calculations to be of particular importance. Its effect on predicted T_c changes from system to system and varies slightly with pressure; in particular, in the calculations we present in this Chapter the default minimum smearing employed by QUANTUM ESPRESSO overestimates T_c for LaH_{10} by $\sim$20 K and YH_{10} by $\sim$30 K when compared to optimal smearing calculated by comparing **k**-point grids. It is crucial to determine an appropriate smearing value for your system in order to calculate a meaningful T_c within a DFT framework; this is an important lesson that we apply in our work going forward.

Chapter 5

Prediction of low-pressure hydride superconductors using machine learning

5.1 Motivation

As we have seen, metal hydrides are predicted to exhibit similar behaviour to highly compressed hydrogen and are therefore good candidates for conventional superconductivity [141, 184]. In recent years, the potential for superconductivity has been investigated in a huge variety of these systems - not just in rare-earth hydrides, as studied in Chapter 4, but in hydrides of elements from across the whole periodic table. Inspired by known superconductors, researchers have also attempted to increase T_c by chemical means; replacing atoms in known structures and assessing stability and superconductivity [97], doping known binaries with additional elements to make ternary hydrides [185], and even mapping out alchemical phase diagrams [186].

Recent experimental measurements of superconductivity in high-pressure hydrides have helped to address several misconceptions about conventional superconductivity, fuelling hope that it may be achieved at ambient temperature and thus waving a definitive farewell to the Cohen-Anderson limit [187]. The corresponding theoretical studies, such as the one presented in Chapter 4, have demonstrated that the crystal structures and superconducting properties of real materials can now be accurately predicted from first principles. This has led to huge growth in the field and encouraged an active dialogue between experimentalists and theorists.

Given the abundance of computed T_c values now available in the literature, rather than focusing again on individual systems, we now turn our attention to training a machine learning model for superconducting binary hydrides. Machine learning has previously been used in

modelling hydride superconductors, with a focus on predicting the maximum obtainable critical temperature for a given composition [188]. However, our aim here is rather different. On examination of the literature (see the circular points of Fig. 5.1), it becomes apparent that the ultimate pursuit of superconductivity close to ambient conditions is as much about reducing the required pressure as it is about increasing T_c. This is especially important given that working at high pressure can often present far greater experimental challenges than working at low temperature. We therefore model critical temperature and operational pressure on an equal footing, rather than treating the latter as an additional input as would traditionally be done. Our trained model can then be used to inform the choice of composition for crystal structure prediction and subsequent electron-phonon calculations, with the aim of extending the operational region of hydride superconductors towards ambient conditions.

Large parts of the work presented in this Chapter were published as Ref. [101]. As detailed in the Preface, M. J. Hutcheon and I chose model inputs and built the literature dataset together. M. J. Hutcheon trained and validated the machine learning model and extracted predictions. I performed structure searching calculations, constructed enthalpy plots, implemented Gaspari-Gyorffy theory, and tested two potential T_c ranking methods. M. J. Hutcheon then performed the final electron-phonon calculations.

5.2 Trends in superconducting hydrides

Despite limiting our focus here to binary hydrides, we find that a large amount of computational (and some experimental) data is available for these materials in the literature. The dataset we use in this Chapter was built from data collected from Refs. [147, 149, 150, 153, 155, 156, 157, 158, 159, 160, 161, 164, 165, 188, 188, 189, 190, 191, 192, 193, 194, 195, 196, 197, 198, 199, 200, 201, 202, 203, 204, 205, 206, 207, 208, 209, 210, 211, 212, 212, 213, 214, 215, 216, 217, 218, 219, 220, 221, 222, 223, 224, 225, 226, 227, 228, 229, 230, 231, 232, 233, 234]; the pressure-critical temperature (P-T_c) points for this dataset are plotted in Fig. 5.1. This literature dataset contains 222 points and covers 62 different non-hydrogen elements. The average number of hydrogen atoms per non-hydrogen atom in the dataset is 6.35 (with the full range being 1-16).

In certain groups of the binary hydrides, some observable material properties show a simple dependence on the properties of the non-hydrogen element. For example, in the alkaline earth hydrides, the van der Waals radius of the alkaline earth metal atom is well-correlated with the hydride's metallisation pressure [235]. However, obtaining strong electron-phonon coupling (while also maintaining some degree of stability) is a more complicated process; simple correlations between composition and critical temperature or operational

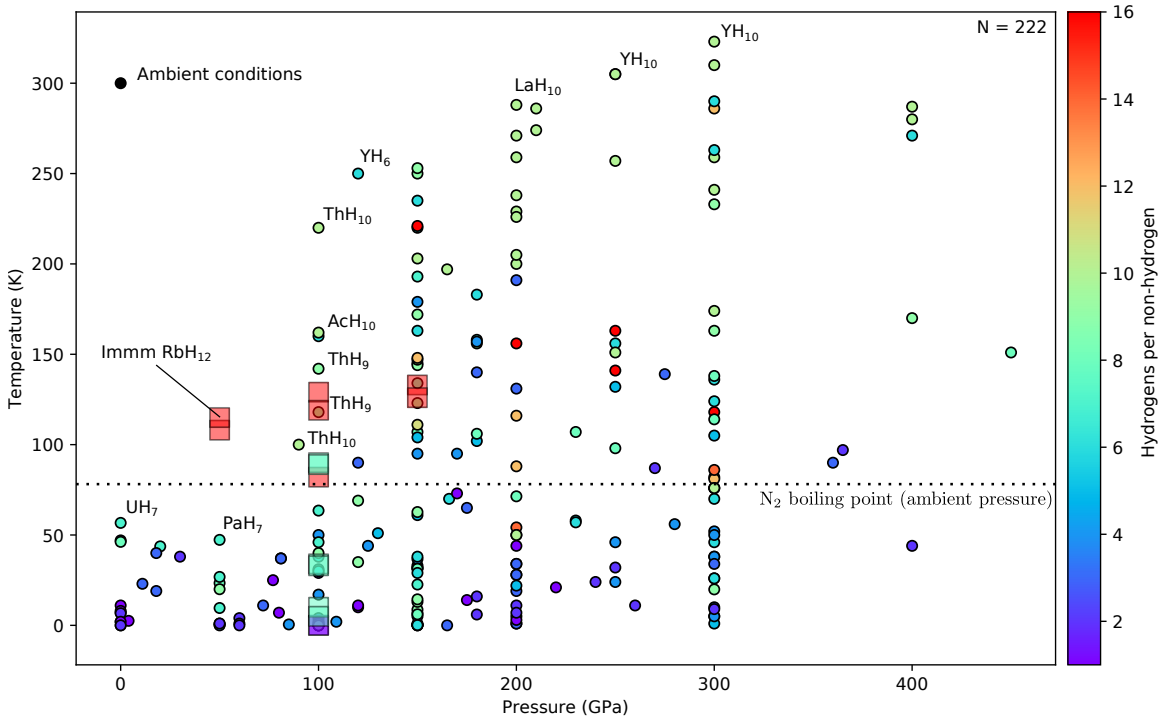

Fig. 5.1 Binary hydride critical temperatures collected from the literature, and forming our dataset, are shown as circles. Materials on the frontier towards ambient conditions are labelled. Multiple points labelled with the same stoichiometry arise from situations where T_c values are calculated for a particular phase at different pressures or for different structural phases with the same stoichiometry. We do not distinguish between these two situations here as the descriptors for our model only describe the composition and the atomic properties of the non-hydrogen element, not the material's geometric structure or symmetry. New structures found in this Chapter, with T_c values calculated using DFPT (as reported in Table 5.1), are shown as translucent squares; of particular note is *Immm*-RbH_{12} (see Fig. 5.8), which extends the frontier significantly towards ambient conditions compared to our dataset.

pressure are therefore absent in the dataset as a whole. In this Chapter, we examine more complicated trends by constructing a machine learning model of critical temperature and operational pressure, which takes a set of easily-obtainable material descriptors as input. For a particular element E and corresponding binary hydride EH_n, these descriptors are:

- hydrogen content (n)
- van der Waals radius of E
- atomic number of E
- mass number of E
- numbers of s, p, d, and f electrons in the electron configuration of E

Once constructed and trained, we apply the model to all materials with the chemical composition EH_n, where E is any element in the periodic table and $n \in [1,2,\ldots,32)$, to obtain T_c and P predictions. A maximum of 31 hydrogens per non-hydrogen atom was chosen to avoid over-extrapolation from the dataset (where the maximum n is 16). It is also highly unlikely that hydrides with a higher hydrogen content than this would be metallic in the lower pressure region we are interested in. For this large set of potential materials, the proximity of predicted superconductivity to ambient conditions then serves as a guide for our searches for new binary hydrides.

5.2.1 Neural network construction

We train a fully-connected neural network with the topology shown in Fig. 5.2 on the literature dataset shown in Fig. 5.1. The Keras frontend [236] to the Tensorflow machine-learning library [237] was used to construct and train the model. The squared absolute error between the predicted and literature values, $|(\Delta T_c, \Delta P)|^2$, served as a cost function and was minimised using the *Adam* stochastic optimiser [238]. The input (and expected output) data is positive definite and it therefore has a non-zero mean and cannot be normally distributed; we therefore used self-normalising activation functions [239, 240] to improve training behaviour. Despite encompassing a large portion of the available literature data, our dataset contains only 222 separate points, making it a rather small dataset for a machine learning project. The main consequence of this is that the risk of over-fitting becomes significant since the number of data points is comparable to the number of parameters in our network. To mitigate this risk, each time the model is trained the data is randomly partitioned into a validation set (consisting of 25% of the data points) and a training set (consisting of the remaining 75%). Once the model starts over-fitting to the training data, the validation set error starts to increase, allowing us to choose the model parameters from the training process for which the validation set error is minimal. We cross-validate the results by repeating this process of

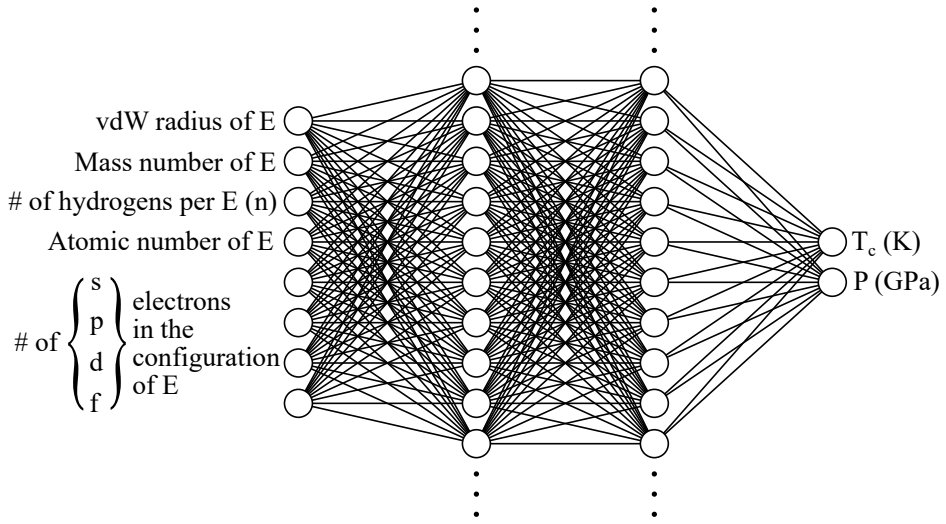

Fig. 5.2 Topology of our neural network model. The material descriptors for the hydride EH_n are each fed to one input node. This layer then feeds two densely-connected intermediate layers, each consisting of 32 nodes. The second of these then feeds the output layer which consists of one critical temperature node and one pressure node.

random partitioning and training 64 times and averaging the predictions (i.e., the T_c and P outputs) for each material considered. We also apply L_2-regularisation to the parameters in the intermediate dense nodes (achieved by including a penalty term in the cost function) to decrease the propensity for over-fitting and improve the convergence of this cross-validation scheme.

5.2.2 Assessing model behaviour and predictions

The basic behaviour of the machine learning model is shown in Fig. 5.3. From the panels on the left-hand side, we see that it achieves reasonable correlation with the literature values for both operational pressure and critical temperature. The panels on the right-hand side show that the model also predicts sensible pressures and critical temperatures for unseen materials, with maximum values and peaks which do not contradict what has been observed in hydrides previously (and what is reflected in our dataset).

To gain insight into which properties favour superconductivity closer to ambient conditions, we define a measure of distance $D = |(P, T_c - 293)| = \sqrt{P^2 + (T_c - 293)^2}$, where P is in GPa and T_c is in K. Despite these being different units for different observables, they are treated on an equal footing (and then combined) because the range of values they take across the spectrum of superconducting hydrides is very similar. From its definition, D is the distance from ambient conditions (taken here to be atmospheric pressure, $P_0 = 101$ kPa ~ 0 GPa, and room temperature, $T = 293$ K) and it clearly decreases as we move towards

ambient conditions from the pressure-temperature region containing the majority of the known hydrides in our dataset (see Fig. 5.1).

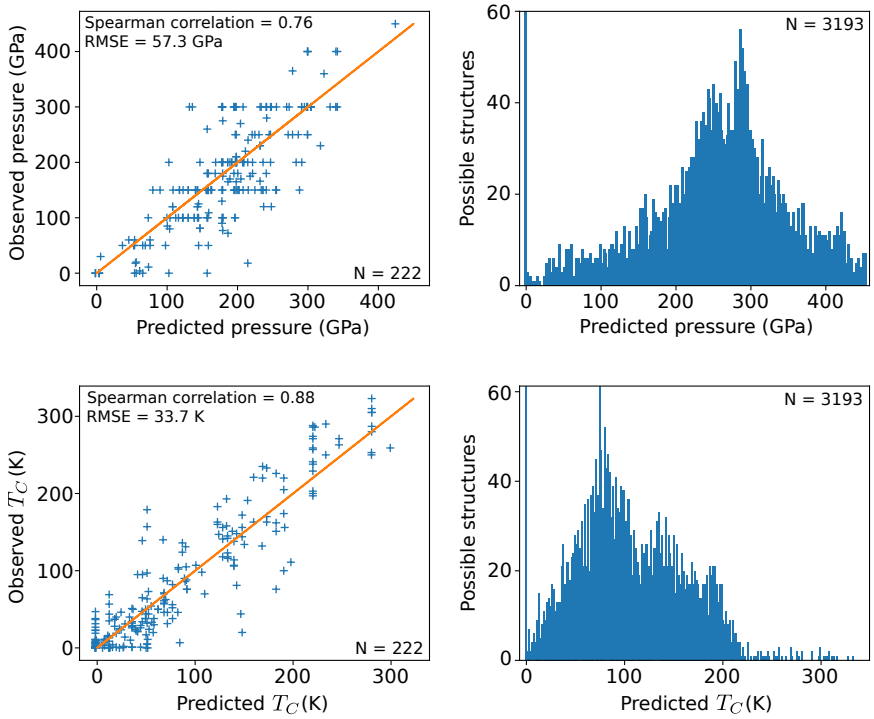

Fig. 5.3 Behaviour of our machine learning model of critical temperatures and associated operational pressures for binary hydrides. The left-hand panels show the correlation between the predicted and observed values for the structures in the literature dataset. The right-hand panels show the distribution of pressures and critical temperatures obtained when the model is applied to the set of all possible binary hydrides as defined in Section 5.2.

In Fig. 5.4, we plot the distribution of material properties for the 10% of hydrides predicted to exhibit superconductivity closest to ambient conditions (i.e., the 10% with lowest D according to our model). We can see that the model predicts the heavy alkali and alkaline earth metal hydrides to be the best candidates, with the number of close-to-ambient materials then decreasing as we go across each period. The distribution in terms of hydrogen content is more uniform, suggesting it is necessary to consider a range of different stoichiometries for each element. Both of these observations can be directly applied in our subsequent structure searches, allowing the model findings to guide our study. The conclusions reached here were reinforced by the construction of a simple linear regression model, which reproduced the general trends exhibited by the machine learning model (but, unsurprisingly, produced predictions with worse correlation with the literature values). The

predicted optimal (minimum D) hydride compositions from the machine learning model are shown for *each element* of the periodic table in Fig. 5.5.

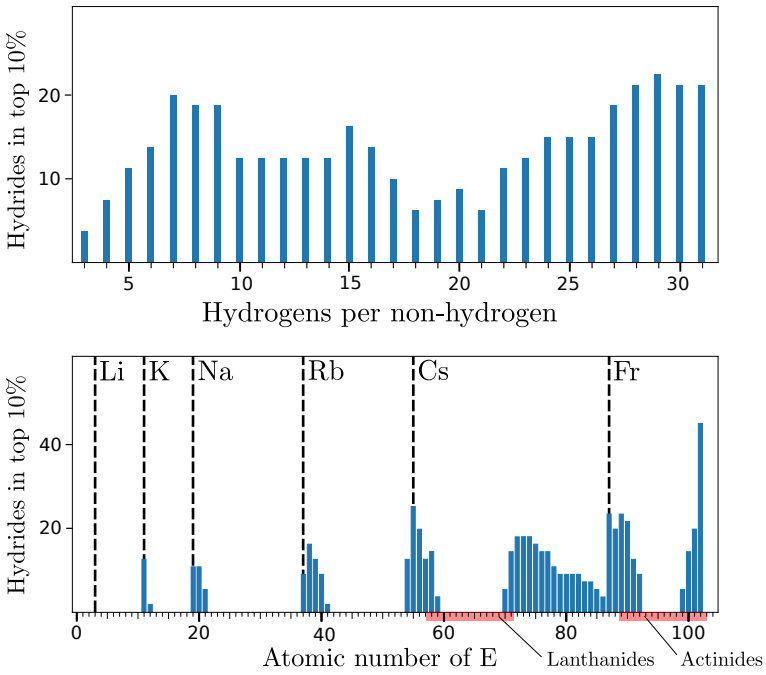

Fig. 5.4 Distribution of hydrogen content (number of hydrogen atoms per non-hydrogen atom, n) and atomic number of the non-hydrogen element for the 10% of hydrides predicted to exhibit superconductivity closest to ambient conditions (i.e., the 10% with lowest D according to our machine learning model). The black dashed lines indicate the atomic numbers of alkali metals.

We note that the points included in our dataset will be of varying quality, come from different research groups, and are of both experimental and theoretical origin. The majority are theoretical and calculated within the harmonic approximation, as will be used for all calculations of superconducting properties in this thesis. Although it has been shown that anharmonicity can have an impact on predicted T_c for hydrides [75, 241], these calculations are very expensive and there is insufficient data in the literature to build a model from anharmonic results. Since, here, we only seek to extract general trends to inform areas of focus for structure searching and will only be performing harmonic calculations ourselves, the dataset used is sufficient for our purposes.

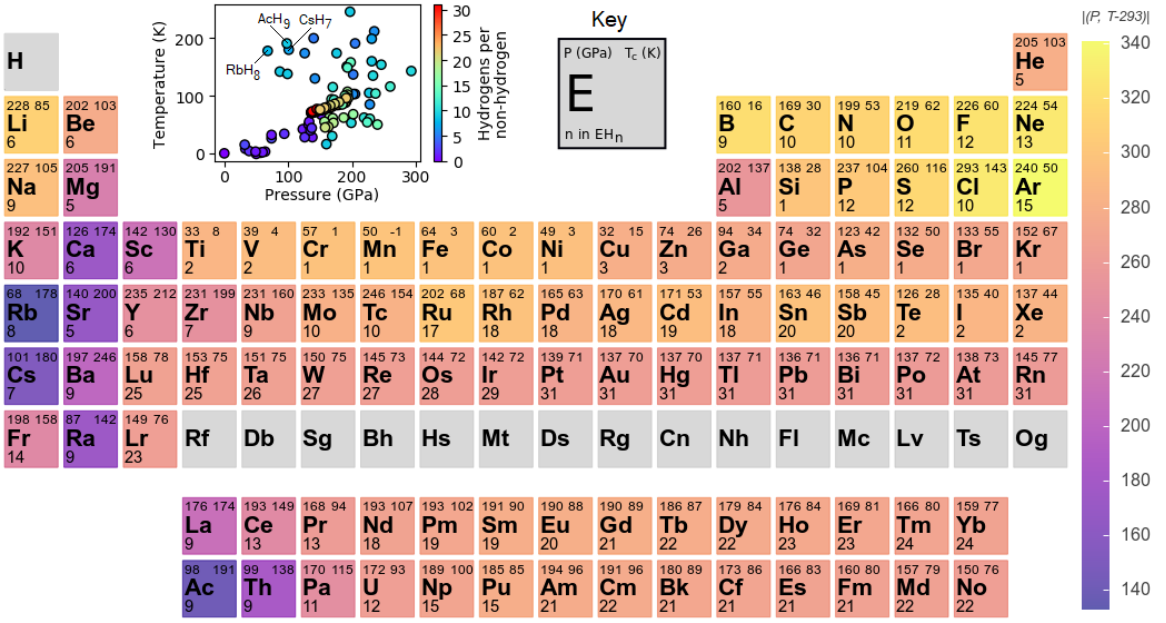

Fig. 5.5 The periodic table of optimal (minimum D) binary hydrides according to the predictions of our machine learning model. The predicted critical temperature, corresponding pressure and optimal hydrogen content is shown for each element. Elements are coloured according to the predicted distance from ambient-condition superconductivity, D. The inset shows the distribution in pressure-temperature space of these optimal predictions. We note that during the construction of the model we did not explicitly prevent the neural network from predicting negative critical temperatures and it does so for MnH. However, in general, the machine learning model has learned that critical temperatures should be positive, despite this lack of constraint, as can be seen from the lower right panel of Fig. 5.3.

5.3 Selection of candidate structures

5.3.1 Structure searching for promising compositions

The model constructed in this Chapter points towards the alkali and alkaline earth metal hydrides as some of the best candidates for superconductivity near ambient conditions. From these, we study caesium and rubidium hydrides in more detail; these systems were chosen both due to their predicted proximity to superconductivity at ambient conditions (see Figs. 5.4 and 5.5) and due to the fact that they had not been studied extensively in the past. Caesium and rubidium polyhydrides were studied using structure searching methods in Refs. [242] and [243], respectively, although potential superconductivity was not investigated in either case.

The structure searching calculations here were, again, performed using AIRSS and CASTEP. Since our model suggests that a wide range of stoichiometries should be considered, static-lattice convex hulls were constructed using AIRSS and qhull [168] in order to identify those which are stable or metastable at 50, 100 and 200 GPa. The PBE functional, CASTEP QC5 pseudopotentials, a 400 eV plane-wave cut-off and a **k**-point spacing of $2\pi\times0.05$ Å^{-1} were used in all searches.

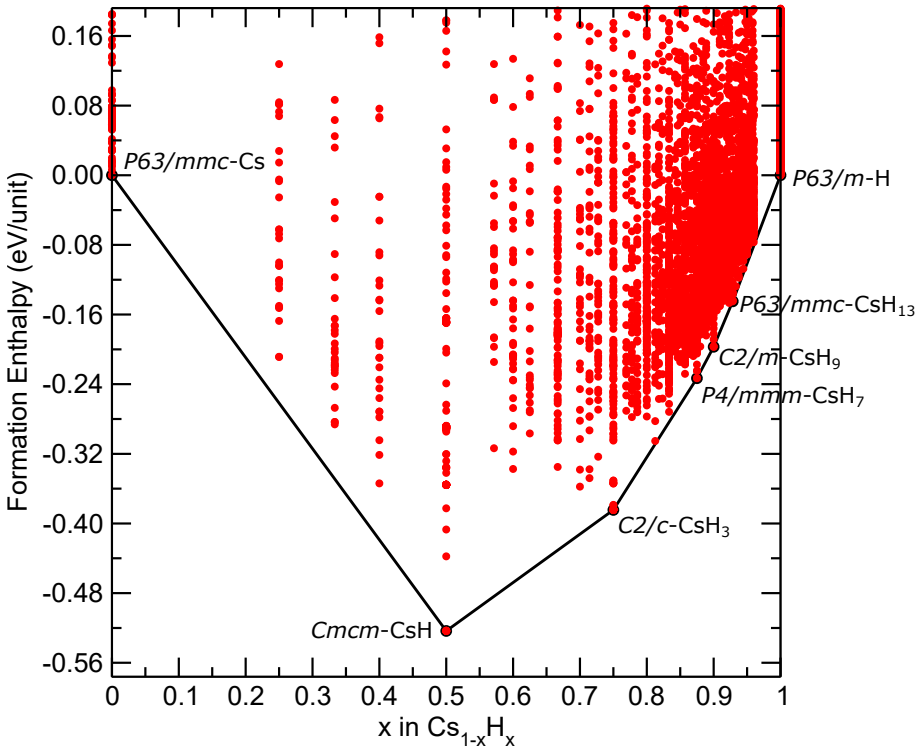

Fig. 5.6 Convex hull for Cs-H system at 50 GPa.

As shown in Fig. 5.6, CsH, CsH_3, CsH_7, CsH_9 and CsH_{13} are on the hull at 50 GPa. There are also many compositions that are very close to the hull at this pressure, including Cs_3H_{13}, CsH_{24}, CsH_{17}, CsH_{14}, CsH_{12}, and CsH_{15}. At 100 GPa, CsH, CsH_3, Cs_3H_{13}, CsH_7, CsH_{13} and CsH_{15} are on the hull; CsH_7 and CsH_{15} remain on the hull at 200 GPa, while CsH_{13} is found slightly above it. We also note that CsH_5 is on the hull at 200 GPa. Given this information, we chose to investigate the CsH_5, CsH_7, CsH_{13} and CsH_{15} stoichiometries further. The Cs-H convex hulls calculated here at 100 and 200 GPa both partially match with the hull calculated at 150 GPa in Ref. [242], suggesting agreement with previous results.

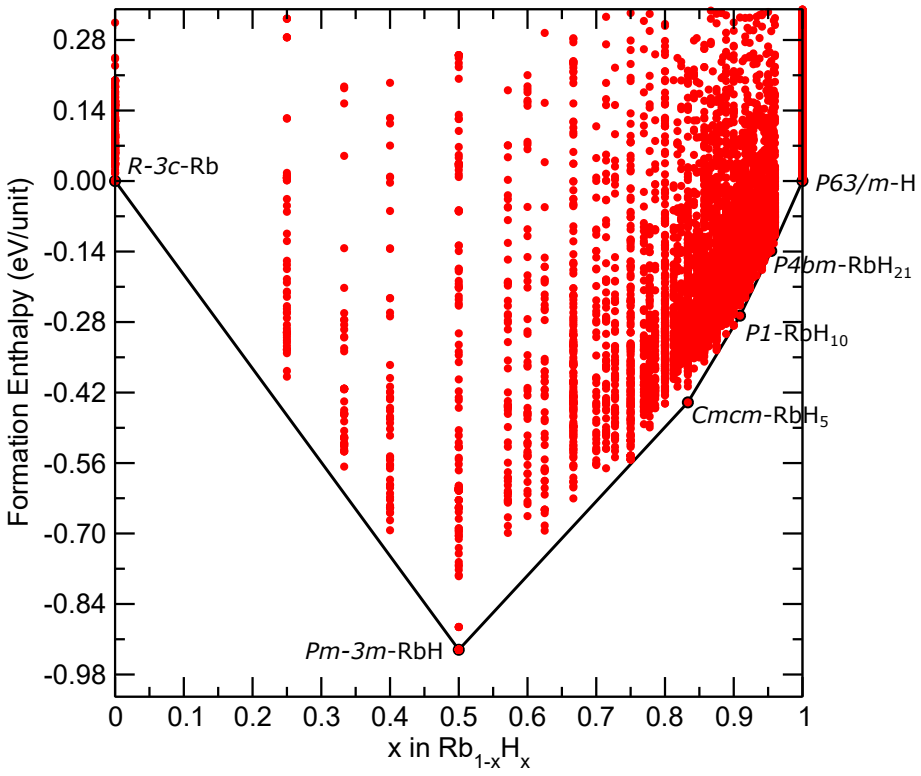

Fig. 5.7 Convex hull for Rb-H system at 50 GPa.

As shown in Fig. 5.7, RbH, RbH_5, RbH_{10} and RbH_{21} are on the hull at 50 GPa. There are also many compositions close to the hull at this pressure, including RbH_{16}, RbH_9, RbH_{23}, RbH_{19}, RbH_{17}, RbH_8, RbH_7, RbH_3, RbH_{14} and RbH_{12}. At 100 GPa, RbH, RbH_3, RbH_5, RbH_9 and RbH_{12} are on the hull. Then at 200 GPa, RbH_{12} is above the hull, but remains close to it, while RbH_5 and RbH_9 are found further away. RbH_3 and RbH_{11} are also on the hull at 200 GPa. We therefore chose to investigate the RbH_3, RbH_5, RbH_9, RbH_{11} and RbH_{12} stoichiometries further.

5.3.2 Enthalpy and metallicity

Additional, more extensive searches were carried out using AIRSS at 100 and 200 GPa for the selected stoichiometries using the same parameters and pseudopotentials as the original convex hull calculations. Between 5,000 and 10,000 initial structures were generated for each chosen stoichiometry at each pressure, with each structure containing between 1 and 3 formula units in its simulation cell. For each selected stoichiometry, the enthalpy was then calculated as a function of pressure (over a 25-225 GPa range) for the most competitive structures arising from these detailed searches. The geometry optimisations were performed using QUANTUM ESPRESSO [42, 43], the PBE functional, a 950 eV cut-off, scalar-relativistic

ultrasoft pseudopotentials downloaded from the QUANTUM ESPRESSO website, and a **k**-point spacing of $2\pi\times0.02$ Å^{-1}. The DOS at the Fermi energy, $N(E_F)$, was also evaluated for each structure at 50 GPa and 150 GPa in order to identify non-metallic structures which could be eliminated from further investigation. Using the results of these calculations, we were able to focus our efforts on structures which were both energetically competitive according to the enthalpy plots and had a considerable $N(E_F)$ value in the low-pressure region. The specific selection process is briefly described below in relation to the actual structures studied, while Appendix C contains the enthalpy plots and $N(E_F)$ values used to make these decisions. Enthalpy plots for the stoichiometries which were not considered further in this Chapter are contained in the Supplementary Material of Ref. [101].

Based on the initial DOS calculations, RbH_{12} was chosen as one of the most promising compositions as it has several metallic structures down to pressures of 50 GPa. The lowest enthalpy structures across the whole 25-225 GPa pressure range were ones of *Cmcm*-2, *Cmcm*-3, $C2/m$-1, *Immm*-1 and *Immm*-2 symmetry, where the number following the space group indicates the number of formula units in the unit cell. On refining the structures, *Cmcm*-3 reduced to the structure with 2 formula units and similar behaviour was seen between the two *Immm* structures - this meant the two larger cell structures could be automatically eliminated from consideration. All of the remaining structures were metallic at 50 GPa according to the initial DOS calculations and subsequent electron-phonon calculations were therefore performed for all of them.

According to the initial DOS calculations, CsH_7 was also a promising stoichiometry. The enthalpy plot showed that *Imm*2-2, $I4/mmm$-2, *Cm*-3, *P*4*mm*-2 are competitive at $P < 90$ GPa and *I*4*mm*-1, *P*1-3, $Cmc2_1$-2, *I*4*mm*-2 are competitive at slightly higher pressures. Electron-phonon calculations were therefore performed for the majority of these structures.

Next, we considered RbH_3. Ignoring the most energetically unfavourable structures at the static-lattice level, we were left with $I4_1/amd$-2, $C2/c$-2, *Cmmm*-1, *Cccm*-2, $P2/m$-3, $P6_222$-3 and *Pmma*-2. However, $I4_1/amd$-2 and $C2/c$-2 were not metallic, meaning they were eliminated from consideration. Due to the expensive nature of electron-phonon calculations, it was only possible to study a small selection of the remaining structures further.

5.4 Superconducting properties

Electron-phonon calculations were performed for the selected structures of RbH_{12}, CsH_7, and RbH_3 at pressures between 50 and 150 GPa. As in Chapter 4, we calculated the electronic Kohn-Sham eigenvalues, phonon frequencies, and electron-phonon coupling strengths in QUANTUM ESPRESSO, using DFPT where appropriate. The electron-phonon Hamiltonian

was treated within Migdal-Eliashberg theory and we solved the Eliashberg equations using the ELK code to obtain T_c. To carry out these calculations, we used the PBE functional, the same ultrasoft pseudopotentials as in the geometry optimisations, an 820 eV plane-wave cut-off, and a **q**-point grid with a spacing of $\sim 2\pi \times 0.1$ Å^{-1} (corresponding to a $2 \times 2 \times 2$ grid for a 26-atom unit cell of RbH_{12}). We used the same method as in Chapter 4 to determine the optimal double-delta smearing width.

The results of these calculations are shown in Table 5.1. We note that some rather high T_c values are obtained even at these low pressures, indicating that using our model to guide structure searching directions has been successful.

Stoichiometry	Space group	Pressure (GPa)	T_c (K)
RbH_{12}	$C2/m$	50	108
RbH_{12}	$C2/m$	100	129
RbH_{12}	$C2/m$	150	133
RbH_{12}	$Cmcm$	100	82
RbH_{12}	$Immm$	50	115
RbH_{12}	$Immm$	100	119
RbH_{12}	$Immm$	150	126
CsH_7	$P1$	100	90
CsH_7	$I4mm$	100	34
CsH_7	$P4mm$	100	33
CsH_7	$I4/mmm$	100	10
CsH_7	Cm	100	5
CsH_7	$Cmc2_1$	100	89
RbH_3	$Pmma$	100	0
RbH_3	$Cmmm$	100	0

Table 5.1 Critical temperatures calculated using DFPT for structures found in this Chapter using AIRSS. The structures are available in an online repository [244]. The data in this Table is also plotted in Fig. 5.1 for comparison with our literature dataset.

The highest T_c results arise from structures with a cage-like arrangement of hydrogen atoms surrounding a central non-hydrogen element. The electronic states that originate from these cages are near the Fermi level and are strongly coupled by cage vibrations. Combined with a high average phonon frequency, owing to the light mass of the hydrogen atoms, this results in a high critical temperature. This can be seen directly by looking at the Eliashberg function, shown in Fig. 5.8, for two illustrative structures from Table 5.1. The enhanced high-frequency portion of the Eliashberg function for the high-T_c cage-like $Immm$-RbH_{12}

structure is apparent. In contrast, strong electron-phonon coupling is absent at high phonon frequencies for states near the Fermi level in the layered *Pmma*-RbH_3 structure, leading to a negligible T_c. A negligible T_c is also predicted for *Cmmm*-RbH_3. While it may be disappointing that our model can lead us to structures such as these, it is unsurprising that it suggests some potentially undesirable compositions. As noted before, the descriptors that serve as inputs for our model do not provide any information about the specific structure or atomic arrangement and the model is trained on mostly cage-like structures as these have typically given the highest T_c results in the past (and are therefore over-represented in the literature). As a result, the model may implicitly assume that compositions it is given will behave as if they adopt favourable, perhaps cage-like, arrangements, leading to an overestimation of T_c in cases where this is not true. Despite this, we do find a number of relatively high-T_c superconductors; of these *Immm*-RbH_{12} is one of the stand-out structures due to its predicted location in Fig. 5.1.

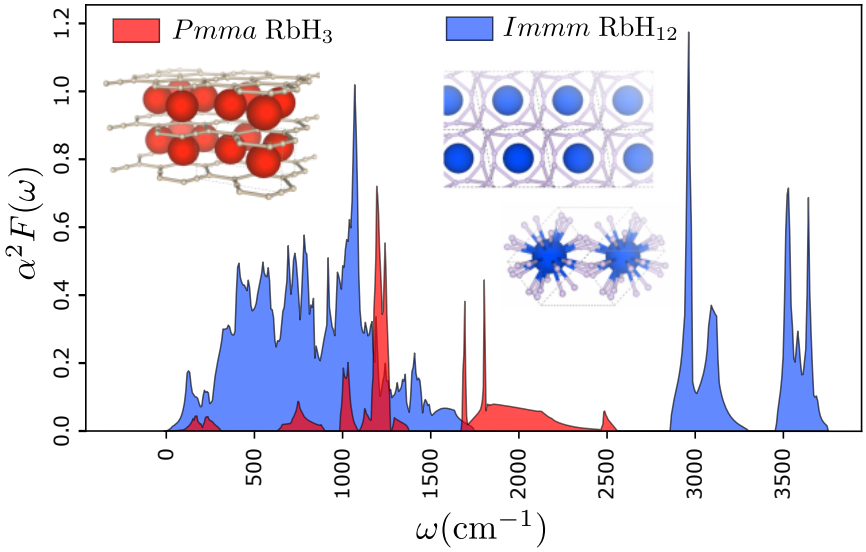

Fig. 5.8 The Eliashberg function for *Immm*-RbH_{12} and *Pmma*-RbH_3. The enhanced high-frequency part of the Eliashberg function for *Immm*-RbH_{12}, arising from the hydrogen cage, is clear. In contrast, the Eliashberg function for the layered RbH_3 structure does not extend to such high frequencies.

It is clear that supplementing structure searching techniques with predictions from machine learning has allowed us to efficiently target novel regions of pressure-temperature space. We have been able to identify low-pressure hydride superconductors with reasonable T_c values without having to perform a large number of expensive electron-phonon calculations. It can be seen from Fig. 5.1 that the hydrides predicted in this Chapter are biased towards ambient conditions when compared to the dataset as a whole. Some of our best predicted

structures even extend the frontier seen in this plot towards ambient conditions. Our findings also highlight the importance of considering stoichiometries which lie slightly above the static-lattice convex hulls. Although CsH_7 is found on the hull at both 50 and 100 GPa, our star stoichiometry RbH_{12} lies slightly above the hull at 50 GPa (the pressure where it strongly influences the P-T_c frontier). Stoichiometries which lie above the static-lattice hull may be stabilised by vibrational effects or may remain metastable (and still accessible in experiment) once these are included. Our results also demonstrate that T_c values can vary significantly between different structures of the same stoichiometry; we will begin developing methods that take this effect into account in Section 5.5.

5.5 Potential critical temperature ranking techniques

Motivated by the large T_c differences that can be observed even within a fixed stoichiometry, we next tested two potential methods for cheaply estimating T_c ordering between structures of the same stoichiometry at the same pressure. Good superconductivity in hydrides generally requires hydrogenic states close to the Fermi level, which (as exemplified by the findings of this Chapter) can often mean favouring cage-like structures and avoiding structures with molecular-character hydrogen units (there are, of course, some exceptions [245], particularly when charge transfer to molecular hydrogen has occurred). The first quantity we test is therefore the hydrogen-derived (or "projected") DOS normalised by the total DOS at the Fermi energy, $N_H(E_F)/N(E_F)$. The second quantity we test, on the basis that most of the coupling in hydrides tends to arise from the hydrogen atoms and that different structures of the same stoichiometry tend to have similar average phonon frequencies, is the hydrogen-derived electron-phonon coupling estimate from Gaspari-Gyorffy theory, η_H. This theory is explained in Section 2.6 and was implemented in the ELK code [89] for this work.

To test whether these two quantities provide a method for cheaply ranking structures, we performed a number of preliminary tests on structures available in the literature (see results in Table 5.2). Comparing our calculated η values for H_3X (X=S, As, Se, Br, Sb, Te and I) to those in Ref. [97] allowed a rough validation of our implementation of GG theory. The other test cases chosen were various structures of LaH_{10} and YH_{10} found in Chapter 4 [163], $I4/mmm$-FeH_5 [170, 216] and $Im\bar{3}m$-YH_6 [150, 165]. Using η_H to rank the various LaH_{10} and YH_{10} structures, we arrive at $Fm\bar{3}m > P6_3/mmc > C2/m$ for LaH_{10} and $Fm\bar{3}m > Cmcm > P6_3/mmc$ for YH_{10}. Full agreement with the calculated T_c order of Chapter 4 is therefore seen in both cases, while $N_H(E_F)/N(E_F)$ predicts a slightly incorrect ordering for LaH_{10}. An extremely low η_H is calculated for $I4/mmm$-FeH_5, indicating that this material will not be a good superconductor - a result reflecting the high-quality T_c

calculations of Ref. [170]. We also observe high η_H and $N_H(E_F)/N(E_F)$ values for the $Im\bar{3}m$-YH_6 structure, suggesting a high T_c, which is in agreement with recent experiment work [165].

Structure	P/GPa	η_H (eV/Å^2)	$N_H(E_F)/N(E_F)$	T_c/K
$Fm\bar{3}m$-LaH_{10}	250	5.58906	0.28996	234-259 [163]
$P6_3/mmc$-LaH_{10}	250	5.45099	0.29676	224-250 [163]
$C2/m$-LaH_{10}	250	4.48316	0.28758	205-228 [163]
$Fm\bar{3}m$-YH_{10}	400	11.45718	0.32971	247-282 [163]
$Cmcm$-YH_{10}	400	10.49255	0.29863	233-270 [163]
$P6_3/mmc$-YH_{10}	400	9.85728	0.30800	223-262 [163]
$Im\bar{3}m$-YH_6	160	4.44873	0.34787	223-247 [163]
$I4/mmm$-FeH_5	150	0.05468	0.04091	33.6-45.8 [216] or $\leq$1 [170]
$C2/m$-RbH_{12}	50	0.90524	0.15568	108
$C2/m$-RbH_{12}	100	1.45034	0.18652	129
$C2/m$-RbH_{12}	150	1.97268	0.20542	133
$Cmcm$-RbH_{12}	100	1.21876	0.17611	82
$Immm$-RbH_{12}	50	0.92471	0.15554	115
$Immm$-RbH_{12}	100	1.45016	0.18709	119
$Immm$-RbH_{12}	150	2.02193	0.20732	126
$Cmc2_1$-CsH_7	100	0.78707	0.15403	89
$I4mm$-CsH_7	100	0.78877	0.15737	34
$I4/mmm$-CsH_7	100	0.00753	0.19421	10
$P1$-CsH_7	100	0.77077	0.15734	90
$P4mm$-CsH_7	100	0.53524	0.21268	33
Cm-CsH_7	100	0.57309	0.21174	5
$Cmmm$-RbH_3	100	0.24435	0.14831	0
$Pmma$-RbH_3	100	0.28952	0.11262	0

Table 5.2 Testing the ability of two quantities, η_H and $N_H(E_F)/N(E_F)$, to rank binary hydride structures of the same stoichiometry at the same pressure in terms of T_c.

The structures found in this Chapter provide us with additional test cases; we calculated $N_H(E_F)/N(E_F)$ and η_H values for the various final RbH_{12}, CsH_7 and RbH_3 structures. These results are given, alongside their DFPT T_c values, in Table 5.2. η_H correctly predicts the T_c ordering for the RbH_{12} structures at fixed pressure and $N_H(E_F)/N(E_F)$ also comes close to doing so. A number of CsH_7 structures have promising $N_H(E_F)/N(E_F)$ and η_H values,

in particular $Cmc2_1$-2, $I4mm$-1 and $P1$-3. Unfortunately, $N_H(E_F)/N(E_F)$ appears to be less predictive for the CsH_7 structures and the performance of η_H was also mixed. The screening methods did correctly identify $Cmc2_1$-2 and $P1$-3 as two of the best candidates, however. The use of these quantities for structure ranking therefore shows promise, but needs to be developed further.

5.6 Conclusions

Having identified the need to reduce the operational pressure of hydride superconductors, we searched for crystal structures that could exhibit superconductivity in novel regions of pressure-temperature space. We found that guiding structure searching techniques using a machine learning model allowed us to efficiently target regions closer to ambient conditions. Several systems were identified as promising in this regard; here we focused on Cs and Rb hydrides. Other promising candidates according to our model included Ca, Sr, Ba, Ra, Ac, Th, La and Sc hydrides, most of which had already been theoretically studied to some extent [147, 155, 156, 158, 169, 194, 195, 203, 223, 229, 246, 247]. Of note in our results, a T_c of up to 115 K was calculated for RbH_{12} at 50 GPa, which represents a significant extension towards ambient-condition superconductivity compared to our literature dataset. We also identified and tested two physically motivated parameters, aimed at ranking hydride structures of the same stoichiometry at the same pressure in terms of superconducting ability.

Chapter 6

High-throughput discovery of high-temperature superconductors

6.1 Motivation

A huge number of binary hydrides from across the periodic table have been studied theoretically by groups around the world, with these results utilised in Chapter 5. An extensive study of these materials aiming to identify as many high-T_c candidates as possible is, however, still missing. Papers in this field often tend to present results for just one or two systems over a limited pressure range. The reason for this is two-fold. Firstly, electron-phonon calculations, used to determine T_c, are very computationally expensive. Coupled with this, a huge variety of hydride stoichiometries and structures are either stable or metastable under pressure, even when the discussion is limited solely to binaries (of the form X_nH_m). This means that exhaustive theoretical investigation of this class of materials is a huge challenge. The second part of the problem is therefore that it is not necessarily clear *before* performing expensive calculations which of these numerous candidates might be most promising.

We aim to provide a solution to this two-part problem here, firstly through optimisation of an existing electron-phonon code to reduce the underlying cost of the calculations and secondly by designing a screening protocol to identify good candidates arising from structure searching. The work presented in Chapter 5 (published as Ref. [101]) indicated that the hydrogen-derived electron-phonon coupling estimate from Gaspari-Gyorffy theory, η_H, and the hydrogen-derived DOS normalised by the total DOS at the Fermi energy, $N_H(E_F)/N(E_F)$, may provide a reasonable T_c ranking for structures of the same stoichiometry at the same pressure. We build on these ideas to design our screening approach and construct a high-throughput workflow for conventional superconductivity in hydrides. This allows us to

conduct one of the most comprehensive studies of superconductivity in the binary hydrides ever performed.

Parts of the work presented in this Chapter have been submitted for publication and are available to read online [248]. As detailed in the Preface, C. J. Pickard performed all structure searching. I screened the resulting structures, first based on stability, then based on the predictions of a T_c model built from physically motivated parameters. I calculated the necessary descriptors for a large number of literature structures, constructed, trained and validated the T_c model, and made predictions for structures found in our searches. M. J. Hutcheon optimised code and performed electron-phonon calculations. I fed these results back into the model, so that it was updated iteratively. I also devised and tested the two geometry-based screening methods presented at the end of this Chapter.

6.2 Methodology

6.2.1 Physically motivated descriptors

In Chapter 5, we briefly examined the ability of two quantities, η_H and $N_H(E_F)/N(E_F)$, to predict T_c ordering between structures of the same stoichiometry at the same pressure. The Gaspari-Gyorffy (GG) electron-phonon coupling estimate, η, was thought to be useful in this regard because it directly links to the estimated coupling constant, λ, via Eq. 2.119. In particular, the hydrogen component of the GG coupling estimate, η_H, was selected as the potential ranking quantity due to the ease of its calculation and the overall impact it should have on λ and the final T_c. From the form of Eq. 2.120, with atomic mass in the denominator, it is clear that the hydrogen atoms may provide a considerable fraction of λ, even if the Hopfield parameter of the other atom type is similar in magnitude [97]. Adding to this effect, the materials we investigate often have high hydrogen content and Ref. [249], which studied hydrides of the form H_nX, found that even though the non-hydrogen atom can provide 15-25% of λ, coupling from this atom enhances T_c by 3% at best.

As explained in Chapter 5, the second quantity examined there was also selected for physically motivated reasons. Linked to the success of cage-like structures in generating high T_c values, it is the states near the Fermi level which couple to the vibrational degrees of freedom to produce conventional superconductivity and it is beneficial if these states are derived from the light hydrogen atoms. The hydrogen-derived DOS normalised by the total DOS at the Fermi energy, $N_H(E_F)/N(E_F)$, may therefore give some indication of whether a particular hydride structure will exhibit high-T_c superconductivity.

In order to investigate these two quantities further, we constructed a set of 160 binary hydride structures (of the form X_nH_m where X is a non-hydrogen atom) and corresponding T_c values from the literature, collected from Refs. [101, 151, 153, 154, 163, 169, 170, 188, 190, 191, 194, 195, 197, 199, 200, 202, 203, 206, 211, 212, 213, 217, 219, 221, 224, 226, 227, 233, 241, 247, 250, 251, 252, 253, 254, 255, 256, 257, 258, 259, 260, 261, 262, 263, 264, 265]. This literature set differs in size from the one used in Chapter 5 since only entries for which the structure file was provided by the authors could be included in this study. Where the structure was not given at the same pressure as T_c was reported, the structure was relaxed at the correct pressure using CASTEP [41]. Refs. [142, 143, 144, 246] and the data tables within were found to be helpful for identifying additional points to include in the literature set. For each of these structures, η_H and $N_H(E_F)/N(E_F)$, as well as the X-derived GG electron-phonon coupling estimate, η_X, were calculated using our modified version of ELK from Chapter 5. We first test to see how well each of these quantities correlates with T_c (see Figs. 6.1, 6.2, and 6.3).

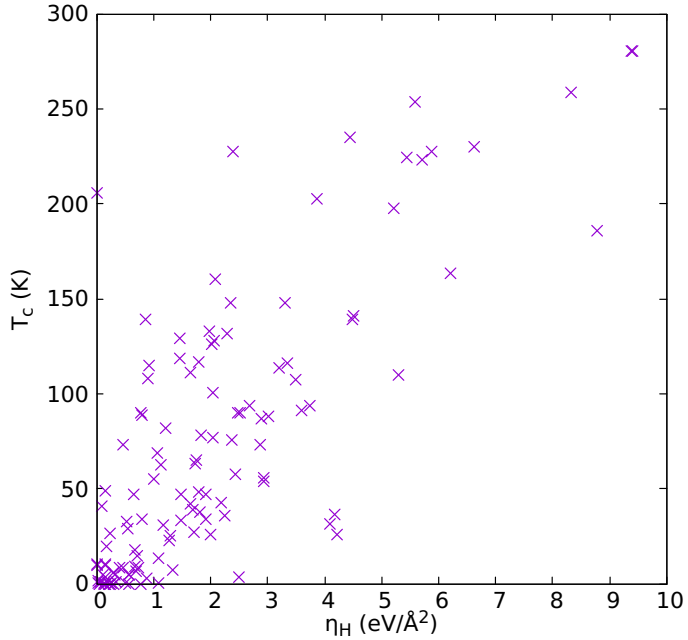

Fig. 6.1 η_H plotted against T_c for the literature set - correlation: 0.7876

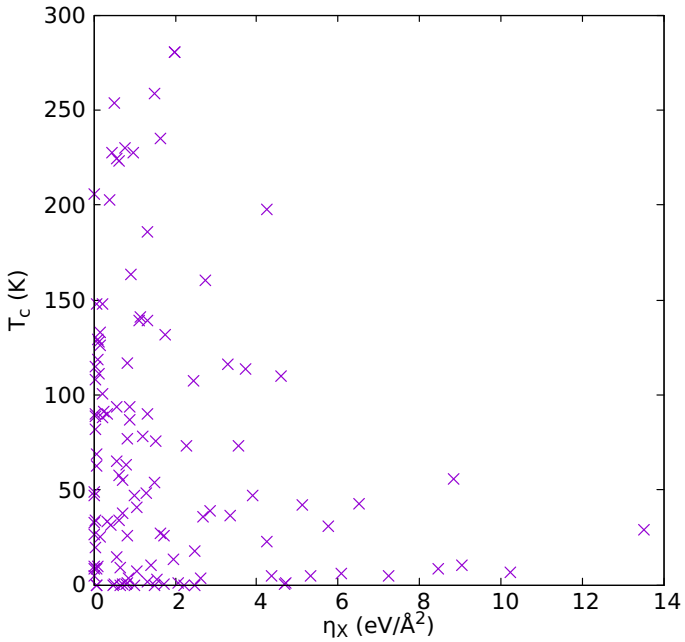

Fig. 6.2 η_X plotted against T_c for the literature set - correlation: -0.2001

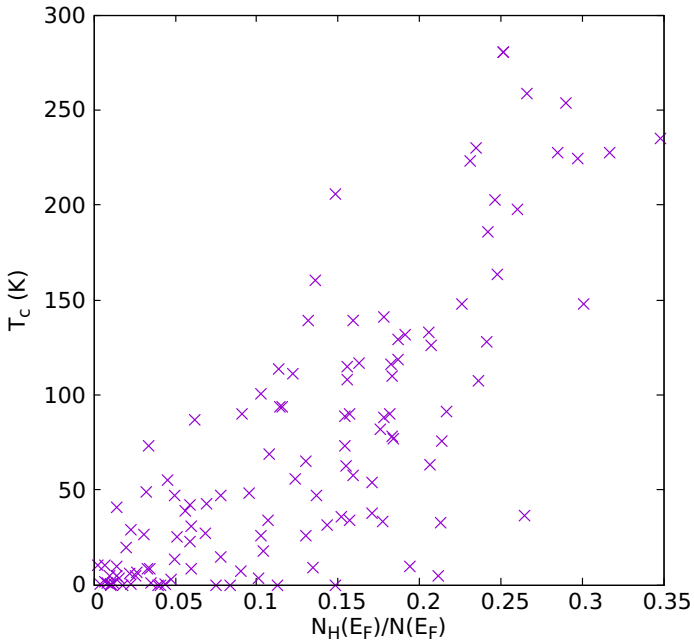

Fig. 6.3 $N_H(E_F)/N(E_F)$ plotted against T_c for the literature set - correlation: 0.7863

The traditional way to use η values is to calculate the average phonon frequency and use this to estimate λ from Eq. 2.119, which in turn can be used to obtain T_c from the McMillan or Allen-Dynes equations. However, the required phonon calculation means

that this approach would not be useful in a high-throughput screening scenario. Given the breadth of structures contained in the literature set, it is therefore encouraging to see a high correlation between η_H and T_c as it means we may be able to use η_H itself. It is clear that η_X is much less predictive than η_H, as expected from the reasoning above. $N_H(E_F)/N(E_F)$ is also well-correlated with T_c. In order to determine whether η_H and $N_H(E_F)/N(E_F)$ provide complementary information, we plot one against the other and calculate the correlation (see Fig. 6.4).

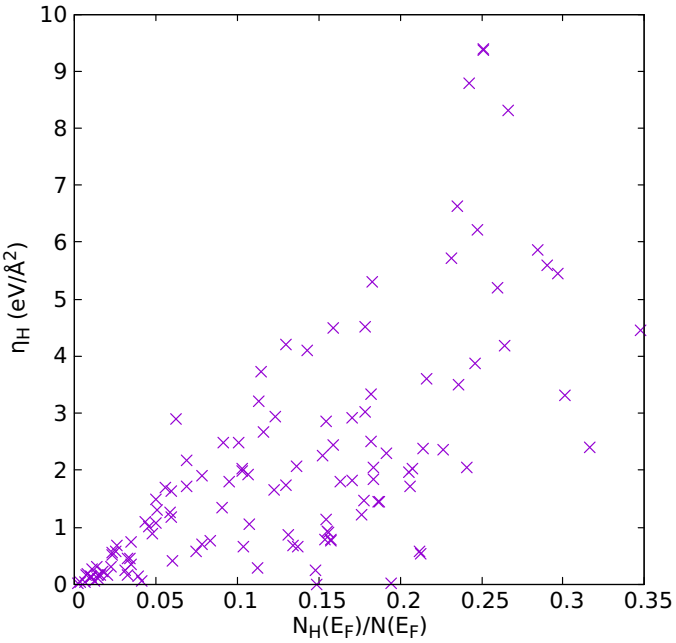

Fig. 6.4 $N_H(E_F)/N(E_F)$ plotted against η_H for the literature set - correlation: 0.6989

A correlation of just under 0.7 between η_H and $N_H(E_F)/N(E_F)$, coupled with the fact that the most obvious outliers in Figs. 6.1 and 6.3 are not associated with the same structures, suggests that these two quantities may complement one another. The best course of action is therefore to combine them into a regression model for T_c, which can be trained initially on the literature set considered here. The descriptors for the model will be η_H, η_X and $N_H(E_F)/N(E_F)$, along with the mass of atom X in atomic units (M_X) and the total DOS at the Fermi level ($N(E_F)$). M_X is used because it appears in the denominator of the expression for λ and might indirectly provide information related to the average phonon frequency too. $N(E_F)$ is included to help prevent over-estimation of predicted T_c for structures that are non-metallic or only weakly metallic (since such structures will have artificially enhanced η_j and $N_H(E_F)/N(E_F)$ values). Once trained, this model can be used to make T_c predictions for unseen structures arising from structure searching. A full discussion of the model's type,

as well as details about how it is trained and validated will be given in Section 6.2.2, while a description of how the model is used in our so-called training phase will be given in Section 6.2.3.

6.2.2 Calculation details: searching, regression, and superconductivity

Initial structure searching

The structure searching calculations in this Chapter were performed using AIRSS and CASTEP. The PBE functional, CASTEP QC5 pseudopotentials, a 340 eV plane-wave cut-off and a **k**-point spacing of $2\pi\times0.07$ Å^{-1} were used. For the initial "training" stage (described in Section 6.2.3), which investigated binary hydrides from across the whole periodic table, sp-AIRSS [54] was utilised and structures with 8-48 symmetry operations were generated. This served the dual purpose of (1) reducing the computational cost of the searches and subsequent calculations during the training phase, and (2) allowing us to explore high-symmetry structures (which may be metastable or stabilised at non-zero temperatures). For each element, X, in the periodic table, a convex hull was produced at 10, 100, 200, 300 and 500 GPa in order to assess the stability of binary hydrides of the form X_nH_m (in all searches, $n = 0-4$, $m = 0-24$ and each initial simulation cell contained between 1 and 4 formula units). Structures on or near these static-lattice convex hulls were then selected for further investigation at the pressure of interest. In order to discuss stability more clearly, it is important to recognise that there are two quantities to consider: the distance of the given stoichiometry from the static-lattice convex hull, E_{stoic}, and the distance of the given structure from the lowest energy structure of the same stoichiometry, E_{struc}. In the training phase, stoichiometries within 80 meV/formula unit (f.u.) of the hull were selected and, for each of these stoichiometries, just the lowest energy structure was chosen. We are therefore selecting structures with $E_{stoic} \leq 80$ meV/f.u. and $E_{struc} = 0$ here.

Gaussian process regression

We must make a choice about how to construct a regression model for T_c; Gaussian process regression (GPR) provides us with a Bayesian approach. GPR has the benefit of working well on small datasets and also provides uncertainty measurements on the resulting predictions [266], both of which are important considerations in this Chapter. Other machine learning approaches, such as the one used in Chapter 5, learn exact values for every parameter appearing in the given function or network, whereas a Bayesian approach instead obtains a probability distribution over all possible parameter values [266].

Following Ref. [267], we can describe GPR in either a weight-space view or a function-space view. We will discuss the former first. The weight-space view concepts are easiest to demonstrate by starting with a linear system, $f(\mathbf{x}) = \mathbf{x}^T\mathbf{w}$, where $\mathbf{x}$ is the input vector and $\mathbf{w}$ is the vector of parameters. We add a noise term to $f(\mathbf{x})$ to obtain the final function y, although we do not explicitly consider this term here. Bayes' rule tells us

$$p(\mathbf{w}|\mathbf{y},X) = \frac{p(\mathbf{y}|X,\mathbf{w})p(\mathbf{w})}{p(\mathbf{y}|X)}, \tag{6.1}$$

where the notation $p(a|b)$ means the probability of a given b. In this expression, the posterior, $p(\mathbf{w}|\mathbf{y},X)$, describes what we know about the parameters in our function and the prior, $p(\mathbf{w})$, describes our knowledge of the parameters before the training data has been considered. $p(\mathbf{y}|X,\mathbf{w})$ is the likelihood and the denominator (which simply acts as a normalising constant and is calculated as $p(\mathbf{y}|X) = \int p(\mathbf{y}|X,\mathbf{w})p(\mathbf{w})d\mathbf{w}$) is the marginal likelihood. Predictions for an unseen point of interest can be obtained by calculating the *predictive distribution* by weighting all possible predictions by their calculated posterior,

$$p(f^*|x^*,\mathbf{y},X) = \int_w p(f^*|x^*,\mathbf{w})p(\mathbf{w}|\mathbf{y},X)d\mathbf{w}. \tag{6.2}$$

In GPR, the prior and the likelihood are assumed to be Gaussian so that the integration is tractable [266]. Under this assumption, we obtain a Gaussian predictive distribution as the result - from this we can obtain a single point prediction from the distribution's mean and quantify uncertainty using its variance. However, it is clear that a linear model will not always be appropriate and will prove very limited. A way to overcome this problem is to first project the inputs into some higher dimensional space and then apply the linear model in this space instead of directly on the inputs themselves [267]. For example, a scalar input x could be projected into the space of powers of x.

The function-space view is an alternative way of reaching equivalent results [267]. GPR is non-parametric, meaning it is not limited to a particular functional form and, rather than calculating a probability distribution of parameters of a specific function, it actually calculates the probability distribution over all permissible functions [266]. We can use a Gaussian process (a collection of random variables, any finite number of which have a joint Gaussian distribution) to describe a distribution over functions [267]. We write a Gaussian process as

$$f(\mathbf{x}) \sim GP(m(\mathbf{x}), k(\mathbf{x},\mathbf{x}')) \tag{6.3}$$

where $m(\mathbf{x})$ is the mean (which will typically be zero or take a constant value) and $k(\mathbf{x},\mathbf{x}')$ is the covariance function (which can have many different functional forms, including constant,

linear, and square exponential). In GPR, the form of the mean and covariance kernel functions in the Gaussian process prior is chosen and tuned during model selection. “Hyperparameters" (such as length scales) are parameters that appear in the kernel itself and must be determined - a popular approach to tune these is to maximise the log marginal likelihood of the training data [266].

To train and test our GPR model in this Chapter, we have an outer loop that splits the data into a training set (75% of the points) and a validation set (the remaining 25%). The training set is passed to an inner loop, in which model selection occurs and parameters and hyperparameters are optimised (this is performed internally by MATLAB [268]). Comparing the predictions of the model to the actual T_c values for the validation set then allows us to assess the model's performance for unseen data, and calculate the correlation and confidence intervals. This random splitting and training process is repeated a number of times each time the model is used and the predictions averaged, forming a nested cross-validation procedure.

Electron-phonon coupling calculations

Throughout this Chapter electron-phonon calculations are performed using QUANTUM ESPRESSO to obtain critical temperatures. In the training phase (defined later and depicted in Fig. 6.5), T_c is only obtained from the Allen-Dynes formula (with the strong-coupling modifications), whereas in the results stage T_c values are also calculated via direct solution of the Eliashberg equations using ELK. In all cases, our **k**-point grids are taken to be multiples of our **q**-point grids and are converged in this way. The optimal double-delta smearing parameter for each structure is determined in the same way as in Chapters 4 and 5.

Before performing electron-phonon calculations, we profiled the QUANTUM ESPRESSO code for our specific use cases and implemented a number of optimisations. These optimisations led to an overall (up to) 8 times speed-up for the electron-phonon code and they have been submitted to the QUANTUM ESPRESSO developers. We also parallelised the electron-phonon calculation over phonon modes, thus allowing better utilisation of multi-node supercomputers.

6.2.3 T_c model and the iterative training phase

As already addressed, the model constructed for T_c in this Chapter is a GPR model with descriptors η_H, η_X, $N_H(E_F)/N(E_F)$, M_X and $N(E_F)$, trained in MATLAB using the process described in Section 6.2.2. The initial dataset used by the model consisted of the 160 structures detailed in Section 6.2.1. Despite the fixed initial training set, the overall process used during the training phase was iterative; at each iteration, the model was retrained and

predictions were made for a set of our search structures at a different pressure or level of stability. Structures were then selected for further study based on the predictions of the model, with T_c values for the best predicted structures calculated explicitly using DFPT and fed back into the model's training set for use in the next iteration. In order to make the electron-phonon calculations more feasible, a relatively sparse **q**-point sampling was used in the training stage, chosen to reproduce observations for the well-known $Fm\bar{3}m$ phase of LaH_{10} [161, 163] (as studied in Chapter 4). This corresponds to a **q**-point spacing of $2\pi\times0.15\text{Å}^{-1}$ (a $2\times2\times2$ grid for $Fm\bar{3}m$-LaH_{10} at 200 GPa). Our method is summarised in Fig. 6.5.

Fig. 6.6 is a logarithmic plot of the number of structures considered at each stage of the training process - given the relatively large cost of electron-phonon calculations (even in high-throughput operation and with our optimisations in place), this figure highlights the importance of the stability filtering and model-based screening steps in our method. In total, 119 new DFPT data points were added to the model during the training phase. All predictions were recalculated using the final model to ensure nothing promising was missed in earlier iterations. Most of the electron-phonon calculations performed at this stage were for structures with high predicted T_c values according to our model, however, occasionally structures with mid-range or low T_c predictions were considered in order to improve the behaviour of the model.

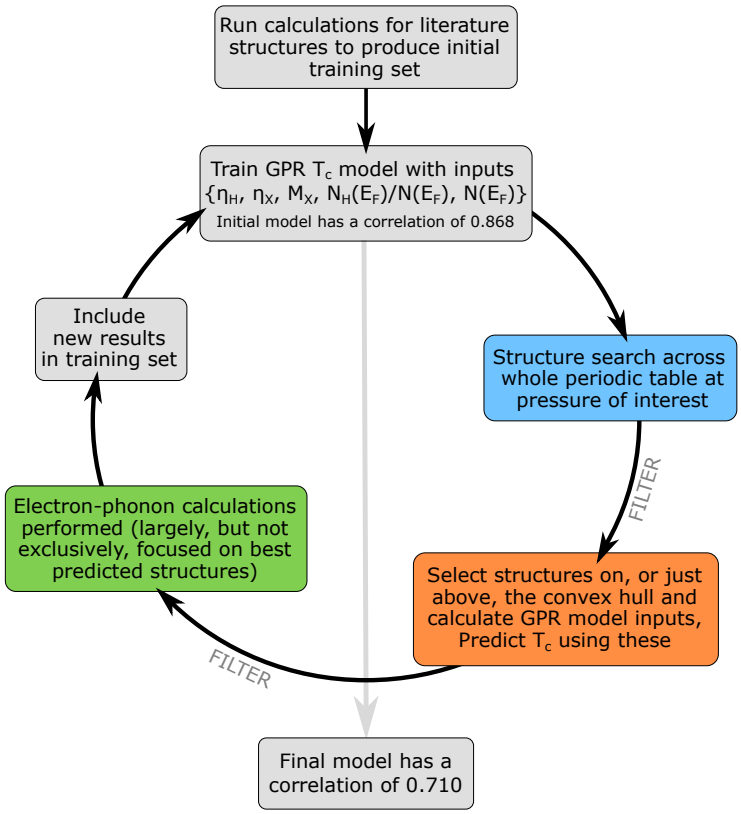

Fig. 6.5 A flowchart of the training phase of our high-throughput methodology. The final model is used to make predictions and select promising candidates in the results stage.

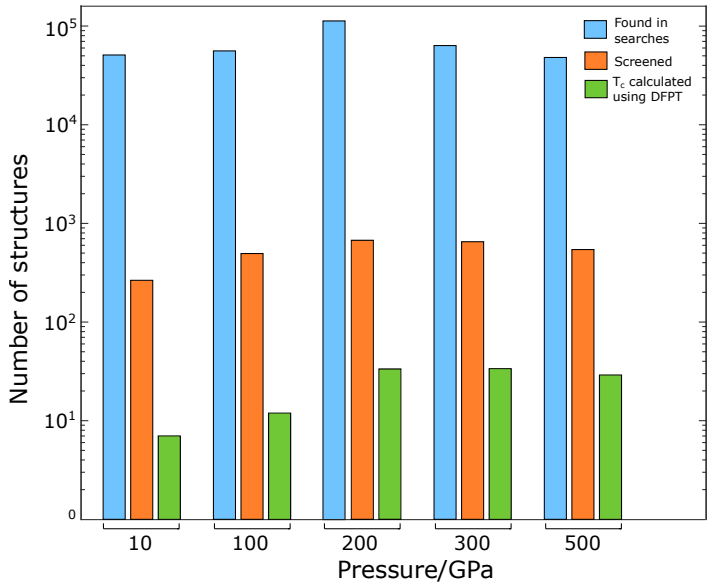

Fig. 6.6 A logarithmic summary of the number of structures studied at each stage of the training process. This clearly highlights the importance of screening to efficiently identify energetically competitive high-T_c candidates from large volumes of searching data.

The correlation between the predicted and calculated T_c values across the training set decreased slightly on addition of more data (see Fig. 6.5). This is not surprising as the results we add to the training set are computed in a high-throughput manner and will therefore be somewhat under-converged compared to typical values found in the literature. Adding to this, the original (literature-based) training set contained 160 entries for hydrides of 45 different elements largely focused around 100-350 GPa, whereas the final training set contains 279 entries for hydrides of 57 different elements from 10 to 500 GPa.

During the training stage, we identified a number of systems with structures exhibiting high-T_c superconductivity; these are studied further in Sec 6.2.4. Among the training phase results, we efficiently rediscovered a number of relatively high-T_c binary hydrides which had been reported previously, including the structures $Im\bar{3}m$-H_3S [162, 241, 257], $Im\bar{3}m$-LaH_6 [156], $I4/mmm$-AcH_{12} [247], $Im\bar{3}m$-SeH_3 [258], $R\bar{3}m$-SrH_6 [246], $R\bar{3}m$-LiH_6 [189, 269], $Fm\bar{3}m$-LaH_{10} [155, 156, 160, 161, 163, 169], $Fm\bar{3}m$-YH_{10} [156, 163], $Im\bar{3}m$-ScH_6 [156, 219, 270], $P6_3/mmc$-ThH_9 [203], $R\bar{3}m$-SrH_{10} [223], $Pm\bar{3}m$-SiH_3 [233], $C2/m$-LaH_7 [169], $Im\bar{3}m$-CaH_6 [195], $Im\bar{3}m$-MgH_6 [198], and $Fm\bar{3}m$-ThH_{10} [194, 203], and the stoichiometries, KH_6 [190], LaH_8 [155, 169], BaH_{12} [188], LaH_5 [169], AcH_{10} [247], LiH_8 [189], LaH_{11} [169], MgH_{12} [192], YH_9 [156, 165], and ScH_{12} [219]. Only half of these 26 stoichiometries were in our original literature data set, highlighting the predictive capability of our method.

6.2.4 Promising systems and focused searches

Based on the DFPT T_c results obtained in the training phase, more detailed structure searches were performed for hydrides of Na, Ca, La, Ac, and K at 100 GPa, hydrides of La, Ac, S, Mg, and Na at 200 GPa, hydrides of Li, Sr, K, Mg, Na, and Sc at 300 GPa, and hydrides of Li, Sr, Mg, Na, Yb, Y, and Ca at 500 GPa. No particularly high T_c results were found at pressures as low as 10 GPa at the training stage (in fact, a large proportion of the structures were not even metallic), so no additional searches were performed at this pressure. The previous symmetry constraints were relaxed for these searches, but all other parameters remained unchanged. Over 270,000 structures were generated in total in the focused searches.

On completion of the focused searches, we again employ our modified version of ELK to calculate η_H, η_X, $N(E_F)$ and $N_H(E_F)/N(E_F)$ for the stable and metastable structures. At this stage, stoichiometries with $E_{stoic} \leq 25$ meV/f.u. were selected. For the stoichiometries on the hull ($E_{stoic} = 0$), 2-5 of the most stable structures (with $E_{struc} \lesssim 100$ meV/f.u.) were chosen. For the selected off-hull stoichiometries ($E_{stoic} \neq 0$), only the lowest energy structure ($E_{struc} = 0$) was chosen. The inputs were then fed into the final T_c model from Section 6.2.3 and fully converged electron-phonon calculations are performed for the structures with the

highest predicted T_c values at each pressure. Converged T_c calculations are also performed for several of the most promising candidates identified during the training phase.

6.3 Results and discussion

Our final results are shown in Figs. 6.7 and 6.8. Promising structures that remained dynamically stable after **q**-point convergence are also listed in Table 6.1. In total, we identify 35 100 K+ and 15 200 K+ superconductors and find near room-temperature superconductors at every pressure considered. We discuss some of the highest T_c structures in more detail in the following sections.

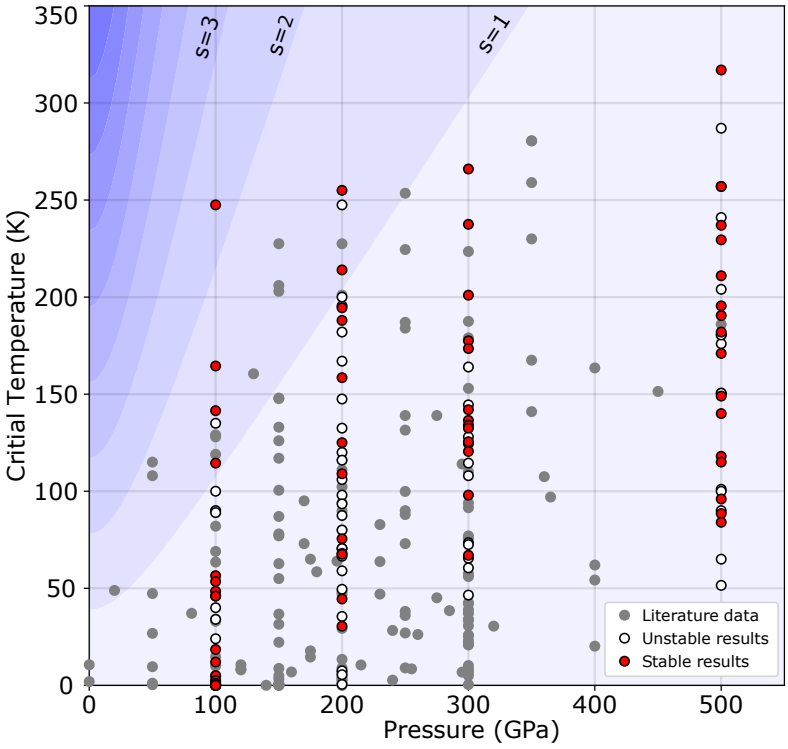

Fig. 6.7 Final (Allen-Dynes) T_c values obtained from converged DFPT calculations for the most promising candidates identified in this Chapter. Results for both dynamically stable and dynamically unstable structures are shown. The background is shaded according to the figure of merit S, introduced in Ref. [146], and our original literature dataset is also plotted.

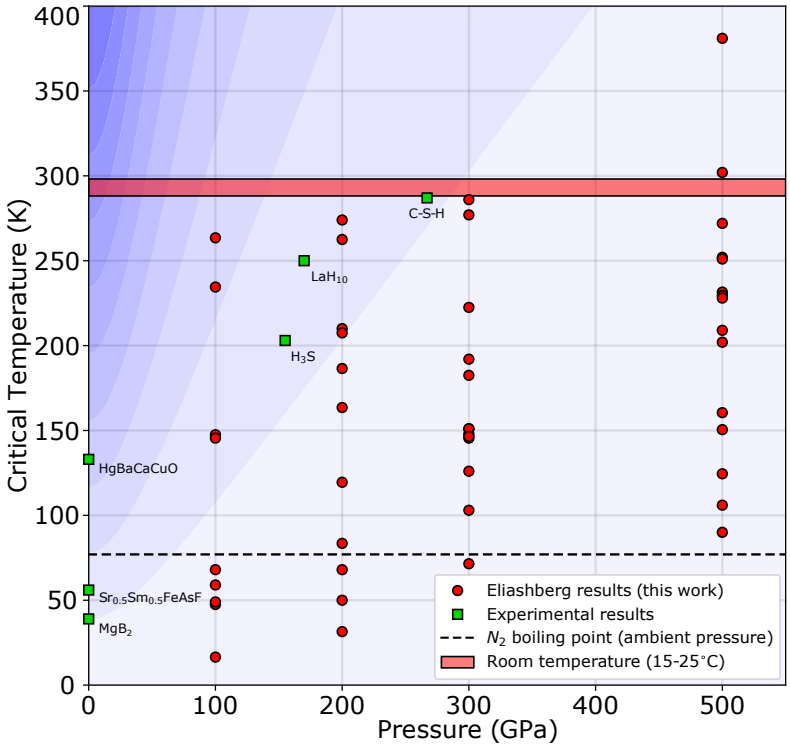

Fig. 6.8 As Fig. 6.7, but with T_c values for the structures found in this Chapter calculated directly from the Eliashberg equations plotted alongside notable experimental results (in order of increasing T_c, these originate from Refs. [271], [272], [273], [162], [161] and [274]).

6.3.1 Aside: dealing with dynamic instabilities

It is important to recognise that since we are using the harmonic approximation, we are only able to extract critical temperatures for structures which are dynamically stable at this level of theory (these are the results given in Table 6.1). For example, it may be noted in the following that the well-known, experimentally-verified superconductor $Fm\bar{3}m$-LaH_{10} is missing from our 200 GPa results. This structure was found in our structure searches and identified as a good candidate by our T_c model, but it was found to be dynamically unstable at 200 GPa (as has been noted previously [157, 158, 163], including in Chapter 4). It is therefore not simple to extract a critical temperature.

As addressed before, there are three main ways of dealing with these instabilites. The first option is perform a further geometry optimisation which allows both breaking of crystal symmetry and increase in simulation cell size, meaning we follow the unstable phonon mode to a locally stable structure. This method neglects anharmonic effects, takes us away from the structure that was originally screened by the T_c model, and could potentially lead to a drastic increase in computational cost as the symmetry and size of the system changes. The

Stoichiometry	Space group	Pressure (GPa)	A-D T_c (K)	Eliashberg T_c (K)	λ	E_{stoic}, E_{struc} (meV/f.u.)
NaH_6	$Pm\bar{3}m$	100	228-267	248-279	2.54	28, 0
CaH_6	$Im\bar{3}m$	100	150-179	216-253	5.81	9, 137
Na_2H_{11}	$Cmmm$	100	127-156	134-161	1.28	0, 0
KH_{10}	$C2/m$	100	105-124	134-157	2.45	0, 0
NaH_{16}	$Fmm2$	100	47-60	61-75	1.10	0, 0
AcH_5	$P\bar{1}$	100	48-65	49-69	0.91	0, 0
LaH_5	$P\bar{1}$	100	37-55	40-58	0.83	0, 0
NaH_{24}	$R\bar{3}$	100	40-57	40-55	0.82	0, 0
AcH_{11}	$C2/m$	100	14-23	13-20	0.71	0, 0
NaH_6	$Pm\bar{3}m$	200	235-275	260-288	2.06	39, 16
AcH_{12}	$P6_3mc$	200	197-231	245-280	3.92	11, 0
MgH_{13}	$Fm\bar{3}m$	200	179-210	196-224	1.98	17, 635
SH_3	$Im\bar{3}m$	200	173-203	196-219	1.77	0, 0
AcH_6	$Fmmm$	200	110-140	169-204	2.01	0, 14
NaH_8	$I4/mmm$	200	146-171	152-175	1.63	26, 124
Na_2H_{11}	$Cmmm$	200	120-156	129-162	1.11	0, 0
MgH_{14}	$P\bar{1}$	200	106-132	112-134	1.35	23, 0
LaH_7	$C2/m$	200	98-120	105-134	1.23	3, 0
MgH_4	$I4/mmm$	200	63-88	73-94	0.98	0, 101
SH_7	$Fmmm$	200	57-78	58-78	0.91	29, 0
Mg_2H_7	$C2/m$	200	55-75	56-75	0.98	22, 0
AcH_4	$Cmcm$	200	35-54	42-58	0.99	19, 0
Mg_2H_5	$R\bar{3}m$	200	22-39	24-39	0.74	139, 21
MgH_6	$Im\bar{3}m$	300	248-284	271-301	2.28	19, 437
YH_9	$F\bar{4}3m$	300	220-255	261-293	2.58	2, 0
ScH_8	$Immm$	300	185-217	212-233	2.06	3, 0
LiH_2	$P6/mmm$	300	162-193	177-207	1.45	40, 75
NaH_7	$C2/m$	300	157-190	167-198	1.48	3, 0
ScH_{12}	$P\bar{1}$	300	127-157	137-165	1.28	0, 103
NaH_5	$P4/mmm$	300	121-144	138-164	1.92	1, 0
LiH_6	$C2/m$	300	109-142	130-163	1.16	0, 14
LiH_6	$R\bar{3}m$	300	121-152	130-161	1.30	0, 0
ScH_6	$Im\bar{3}m$	300	118-150	135-161	1.26	0, 0
LiH_3	$Cmcm$	300	104-137	112-140	1.06	1, 0
ScH_{14}	$P\bar{1}$	300	87-109	91-115	1.20	6, 0
MgH_4	$I4/mmm$	300	53-81	59-84	0.76	0, 0
MgH_{12}	$Pm\bar{3}$	500	294-340	360-402	2.65	0, 259
SrH_{10}	$Fm\bar{3}m$	500	239-275	285-319	2.22	8, 120
MgH_{13}	$P3m1$	500	239-275	257-287	2.21	12, 0
MgH_{10}	$C2/m$	500	209-250	232-270	1.63	9, 0
NaH_9	$P6_3/mmc$	500	218-256	235-269	1.67	0, 0
YH_{18}	$P\bar{1}$	500	179-212	213-246	1.99	25, 0
SrH_{24}	$R\bar{3}$	500	195-227	218-245	1.88	9, 0
YH_{20}	$P\bar{1}$	500	176-205	212-244	2.21	39, 0
SrH_{10}	$R\bar{3}m$	500	165-199	190-228	1.31	8, 0
CaH_{10}	$R\bar{3}m$	500	155-187	184-220	1.51	3, 0
Na_2H_{11}	$Cmmm$	500	132-166	141-180	1.12	0, 0
CaH_{15}	$P\bar{6}2m$	500	120-160	134-167	1.01	0, 0
SrH_{15}	$P\bar{6}2m$	500	100-136	110-139	0.93	0, 0
MgH_8	$C2/m$	500	82-110	91-121	0.96	0, 0
Na_2H_{11}	$I4/mmm$	500	72-105	76-104	0.80	0, 297

Table 6.1 Allen-Dynes and Eliashberg T_c values for dynamically stable superconductors found in this Chapter, along with calculated λ and the two stability measures.

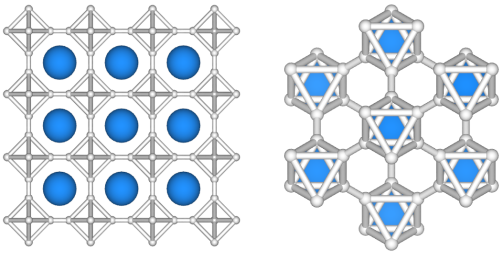

Fig. 6.9 The 100 GPa structure of $Pm\bar{3}m$ NaH_6 along the [100] and [111] directions, respectively.

second option is to employ some method of dealing with anharmonicity; there are many different methods available, some of which are detailed in Chapter 2. Effective anharmonic "frequencies" can then be defined and used to get first order corrections to T_c [275]. However, this process is far too expensive to use in such a large-scale study. The final option is to recognise that, for many hydrides, the high-frequency phonon modes contribute most to T_c. Therefore, we can get a rough estimate of T_c by simply neglecting the unstable modes in the Eliashberg function [163, 276] while maintaining its normalisation. This was the approach taken for $Fm\bar{3}m$-LaH_{10} in the low pressure region in Chapter 4. For the dynamically unstable structures identified in this Chapter, we plot the results of this third method in Fig. 6.7 - the individual structures and their corresponding T_c values are listed in the Supplementary Material of Ref. [248]. We do not discuss these results further here, preferring to focus on dynamically stable structures for which T_c is well-defined at this level of theory, but future work could investigate the most promising of these dynamically unstable candidates using alternative methods.

6.3.2 Dynamically stable superconductors

100 GPa

Of particular note at 100 GPa is a $Pm\bar{3}m$ structure of NaH_6; at the static-lattice level, we find this cubic structure to be the most stable arrangement for NaH_6, but the stoichiometry itself is metastable. Ref. [277] also found a $Pm\bar{3}m$ structure, predicting that it becomes stable to $P1$ above 150 GPa. The structure consists of a cubic lattice of H octahedra with Na at the body-centred positions (see Fig. 6.9). While synthesis of sodium polyhydrides has been demonstrated [278], superconductivity in the system seems somewhat under-studied given its potential; here we calculate a T_c of 248-279 K from the Eliashberg equations. This places the structure at a crucial position in P-T_c space as it strongly influences the maximum T_c value at low pressure (see Fig. 6.7).

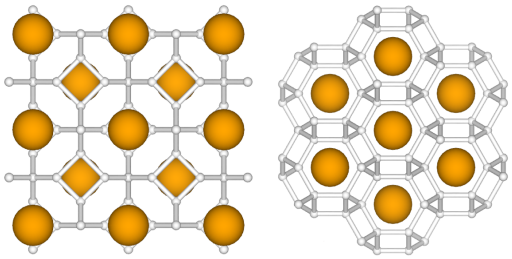

Fig. 6.10 The 100 GPa structure of $Im\bar{3}m$ CaH_6 along the [100] and [111] directions, respectively. The $Im\bar{3}m$ structure of MgH_6 investigated at 300 GPa can be obtained by substituting the Ca atoms with Mg atoms.

Also of interest at 100 GPa is an $Im\bar{3}m$ structure of CaH_6, shown in Fig. 6.10. This structure is also found to be metastable, in agreement with Ref. [195] which found the CaH_6 stoichiometry to be metastable at the static-lattice level until above 150 GPa. However, despite strong electron-phonon coupling (leading to a λ of 5.81), its critical temperature (216-253 K) is found to be slightly lower than that of $Pm\bar{3}m$-NaH_6, due to a lower average phonon frequency. Our T_c result for $Im\bar{3}m$-CaH_6 is comparable to the value of 220-235 K calculated at the slightly higher pressure of 150 GPa in Ref. [195] (also via solution of the Eliashberg equations). We also note that, as a result of coupling to soft phonon modes, the Allen-Dynes equation drastically underestimates T_c in this system. Given the form of the Eliashberg function for this system (see Fig. 6.11) with a small peak appearing at low frequencies, this observation is perhaps unsurprising as the Allen-Dynes equation is known to be sensitive to changes in the spectral function $\alpha^2F(\omega)$ at small ω. In fact, the functional derivative $\delta T_c^{AD}/\delta\alpha^2F(\omega)$ diverges as $\omega \to 0$ [279]; in this case towards $-\infty$, which leads to the significant reduction in predicted T_c.

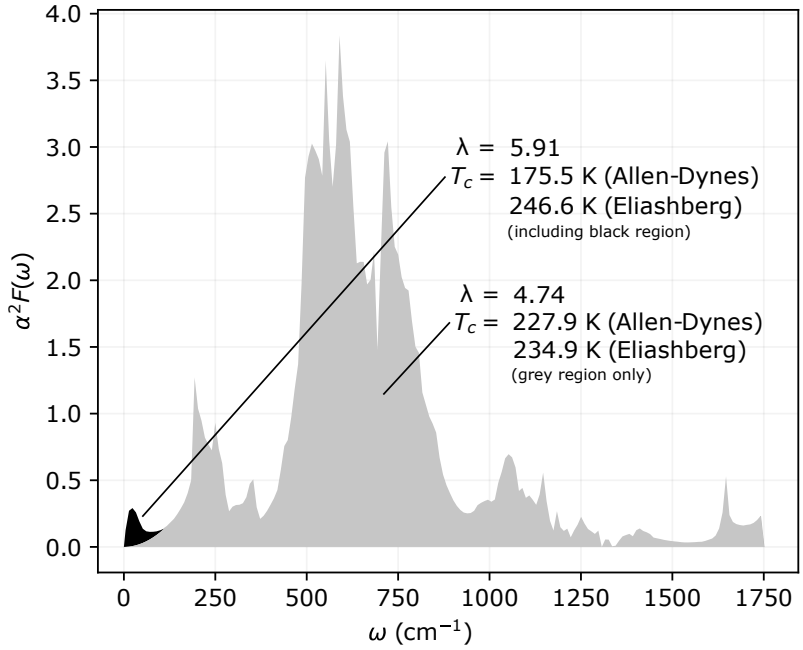

Fig. 6.11 The Eliashberg function of $Im\bar{3}m$ CaH_6 at 100 GPa, demonstrating the suppression of T_c from the Allen-Dynes equation relative to the value obtained by solving the Eliashberg equations. This suppression is due to electrons coupling to low frequency phonon modes. We believe the small peak at very low frequencies, which alone increases λ by $\sim$1.2 and is responsible for the reduction of the Allen-Dynes T_c, arises at 100 GPa due to proximity to a dynamical instability. We note that this behaviour was not observed at 150 GPa in Ref. [195], presumably because this higher pressure is further away from the point of instability.

While the next best structures at 100 GPa ($Cmmm$-Na_2H_{11} and $C2/m$-KH_{10}) have similar average phonon frequencies to $Pm\bar{3}m$-NaH_6, they do not exhibit such high coupling strengths, leading to considerably lower T_c values (134-161 K and 134-157 K, respectively). Superconductivity of KH_{10} has been studied previously [188]; it was found to be on the convex hull at 150 GPa with a T_c of 148 K calculated for the *Immm* structure, which is within the range we calculate here for the $C2/m$ structure at 100 GPa. In contrast to our findings, Ref. [280] found KH_{10} to be above the convex hull at 100 GPa, and instead found metastable metallic structures of other stoichiometries, but superconductivity was not investigated.

200 GPa

At 200 GPa, the $Pm\bar{3}m$ structure of NaH_6 remains the highest T_c structure found, with T_c rising slightly from its 100 GPa value to 260-288 K. However, we find that its stability at the static-lattice level decreases with pressure; at 200 GPa the stoichiometry is found further away from the convex hull and the structure itself is no longer the most stable one found for NaH_6. Despite this, the energies involved are fairly small and we still consider it competitive

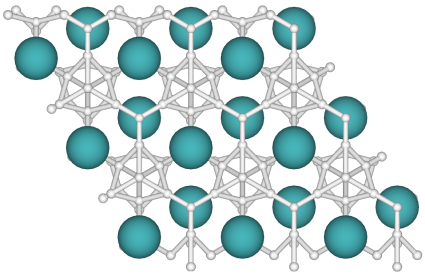

Fig. 6.12 The 200 GPa $P6_3mc$ structure of AcH_{12} along the [001] direction.

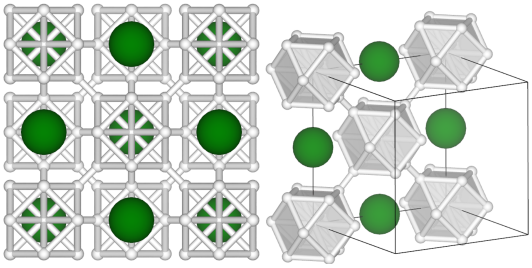

Fig. 6.13 The 200 GPa $Fm\bar{3}m$ structure of MgH_{13}. The structure consists of Mg atoms and axis-aligned cuboctahedra of hydrogen in a checkerboard pattern. Each cuboctahedra has an additional hydrogen atom at its centre to make up the necessary 13.

enough to be potentially stabilised by vibrational effects and/or synthesised in experiment. Similarly to Ref. [247], we find several actinium hydride superconductors at this pressure, most notably a $P6_3mc$ structure of the metastable AcH_{12} stoichiometry (see Fig. 6.12) with an Eliashberg T_c of 245-280 K.

200 GPa also marks the appearance of magnesium hydrides in our results; these structures become increasingly prevalent with pressure. Of particular note is a cubic structure of MgH_{13} with the space group $Fm\bar{3}m$ (see Fig. 6.13), with a slightly higher calculated T_c than that of the experimentally-verified $Im\bar{3}m$-H_3S [162] at the same pressure. However, this structure arose in the training phase searches, which had high-symmetry constraints applied, and it is found to be rather uncompetitive in the focused searches (as demonstrated by its large E_{struc} value). Ref. [192] also found MgH_{13} to lie above the convex hull at 200 GPa and reported significantly lower critical temperatures for on-hull structures - coupled with our high-T_c result for the off-hull cubic MgH_{13} structure, this demonstrates the importance of considering structures above the hull in theoretical studies.

300 GPa

At 300 GPa an $Im\bar{3}m$ structure of MgH_6 exhibits the highest calculated critical temperature, with a T_c of 271-301 K (or 248-284 K using the Allen-Dynes equation) in agreement with

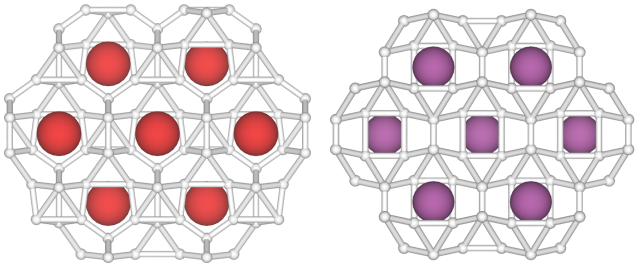

Fig. 6.14 The 300 GPa $F\bar{4}3m$ structure of YH_9 along the [110] direction and the 300 GPa $Immm$ structure of ScH_8 along the [100] direction, respectively.

previous calculations [198]. This structure can be obtained by substituting Ca for Mg in the CaH_6 structure investigated at 100 GPa (see Fig. 6.10).

With an Eliashberg T_c of 261-293 K, an $F\bar{4}3m$ structure of YH_9 (shown in Fig. 6.14) is the next highest temperature superconductor found at this pressure. A $P6_3/mmc$ structure of this stoichiometry has recently been synthesised at slightly lower pressures and was found to exhibit a critical temperature of 243 K at 201 GPa [165]. Y-H systems has been extensively studied theoretically [150, 156, 163] with critical temperatures in excess of 200 K calculated for many different stoichiometries.

We predict that an $Immm$ structure of ScH_8 with a similar motif to $F\bar{4}3m$-YH_9 (see Fig. 6.14) is also a high-temperature superconductor at this pressure with a critical temperature of 212-233 K. However, even our Allen-Dynes T_c result (185-217 K) is significantly higher than the value of $\sim$115 K obtained previously in Ref. [281] using the Allen-Dynes equation without strong-coupling corrections, a $16 \times 16 \times 16$ **k**-point grid and a pseudopotential with 3 valence electrons for scandium. In contrast, we use a $36 \times 36 \times 36$ **k**-point grid and a pseudopotential with 11 valence electrons, although a more substantial investigation is needed to fully solve this discrepancy. Eliashberg critical temperatures of 213 K and 233 K (remarkably close to our ScH_8 result) were previously obtained at 300 GPa for ScH_7 and ScH_9, respectively, in Ref. [219].

The next structure of note at 300 GPa is the metastable $P6/mmm$-LiH_2, which is interesting both because of its relatively low hydrogen content and because its structure is analogous to the well-known ambient-pressure superconductor MgB_2 [271] (see Fig. 6.15). Superconductivity in lithium hydrides has been investigated previously at lower pressures [189], where it was found that the LiH_2 stoichiometry did not exhibit superconductivity at 150 GPa. We note that the LiH_2 stoichiometry does not fall on the convex hull at 300 GPa, in disagreement with Ref. [282], but that we were able to stabilise this stoichiometry and obtain agreement with the previous work by using harder pseudopotentials and more converged

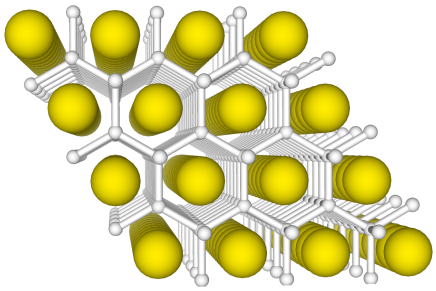

Fig. 6.15 The 300 GPa $P6/mmm$ structure of LiH_2 along the [001] direction.

parameters in the searching calculations. We note also that the $P6/mmm$ structure is not the most stable LiH_2 structure at the static-lattice level. It appears, again, that considering metastable structures might be important in obtaining higher T_c values.

500 GPa

As we increase pressure further, hydrides with higher hydrogen content can be metallised. At 500 GPa, we see the appearance of several MgH_n superconductors with $n \geq 10$. The highest critical temperature belongs to MgH_{12}, a stoichiometry which we find to be on the convex hull, where a $Pm\bar{3}$ structure (see Fig. 6.16) has a predicted T_c of 360-402 K. This value lies far above room-temperature. Moving slightly above the static-lattice convex hull to the MgH_{13} stoichiometry, a T_c of 257-287 K is calculated for the lowest energy structure which has $Pm31$ symmetry. Electron-phonon coupling appears to be enhanced substantially in this system with increasing pressure; the MgH_{12} stoichiometry was previously investigated at lower pressures [192], where it was also found to lie on the convex hull, but with a T_c of only 47-60 K at 140 GPa.

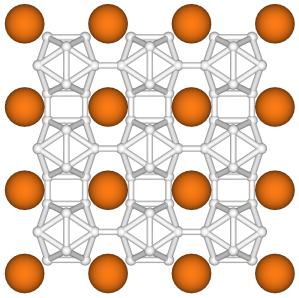

Fig. 6.16 The 500 GPa $Pm\bar{3}$ structure of MgH_{12} along the [010] direction.

At 500 GPa, we also find that a high-symmetry metastable $Fm\bar{3}m$ phase of SrH_{10} exhibits room-temperature superconductivity with a T_c of 285-319 K (12-46°C). This is significantly higher than the 190-228 K we calculate for the ground-state structure, which we find to have

$R\bar{3}m$ symmetry in agreement with previous calculations at 300 GPa [283]. A T_c of 259 K had been calculated for the $R\bar{3}m$ structure previously at this lower pressure [223].

6.3.3 Comments on the Allen-Dynes equation

Having a large number of superconductors for which the Eliashberg equations have been solved directly provides a unique opportunity to test the Allen-Dynes equation. This comparison is made in Fig. 6.17 (a); it is clear that, while the correlation between the two T_c values is relatively good, the Allen-Dynes equation systematically underestimates the Eliashberg result (at least for the binary hydrides studied here). We therefore fit a modified version of the Allen-Dynes equation of the form

$$T_c = T_c^{(\mathrm{AD})}(a + b\lambda) \tag{6.4}$$

to the data of Table 6.1, giving $a = 1.0083$ and $b = 0.0654$. As can be seen in Fig. 6.17 (b) this removes the systematic underestimation and reduces the variance of the prediction. This modified Allen-Dynes equation could find good use in future studies of binary hydrides, although we would always recommend full solution of the Eliashberg equations where possible.

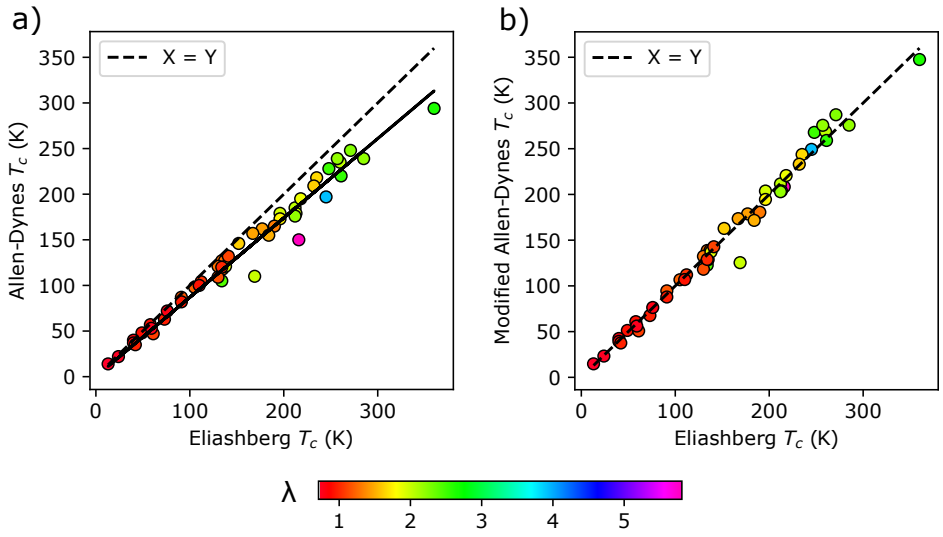

Fig. 6.17 (a) Allen-Dynes critical temperatures, plotted against critical temperatures from solution of the Eliashberg equations (data from Table 6.1). (b) The same as the first panel, but using the modified Allen-Dynes equation, Eq. 6.4.

6.4 Geometry-based screening for high-T_c hydrides

High-throughput approaches are used throughout this thesis in order to determine which stoichiometries are stable to decomposition and then to identify the relevant low-lying structures of interest. However, if we are interested in studying materials with a particular property (besides stability or metastability), it is clearly useful to incorporate some estimation of this property directly into our high-throughput workflow. This is the logic we followed in designing the methodology we use in this Chapter, where the model-based screening has allowed us to efficiently identify potential high-T_c candidates. That said, to increase the number of structures that can be considered in a high-throughput scenario, it is desirable to have a screening protocol that is cheap enough to be employed directly at the structure searching level. With this in mind, we now introduce and test two geometric measures that are virtually free to calculate and are aimed at grouping hydrides based on their potential superconducting abilities.

6.4.1 Introducing geometry-based measures

Using the same set of structures contained in the *final* training set of the T_c model built in this Chapter, we investigate the predictive abilities of two simple geometric measures. Firstly, we investigate whether there is a link between the shortest hydrogen-hydrogen distance within a structure and its calculated T_c. The basis of this idea is that hydrides mimic the properties of more highly compressed pure hydrogen and the hydrogen-hydrogen distance may give some measure of the degree of effective compression. Fig. 6.18 shows the dependence of calculated T_c on the shortest hydrogen-hydrogen distance found in the structure.

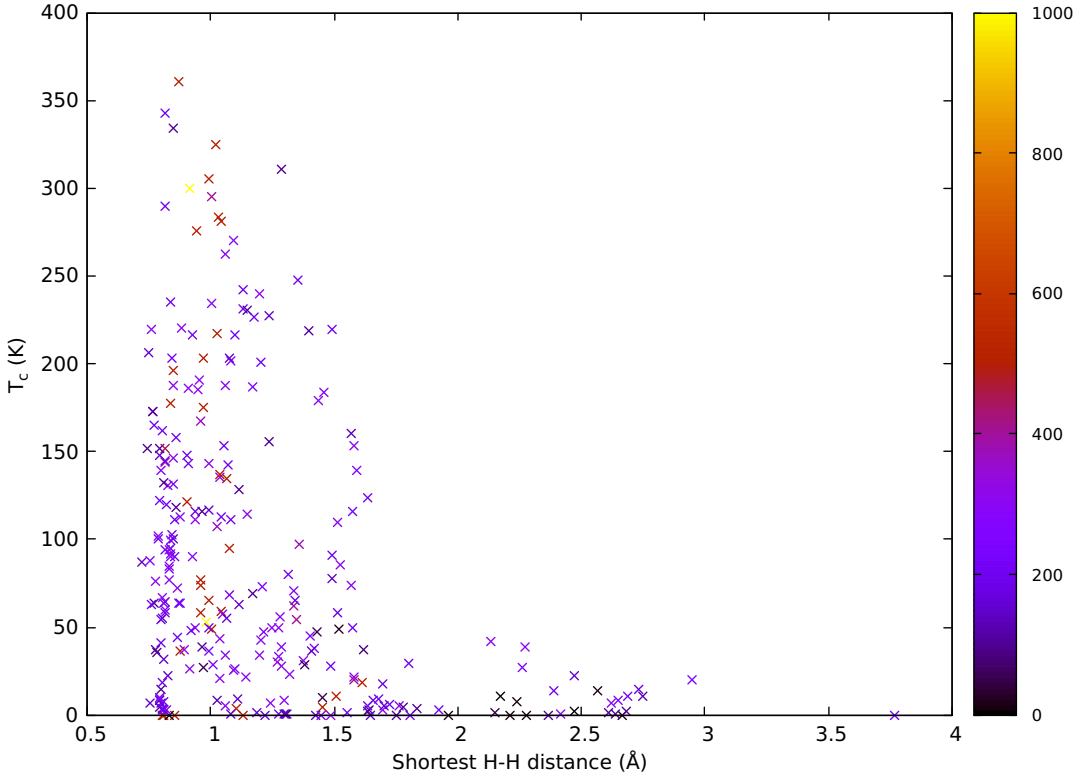

Fig. 6.18 Shortest hydrogen-hydrogen distance plotted against T_c - the points are coloured according to pressure, with the pallette in units of GPa.

A smaller value for the shortest hydrogen-hydrogen distance appears to indicate that a large T_c may be *possible*, but does not guarantee it - a whole range of T_c values are observed at this end of the scale. Large shortest hydrogen-hydrogen distances seem to indicate low T_c, so it may be possible to remove these structures from further study if finding high-T_c materials is the aim. The results for this dataset, for example, suggest that removing any structures with a shortest hydrogen-hydrogen distance greater than 1.75-2 Å might be sensible.

Secondly, based on the observation that hydrides with a cage-like arrangement of hydrogen atoms appear to be good superconductors and those with layer-like structures do not (as discussed in Chapter 5), we also define a "cage-measure" to test against T_c. With a cage-like arrangement of hydrogen atoms surrounding a central non-hydrogen element, if we move directly from one non-hydrogen atom to a nearby one we should expect to encounter a hydrogen atom somewhere close to our path. In a structure with a layer-like arrangement, there may be some directions in which we are able to move from one non-hydrogen atom to another without closely encountering a hydrogen atom. To define a cage measure, we therefore consider each possible distinct pair of X-X atoms in a small supercell. For each pair, we calculate the distance of each hydrogen atom in the cell from the straight line that

joins the two X atoms as

$$D = \frac{|(\mathbf{x}_2 - \mathbf{x}_1) \times (\mathbf{x}_1 - \mathbf{x}_0)|}{|\mathbf{x}_2 - \mathbf{x}_1|}, \tag{6.5}$$

where $\mathbf{x}_1$ and $\mathbf{x}_2$ are the positions of the pair of X atoms under consideration and $\mathbf{x}_0$ is the hydrogen atom position. For a given pair of X atoms, D is calculated for each $\mathbf{x}_0$ individually and we then take the minimum of these values to find the closest distance of approach. This is then repeated for other distinct X-X pairs; the result of this procedure is a set of values for each structure, each one associated with a different X-X pair. Smaller values are associated with a more cage-like arrangement of hydrogen atoms and larger values with a more layer-like arrangement. In Fig. 6.19, we plot the maximum of these values against calculated T_c.

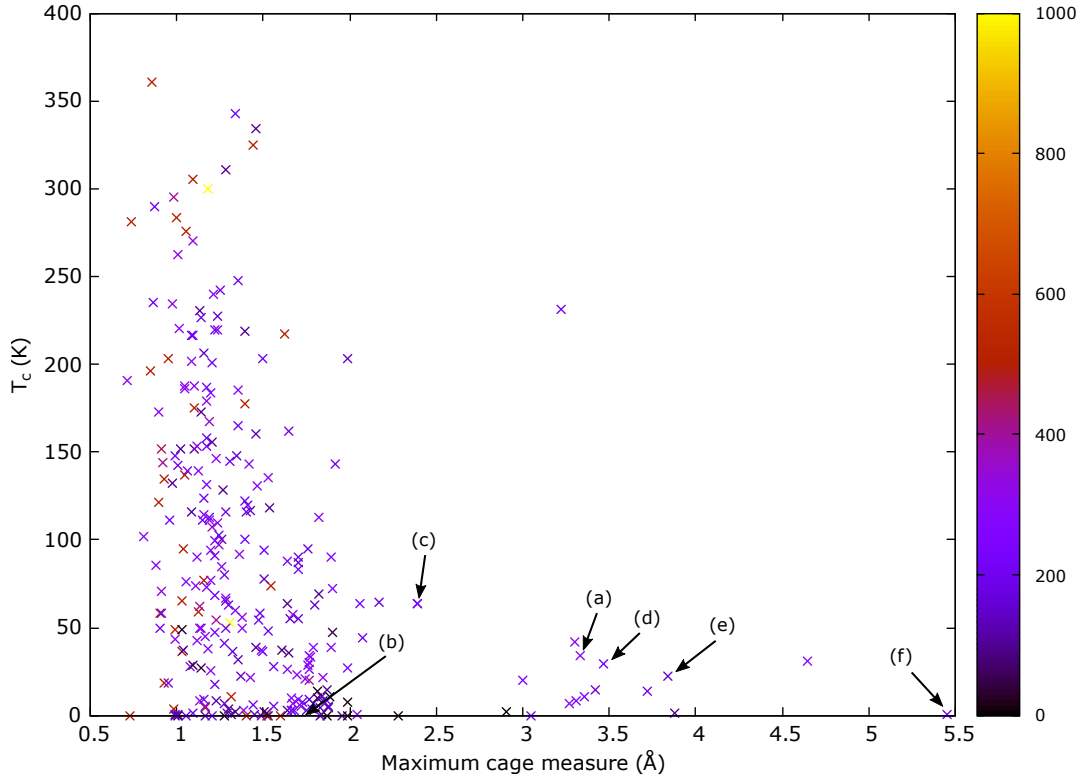

Fig. 6.19 Maximum value of cage measure for each structure plotted against the corresponding T_c - the points are coloured according to pressure, with the pallette in units of GPa. Labelled points correspond to structures discussed in the main text.

There are some outliers, but in general it seems that a lower maximum cage value is associated with the *possibility* of a high T_c. To put this measure into practice, we could therefore use it to remove candidates that have a large maximum cage value. This quantity, along with the shortest hydrogen-hydrogen distance, is clearly not as instructive as η_H or

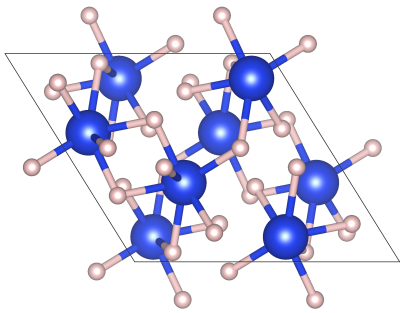

(a) $C2/c$-Si_2H_6 at 300 GPa

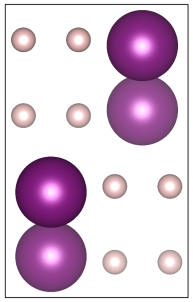

(b) $Pnma$-H_2I at 200 GPa

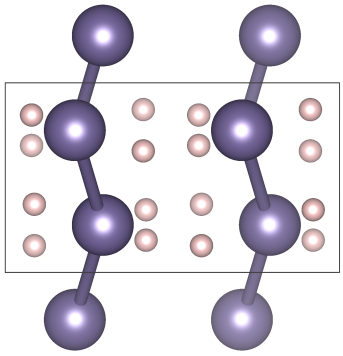

(c) $C2/c$-GeH_4 at 220 GPa

Fig. 6.20 A selection of structures with high maximum cage measures, as labelled in Fig. 6.19.

$N_H(E_F)/N(E_F)$. Selecting some structures with a high cage measure, we can check that the process is working as intended and see what the value reflects about the structure itself. The structures we have chosen for this test are labelled (a)-(f) in Fig. 6.19 - some of which are shown in Fig. 6.20.

The structure labelled (a), shown in Fig. 6.20a, appears rather cage-like, but there are directions in which hydrogen atoms are not found between silicon atoms - the hydrogen in the structure is therefore not highly compressed. For the structure labelled (b), shown in Fig. 6.20b, it is clear that the hydrogen and iodine atoms are found in distinct parts of the unit cell. The structure labelled (c), shown in Fig. 6.20c, is layered and the hydrogen atoms are not highly compressed by the germanium chains. The structure labelled (d) is $C2/c$-HS_2 at 200 GPa, which does not have a high enough hydrogen content to produce a high T_c value; the same goes for structure (e), $P4/nmm$-TeH at 150 GPa. The structure labelled (f) is $I4/mmm$-FeH_5 at 200 GPa, a layered structure whose lack of superconductivity has already been discussed in Ref. [170].

6.4.2 Use in high-throughput search scenarios

Plotting the two measures tested here against one another suggests that they provide complementary information and could be combined. Normalising the peaks in both Fig. 6.18 and Fig. 6.19 to 1 (by dividing the values by 1 Å and 1.25 Å, respectively) and multiplying these two scaled quantities together gives a combined geometric measure. This is plotted in Fig. 6.21, where it becomes apparent that a result close to 1 indicates a possibility of obtaining a high T_c.

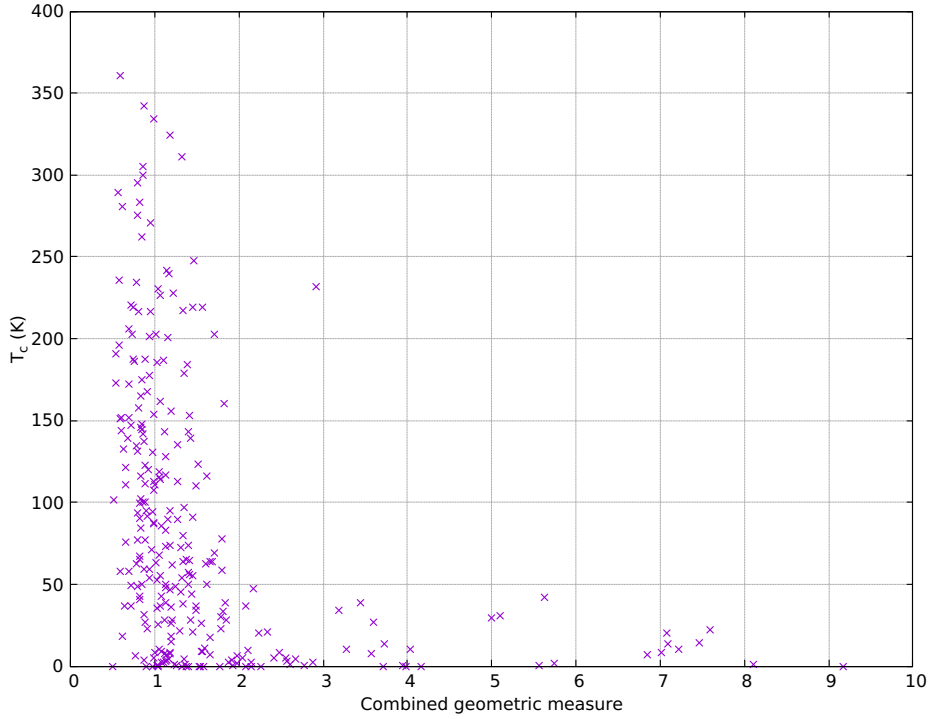

Fig. 6.21 Plotting the combined geometric measure described above against T_c.

Even slight deviations away from 1 seem to reduce the potential for high-temperature superconductivity, meaning this method could be applied directly to future AIRSS search outputs for hydrides to eliminate unpromising candidates. For example, here the mean T_c of the 276 points is 86.3 K. Removing any structures for which the absolute difference between the combined geometric measure and 1 is $\geq$0.75 eliminates 58 structures with an average T_c of 20.9 K. Only two of the 98 structures with $T_c \geq 100$ K are removed in this way and all 6 of the structures with $T_c \geq 300$ K are retained. Attempting an even more drastic approach, removing any structures for which the absolute difference between the combined geometric measure and 1 is $\geq$0.4 eliminates 103 structures with an average T_c of 54.1 K. Only 20 of the

98 structures with $T_c \geq 100$ K and just 1 of the structures with $T_c \geq 300$ K are removed in this way.

Since the components of this combined geometric measure are free to calculate for a given input geometry, any number of structures could be screened in this way. This method clearly has some promise and, in future work, may find use as a pre-cursor step to the workflow already designed in this Chapter. It would, however, be desirable to test how it performs on the output of a general AIRSS search, rather than the set of structures considered here which are biased heavily towards non-zero (and often high) T_c values.

6.5 Conclusions

We have developed a screening method and associated high-throughput workflow that can be used to efficiently discover energetically competitive high-T_c binary hydrides. As well as establishing this new methodology, the findings of this Chapter add considerably to the known P-T_c behaviour of the high-pressure hydrides.

We have performed a total of 240 T_c calculations using DFPT, split roughly equally between the high-throughput training phase and the converged final results. This represents an unprecedented number of computationally intensive calculations, made possible by our optimisation of the QUANTUM ESPRESSO electron-phonon code. In our final results, we identify 36 dynamically stable superconductors with $T_c > 100$ K (to the best of our knowledge, superconductivity has not been investigated previously in 27 of these) and 18 with $T_c > 200$ K. Since our final results contain 48 dynamically stable structures in total, the identification of 36 100 K+ superconductors suggests that our screening method is extremely effective. Of particular note, as well as rediscovering the well-known $Im\bar{3}m$-CaH_6, we find a $Pm\bar{3}m$ structure of NaH_6 with a T_c of 248-279 K at 100 GPa, hinting at the exciting possibility of other low-pressure high-temperature superconductors. We also identify $Pm\bar{3}$-MgH_{12} and $Fm\bar{3}m$-SrH_{10} as above-room-temperature superconductors at 500 GPa, as well as several near-room-temperature superconductors at lower pressures.

Throughout this work, our aim has been to consider as wide a range of binary compositions as possible, extending across the entire periodic table and a large pressure range. Therefore, since our focus is on breadth, we make no claim that the searches presented in this Chapter are exhaustive. Despite this, we still identify a large number of high-T_c candidates, suggesting that the binaries have more to offer and even more promising structures could be uncovered in future, more focused studies. We also note that the highest critical temperature results at each pressure arise from metastable structures or off-hull stoichiometries. This suggests that the additional freedom afforded by allowing some degree of metastability could

lead us to superconductors with higher T_c values. We see this explicitly in the case of SrH_{10} at 500 GPa, where the ground state $R\bar{3}m$ structure has a critical temperature nearly 100 K lower than a metastable $Fm\bar{3}m$ structure. Exploring avenues such as metastability will be important in future work in order to push the boundaries of high-temperature superconductivity.

The study of ternary hydrides is set to become a more active field in the coming years. The added complexity of these systems means that there are many more structures to consider and screening-based methods, such as the one presented in this Chapter, are likely to become increasingly important in the future. Through slight redefinition of the descriptors, the workflow we design here could easily be generalised to work for ternary systems. In this Chapter we also introduced and tested two geometry-based screening techniques with the hope that they could be deployed at the structure searching level to filter out unpromising candidates. Our combined geometric measure showed surprising promise given its simplicity. The testing was presented here for binary hydride systems, but these quantities and ideas are also easily generalised to ternaries.

Chapter 7

Conclusions

As this thesis has demonstrated, by combining crystal structure prediction methods, efficient DFT and phonon codes, and methods for treating conventional superconductivity and anharmonicity, it is possible to make accurate predictions about the structure and superconducting properties of materials from first principles. Since the properties calculated by theorists can be used as a predictive guide for future experimental targets, as well as being compared to existing experimental results, experimentalists and theorists are now able to work truly in tandem. This relationship is clearly evident in the case of the high-pressure hydrides.

The goals of this thesis are fairly clear: to add to the tools used to study light-atom systems under high pressure, with a specific focus on the prediction and optimisation of conventional superconductivity. Looking at the key experimental systems of solid hydrogen, LaH_{10}, and YH_{10}, the work presented here assesses the suitability of current theoretical tools, offers interpretations of previous experimental observations, and makes predictions for future experiments. This thesis also demonstrates that specific material properties - such as conventional superconductivity at lower pressures - can be efficiently targeted by using machine learning methods to guide structure searching efforts. This idea is easily transferable to other regions of P-T_c space, depending on experimental or technological needs, or to other properties altogether. Perhaps most importantly, this thesis recognises the impossibility of exhaustively studying superconductivity even in just the binary hydrides and demonstrates how a high-throughput methodology can be designed to circumvent this problem. This work leads to one of the most comprehensive studies of superconductivity in binary hydrides ever carried out, in turn providing a survey of the overall behaviour of these systems and demonstrating discovery of numerous high-T_c candidates.

Directions for future research

A number of future research directions can be identified directly from the ideas developed in this thesis. First of all, this thesis highlights a number of individual points that we hope will influence the field going forward, including the impact of the double-delta smearing parameter and the importance of considering metastable structures. It is crucial to consider metastable structures both because they may be stabilised by vibrations (or at a higher level of theory) and because metastable structures themselves may still be accessible in experiment. Some of the highest-T_c structures we identify in this thesis are metastable at the static-lattice level.

We have seen that anharmonicity can be important in light-atom systems and we have methods for incorporating it (just as we did for solid hydrogen in Chapter 3). Effective anharmonic frequencies can also be used to get first order corrections to T_c [275], although this would not be feasible in larger-scale searching projects and we have seen in Chapter 4 that there are other approximations at play too. However, it is true that anharmonicity can be crucial in certain cases and in the future it would be desirable to have a method for determining whether anharmonicity will be particularly important in a given system.

Other ideas for future research come from considering which systems are likely to be of theoretical and experimental interest in the coming years. Now that binary hydrides have been so extensively studied, it is likely that the search for superconductivity will continue in the ternary hydrides. It is thought that even larger T_c values could be achieved in these systems and, in fact, a recent computational study predicted a T_c of 473 K at 250 GPa in Li_2MgH_{16} [185] and an experimental measurement of T_c = 288 K at 267 GPa has even been reported in the C-S-H system [274]. The high-throughput methodology developed in Chapter 6 of this thesis could, in theory, be applied to ternary hydrides. Slight modifications would need to be made in calculation of the η_j parameters as it would no longer possible to assume separation of the vibrational modes if the two non-hydrogen atoms had a similar mass. The method of model training may also have to be reconsidered as there are not a large number of results in the literature for ternary hydrides at present. In fact, screening approaches will become even more important as the community moves towards these more complicated systems; the number of potential compositions to consider increases substantially on moving from binary to ternary hydrides, making it even more difficult to consider every relevant structure explicitly.

The study of superconductivity in other (non-hydrogen) light binaries using the methods developed in this thesis is another research direction that we consider to hold great promise. Moving away from hydrogen, we are able to look at considerably lower pressures. In particular, we have begun some exploratory work on carbides and nitrides at atmospheric

pressure; the descriptors used in Chapter 6 can be calculated for these systems provided separation of the vibrational modes can be assumed when calculating η_j. Others have found that this assumption is acceptable for transition-metal carbides [284]. Our early results have indicated that for carbides of the form X_mC_n or nitrides of the form X_mN_n (where $M_X > M_{C/N}$), higher $\eta_{C/N}$ values tend to be associated with a larger T_c and it may be possible to find reasonable superconducting carbides and nitrides at atmospheric pressure.

In addition, this thesis provides a guide for building other high-throughput workflows focused on optimising specific material properties. Combined searching and screening approaches could be designed for other desirable properties provided good descriptors can be identified, and this work highlights the benefits of looking slightly outside your immediate research field in order to find these.

Finally, one of the ultimate goals of computational materials science is first-principles material design - the ability to choose atomic arrangements or modify existing structures in order to produce or enhance a specific material property. In order for this to be possible, we need to identify descriptors that both correlate well with the desired property and can be *reverse-engineered*. Steps in this direction for superconductivity in hydrides are implicitly presented in this thesis; it may be possible to encourage desirable values of the geometric measures introduced in Chapter 6 at the structure searching level and electronic quantities, such as $N_H(E_F)/N(E_F)$, may be somewhat controllable if we allow doping.

References

[1] M. Miao, Y. Sun, E. Zurek, and H. Lin, "Chemistry under high pressure," *Nat. Rev. Chem.*, pp. 1–20, 2020.

[2] A. Jayaraman, "Ultrahigh pressures," *Rev. Sci. Instrum.*, vol. 57, no. 6, pp. 1013–1031, 1986.

[3] R. A. Forman, G. J. Piermarini, J. D. Barnett, and S. Block, "Pressure measurement made by the utilization of ruby sharp-line luminescence," *Science*, vol. 176, no. 4032, pp. 284–285, 1972.

[4] M. Fierz, "About the relativistic theory of force-free particles with arbitrary spin," *Helvetica Physica Acta*, vol. 12, pp. 3–37, 1939.

[5] W. Pauli, "The connection between spin and statistics," *Phys. Rev.*, vol. 58, no. 8, p. 716, 1940.

[6] J. C. Slater, "The theory of complex spectra," *Phys. Rev.*, vol. 34, no. 10, p. 1293, 1929.

[7] M. Born and R. Oppenheimer, "Zur quantentheorie der molekeln," *Annalen der Physik*, vol. 389, no. 20, pp. 457–484, 1927.

[8] S. Pisana, M. Lazzeri, C. Casiraghi, K. S. Novoselov, A. K. Geim, A. C. Ferrari, and F. Mauri, "Breakdown of the adiabatic Born-Oppenheimer approximation in graphene," *Nat. Mat*, vol. 6, no. 3, p. 198, 2007.

[9] I. Rahinov, R. Cooper, D. Matsiev, C. Bartels, D. J. Auerbach, and A. M. Wodtke, "Quantifying the breakdown of the Born-Oppenheimer approximation in surface chemistry," *Phys. Chem. Chem. Phys*, vol. 13, no. 28, pp. 12680–12692, 2011.

[10] M. Head-Gordon and E. Artacho, "Chemistry on the computer," *Phys. Today*, vol. 61, no. 4, p. 58, 2008.

[11] R. M. Martin, *Electronic structure: Basic theory and practical methods*. Cambridge University Press, 2004.

[12] D. R. Hartree, "The wave mechanics of an atom with a non-Coulomb central field. Part I: theory and methods," in *Mathematical Proceedings of the Cambridge Philosophical Society*, vol. 24, pp. 89–110, Cambridge University Press, 1928.

[13] V. Fock, "Approximation method for the solution of the quantum mechanical multibody problems," *Zeitschrift fur Physik*, vol. 61, pp. 126–148, 1930.

[14] J. C. Slater, "A simplification of the Hartree-Fock method," *Phys. Rev.*, vol. 81, no. 3, p. 385, 1951.

[15] C. Møller and M. S. Plesset, "Note on an approximation treatment for many-electron systems," *Phys. Rev.*, vol. 46, no. 7, p. 618, 1934.

[16] R. J. Bartlett and M. Musiał, "Coupled-cluster theory in quantum chemistry," *Rev. Mod. Phys*, vol. 79, no. 1, p. 291, 2007.

[17] P. Hohenberg and W. Kohn, "Inhomogeneous electron gas," *Phys. Rev.*, vol. 136, no. 3b, p. b864, 1964.

[18] M. Levy, "Universal variational functionals of electron densities, first-order density matrices, and natural spin-orbitals and solution of the v-representability problem," *Proc. Nat. Acad. Sci*, vol. 76, no. 12, pp. 6062–6065, 1979.

[19] M. Levy, "Electron densities in search of Hamiltonians," *Phys. Rev. A*, vol. 26, no. 3, p. 1200, 1982.

[20] W. Kohn and L. J. Sham, "Self-consistent equations including exchange and correlation effects," *Phys. Rev.*, vol. 140, no. 4a, p. a1133, 1965.

[21] J. F. Janak, "Proof that $\partial e/\partial n_i = \varepsilon$ in density-functional theory," *Phys. Rev. B*, vol. 18, no. 12, p. 7165, 1978.

[22] J. P. Perdew, R. G. Parr, M. Levy, and J. L. Balduz Jr, "Density-functional theory for fractional particle number: Derivative discontinuities of the energy," *Phys. Rev. Lett.*, vol. 49, no. 23, p. 1691, 1982.

[23] J. P. Perdew and M. Levy, "Comment on "significance of the highest occupied Kohn-Sham eigenvalue"," *Phys. Rev. B*, vol. 56, no. 24, p. 16021, 1997.

[24] J. P. Perdew and M. Levy, "Extrema of the density functional for the energy: Excited states from the ground-state theory," *Phys Rev B*, vol. 31, no. 10, p. 6264, 1985.

[25] S. M. Valone, "A one-to-one mapping between one-particle densities and some n-particle ensembles," *J. of Chem Phys*, vol. 73, no. 9, pp. 4653–4655, 1980.

[26] R. van Leeuwen, "Density functional approach to the many-body problem: Key concepts and exact functionals," *Advances in Quant. Chem*, vol. 43, pp. 25–94, 2003.

[27] E. H. Lieb, "Density functionals for Coulomb systems," in *Density Functional Methods in Physics*, pp. 31–80, Springer, 1985.

[28] H. Englisch and R. Englisch, "Exact density functionals for ground-state energies: I. General results," *Physica Status Solidi (b)*, vol. 123, no. 2, pp. 711–721, 1984.

[29] W. Kutzelnigg, "Density functional theory in terms of a Legendre transformation for beginners," *J. Molecular Struct: Theo. Chem*, vol. 768, no. 1-3, pp. 163–173, 2006.

[30] E. H. Lieb and S. Oxford, "Improved lower bound on the indirect Coulomb energy," *Int. J. Quantum Chem.*, vol. 19, no. 3, pp. 427–439, 1981.

[31] A. E. Mattsson, P. A. Schultz, M. P. Desjarlais, T. R. Mattsson, and K. Leung, "Designing meaningful density functional theory calculations in materials science: A primer," *Model. Simul. Mater. Sci. Eng.*, vol. 13, no. 1, 2004.

[32] J. P. Perdew and A. Zunger, "Self-interaction correction to density-functional approximations for many-electron systems," *Phys. Rev. B*, vol. 23, no. 10, p. 5048, 1981.

[33] D. M. Ceperley and B. J. Alder, "Ground state of the electron gas by a stochastic method," *Phys. Rev. Lett.*, vol. 45, no. 7, p. 566, 1980.

[34] J. P. Perdew, "Accurate density functional for the energy: Real-space cutoff of the gradient expansion for the exchange hole," *Phys. Rev. Lett.*, vol. 55, no. 16, p. 1665, 1985.

[35] J. P. Perdew, K. Burke, and M. Ernzerhof, "Generalized gradient approximation made simple," *Phys. Rev. Lett.*, vol. 77, no. 18, p. 3865, 1996.

[36] J. P. Perdew and Y. Wang, "Accurate and simple analytic representation of the electron-gas correlation energy," *Phys. Rev. B*, vol. 45, no. 23, p. 13244, 1992.

[37] A. D. Becke, "Density-functional exchange-energy approximation with correct asymptotic behavior," *Phys. Rev. A*, vol. 38, no. 6, p. 3098, 1988.

[38] C. Lee, W. Yang, and R. G. Parr, "Development of the Colle-Salvetti correlation-energy formula into a functional of the electron density," *Phys. Rev. B*, vol. 37, no. 2, p. 785, 1988.

[39] M. Dion, H. Rydberg, E. Schröder, D. C. Langreth, and B. I. Lundqvist, "Van der Waals density functional for general geometries," *Phys. Rev. Lett.*, vol. 92, no. 24, p. 246401, 2004.

[40] K. Lee, E. D. Murray, L. Kong, B. I. Lundqvist, and D. C. Langreth, "Higher-accuracy Van der Waals density functional," *Phys. Rev. B*, vol. 82, no. 8, p. 081101, 2010.

[41] S. J. Clark, M. D. Segall, C. J. Pickard, P. J. Hasnip, M. I. J. Probert, K. Refson, and M. C. Payne, "First principles methods using CASTEP," *Zeitschrift für Kristallographie-Crystalline Materials*, vol. 220, no. 5/6, pp. 567–570, 2005.

[42] P. Giannozzi, S. Baroni, N. Bonini, M. Calandra, R. Car, C. Cavazzoni, D. Ceresoli, G. L. Chiarotti, M. Cococcioni, I. Dabo, A. Dal Corso, S. de Gironcoli, S. Fabris, G. Fratesi, R. Gebauer, U. Gerstmann, C. Gougoussis, A. Kokalj, M. Lazzeri, L. Martin-Samos, N. Marzari, F. Mauri, R. Mazzarello, S. Paolini, A. Pasquarello, L. Paulatto, C. Sbraccia, S. Scandolo, G. Sclauzero, A. P. Seitsonen, A. Smogunov, P. Umari, and R. M. Wentzcovitch, "QUANTUM ESPRESSO: A modular and open-source software project for quantum simulations of materials," *J. Phys. Condens. Matter*, vol. 21, no. 39, p. 395502 (19pp), 2009.

[43] P. Giannozzi, O. Andreussi, T. Brumme, O. Bunau, M. B. Nardelli, M. Calandra, R. Car, C. Cavazzoni, D. Ceresoli, M. Cococcioni, N. Colonna, I. Carnimeo, A. D. Corso, S. de Gironcoli, P. Delugas, R. A. D. Jr, A. Ferretti, A. Floris, G. Fratesi,

G. Fugallo, R. Gebauer, U. Gerstmann, F. Giustino, T. Gorni, J. Jia, M. Kawamura, H.-Y. Ko, A. Kokalj, E. Küçükbenli, M. Lazzeri, M. Marsili, N. Marzari, F. Mauri, N. L. Nguyen, H.-V. Nguyen, A. O. de-la Roza, L. Paulatto, S. Poncé, D. Rocca, R. Sabatini, B. Santra, M. Schlipf, A. P. Seitsonen, A. Smogunov, I. Timrov, T. Thonhauser, P. Umari, N. Vast, X. Wu, and S. Baroni, "Advanced capabilities for materials modelling with QUANTUM ESPRESSO," *J. Phys. Condens. Matter*, vol. 29, no. 46, p. 465901, 2017.

[44] G. P. Srivastava and D. Weaire, "The theory of the cohesive energies of solids," *Advances in Physics*, vol. 36, no. 4, pp. 463–517, 1987.

[45] D. R. Hamann, M. Schlüter, and C. Chiang, "Norm-conserving pseudopotentials," *Phys. Rev. Lett.*, vol. 43, no. 20, p. 1494, 1979.

[46] D. Vanderbilt, "Soft self-consistent pseudopotentials in a generalized eigenvalue formalism," *Phys. Rev. B*, vol. 41, no. 11, p. 7892, 1990.

[47] H. J. Monkhorst and J. D. Pack, "Special points for Brillouin-zone integrations," *Phys. Rev. B*, vol. 13, no. 12, p. 5188, 1976.

[48] H. Hellmann, "Einführung in die quantenchemie," *Franz Deuticke, Leipzig*, p. 285, 1937.

[49] R. P. Feynman, "Forces in molecules," *Phys. Rev.*, vol. 56, no. 4, p. 340, 1939.

[50] C. J. Pickard and R. J. Needs, "Ab initio random structure searching," *J. Phys: Condens. Matt*, vol. 23, no. 5, p. 053201, 2011.

[51] C. J. Pickard and R. J. Needs, "High-pressure phases of silane," *Phys. Rev. Lett.*, vol. 97, no. 4, p. 045504, 2006.

[52] R. J. Needs and C. J. Pickard, "Perspective: Role of structure prediction in materials discovery and design," *APL Materials*, vol. 4, no. 5, p. 053210, 2016.

[53] M. G. Evans and M. Polanyi, "Further considerations on the thermodynamics of chemical equilibria and reaction rates," *Transactions of the Faraday Society*, vol. 32, pp. 1333–1360, 1936.

[54] B. Monserrat, N. D. Drummond, P. Dalladay-Simpson, R. T. Howie, P. López Ríos, E. Gregoryanz, C. J. Pickard, and R. J. Needs, "Structure and metallicity of phase V of hydrogen," *Phys. Rev. Lett.*, vol. 120, no. 25, p. 255701, 2018.

[55] S. Kirkpatrick, C. D. Gelatt, and M. P. Vecchi, "Optimization by simulated annealing," *Science*, vol. 220, no. 4598, pp. 671–680, 1983.

[56] J. Pannetier, J. Bassas-Alsina, J. Rodriguez-Carvajal, and V. Caignaert, "Prediction of crystal structures from crystal chemistry rules by simulated annealing," *Nature*, vol. 346, no. 6282, pp. 343–345, 1990.

[57] L. Ingber, "Simulated annealing: Practice versus theory," *Mathematical and Computer Modelling*, vol. 18, no. 11, pp. 29–57, 1993.

[58] A. R. Oganov and C. W. Glass, "Crystal structure prediction using ab initio evolutionary techniques: Principles and applications," *J. Chem. Phys.*, vol. 124, no. 24, p. 244704, 2006.

[59] Y. Wang, J. Lv, L. Zhu, and Y. Ma, "Crystal structure prediction via particle-swarm optimization," *Phys. Rev. B*, vol. 82, no. 9, p. 094116, 2010.

[60] A. R. Oganov, C. J. Pickard, Q. Zhu, and R. J. Needs, "Structure prediction drives materials discovery," *Nat. Rev. Mater.*, vol. 4, p. 331, 2019.

[61] M. S. Johnson, "Accelerating vibrational free energy calculations for anharmonic crystals (doctoral thesis)," 2020.

[62] J. H. Lloyd-Williams and B. Monserrat, "Lattice dynamics and electron-phonon coupling calculations using nondiagonal supercells," *Phys. Rev. B*, vol. 92, no. 18, p. 184301, 2015.

[63] S. Baroni, P. Giannozzi, and A. Testa, "Green's-function approach to linear response in solids," *Phys. Rev. Lett.*, vol. 58, no. 18, p. 1861, 1987.

[64] X. Gonze, "Perturbation expansion of variational principles at arbitrary order," *Phys. Rev. A*, vol. 52, no. 2, p. 1086, 1995.

[65] R. M. Sternheimer, "Electronic polarizabilities of ions from the Hartree-Fock wave functions," *Phys. Rev.*, vol. 96, no. 4, p. 951, 1954.

[66] R. M. Sternheimer, "On nuclear quadrupole moments," *Phys. Rev.*, vol. 84, no. 2, p. 244, 1951.

[67] R. M. Sternheimer and H. M. Foley, "Nuclear quadrupole coupling in the Li_2 molecule," *Phys. Rev.*, vol. 92, no. 6, p. 1460, 1953.

[68] S. Baroni, S. De Gironcoli, A. Dal Corso, and P. Giannozzi, "Phonons and related crystal properties from density-functional perturbation theory," *Rev. Mod. Phys.*, vol. 73, no. 2, p. 515, 2001.

[69] E. A. Hylleraas, "About the basic term of the two-electron problems of H^-, He, Li^+, Be^{++} etc," *Zeitschrift für Physik*, vol. 65, no. 3-4, pp. 209–225, 1930.

[70] X. Gonze and J.-P. Vigneron, "Density-functional approach to nonlinear-response coefficients of solids," *Phys. Rev. B*, vol. 39, no. 18, p. 13120, 1989.

[71] F. Birch, "Finite elastic strain of cubic crystals," *Phys. Rev.*, vol. 71, pp. 809–824, Jun 1947.

[72] E. A. Engel, B. Monserrat, and R. J. Needs, "Anharmonic nuclear motion and the relative stability of hexagonal and cubic ice," *Phys. Rev. X*, vol. 5, no. 2, p. 021033, 2015.

[73] E. A. Engel, B. Monserrat, and R. J. Needs, "Vibrational effects on surface energies and band gaps in hexagonal and cubic ice," *J. Chem. Phys*, vol. 145, no. 4, p. 044703, 2016.

[74] N. D. Drummond, B. Monserrat, J. H. Lloyd-Williams, P. López Ríos, C. J. Pickard, and R. J. Needs, "Quantum monte carlo study of the phase diagram of solid molecular hydrogen at extreme pressures," *Nat. Comm*, vol. 6, p. 7794, 2015.

[75] I. Errea, M. Calandra, and F. Mauri, "First-principles theory of anharmonicity and the inverse isotope effect in superconducting palladium-hydride compounds," *Phys. Rev. Lett.*, vol. 111, no. 17, p. 177002, 2013.

[76] V. Kapil, E. Engel, M. Rossi, and M. Ceriotti, "Assessment of approximate methods for anharmonic free energies," *J. Chem. Theory Comput.*, vol. 15, no. 11, pp. 5845–5857, 2019.

[77] S. Hirata, M. Keçeli, Y.-y. Ohnishi, O. Sode, and K. Yagi, "Extensivity of energy and electronic and vibrational structure methods for crystals," *Annu. Rev. Phys. Chem.*, vol. 63, pp. 131–153, 2012.

[78] B. Monserrat, N. D. Drummond, and R. Needs, "Anharmonic vibrational properties in periodic systems: Energy, electron-phonon coupling, and stress," *Phys. Rev. B*, vol. 87, no. 14, p. 144302, 2013.

[79] J. G. Kirkwood, "Statistical mechanics of fluid mixtures," *J. Chem. Phys.*, vol. 3, no. 5, pp. 300–313, 1935.

[80] J. Bardeen, L. N. Cooper, and J. R. Schrieffer, "Theory of superconductivity," *Phys. Rev.*, vol. 108, no. 5, p. 1175, 1957.

[81] F. Marsiglio and J. P. Carbotte, "Electron-phonon superconductivity," in *Superconductivity*, pp. 73–162, Springer, 2008.

[82] G. M. Eliashberg, "Interactions between electrons and lattice vibrations in a superconductor," *Sov. Phys. JETP*, vol. 11, no. 3, pp. 696–702, 1960.

[83] A. B. Migdal, "Interaction between electrons and lattice vibrations in a normal metal," *Sov. Phys. JETP*, vol. 7, no. 6, pp. 996–1001, 1958.

[84] W. L. McMillan, "Transition temperature of strong-coupled superconductors," *Phys. Rev.*, vol. 167, no. 2, p. 331, 1968.

[85] P. B. Allen and R. C. Dynes, "Transition temperature of strong-coupled superconductors reanalyzed," *Phys. Rev. B*, vol. 12, no. 3, p. 905, 1975.

[86] F. Giustino, "Electron-phonon interactions from first principles," *Rev. Mod. Phys.*, vol. 89, no. 1, p. 015003, 2017.

[87] M. Wierzbowska, S. de Gironcoli, and P. Giannozzi, "Origins of low-and high-pressure discontinuities of T_c in niobium," *arXiv:cond-mat/0504077*, 2005.

[88] F. Marsiglio, "Eliashberg theory: A short review," *Annals of Physics*, vol. 417, p. 168102, 2020.

[89] http://elk.sourceforge.net/. The ELK FP-LAPW code.

[90] G. Ummarino. https://www.cond-mat.de/events/correl13/manuscripts/ummarino.pdf. Eliashberg theory.

[91] P. Morel and P. W. Anderson, "Calculation of the superconducting state parameters with retarded electron-phonon interaction," *Phys. Rev.*, vol. 125, pp. 1263–1271, Feb 1962.

[92] R. C. Dynes, "Mcmillan's equation and the T_c of superconductors," *Solid State Communications*, vol. 10, no. 7, pp. 615–618, 1972.

[93] J. J. Hopfield, "Angular momentum and transition-metal superconductivity," *Phys. Rev.*, vol. 186, no. 2, p. 443, 1969.

[94] G. D. Gaspari and B. L. Gyorffy, "Electron-phonon interactions, d resonances, and superconductivity in transition metals," *Phys. Rev. Lett.*, vol. 28, no. 13, p. 801, 1972.

[95] D. A. Papaconstantopoulos, B. Klein, M. J. Mehl, and W. E. Pickett, "Cubic H_3S around 200 GPa: An atomic hydrogen superconductor stabilized by sulfur," *Phys. Rev. B*, vol. 91, no. 18, p. 184511, 2015.

[96] L. Shi and D. A. Papaconstantopoulos, "Theoretical predictions of superconductivity in alkali metals under high pressure," *Phys. Rev. B*, vol. 73, no. 18, p. 184516, 2006.

[97] P.-H. Chang, S. Silayi, D. A. Papaconstantopoulos, and M. J. Mehl, "Pressure-induced high-temperature superconductivity in hypothetical H_3X (X= As, Se, Br, Sb, Te and I) in the H_3S structure with $Im\bar{3}m$ symmetry," *J. Phys. Chem. Solids*, vol. 139, p. 109315, 2020.

[98] W. H. Butler, J. J. Olson, J. S. Faulkner, and B. L. Gyorffy, "Electron-phonon interaction in cubic systems: Application to niobium," *Phys. Rev. B*, vol. 14, no. 9, p. 3823, 1976.

[99] G. Grimvall, "The electron-phonon interaction in metals. vol. 16," *North-Holland Publishing Co.*, p. 304, 1981.

[100] J. J. Sakurai and J. Napolitano, *Scattering theory*, p. 386–445. Cambridge University Press, 2nd ed., 2017.

[101] M. J. Hutcheon, A. M. Shipley, and R. J. Needs, "Predicting novel superconducting hydrides using machine learning approaches," *Phys. Rev. B*, vol. 101, no. 14, p. 144505, 2020.

[102] H.-K. Mao and R. J. Hemley, "Ultrahigh-pressure transitions in solid hydrogen," *Rev. Mod. Phys*, vol. 66, no. 2, p. 671, 1994.

[103] N. W. Ashcroft, "Metallic hydrogen: A high-temperature superconductor?," *Phys. Rev. Lett.*, vol. 21, no. 26, p. 1748, 1968.

[104] C.-S. Zha, R. E. Cohen, H.-K. Mao, and R. J. Hemley, "Raman measurements of phase transitions in dense solid hydrogen and deuterium to 325 GPa," *Proceedings of the National Academy of Sciences*, vol. 111, no. 13, pp. 4792–4797, 2014.

[105] I. Goncharenko and P. Loubeyre, "Neutron and x-ray diffraction study of the broken symmetry phase transition in solid deuterium," *Nature*, vol. 435, no. 7046, p. 1206, 2005.

[106] C. Ji, B. Li, W. Liu, J. S. Smith, A. Majumdar, W. Luo, R. Ahuja, J. Shu, J. Wang, S. Sinogeikin, Y. Meng, V. B. Prakapenka, E. Greenberg, R. Xu, X. Huang, W. Yang, G. Shen, W. L. Mao, and H.-K. Mao, "Ultrahigh-pressure isostructural electronic transitions in hydrogen," *Nature*, vol. 573, no. 7775, pp. 558–562, 2019.

[107] A. F. Goncharov and V. V. Struzhkin, "Raman spectroscopy of metals, high-temperature superconductors and related materials under high pressure," *J. Raman Spectroscopy*, vol. 34, no. 7-8, pp. 532–548, 2003.

[108] I. B. Magdău and G. J. Ackland, "Infrared peak splitting from phonon localization in solid hydrogen," *Phys. Rev. Lett.*, vol. 118, no. 14, p. 145701, 2017.

[109] B. Monserrat, S. E. Ashbrook, and C. J. Pickard, "Nuclear magnetic resonance spectroscopy as a dynamical structural probe of hydrogen under high pressure," *Phys. Rev. Lett.*, vol. 122, no. 13, p. 135501, 2019.

[110] J. R. Trail, P. López Ríos, and R. J. Needs, "Energetics of H_2 clusters from density functional and coupled cluster theories," *Phys. Rev. B*, vol. 95, no. 11, p. 115116, 2017.

[111] C. J. Pickard and R. J. Needs, "Structures at high pressure from random searching," *Physica Status Solidi (B)*, vol. 246, no. 3, pp. 536–540, 2009.

[112] R. J. Hemley and H. K. Mao, "Phase transition in solid molecular hydrogen at ultrahigh pressures," *Phys. Rev. Lett.*, vol. 61, no. 7, p. 857, 1988.

[113] Y. Akahama, M. Nishimura, H. Kawamura, N. Hirao, Y. Ohishi, and K. Takemura, "Evidence from x-ray diffraction of orientational ordering in phase III of solid hydrogen at pressures up to 183 GPa," *Phys. Rev. B*, vol. 82, no. 6, p. 060101, 2010.

[114] M. Eremets and I. Troyan, "Conductive dense hydrogen," *Nat. Mater.*, vol. 10, no. 12, pp. 927–931, 2011.

[115] R. T. Howie, C. L. Guillaume, T. Scheler, A. F. Goncharov, and E. Gregoryanz, "Mixed molecular and atomic phase of dense hydrogen," *Phys. Rev. Lett.*, vol. 108, no. 12, p. 125501, 2012.

[116] C.-S. Zha, Z. Liu, M. Ahart, R. Boehler, and R. J. Hemley, "High-pressure measurements of hydrogen phase IV using synchrotron infrared spectroscopy," *Phys. Rev. Lett.*, vol. 110, no. 21, p. 217402, 2013.

[117] P. Dalladay-Simpson, R. T. Howie, and E. Gregoryanz, "Evidence for a new phase of dense hydrogen above 325 gigapascals," *Nature*, vol. 529, no. 7584, p. 63, 2016.

[118] M. I. Eremets, I. A. Troyan, and A. P. Drozdov, "Low temperature phase diagram of hydrogen at pressures up to 380 GPa. a possible metallic phase at 360 GPa and 200 K," *arXiv preprint arXiv:1601.04479*, 2016.

[119] A. Goncharov, "Phase diagram of hydrogen at extreme pressures and temperatures; updated through 2019," *Low Temperature Physics*, vol. 46, no. 2, pp. 97–103, 2020.

[120] B. Monserrat, R. J. Needs, E. Gregoryanz, and C. J. Pickard, "Hexagonal structure of phase III of solid hydrogen," *Phys. Rev. B*, vol. 94, no. 13, p. 134101, 2016.

[121] Y. Akahama, Y. Mizuki, S. Nakano, N. Hirao, and Y. Ohishi, "Raman scattering and x-ray diffraction studies on phase III of solid hydrogen," in *J. Phys.: Conference Series*, vol. 950, p. 042060, IOP Publishing, 2017.

[122] S. Azadi and T. D. Kühne, "Unconventional phase III of high-pressure solid hydrogen," *Phys. Rev. B*, vol. 100, no. 15, p. 155103, 2019.

[123] S. Azadi and G. J. Ackland, "The role of Van der Waals and exchange interactions in high-pressure solid hydrogen," *Phys. Chem. Chem. Phys.*, vol. 19, no. 32, pp. 21829–21839, 2017.

[124] C. J. Pickard, M. Martinez-Canales, and R. J. Needs, "Density functional theory study of phase IV of solid hydrogen," *Phys. Rev. B*, vol. 85, no. 21, p. 214114, 2012.

[125] I. B. Magdău and G. J. Ackland, "Identification of high-pressure phases III and IV in hydrogen: Simulating raman spectra using molecular dynamics," *Phys. Rev. B*, vol. 87, no. 17, p. 174110, 2013.

[126] I. B. Magdău and G. J. Ackland, "High temperature raman analysis of hydrogen phase IV from molecular dynamics," in *J. Phys.: Conference Series*, vol. 500, p. 032012, IOP Publishing, 2014.

[127] G. J. Ackland and I. B. Magdau, "Efficacious calculation of raman spectra in high pressure hydrogen," *High Press. Res.*, vol. 34, no. 2, pp. 198–204, 2014.

[128] S. Azadi, R. Singh, and T. D. Kühne, "Nuclear quantum effects induce metallization of dense solid molecular hydrogen," *J. Comp. Chem.*, vol. 39, no. 5, pp. 262–268, 2018.

[129] J. M. McMahon and D. M. Ceperley, "Ground-state structures of atomic metallic hydrogen," *Phys. Rev. Lett.*, vol. 106, no. 16, p. 165302, 2011.

[130] S. A. Bonev, E. Schwegler, T. Ogitsu, and G. Galli, "A quantum fluid of metallic hydrogen suggested by first-principles calculations," *Nature*, vol. 431, no. 7009, p. 669, 2004.

[131] R. C. Clay III, J. McMinis, J. M. McMahon, C. Pierleoni, D. M. Ceperley, and M. A. Morales, "Benchmarking exchange-correlation functionals for hydrogen at high pressures using quantum monte carlo," *Phys. Rev. B*, vol. 89, no. 18, p. 184106, 2014.

[132] M. A. Morales, J. M. McMahon, C. Pierleoni, and D. M. Ceperley, "Towards a predictive first-principles description of solid molecular hydrogen with density functional theory," *Phys. Rev. B*, vol. 87, no. 18, p. 184107, 2013.

[133] S. Azadi and W. M. C. Foulkes, "Fate of density functional theory in the study of high-pressure solid hydrogen," *Phys. Rev. B*, vol. 88, no. 1, p. 014115, 2013.

[134] C. J. Pickard, M. Martinez-Canales, and R. J. Needs, "Erratum: Density functional theory study of phase IV of solid hydrogen," *Phys. Rev. B*, vol. 85, no. 21, p. 214114, 2012.

[135] Personal communication with Mark S. Johnson.

[136] J. M. McMahon, M. A. Morales, C. Pierleoni, and D. M. Ceperley, "The properties of hydrogen and helium under extreme conditions," *Rev. Mod. Phys*, vol. 84, no. 4, p. 1607, 2012.

[137] H.-K. Mao and R. J. Hemley, "Optical studies of hydrogen above 200 gigapascals: Evidence for metallization by band overlap," *Science*, vol. 244, no. 4911, pp. 1462–1465, 1989.

[138] P. Dalladay-Simpson, R. T. Howie, and E. Gregoryanz, "Evidence for a new phase of dense hydrogen above 325 gigapascals," *Nature*, vol. 529, no. 7584, pp. 63–67, 2016.

[139] R. P. Dias and I. F. Silvera, "Observation of the Wigner-Huntington transition to metallic hydrogen," *Science*, vol. 355, no. 6326, pp. 715–718, 2017.

[140] P. Loubeyre, F. Occelli, and P. Dumas, "Synchrotron infrared spectroscopic evidence of the probable transition to metal hydrogen," *Nature*, vol. 577, no. 7792, pp. 631–635, 2020.

[141] N. W. Ashcroft, "Hydrogen dominant metallic alloys: High temperature superconductors?," *Phys. Rev. Lett.*, vol. 92, no. 18, p. 187002, 2004.

[142] D. Duan, Y. Liu, Y. Ma, Z. Shao, B. Liu, and T. Cui, "Structure and superconductivity of hydrides at high pressures," *National Science Review*, vol. 4, no. 1, pp. 121–135, 2017.

[143] E. Zurek and T. Bi, "High-temperature superconductivity in alkaline and rare earth polyhydrides at high pressure: A theoretical perspective," *J. Chem. Phys.*, vol. 150, no. 5, p. 050901, 2019.

[144] J. A. Flores-Livas, L. Boeri, A. Sanna, G. Profeta, R. Arita, and M. Eremets, "A perspective on conventional high-temperature superconductors at high pressure: Methods and materials," *Physics Reports*, 2020.

[145] L. Boeri and G. B. Bachelet, "Viewpoint: The road to room-temperature conventional superconductivity," *J. Phys: Condens. Matt.*, vol. 31, no. 23, p. 234002, 2019.

[146] C. J. Pickard, I. Errea, and M. I. Eremets, "Superconducting hydrides under pressure," *Annu. Rev. Condens. Matter Phys.*, vol. 11, p. 57, 2020.

[147] A. Durajski and R. Szczesniak, "Properties of the pressure-induced superconducting state in trihydrides ScH_3 and LaH_3," *Supercond. Sci. Technol.*, vol. 27, no. 11, p. 115012, 2014.

[148] D. Y. Kim, R. H. Scheicher, and R. Ahuja, "Predicted high-temperature superconducting state in the hydrogen-dense transition-metal hydride YH_3 at 40 K and 17.7 GPa," *Phys. Rev. Lett.*, vol. 103, no. 7, p. 077002, 2009.

[149] Y. Li, J. Hao, H. Liu, S. T. John, Y. Wang, and Y. Ma, "Pressure-stabilized superconductive yttrium hydrides," *Sci. Rep.*, vol. 5, p. 9948, 2015.

[150] C. Heil, S. Di Cataldo, G. B. Bachelet, and L. Boeri, "Superconductivity in sodalite-like yttrium hydride clathrates," *Phys. Rev. B*, vol. 99, no. 22, p. 220502, 2019.

[151] N. P. Salke, M. M. D. Esfahani, Y. Zhang, I. A. Kruglov, J. Zhou, Y. Wang, E. Greenberg, V. B. Prakapenka, J. Liu, A. R. Oganov, and J.-F. Lin, "Synthesis of clathrate cerium superhydride CeH_9 at 80-100 GPa with atomic hydrogen sublattice," *Nat. Commun.*, vol. 10, no. 1, pp. 1–10, 2019.

[152] X. Li, X. Huang, D. Duan, C. J. Pickard, D. Zhou, H. Xie, Q. Zhuang, Y. Huang, Q. Zhou, B. Liu, and T. Cui, "Polyhydride CeH_9 with an atomic-like hydrogen clathrate structure," *Nat. Commun.*, vol. 10, no. 1, p. 3461, 2019.

[153] D. Zhou, D. V. Semenok, D. Duan, H. Xie, W. Chen, X. Huang, X. Li, B. Liu, A. R. Oganov, and T. Cui, "Superconducting praseodymium superhydrides," *Sci. Adv.*, vol. 6, no. 9, p. eaax6849, 2020.

[154] D. Zhou, D. V. Semenok, H. Xie, X. Huang, D. Duan, A. Aperis, P. M. Oppeneer, M. Galasso, A. I. Kartsev, A. G. Kvashnin, A. R. Oganov, and T. Cui, "High-pressure synthesis of magnetic neodymium polyhydrides," *J. Am. Chem. Soc.*, vol. 142, no. 6, pp. 2803–2811, 2020.

[155] H. Liu, I. I. Naumov, R. Hoffmann, N. Ashcroft, and R. J. Hemley, "Potential high-T_c superconducting lanthanum and yttrium hydrides at high pressure," *Proceedings of the National Academy of Sciences*, vol. 114, no. 27, pp. 6990–6995, 2017.

[156] F. Peng, Y. Sun, C. J. Pickard, R. J. Needs, Q. Wu, and Y. Ma, "Hydrogen clathrate structures in rare earth hydrides at high pressures: Possible route to room-temperature superconductivity," *Phys. Rev. Lett.*, vol. 119, no. 10, p. 107001, 2017.

[157] Z. M. Geballe, H. Liu, A. K. Mishra, M. Ahart, M. Somayazulu, Y. Meng, M. Baldini, and R. J. Hemley, "Synthesis and stability of lanthanum superhydrides," *Angewandte Chemie International Edition*, vol. 57, no. 3, pp. 688–692, 2018.

[158] H. Liu, I. I. Naumov, Z. M. Geballe, M. Somayazulu, S. T. John, and R. J. Hemley, "Dynamics and superconductivity in compressed lanthanum superhydride," *Phys. Rev. B*, vol. 98, no. 10, p. 100102, 2018.

[159] I. Errea, F. Belli, L. Monacelli, A. Sanna, T. Koretsune, T. Tadano, R. Bianco, M. Calandra, R. Arita, F. Mauri, and J. Flores-Livas, "Quantum crystal structure in the 250-kelvin superconducting lanthanum hydride," *Nature*, vol. 578, no. 7793, pp. 66–69, 2020.

[160] M. Somayazulu, M. Ahart, A. K. Mishra, Z. M. Geballe, M. Baldini, Y. Meng, V. V. Struzhkin, and R. J. Hemley, "Evidence for superconductivity above 260 K in lanthanum superhydride at megabar pressures," *Phys. Rev. Lett.*, vol. 122, no. 2, p. 027001, 2019.

[161] A. Drozdov, P. Kong, V. Minkov, S. Besedin, M. Kuzovnikov, S. Mozaffari, L. Balicas, F. Balakirev, D. Graf, V. Prakapenka, E. Greenberg, D. Knyazev, M. Tkacz, and M. Eremets, "Superconductivity at 250 K in lanthanum hydride under high pressures," *Nature*, vol. 569, no. 7757, p. 528, 2019.

[162] A. Drozdov, M. Eremets, I. Troyan, V. Ksenofontov, and S. Shylin, "Conventional superconductivity at 203 kelvin at high pressures in the sulfur hydride system," *Nature*, vol. 525, no. 7567, p. 73, 2015.

[163] A. M. Shipley, M. J. Hutcheon, M. S. Johnson, R. J. Needs, and C. J. Pickard, "Stability and superconductivity of lanthanum and yttrium decahydrides," *Phys. Rev. B*, vol. 101, no. 22, p. 224511, 2020.

[164] I. A. Troyan, D. V. Semenok, l. G. Kvashnin, A. V. Sadakov, O. A. Sobolevskiy, V. M. Pudalov, A. G. Ivanova, V. B. Prakapenka, E. Greenberg, A. G. Gavriliuk, V. V. Struzhkin, A. Bergara, I. Errea, R. Bianco, M. Calandra, F. Mauri, L. Monacelli, R. Akashi, and A. R. Oganov, "Anomalous high-temperature superconductivity in YH_6," *arXiv preprint arXiv:1908.01534*, 2019.

[165] P. Kong, V. Minkov, M. Kuzovnikov, S. Besedin, A. Drozdov, S. Mozaffari, L. Balicas, F. Balakirev, V. Prakapenka, E. Greenberg, D. Knyazev, and E. MI, "Superconductivity up to 243 K in yttrium hydrides under high pressure," *arXiv preprint arXiv:1909.10482*, 2019.

[166] P. Blaha, K. Schwarz, G. K. Madsen, D. Kvasnicka, and J. Luitz. http://www.wien2k.at/reg_user/textbooks/usersguide.pdf/, 2001. Wien2k user guide.

[167] M. Rutter, "C2x: A tool for visualisation and input preparation for CASTEP and other electronic structure codes," *Computer Physics Communications*, vol. 225, pp. 174–179, 2018.

[168] C. B. Barber, D. P. Dobkin, and H. T. Huhdanpaa, "The quickhull algorithm for convex hulls," *ACM Trans. on Mathematical Software*, vol. 22, no. 4, pp. 469–483, 1996.

[169] I. A. Kruglov, D. V. Semenok, H. Song, R. L. Szczesniak, I. A. Wrona, R. Akashi, M. M. D. Esfahani, D. Duan, T. Cui, A. G. Kvashnin, and A. R. Oganov, "Superconductivity of LaH_{10} and LaH_{16} polyhydrides," *Phys. Rev. B*, vol. 101, no. 2, p. 024508, 2020.

[170] C. Heil, G. B. Bachelet, and L. Boeri, "Absence of superconductivity in iron polyhydrides at high pressures," *Phys. Rev. B*, vol. 97, no. 21, p. 214510, 2018.

[171] W. Sano, T. Koretsune, T. Tadano, R. Akashi, and R. Arita, "Effect of van hove singularities on high-T_c superconductivity in H_3S," *Phys. Rev. B*, vol. 93, no. 9, p. 094525, 2016.

[172] P. B. Allen and V. Heine, "Theory of the temperature dependence of electronic band structures," *J. Phys. C*, vol. 9, no. 12, p. 2305, 1976.

[173] P. B. Allen and M. Cardona, "Theory of the temperature dependence of the direct gap of germanium," *Phys. Rev. B*, vol. 23, no. 4, p. 1495, 1981.

[174] P. B. Allen and M. Cardona, "Temperature dependence of the direct gap of si and ge," *Phys. Rev. B*, vol. 27, no. 8, p. 4760, 1983.

[175] H. Y. Fan, "Temperature dependence of the energy gap in monatomic semiconductors," *Phys. Rev.*, vol. 78, no. 6, p. 808, 1950.

[176] H. Y. Fan, "Temperature dependence of the energy gap in semiconductors," *Phys. Rev.*, vol. 82, no. 6, p. 900, 1951.

[177] S. Poncé, G. Antonius, Y. Gillet, P. Boulanger, J. L. Janssen, A. Marini, M. Côté, and X. Gonze, "Temperature dependence of electronic eigenenergies in the adiabatic harmonic approximation," *Phys. Rev. B*, vol. 90, no. 21, p. 214304, 2014.

[178] A. Marini, C. Hogan, M. Grüning, and D. Varsano, "Yambo: an ab initio tool for excited state calculations," *Computer Physics Communications*, vol. 180, no. 8, pp. 1392–1403, 2009.

[179] D. Sangalli, A. Ferretti, H. Miranda, C. Attaccalite, I. Marri, E. Cannuccia, P. Melo, M. Marsili, F. Paleari, A. Marrazzo, G. Prandini, P. Bonfà, M. O. Atambo, F. Affinito, M. Palummo, A. Molina-Sánchez, C. Hogan, M. Grüning, D. Varsano, and A. Marini, "Many-body perturbation theory calculations using the yambo code," *J. Phys.: Condens. Matter*, vol. 31, p. 325902, may 2019.

[180] Personal communication with Dr Bartomeu Monserrat.

[181] B. Monserrat, E. A. Engel, and R. J. Needs, "Giant electron-phonon interactions in molecular crystals and the importance of nonquadratic coupling," *Phys. Rev. B*, vol. 92, no. 14, p. 140302, 2015.

[182] B. Monserrat, N. Drummond, C. J. Pickard, and R. Needs, "Electron-phonon coupling and the metallization of solid helium at terapascal pressures," *Phys. Rev. Lett.*, vol. 112, no. 5, p. 055504, 2014.

[183] B. Rousseau and A. Bergara, "Giant anharmonicity suppresses superconductivity in AlH_3 under pressure," *Phys. Rev. B*, vol. 82, no. 10, p. 104504, 2010.

[184] J. Gilman, "Lithium dihydrogen fluoride - an approach to metallic hydrogen," *Phys. Rev. Lett.*, vol. 26, no. 10, pp. 546–548, 1971.

[185] Y. Sun, J. Lv, Y. Xie, H. Liu, and Y. Ma, "Route to a superconducting phase above room temperature in electron-doped hydride compounds under high pressure," *Phys. Rev. Lett.*, vol. 123, no. 9, p. 097001, 2019.

[186] C. Heil and L. Boeri, "Influence of bonding on superconductivity in high-pressure hydrides," *Phys. Rev. B*, vol. 92, no. 6, p. 060508, 2015.

[187] M. L. Cohen and P. W. Anderson, "Comments on the maximum superconducting transition temperature," in *AIP Conference Proceedings*, vol. 4, pp. 17–27, AIP, 1972.

[188] D. V. Semenok, I. A. Kruglov, I. A. Savkin, A. G. Kvashnin, and A. R. Oganov, "On distribution of superconductivity in metal hydrides," *Curr. Opin. Solid State Mater. Sci.*, vol. 24, no. 2, p. 100808, 2020.

[189] Y. Xie, Q. Li, A. Oganov, and H. Wang, "Superconductivity of lithium-doped hydrogen under high pressure," *Acta Crystallographica Section C: Structural Chemistry*, vol. 70, no. 2, pp. 104–111, 2014.

[190] D. Zhou, X. Jin, X. Meng, G. Bao, Y. Ma, B. Liu, and T. Cui, "Ab initio study revealing a layered structure in hydrogen-rich KH_6 under high pressure," *Phys. Rev. B*, vol. 86, no. 1, p. 014118, 2012.

[191] S. Yu, Q. Zeng, A. R. Oganov, C. Hu, G. Frapper, and L. Zhang, "Exploration of stable compounds, crystal structures, and superconductivity in the Be-H system," *AIP Advances*, vol. 4, no. 10, p. 107118, 2014.

[192] D. C. Lonie, J. Hooper, B. Altintas, and E. Zurek, "Metallization of magnesium polyhydrides under pressure," *Phys. Rev. B*, vol. 87, no. 5, p. 054107, 2013.

[193] J. S. Tse, Z. Song, Y. Yao, J. S. Smith, S. Desgreniers, and D. D. Klug, "Structure and electronic properties of BaH_2 at high pressure," *Solid State Communications*, vol. 149, no. 43, pp. 1944 – 1946, 2009.

[194] A. G. Kvashnin, D. V. Semenok, I. A. Kruglov, I. A. Wrona, and A. R. Oganov, "High-temperature superconductivity in a th-h system under pressure conditions," *ACS applied materials & interfaces*, vol. 10, no. 50, pp. 43809–43816, 2018.

[195] H. Wang, S. T. John, K. Tanaka, T. Iitaka, and Y. Ma, "Superconductive sodalite-like clathrate calcium hydride at high pressures," *Proceedings of the National Academy of Sciences*, vol. 109, no. 17, pp. 6463–6466, 2012.

[196] T. P. Zemla, K. M. Szczesniak, A. Z. Kaczmarek, and S. V. Turchuk, "Characterization of the superconducting phase in tellurium hydride at high pressure," *Modern Physics Letters B*, p. 1950169, 2019.

[197] I. A. Kruglov, A. G. Kvashnin, A. F. Goncharov, A. R. Oganov, S. S. Lobanov, N. Holtgrewe, S. Jiang, V. B. Prakapenka, E. Greenberg, and A. V. Yanilkin, "Uranium polyhydrides at moderate pressures: Prediction, synthesis, and expected superconductivity," *Sci. Adv.*, vol. 4, no. 10, p. eaat9776, 2018.

[198] X. Feng, J. Zhang, G. Gao, H. Liu, and H. Wang, "Compressed sodalite-like MgH_6 as a potential high-temperature superconductor," *RSC Advances*, vol. 5, no. 73, pp. 59292–59296, 2015.

[199] Q. Gu, P. Lu, K. Xia, J. Sun, and D. Xing, "High-temperature superconducting phase of HBr under pressure predicted by first-principles calculations," *Phys. Rev. B*, vol. 96, no. 6, p. 064517, 2017.

[200] M. M. D. Esfahani, A. R. Oganov, H. Niu, and J. Zhang, "Superconductivity and unexpected chemistry of germanium hydrides under pressure," *Phys. Rev. B*, vol. 95, no. 13, p. 134506, 2017.

[201] Y.-K. Wei, J.-N. Yuan, F. I. Khan, G.-F. Ji, Z.-W. Gu, and D.-Q. Wei, "Pressure induced superconductivity and electronic structure properties of scandium hydrides using first principles calculations," *RSC Advances*, vol. 6, no. 85, pp. 81534–81541, 2016.

[202] L.-L. Liu, H.-J. Sun, C. Wang, and W.-C. Lu, "High-pressure structures of yttrium hydrides," *J. Phys. Condens. Matter*, vol. 29, no. 32, p. 325401, 2017.

[203] D. V. Semenok, A. G. Kvashnin, A. G. Ivanova, V. Svitlyk, V. Y. Fominski, A. V. Sadakov, O. A. Sobolevskiy, V. M. Pudalov, I. A. Troyan, and A. R. Oganov, "Superconductivity at 161 K in thorium hydride ThH_{10}: Synthesis and properties," *Materials Today*, 2019.

[204] N. Zarifi, T. Bi, H. Liu, and E. Zurek, "Crystal structures and properties of iron hydrides at high pressure," *J. Phys. Chem. C*, vol. 122, no. 42, pp. 24262–24269, 2018.

[205] K. V. Shanavas, L. Lindsay, and D. S. Parker, "Electronic structure and electron-phonon coupling in TiH_2," *Sci. Rep.*, vol. 6, no. 1, p. 28102, 2016.

[206] X.-F. Li, Z.-Y. Hu, and B. Huang, "Phase diagram and superconductivity of compressed zirconium hydrides," *Phys. Chem. Chem. Phys.*, vol. 19, no. 5, pp. 3538–3543, 2017.

[207] V. Z. Kresin, "High-T_c hydrides: interplay of optical and acoustic modes and comments regarding the upper limit of T_c," *J. Supercond. Nov. Magn.*, vol. 31, no. 11, pp. 3391–3395, 2018.

[208] Y. Liu, X. Huang, D. Duan, F. Tian, H. Liu, D. Li, Z. Zhao, X. Sha, H. Yu, H. Zhang, B. Liu, and T. Cui, "First-principles study on the structural and electronic properties of metallic HfH_2 under pressure," *Sci. Rep.*, vol. 5, p. 11381, 2015.

[209] D. Ohlendorf and E. Wicke, "Heat capacities between 1.5 and 16 K and superconductivity of v/h and nb/h alloys," *J. Phys. Chem. Solids*, vol. 40, no. 10, pp. 721 – 728, 1979.

[210] C. Chen, F. Tian, D. Duan, K. Bao, X. Jin, B. Liu, and T. Cui, "Pressure induced phase transition in MH_2 (M = V, Nb)," *J. Chem. Phys.*, vol. 140, no. 11, p. 114703, 2014.

[211] G. Gao, R. Hoffmann, N. W. Ashcroft, H. Liu, A. Bergara, and Y. Ma, "Theoretical study of the ground-state structures and properties of niobium hydrides under pressure," *Phys. Rev. B*, vol. 88, no. 18, p. 184104, 2013.

[212] Q. Zhuang, X. Jin, T. Cui, Y. Ma, Q. Lv, Y. Li, H. Zhang, X. Meng, and K. Bao, "Pressure-stabilized superconductive ionic tantalum hydrides," *Inorganic Chemistry*, vol. 56, no. 7, pp. 3901–3908, 2017.

[213] S. Yu, X. Jia, G. Frapper, D. Li, A. R. Oganov, Q. Zeng, and L. Zhang, "Pressure-driven formation and stabilization of superconductive chromium hydrides," *Sci. Rep.*, vol. 5, p. 17764, 2015.

[214] V. I. Spitsyn, V. E. Antonov, O. A. Balakhovskii, I. T. Belash, E. G. Ponyatovskii, V. I. Rashchupkin, and V. S. Shekhtman, "Structure and superconductive properties of the high-pressure phase in the technetium-hydrogen system," vol. 260, no. 1, pp. 795–798, 1982.

[215] F. Li, D. Wang, H. Du, D. Zhou, Y. Ma, and Y. Liu, "Structural evolution of FeH_4 under high pressure," *RSC Adv.*, vol. 7, pp. 12570–12575, 2017.

[216] A. G. Kvashnin, I. A. Kruglov, D. V. Semenok, and A. R. Oganov, "Iron superhydrides FeH_5 and FeH_6: Stability,eelectronic properties, and superconductivity," *J. Phys. Chem. C*, vol. 122, no. 8, pp. 4731–4736, 2018.

[217] Y. Liu, D. Duan, F. Tian, C. Wang, Y. Ma, D. Li, X. Huang, B. Liu, and T. Cui, "Stability and properties of the ru-h system at high pressure," *Phys. Chem. Chem. Phys.*, vol. 18, no. 3, pp. 1516–1520, 2016.

[218] Y. Liu, D. Duan, F. Tian, H. Liu, C. Wang, X. Huang, D. Li, Y. Ma, B. Liu, and T. Cui, "Pressure-induced structures and properties in indium hydrides," *Inorganic Chemistry*, vol. 54, no. 20, pp. 9924–9928, 2015.

[219] X. Ye, N. Zarifi, E. Zurek, R. Hoffmann, and N. Ashcroft, "High hydrides of scandium under pressure: Potential superconductors," *J. Phys. Chem. C*, vol. 122, no. 11, pp. 6298–6309, 2018.

[220] T. Skoskiewicz, A. W. Szafranski, W. Bujnowski, and B. Baranowski, "Isotope effect in the superconducting palladium-hydrogen-deuterium system," *J. Phys. C*, vol. 7, pp. 2670–2676, aug 1974.

[221] X. Li and F. Peng, "Superconductivity of pressure-stabilized vanadium hydrides," *Inorganic Chemistry*, vol. 56, no. 22, pp. 13759–13765, 2017.

[222] I. Errea, M. Calandra, and F. Mauri, "Anharmonic free energies and phonon dispersions from the stochastic self-consistent harmonic approximation: Application to platinum and palladium hydrides," *Phys. Rev. B*, vol. 89, no. 6, p. 064302, 2014.

[223] K. Tanaka, J. Tse, and H. Liu, "Electron-phonon coupling mechanisms for hydrogen-rich metals at high pressure," *Phys. Rev. B*, vol. 96, no. 10, p. 100502, 2017.

[224] C.-H. Hu, A. R. Oganov, Q. Zhu, G.-R. Qian, G. Frapper, A. O. Lyakhov, and H.-Y. Zhou, "Pressure-induced stabilization and insulator-superconductor transition of bh," *Phys. Rev. Lett.*, vol. 110, no. 16, p. 165504, 2013.

[225] Y.-K. Wei, N.-N. Ge, G.-F. Ji, X.-R. Chen, L.-C. Cai, S.-Q. Zhou, and D.-Q. Wei, "Elastic, superconducting, and thermodynamic properties of the cubic metallic phase of AlH_3 via first-principles calculations," *J. Appl. Phys.*, vol. 114, no. 11, p. 114905, 2013.

[226] P. Hou, X. Zhao, F. Tian, D. Li, D. Duan, Z. Zhao, B. Chu, B. Liu, and T. Cui, "High pressure structures and superconductivity of $AlH_3(H_2)$ predicted by first principles," *RSC Advances*, vol. 5, no. 7, pp. 5096–5101, 2015.

[227] X. Li, H. Liu, and F. Peng, "Crystal structures and superconductivity of technetium hydrides under pressure," *Phys. Chem. Chem. Phys.*, vol. 18, no. 41, pp. 28791–28796, 2016.

[228] R. Szczesniak and A. Durajski, "Superconducting state above the boiling point of liquid nitrogen in the GaH_3 compound," *Supercond. Sci. Technol.*, vol. 27, no. 1, p. 015003, 2013.

[229] J. Hooper, B. Altintas, A. Shamp, and E. Zurek, "Polyhydrides of the alkaline earth metals: a look at the extremes under pressure," *J. Phys. Chem. C*, vol. 117, no. 6, pp. 2982–2992, 2013.

[230] Y. Yao, J. S. Tse, Y. Ma, and K. Tanaka, "Superconductivity in high-pressure SiH_4," *Europhysics Letters (EPL)*, vol. 78, p. 37003, apr 2007.

[231] M. Eremets, I. Trojan, S. Medvedev, J. Tse, and Y. Yao, "Superconductivity in hydrogen dominant materials: Silane," *Science*, vol. 319, no. 5869, pp. 1506–1509, 2008.

[232] Y. Li, G. Gao, Y. Xie, Y. Ma, T. Cui, and G. Zou, "Superconductivity at $\tilde{1}00$ K in dense $SiH_4(H_2)_2$ predicted by first principles," *Proceedings of the National Academy of Sciences*, vol. 107, no. 36, pp. 15708–15711, 2010.

[233] X. Jin, X. Meng, Z. He, Y. Ma, B. Liu, T. Cui, G. Zou, and H.-k. Mao, "Superconducting high-pressure phases of disilane," *Proceedings of the National Academy of Sciences*, vol. 107, no. 22, pp. 9969–9973, 2010.

[234] A. P. Drozdov, V. S. Minkov, S. P. Besedin, P. P. Kong, M. A. Kuzovnikov, D. A. Knyazev, and M. I. Eremets, "Superconductivity at 215 K in lanthanum hydride at high pressures," *arXiv preprint arXiv:1808.07039*, 2018.

[235] C. Zhang, X.-J. Chen, R.-Q. Zhang, and H.-Q. Lin, "Chemical trend of pressure-induced metallization in alkaline earth hydrides," *J. Phys. Chem. C*, vol. 114, pp. 14614–14617, Sep 2010.

[236] F. Chollet *et al.*, "Keras." https://keras.io, 2015.

[237] M. Abadi, A. Agarwal, P. Barham, E. Brevdo, Z. Chen, C. Citro, G. S. Corrado, A. Davis, J. Dean, mMatthieu Devin, S. Ghemawat, I. Goodfellow, A. Harp, G. Irving, M. Isard, Y. Jia, R. Jozefowicz, L. Kaiser, M. Kudlur, J. Levenberg, D. Mané, R. Monga, S. Moore, D. Murray, C. Olah, M. Schuster, J. Shlens, B. Steiner, I. Sutskever, K. Talwar, P. Tucker, V. Vanhoucke, V. Vasudevan, F. Viégas, O. Vinyals, P. Warden, M. Wattenberg, M. Wicke, Y. Yu, and X. Zheng, "TensorFlow: Large-scale machine learning on heterogeneous systems," 2015. Software available from tensorflow.org.

[238] D. P. Kingma and J. Ba, "Adam: A method for stochastic optimization," 2014.

[239] G. Klambauer, T. Unterthiner, A. Mayr, and S. Hochreiter, "Self-normalizing neural networks," *Advances in Neural Information Processing Systems (NIPS)*, vol. 30, 2017.

[240] D. A. Clevert, T. Unterthiner, and S. Hochreiter, "Fast and accurate deep network learning by exponential linear units (ELUs)," 2015.

[241] I. Errea, M. Calandra, C. J. Pickard, J. Nelson, R. J. Needs, Y. Li, H. Liu, Y. Zhang, Y. Ma, and F. Mauri, "High-pressure hydrogen sulfide from first principles: A strongly anharmonic phonon-mediated superconductor," *Phys. Rev. Lett.*, vol. 114, no. 15, p. 157004, 2015.

[242] A. Shamp, J. Hooper, and E. Zurek, "Compressed cesium polyhydrides: Cs^+ sublattices and H_3-three-connected nets," *Inorganic Chemistry*, vol. 51, no. 17, pp. 9333–9342, 2012.

[243] J. Hooper and E. Zurek, "Rubidium polyhydrides under pressure: Emergence of the linear H_3- species," *Chemistry–A European Journal*, vol. 18, no. 16, pp. 5013–5021, 2012.

[244] Input files for the structures predicted in the machine learning project (Chapter 5) can be found at https://doi.org/10.17863/CAM.48347.

[245] B. Chen, L. J. Conway, W. Sun, X. Kuang, C. Lu, and A. Hermann, "Phase stability and superconductivity of lead hydrides at high pressure," *Physical Review B*, vol. 103, no. 3, p. 035131, 2021.

[246] T. Bi, N. Zarifi, T. Terpstra, and E. Zurek, "The search for superconductivity in high pressure hydrides," Elsevier, 2019.

[247] D. V. Semenok, A. G. Kvashnin, I. A. Kruglov, and A. R. Oganov, "Actinium hydrides AcH_{10}, AcH_{12}, and AcH_{16} as high-temperature conventional superconductors," *J. Phys. Chem. Lett.*, vol. 9, no. 8, pp. 1920–1926, 2018.

[248] A. M. Shipley, M. J. Hutcheon, R. J. Needs, and C. J. Pickard, "High-throughput discovery of high-temperature conventional superconductors," *arXiv:2105.02296*, 2021.

[249] Y. Quan, S. S. Ghosh, and W. E. Pickett, "Compressed hydrides as metallic hydrogen superconductors," *Phys. Rev. B*, vol. 100, no. 18, p. 184505, 2019.

[250] Y. Fu, X. Du, L. Zhang, F. Peng, M. Zhang, C. J. Pickard, R. J. Needs, D. J. Singh, W. Zheng, and Y. Ma, "High-pressure phase stability and superconductivity of pnictogen hydrides and chemical trends for compressed hydrides," *Chemistry of Materials*, vol. 28, no. 6, pp. 1746–1755, 2016.

[251] K. Abe and N. Ashcroft, "Crystalline diborane at high pressures," *Phys. Rev. B*, vol. 84, no. 10, p. 104118, 2011.

[252] Y. Ma, D. Duan, D. Li, Y. Liu, F. Tian, H. Yu, C. Xu, Z. Shao, B. Liu, and T. Cui, "High-pressure structures and superconductivity of bismuth hydrides," *arXiv preprint arXiv:1511.05291*, 2015.

[253] G. Gao, A. R. Oganov, A. Bergara, M. Martinez-Canales, T. Cui, T. Iitaka, Y. Ma, and G. Zou, "Superconducting high pressure phase of germane," *Phys. Rev. Lett.*, vol. 101, no. 10, p. 107002, 2008.

[254] G. Zhong, C. Zhang, X. Chen, Y. Li, R. Zhang, and H. Lin, "Structural, electronic, dynamical, and superconducting properties in dense $GeH_4(H_2)_2$," *J. Phys. Chem. C*, vol. 116, no. 8, pp. 5225–5234, 2012.

[255] D. Duan, F. Tian, Y. Liu, X. Huang, D. Li, H. Yu, Y. Ma, B. Liu, and T. Cui, "Enhancement of T_c in the atomic phase of iodine-doped hydrogen at high pressures," *Phys. Chem. Chem. Phys.*, vol. 17, no. 48, pp. 32335–32340, 2015.

[256] A. Shamp and E. Zurek, "Superconducting high-pressure phases composed of hydrogen and iodine," *J. Phys. Chem. Lett.*, vol. 6, no. 20, pp. 4067–4072, 2015.

[257] D. Duan, Y. Liu, F. Tian, D. Li, X. Huang, Z. Zhao, H. Yu, B. Liu, W. Tian, and T. Cui, "Pressure-induced metallization of dense $(H_2S)_2H_2$ with high-T_c superconductivity," *Sci. Rep.*, vol. 4, p. 6968, 2014.

[258] S. Zhang, Y. Wang, J. Zhang, H. Liu, X. Zhong, H.-F. Song, G. Yang, L. Zhang, and Y. Ma, "Phase diagram and high-temperature superconductivity of compressed selenium hydrides," *Sci. Rep.*, vol. 5, p. 15433, 2015.

[259] Y. Liu, D. Duan, F. Tian, C. Wang, G. Wu, Y. Ma, H. Yu, D. Li, B. Liu, and T. Cui, "Prediction of stoichiometric PoH_n compounds: Crystal structures and properties," *RSC Advances*, vol. 5, no. 125, pp. 103445–103450, 2015.

[260] X. Zhong, H. Wang, J. Zhang, H. Liu, S. Zhang, H.-F. Song, G. Yang, L. Zhang, and Y. Ma, "Tellurium hydrides at high pressures: High-temperature superconductors," *Phys. Rev. Lett.*, vol. 116, no. 5, p. 057002, 2016.

[261] Y. Liu, D. Duan, X. Huang, F. Tian, D. Li, X. Sha, C. Wang, H. Zhang, T. Yang, B. Liu, and T. Cui, "Structures and properties of osmium hydrides under pressure from first principle calculation," *J. Phys. Chem. C*, vol. 119, no. 28, pp. 15905–15911, 2015.

[262] Y. Ma, D. Duan, D. Li, Y. Liu, F. Tian, X. Huang, Z. Zhao, H. Yu, B. Liu, and T. Cui, "The unexpected binding and superconductivity in SbH_4 at high pressure," *arXiv preprint arXiv:1506.03889*, 2015.

[263] M. M. D. Esfahani, Z. Wang, A. R. Oganov, H. Dong, Q. Zhu, S. Wang, M. S. Rakitin, and X.-F. Zhou, "Superconductivity of novel tin hydrides (Sn_nH_m) under pressure," *Sci. Rep.*, vol. 6, p. 22873, 2016.

[264] S. Zheng, S. Zhang, Y. Sun, J. Zhang, J. Lin, G. Yang, and A. Bergara, "Structural and superconducting properties of tungsten hydrides under high pressure," *Frontiers in Physics*, vol. 6, p. 101, 2018.

[265] K. Abe, "High-pressure properties of dense metallic zirconium hydrides studied by ab initio calculations," *Phys. Rev. B*, vol. 98, no. 13, p. 134103, 2018.

[266] H. Sit. https://towardsdatascience.com/, 2019. Quick Start to Gaussian Process Regression.

[267] C. E. C. E. Rasmussen and C. K. I. Williams, *Gaussian Processes for Machine Learning*. MIT Press, 2006.

[268] https://uk.mathworks.com/help/stats/fitrgp.html. MATLAB GPR fitting documentation.

[269] R. T. Howie, O. Narygina, C. L. Guillaume, S. Evans, and E. Gregoryanz, "High-pressure synthesis of lithium hydride," *Phys. Rev. B*, vol. 86, no. 6, p. 064108, 2012.

[270] K. Abe, "Hydrogen-rich scandium compounds at high pressures," *Phys. Rev. B*, vol. 96, no. 14, p. 144108, 2017.

[271] J. Nagamatsu, N. Nakagawa, T. Muranaka, Y. Zenitani, and J. Akimitsu, "Superconductivity at 39 K in magnesium diboride," *Nature*, vol. 410, pp. 63–64, Mar 2001.

[272] G. Wu, Y. L. Xie, H. Chen, M. Zhong, R. H. Liu, B. C. Shi, Q. J. Li, X. F. Wang, T. Wu, Y. J. Yan, J. J. Ying, and X. H. Chen, "Superconductivity at 56 K in samarium-doped SrFeAsF," *J. Phys.: Condens. Matt*, vol. 21, p. 142203, mar 2009.

[273] A. Schilling, M. Cantoni, J. D. Guo, and H. R. Ott, "Superconductivity above 130 K in the Hg–Ba–Ca–Cu–O system," *Nature*, vol. 363, pp. 56–58, May 1993.

[274] E. Snider, N. Dasenbrock-Gammon, R. McBride, M. Debessai, H. Vindana, K. Vencatasamy, K. V. Lawler, A. Salamat, and R. P. Dias, "Room-temperature superconductivity in a carbonaceous sulfur hydride," *Nature*, vol. 586, no. 7829, pp. 373–377, 2020.

[275] J. E. Moussa and M. L. Cohen, "Two bounds on the maximum phonon-mediated superconducting transition temperature," *Phys. Rev. B*, vol. 74, p. 094520, Sep 2006.

[276] X. Wan, H.-C. Ding, S. Y. Savrasov, and C.-G. Duan, "Electron-phonon superconductivity near charge-density-wave instability in $LaO_{0.5}F_{0.5}BiS_2$: Density-functional calculations," *Phys. Rev. B*, vol. 87, p. 115124, Mar 2013.

[277] P. Baettig and E. Zurek, "Pressure-stabilized sodium polyhydrides: NaH_n ($n > 1$)," *Phys. Rev. Lett.*, vol. 106, p. 237002, Jun 2011.

[278] V. V. Struzhkin, D. Y. Kim, E. Stavrou, T. Muramatsu, H.-k. Mao, C. J. Pickard, R. J. Needs, V. B. Prakapenka, and A. F. Goncharov, "Synthesis of sodium polyhydrides at high pressures," *Nat. Commun.*, vol. 7, p. 12267, Jul 2016.

[279] G. Bergmann and D. Rainer, "The sensitivity of the transition temperature to changes in $\alpha^2F(\omega)$," *Zeitschrift für Physik*, vol. 263, pp. 59–68, Aug 1973.

[280] J. Hooper and E. Zurek, "High pressure potassium polyhydrides: A chemical perspective," *The Journal of Physical Chemistry C*, vol. 116, no. 24, pp. 13322–13328, 2012.

[281] S. Qian, X. Sheng, X. Yan, Y. Chen, and B. Song, "Theoretical study of stability and superconductivity of ScH_n (n= 4–8) at high pressure," *Phys. Rev. B*, vol. 96, no. 9, p. 094513, 2017.

[282] E. Zurek, R. Hoffmann, N. W. Ashcroft, A. R. Oganov, and A. O. Lyakhov, "A little bit of lithium does a lot for hydrogen," *Proceedings of the National Academy of Sciences*, vol. 106, no. 42, pp. 17640–17643, 2009.

[283] Y. Wang, H. Wang, S. T. John, T. Iitaka, and Y. Ma, "Structural morphologies of high-pressure polymorphs of strontium hydrides," *Phys. Chem. Chem. Phys.*, vol. 17, no. 29, pp. 19379–19385, 2015.

[284] B. M. Klein and D. A. Papaconstantopoulos, "Electron-phonon interaction and superconductivity in transition metals and transition-metal carbides," *Phys. Rev. Lett.*, vol. 32, pp. 1193–1195, May 1974.

[285] A. J. Cohen, P. Mori-Sánchez, and W. Yang, "Assessment and formal properties of exchange-correlation functionals constructed from the adiabatic connection," *J. Chem. Phys*, vol. 127, no. 3, p. 034101, 2007.

[286] G. Grosso and G. P. Parravicini, *Band theory of crystals*. Academic Press, 2nd ed., 2013.

Appendix A

The exchange-correlation hole and the sum rule

Derivations of this sort can be found in general electronic structure textbooks, including Ref. [11], and more formal derivations are outlined in, for example, Ref [285].

The energy functional is written as $E[\rho(\mathbf{r})] = E_{KE}[\rho(\mathbf{r})] + \langle \hat{V}_{ee} \rangle + \int d\mathbf{r} V_{ext}(\mathbf{r})\rho(\mathbf{r})$, where $\langle \hat{V}_{ee} \rangle$ is the energetic contribution from all electron-electron interactions (which would, in theory, include the difference between the interacting and non-interacting kinetic energy, although this will not be addressed directly here). Separating out the classical Coulomb contributions,

$$E[\rho(\mathbf{r})] = E_{KE}[\rho(\mathbf{r})] + \left[\int d\mathbf{r} V_{ext}(\mathbf{r})\rho(\mathbf{r}) + E_H[\rho(\mathbf{r})] \right] + \left[\langle \hat{V}_{ee} \rangle - E_H[\rho(\mathbf{r})] \right], \quad \text{(A.1)}$$

where the first set of square brackets contains all classical Coulomb contributions to the energy (from both electron-nucleus and electron-electron interactions). Comparing Eq. A.1 to Eq. 2.30, we see that $E_{XC}[\rho(\mathbf{r})] = \langle \hat{V}_{ee} \rangle - E_H[\rho(\mathbf{r})]$, as expected.

The electron-electron interaction term involves interacting pairs of electrons, prompting us to express it as

$$\langle \hat{V}_{ee} \rangle = \frac{1}{2} \sum_{\sigma,\sigma'} \int d\mathbf{r} d\mathbf{r}' \frac{\rho(\mathbf{r},\sigma;\mathbf{r}',\sigma')}{|\mathbf{r}-\mathbf{r}'|}, \quad \text{(A.2)}$$

where $\rho(\mathbf{r},\sigma;\mathbf{r}',\sigma')$ is the spin-dependent *pair* density, representing the joint probability of finding an electron of spin σ at $\mathbf{r}$ *and* an electron of spin σ' at $\mathbf{r}'$. It is given by

$$\rho(\mathbf{r},\sigma;\mathbf{r}',\sigma') = N(N-1) \sum_{\sigma_3,\ldots\sigma_N} \int d\mathbf{r}_3 \ldots d\mathbf{r}_N |\psi(\mathbf{r},\sigma;\mathbf{r}',\sigma';\mathbf{r}_3,\sigma_3;\ldots\mathbf{r}_N\sigma_N|^2. \quad \text{(A.3)}$$

For a normalised wavefunction, the electron density is expressed in terms of the pair density as

$$\rho(\mathbf{r},\sigma) = \frac{1}{N-1}\sum_{\sigma'}\int d\mathbf{r}'\rho(\mathbf{r},\sigma;\mathbf{r}',\sigma'). \tag{A.4}$$

Integrating both sides of Eq. A.4 over $\mathbf{r}$, summing over σ, and using $\sum_\sigma \int \rho(\mathbf{r},\sigma)d\mathbf{r} = N$, we obtain

$$\sum_{\sigma,\sigma'}\int d\mathbf{r}d\mathbf{r}'\rho(\mathbf{r},\sigma;\mathbf{r}',\sigma') = N(N-1). \tag{A.5}$$

For classical particles, the pair density is simply the product of individual densities (since they are seen as independent or uncorrelated). However, for quantum particles exchange-correlation effects act to reduce the electron density at $\mathbf{r}$ due to the presence of a second electron at another position, $\mathbf{r}'$. Each electron creates a depletion of density around itself; this is expressed mathematically as

$$\rho(\mathbf{r},\sigma;\mathbf{r}',\sigma') = \rho(\mathbf{r},\sigma)\rho(\mathbf{r}',\sigma') + \rho(\mathbf{r},\sigma)\rho_{XC}(\mathbf{r},\sigma;\mathbf{r}',\sigma'), \tag{A.6}$$

where $\rho_{XC}(\mathbf{r},\sigma;\mathbf{r}',\sigma')$ is the spin-dependent exchange-correlation hole density. We can derive a condition that this hole density must obey by integrating Eq. A.6 over $d\mathbf{r}'$, summing over σ' and using the results of Eq. A.4 and $\sum_\sigma \int \rho(\mathbf{r},\sigma)d\mathbf{r} = N$. This gives

$$\begin{aligned}(N-1)\rho(\mathbf{r},\sigma) = N\rho(\mathbf{r},\sigma) + \rho(\mathbf{r},\sigma)\sum_{\sigma'}\int d\mathbf{r}'\rho_{XC}(\mathbf{r},\sigma;\mathbf{r}',\sigma') \\ \rightarrow \sum_{\sigma'}\int d\mathbf{r}'\rho_{XC}(\mathbf{r},\sigma;\mathbf{r}',\sigma') = -1.\end{aligned} \tag{A.7}$$

The final result of Eq. A.7 is called the sum rule. Now, returning to our expression for $E_{XC}[\rho(\mathbf{r},\sigma)]$,

$$\begin{aligned}E_{XC}[\rho(\mathbf{r})] = \langle\hat{V}_{ee}\rangle - E_H[\rho(\mathbf{r})] = \\ \frac{1}{2}\sum_{\sigma,\sigma'}\int d\mathbf{r}d\mathbf{r}'\frac{\rho(\mathbf{r},\sigma)\rho(\mathbf{r}',\sigma') + \rho(\mathbf{r},\sigma)\rho_{XC}(\mathbf{r},\sigma;\mathbf{r}',\sigma')}{|\mathbf{r}-\mathbf{r}'|} - E_H[\rho(\mathbf{r})] = \\ \frac{1}{2}\sum_{\sigma,\sigma'}\int d\mathbf{r}d\mathbf{r}'\frac{\rho(\mathbf{r},\sigma)\rho_{XC}(\mathbf{r},\sigma;\mathbf{r}',\sigma')}{|\mathbf{r}-\mathbf{r}'|},\end{aligned} \tag{A.8}$$

which may be interpreted as the interaction of each electron with its own exchange-correlation hole.

Appendix B

Gaspari-Gyorffy theory proofs

B.1 Expressing matrix elements in terms of phase shifts

The matrix elements appearing in Eq. 2.125 can be evaluated directly. Following Ref. [94] we write $\int_0^{R_{MT}} drr^2 R_l \frac{dV}{dr} R_{l+1} = \int_0^{R_{MT}} dr u_l \frac{dV}{dr} u_{l+1}$. We then differentiate the wave equation for u_l, multiply it by u_{l+1}, and integrate the result. We follow these same three steps with u_{l+1} and u_l exchanged. Adding the two resulting equations, inserting the wave equation and cancelling terms, we come to

$$\int_0^{R_{MT}} drr^2 R_l \frac{dV}{dr} R_{l+1} = \frac{1}{2}[u_l u'_{l+1} - 2u'_l u'_{l+1} + u''_l u_{l+1}]_0^{R_{MT}} + [(l+1)/R][u_l u'_{l+1} - u'_l u_{l+1}]_0^R.$$

For $r > R_{MT}$, we can insert Eq. 2.123 and use the known properties of the spherical Bessel functions and Neumann functions and their derivatives to reach

$$\int_0^{R_{MT}} drr^2 R_l \frac{dV}{dr} R_{l+1} = sin(\delta_{l+1} - \delta_l). \tag{B.1}$$

B.2 Calculating the free-scatterer density of states

The free-scatterer DOS appearing in the GG formula is given by

$$N_l^{(1)} = \frac{\sqrt{E_F}}{\pi}(2l+1)\int_0^{R_{MT}} R_l^2(r, E_F) r^2 dr.$$

In order to evaluate this, we begin from the differential equation Eq. 2.126 and follow Appendix B2 of Ref. [286]. For arbitrarily chosen energies E_1 and E_2, we have $u_l(r, E_1) =$

$rR_l(r,E_1)$ and $u_l(r,E_2) = rR_l(r,E_2)$. Then

$$\frac{d^2u_l(r,E_1)}{dr^2} = \left[V(r) + \frac{l(l+1)}{r^2} - E_1\right]u_l(r,E_1), \tag{B.2}$$

$$\frac{d^2u_l(r,E_2)}{dr^2} = \left[V(r) + \frac{l(l+1)}{r^2} - E_2\right]u_l(r,E_2). \tag{B.3}$$

Multiplying Eq. B.2 by $u_l(r,E_2)$ and Eq. B.3 by $u_l(r,E_1)$ and subtracting one result from the other:

$$\frac{d^2u_l(r,E_1)}{dr^2}u_l(r,E_2) - \frac{d^2u_l(r,E_2)}{dr^2}u_l(r,E_1) = (E_2-E_1)u_l(r,E_1)u_l(r,E_2).$$

Integrating both sides of this expression over the radial co-ordinate

$$\left[u_l(r,E_2)\frac{du_l(r,E_1)}{dr}\right]_0^{R_{MT}} - \int_0^{R_{MT}} \frac{du_l(r,E_1)}{dr}\frac{du_l(r,E_2)}{dr}dr - \left[u_l(r,E_1)\frac{du_l(r,E_2)}{dr}\right]_0^{R_{MT}} + \int_0^{R_{MT}} \frac{du_l(r,E_2)}{dr}\frac{du_l(r,E_1)}{dr}dr$$

$$= \left[u_l(r,E_2)\frac{du_l(r,E_1)}{dr}\right]_0^{R_{MT}} - \left[u_l(r,E_1)\frac{du_l(r,E_2)}{dr}\right]_0^{R_{MT}}$$

$$= (E_2-E_1)\int_0^{R_{MT}} u_l(r,E_1)u_l(r,E_2)dr.$$

Rearranging and considering $\frac{u_l'}{u_l} = \frac{(rR_l)'}{rR_l} = \frac{R_l+rR_l'}{rR_l} = \frac{1}{r} + \frac{R_l'}{R_l}$,

$$\frac{\frac{R_l'(R_{MT},E_2)}{R_l(R_{MT},E_2)} - \frac{R_l'(R_{MT},E_1)}{R_l(R_{MT},E_1)}}{(E_2-E_1)} = \frac{-\int_0^{R_{MT}} r^2R_l(r,E_1)R_l(r,E_2)dr}{R_{MT}^2R_l(R_{MT},E_1)R_l(R_{MT},E_2)}.$$

Then, taking $E_1 \to E_2$,

$$\frac{\partial}{\partial E}\frac{R_l'(R_{MT},E)}{R_l(R_{MT},E)} = \frac{-\int_0^{R_{MT}} r^2R_l^2(r,E)dr}{R_{MT}^2R_l^2(R_{MT},E)},$$

which leads to the relation

$$\int_0^{R_{MT}} R_l^2(r,E)r^2dr = -R_l^2(R_{MT},E)R_{MT}^2\frac{\partial}{\partial E}\frac{R_l'(R_{MT},E)}{R_l(R_{MT},E)}.$$

Appendix C

Cs-H and Rb-H enthalpy plots and metallicity

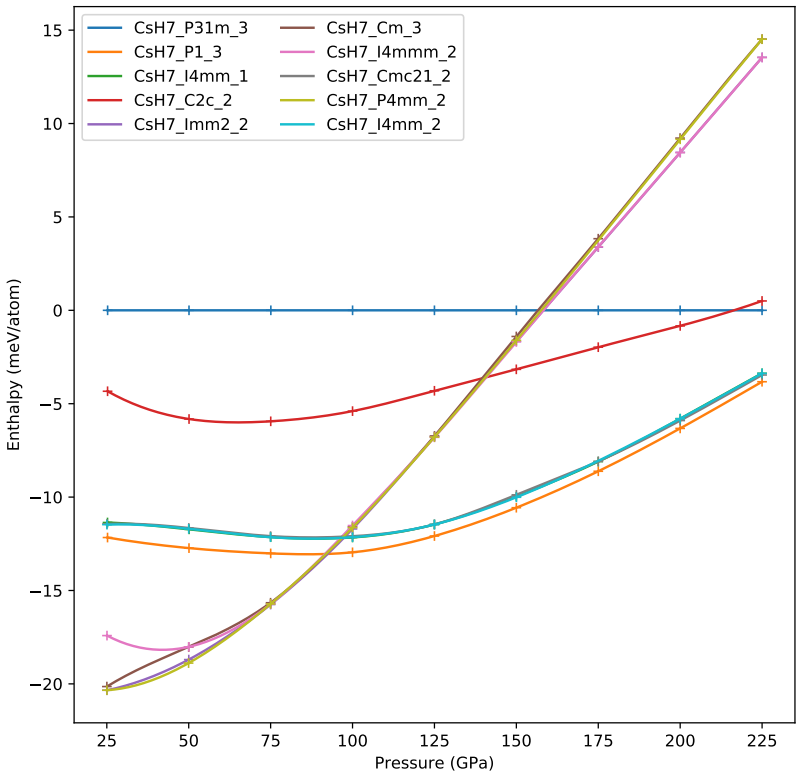

Fig. C.1 Enthalpy vs pressure for CsH_7 structures from AIRSS

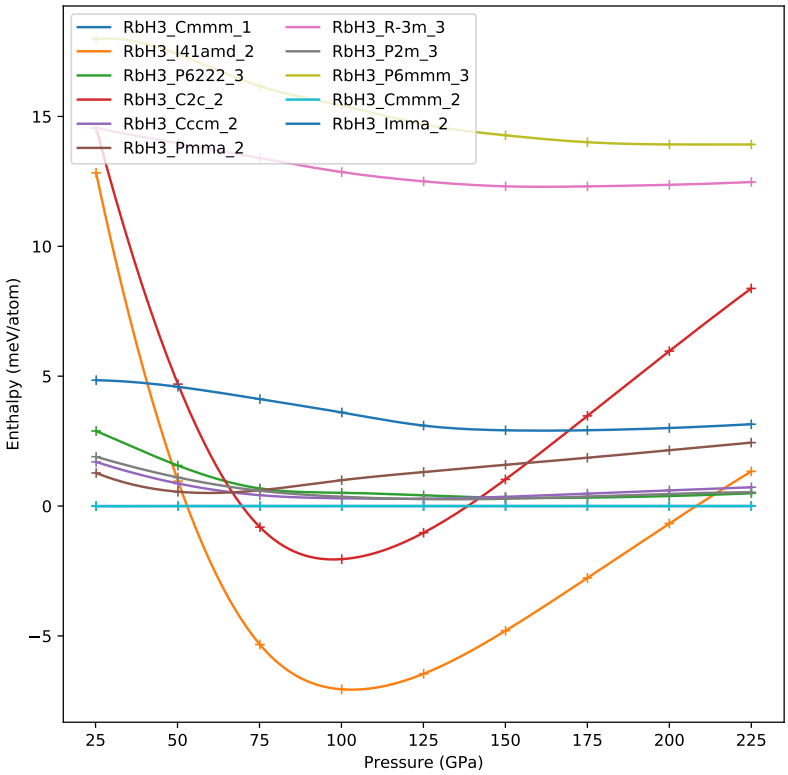

Fig. C.2 Enthalpy vs pressure for RbH_3 structures from AIRSS

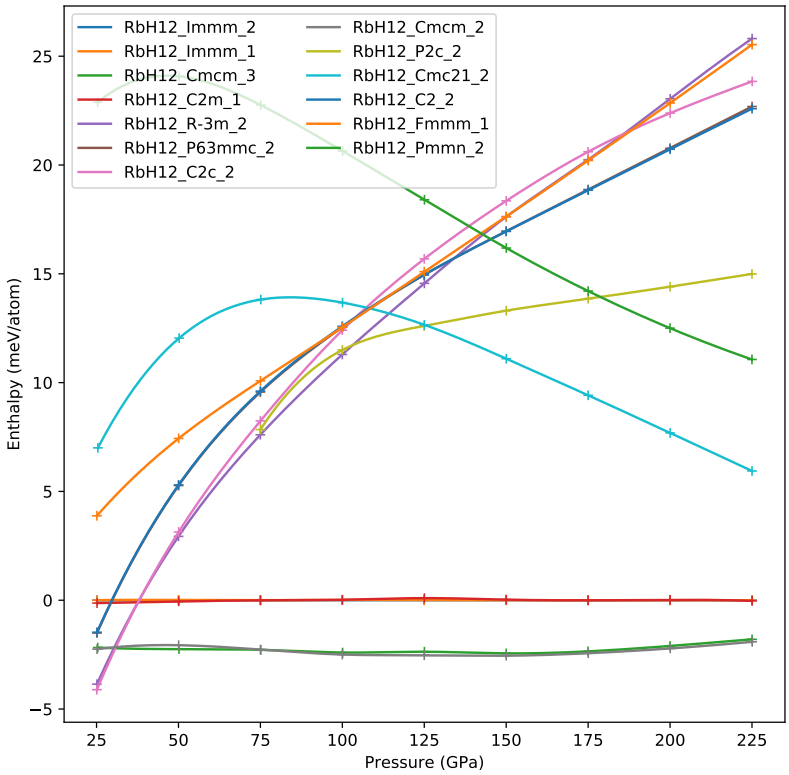

Fig. C.3 Enthalpy vs pressure for RbH_{12} structures from AIRSS

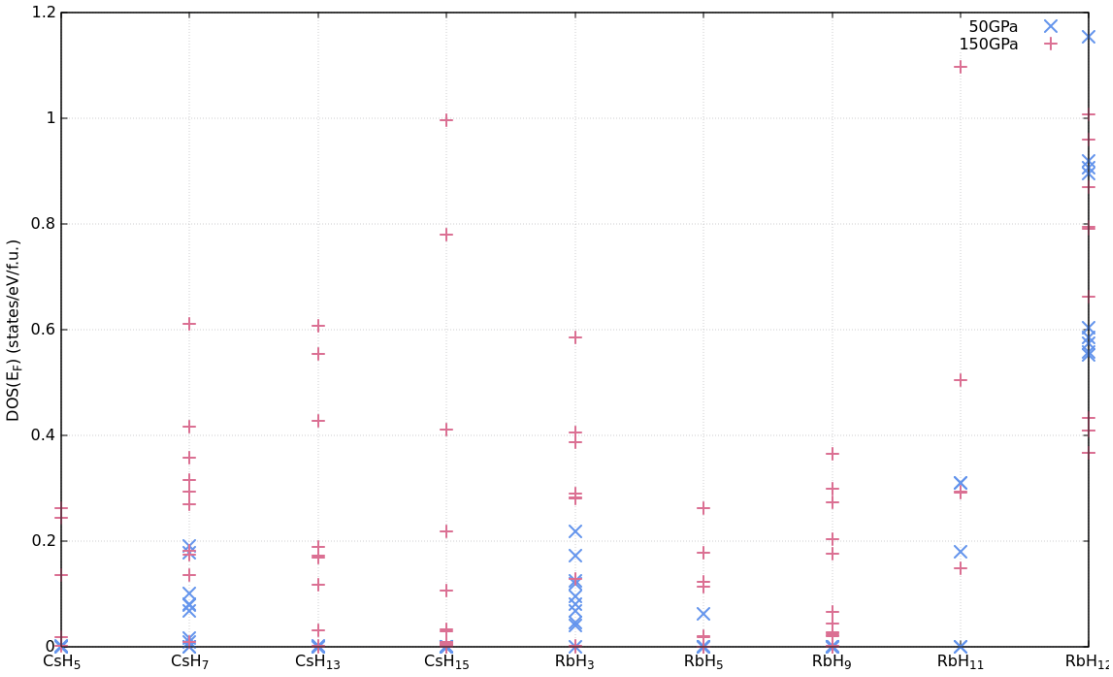

Fig. C.4 A plot summarising N(E_F) at 50 and 150 GPa for structures found using AIRSS. The purpose of this figure is to summarise the results of the DOS calculations; a structure-by-structure break-down is what allowed us to ensure we selected metallic structures for study in Chapter 5.